Dynamics and kinetics of the O_2-evolution step in Photosystem II:
a time-resolved polarography and X-ray spectroscopy study

Dissertation

zur Erlangung des Grades eines Doktors
der Naturwissenschaften (Dr. rer. nat.)

am Fachbereich Physik der Freien Universität Berlin

vorgelegt von

Ricardo Assunção

Berlin, 2022

Erstgutachter:	Prof. Dr. Holger Dau
Zweitgutachterin:	Prof. Dr. Athina Zouni

Tag der Disputation:	28-10-2022

Abstract

Photosystem II is a large oxidoreductase protein complex with a crucial role in oxygenic photosynthesis where it makes use of its unique catalytic ability to facilitate water oxidation. Apart from this fundamental importance, the research on this protein has attracted extra attention over the last couple decades as PSII also serves as a paragon for the development of synthetic catalysts for solar fuel production. Consequently, great advancements have been made, with important contributions from crystallography, spectroscopy, and computational methods, so that the structure and reactive cycle of PSII is now much better understood. Although some questions remain open, like the identities of the substrate water molecules, the type of mechanism involved in the formation of the O-O bond, the proton dynamics around the reaction center of PSII, the role of structural and molecular reorganizations and the impact of special features, like red-shifted pigments in the catalytic cycle. To tackle the first question, and indirectly the second, a temperature dependent study of the interaction of ammonia, a substrate water analogue that binds directly to the Mn-cluster of PSII, was performed. From it, three possible binding spots directly to or in the close vicinity of the Mn-cluster were suggested, one of which might be a substrate water binding site. Further O_2 polarography measurements of several PSII cores with unique point mutations of H-bond active residues offered a broader perspective on the protonation dynamics away from the OEC specially identing the broad channel as the most probable H^+ pathway in $S_3 \rightarrow S_0$, with E65 as a key participant in this process. As most dynamics of the S-state cycle freeze out below 200 K, an investigation of dark-adapted PSII by means of a temperature-dependent EXAFS study identified a breakpoint in the Debye-Waller factor at this exact temperature point, revealing the importance of vibrational mobility and molecular reorganizations in the S-state transitions, which may relate to the much slower τ-value than theoretically predicted for the ET from OEC → $Y_Z^{\bullet+}$. Lastly, the study of PSII containing red-shifted chlorophylls showed for FRL *C. thermalis* a significant slowdown of the O_2 release and an increase in a $\Delta G^{\ddagger}$ 40 mev higher than the average value found for common PSIIs, further supporting that the reaction center of PSII from FRL *C. thermalis* have at least one Chl replaced by a red-shifted one.

Zusammenfassung

Photosystem II ist ein Schlüsselenzym der oxygenen Photosynthese, das als Oxidoreduktase die Wasserspaltung ermöglicht. Neben dieser Eigenschaft, hat das Enzym in den letzten Jahrzehnten zudem weitere Aufmerksamkeit als Vorlage für die Entwicklung synthetischer Katalysatoren für die Gewinnung von Brennstoffen mittels Sonnenenergie erhalten. Durch die Nutzung verschiedener Methoden wie Röntgenkristallographie, Spektroskopie oder Computersimulationen konnten grundlegende Erkenntnisse über dessen Funktion und Struktur gewonnen werden, wobei einige Fragen aber weiterhin offenblieben. So ist weiterhin unklar, welche Wassermoleküle als Substrat dienen, wie die O-O-Bindung im Detail erfolgt, welche Protonierungsdynamiken im Reaktionszentrum ablaufen und wie sich strukturelle und molekulare Umorientierungen im Proteinkomplex , wie z.B. die Einlagerung rot-verschobener Pigmente auf den katalytischen Zyklus auswirken. Um die ersten beiden Fragen zu adressieren, wurden im Rahmen dieser Arbeit, temperaturabhängige und zeitaufgelöste Sauerstoffmessungen mit Ammonium, einem Substratwasseranalogon, das direkt an den PSII-Mangan-Cluster bindet, durchgeführt. Diese zeigen drei Bindungsmöglichkeiten in der unmittelbaren Nähe des Mn-Clusters, mit einer als mögliche Substratwasserbindungsstelle. Weitere Sauerstoffpolarografie-Experimente mit PSII-Varianten bei denen Wasserstoffbrücken-bildende Aminosäuren ausgetauscht wurden, ermöglichten die Untersuchung der Protonierunsgdynamiken um den OEC (oxygen evolving center) und unterstützen die Hypothese, dass der breite Kanal mit E65 als Hauptprotonenweg im $S_3 \rightarrow S_0$ Übergang fungiert. Durch temperaturabhängige EXAFS-Studien an dunkel-adaptiertem PSII konnte ein Umschlagpunkt des Debye-Waller-Faktors bei 200 K bestimmt werden, der auch dem Temperaturpunkt entspricht, an dem der S-Zyklus zum Erliegen kommt. Diese Ergebnisse unterstützen, dass Vibrationsmobilität und molekularer Umorientierung während der S-Zyklus-Übergänge eine entscheidende Rolle spielen und in Verbindung mit dem im Vergleich zur Theorie deutlich verlangsamten τ-Wert beim Elektrontransfer vom OEC zu $Y_Z^{\bullet+}$ stehen könnten. Abschließende Untersuchungen an einer PSII-Variante mit rot-verschobenen Chlorophyllmolekülen, zeigte eine deutliche Verlangsamung der Sauerstofffreisetzung und eine Erhöhung in $\Delta G^{\ddagger}$ um 40 meV im Vergleich zu gewöhnlichen Chlorophyll a-PSII-Varianten. Diese Unterschiede stützen die Hypothese, dass mindestens ein Chlorophyllmolekül im Reaktionszentrum durch ein rot-verschobenes Chlorophyll ersetzt wurde.

Table of contents

Glossary

ATP	Adenosine triphosphate
BBY	PSII enriched membrane particles from spinach
BSA	Bovine serum albumin
CE	Counter electrode
Chl	Chlorophyll
DCBQ	2,6-Dichloro-1,4-benzoquinone
DCMU	(3-(3,4-dichlorophenyl)-1,1-dimethylurea
DF	Delayed chlorophyll fluorescence
$\Delta G^{\ddagger}$	Gibbs free energy of activation
$\Delta H^{\ddagger}$	Enthalpy of activation
$\Delta S^{\ddagger}$	Entropy of activation
Ea	Activation energy
EPR	Electron paramagnetic resonance
ET	Electron transfer
EXAFS	Extended X-ray absorption fine structure
FA	Flash artifact
FaRLiP	Far-red light photoacclimation
Fd	Ferredoxin
FIOPs	Flash-induced oxygen patterns
FNR	Ferredoxin-NADP+ reductase
FRET	Förster resonance energy transfer
FRL	Far-red light
FT	Fourier-transform
FTIR	Fourier-transform infrared spectroscopy
FWHM	Full-width at half-maximum
h	Planck's constant

HEPES	4-(2-hydroxyethyl)-1-piperazineethanesulfonic acid
HPF	High-pass filter
k_B	Boltzmann constant
KIE	Kinetic isotope effect
K_M	Michaelis constant
LED	Light emitting diode
LHC	Light harvesting complex
MES	2-(N-morpholino)ethanesulfonic acid
$NADP^+$/NADPH	Nicotinamide adenine dinucleotide phosphate
OEC	Oxygen evolving complex
P680	Primary electron donor of PSII
P700	Primary electron donor of PSI
PC	Plastocyanin
PDB	Protein Data Bank
PF	Prompt chlorophyll fluorescence
Phe	Pheophytin
PM	Photomultiplier
PMSF	Phenylmethylsulfonylfluorid
PQ	Plastoquinone
PQH_2	Plastoquinol
PSI	Photosystem I
PSII	Photosystem II
PVC	Polyvinylchlorid
Q_A	Primary quinone acceptor of PSII
Q_B	Secondary quinone acceptor of PSII
QM/MM	Quantum mechanics/molecular mechanics
WE	Working electrode
W_f	Fast exchanging substrate water of PSII
WL	White light

WT	Wild-type
W_s	Slow exchanging substrate water of PSII
XANES	X-ray absorption near edge structure
XAS	X-ray absorption spectroscopy
Xrp	X-ray photoreduction
Y_Z	Tyrosine Z (D1-Tyr161) of PSII

Chapter 1 – Introduction

To convert solar energy into electrochemical energy, ancestral photosynthetic organisms found a way to put together the complex series of optimized and interconnected processes, molecules and structures that evolved to make oxygenic photosynthesis possible. Knowing that the Sun provides most of the energy that arrives to the surface of the earth daily, this was a great achievement, that not only sustains most of the life on earth since a few billions of years ago but also made it possible for the development of more complex life across the globe. An urgent goal of our present society, with its ever-increasing energy demand, is to switch progressively to more and more sustainable energy sources. Maybe there is not a single unique end to this problem, but certainly that learning from the biological systems that have been successful in utilizing energy from the sun, may contribute a possible solution. Therefore, in the last decades the study of photosynthesis, especially related to Photosystem II, caught extra attention from researchers who still try to uncover the dynamics and mechanisms of this protein that serves as a source of inspiration for the development of artificial methods and materials for the production of solar fuels (Dau et al., 2010; Faunce et al., 2013; Gust et al., 2009; Lewis & Nocera, 2006).

1.1 Oxygenic phtosynthesis

Photosynthesis is an efficient biological process that captures and stores the light energy arriving from the Sun, through a series of conversion events into chemical energy (Blankenship, 2021; Noring et al., 2008). The excitation of light harvesting pigments by an incident photon causes an electron to be transferred along biochemical pathways that lead to the reduction of CO_2 into a carbohydrate. Particularly in oxygenic photosynthesis, the most widespread form of photosynthesis, electrons are harvested from water molecules (the reductant) to fuel chemical reactions that include the production of glucose and molecular oxygen (Eq. 1.1) (Kiang et al., 2007).

$$6\,CO_2 + 12\,H_2O \xrightarrow{h\nu} (C_6H_{12}O_6) + 6\,H_2O + 6\,O_2 \qquad \textbf{(Eq. 1.1)}$$

Two parts compose this process, the light dependent reactions, and the light independent reactions. The Z-scheme of photosynthesis (Shevela & Björn, 2017) describes the linear electron transport of the light dependent reactions of oxygenic photosynthesis that occur in the thylakoid membranes and where the main protein complexes involved in light capture are located (Dekker & Boekema, 2005). The main goal of these reactions is to fix the energy and convert it into energy carriers either by the production of NADPH by the ferredoxin-NADP-reductase (FNR), or by pumping protons across the membrane to the lumen side to create the proton motive force required to produce ATP by the ATP synthase. A summary scheme that describes these reactions can be seen on Fig. 1.1.

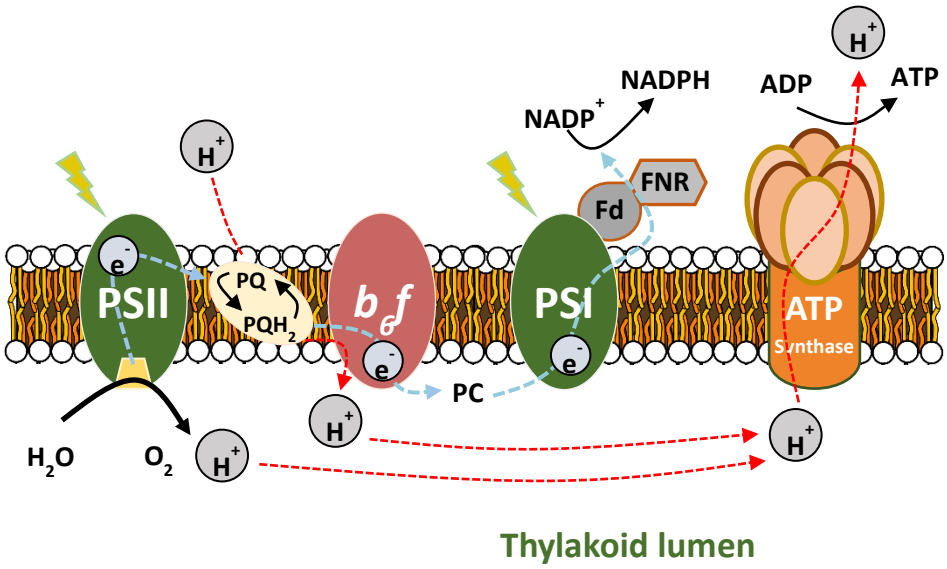

Figure 1.1 – Generic scheme of the thylakoid membrane showing the key proteins and processes involved in photosynthesis. The blue line-arrows show the linear electron flow and the red arrows the proton movement/pumping. PSII is the oxy-reductase photosystem II that contains the oxygen evolving complex which splits water and evolves oxygen, extracting electrons from the water to facilitate the reduction of plastoquinones (PQ). The Cytochrome b_6f mediates the electron transfer from the plastoquinol (PQH_2) to the Plastocyanin (PC) while pumping a proton to the lumen side of the membrane. Photosystem I (PSI) utilizes light energy to promote the reduction of ferredoxin (Fd) by the transfering of electrons across the membrane from PC. FNR (ferredoxin-NADP-reductase) utilizes the reduced Fd to reduce $NADP^+$ to NADPH. Lastly ATP synthase can use the proton gradient to produce ATP from ADP. The cyclic electron flow (from reduced Fd to b_6f) is not shown for simplicity.

The light independent reactions make use of the produced energy carriers (NADPH and ATP) and captured CO_2 to produce glucose in a series of cyclic reactions called the Calvin cycle (Raines, 2003). Even though these are known to be light independent because they don't require photon activation, they mostly do not occur in the absence of light since they rely on the short lived NADPH produced in the light dependent reactions (Lonergan, 2000).

1.2 Photosystem II

Photosystem II (PSII) is a large oxy-reductase protein-complex that is involved in the first step of light dependent reactions in oxygenic photosynthesis. Its main task is to extract electrons from H_2O, making use of an excited state promoted by photon absorption, to reduce a plastoquinone to plastoquinol, which serves as an electron carrier along the thylakoid membrane. Generally this protein complex functions as a dimer but the occurrence of monomers can be seen in isolation extracts as they may be an intermediate in the dimmer's assembly and/or reparation mechanism (Hankamer et al., 1997).

1.2.1 Structure

Each monomer is then composed of at least 20 subunits, the exact amount varying slightly on the specific organism. Among them the main subunits are the PsbA (D1 protein) that contains most of the reaction center, the PsbB (CP47) and PsbC (CP 43) that are light harvesting complexes (LHC), the PsbD (D2 protein) which envelop part of the reaction center and the PsbO which is the manganese stabilizing protein (Barber, 2002). Understanding the structure of the protein has been one of the main paths towards the comprehension of its function. In 2001 a great leap forward was made with the first x-ray crystal structure of PSII at a resolution of 3.8 Å, which gave a much better perspective on the spatial organization of the subunits and cofactors (Zouni et al., 2001), when compared with the previously available 15-30 Å resolution electron microscopy

structure for active PSII (Nield et al., 2000) or the 8 Å electron crystallography of two-dimensional crystals of unactive PSII core fragments. From there, further experimental improvements made it possible to progressively increase the resolution (3.5-3 Å) of new crystal structures (K. N. Ferreira et al., 2004; Loll et al., 2005), which allowed to understand the arrangement of the cofactors more precisely, especially the positions of the metal atoms of the oxygen evolving complex (OEC). Furthermore in 2011, a structure with even higher 1.9 Å-resolution made it possible to access the distribution of water molecules in PSII including the ones connected to the manganese cluster and its composing oxygen atoms arranged in μ-oxo bridges (Umena et al., 2011). The structure was later confirmed to be very similar to the PSII structure at room temperature (Young et al., 2016). Fig 1.2 shows a representation of a more recent structure of dark adapted PSII at room temperature (6DHE from PDB) (Kern et al., 2018).

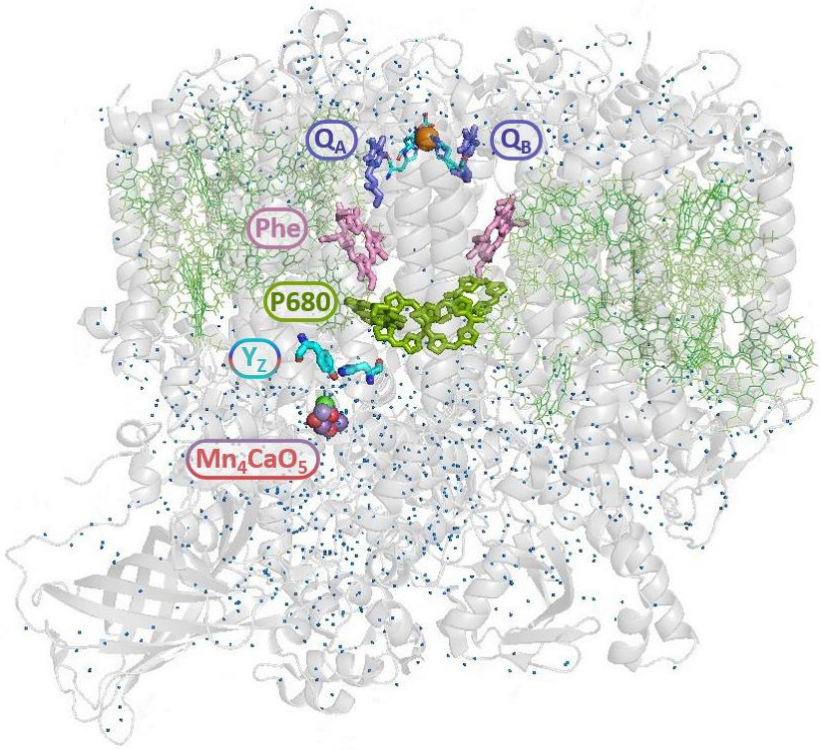

Figure 1.2 – Structure of a dark adapted PSII monomer with highlighted cofactors from the reaction center, including the OEC, which is identified by the chemical formula Mn_4CaO_5, the redox active tyrosine Y_Z, the special chlorophyll unit P680, the pheophytins (Phe) and the quinones Q_A and Q_B. Also, the distribution of the other chlorophylls in the protein can be seen as thin green lines and resolved water molecules as small blue dots. Figure made with pymol based on the structure 6DHE from PDB (Kern et al., 2018).

The OEC is an inorganic Mn_4CaO_5 cluster that appears as a Mn_3CaO_4 structure where the metal atoms are linked through μ-oxo bridges in a hetero-cubane manner that is then connected to an extra dangler Mn via an additional μ-oxo bridge (Fig. 1.3) (Vinyard & Brudvig, 2017). The Mn atoms are numbered from 1 to 4 as well as the five bridging oxygen atoms which are numbered from 1 to 5, furthermore four water molecules are bond to the manganese cluster in the $S_0 - S_2$ states, two of them are bound to the dangler Mn4 which are named W1 and W2 and the other two to the Calcium atom and are named W3 and W4 (Fig 1.3) (Umena et al., 2011). The Mn cluster is ligated to the protein environment by several amino acid residues mostly via carboxylate groups (Debus, 2008).

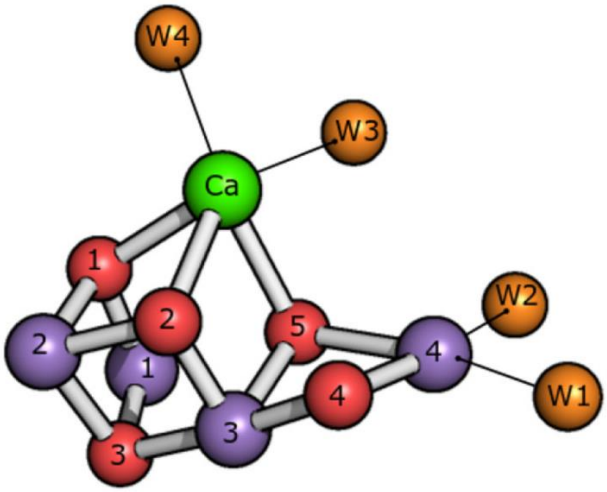

Figure 1.3 – Structure of the Mn_4CaO_5 cluster from dark adapted PSII centers according to the X-ray structure 3WU2 from PDB (Umena et al., 2011). The purple spheres represent the four Mn atoms, the red spheres the five bridging oxygens, the orange balls the four water molecules and in green the coordinated Ca^{2+} ion can be seen (Figure from Assunção et al. (2019)).

1.2.2 Photochemistry and electron transfer pathway

The photochemistry of PSII starts with light absorption by one of the chlorophylls (Chl) that will quickly funnel via FRET the excitation energy to the special Chl unit (P_{680}) in the reaction center, unless it directly absorbs a photon. The created excited state P680* drives a series of redox reactions (Fig 1.4), starting with electron transfer to the

pheophytin (Phe) that in turn transfers the electron to quinone A (Q_A) these initial two reactions happen within 20 and 300 ps, respectively, ending up with the redox pair $P_{680}^{+}Q_A^{-}$ (Klauss, Haumann, et al., 2012). The Q_A is strongly bound and thus not mobile, neither in the oxidized nor the reduced state, and is stereochemically unable to be reduced through the same process a second time. Q_B is the final electron acceptor in PSII and receives the electron from Q_A^{-} with a 0.5-10 ms time constant via the non-heme Fe(II). Q_B is loosely bound but the formation of an extra hydrogen bond after the first reduction increases its affinity to its binding site, ensuring that the Q_B^{-}/Q_BH intermediate will not be replaced and will serve as the substrate for the second reduction. This way the final quinol product, Q_BH_2, is formed, which then leaves PSII and works as an electron transporter towards cytochrome *b_6f* (Muh et al., 2012). This process in the acceptor side of the PSII reaction center has a cycle that comprises of two light absorption instances that correspond to the two reductions of the Q_B which after being fully reduced to Q_BH_2 is replaced by a nearby quinone to restart the cycle. On the donor side, the positive charge at the $P680^{\bullet+}$ is reduced by the nearby redox active tyrosine (Y_Z) within 100 ns of the radical formation. Furthermore, $Y_Z^{\bullet+}$ oxidizes the Mn_4CaO_5-cluster with time constants varying between 40 µs and 2 ms depending on the oxidation state of the OEC (Haumann, Liebisch, et al., 2005; Klauss, Haumann, et al., 2012).

For the OEC to split water, it needs to accumulate four oxidizing equivalents achieved through the absorption of four photons. This four-step reaction cycle of the Mn-cluster is most commonly called the extended S-state cycle (Klauss, Haumann, et al., 2012), which is a more complete version of the initial Kok cycle (Kok et al., 1970). In this cycle's nomenclature, S stands for state and the subscript, from 0 to 4 corresponds to the number of oxidations above the most reduced state S_0 where three Mn atoms are in the oxidation state III and one in IV (Kulik et al., 2007).

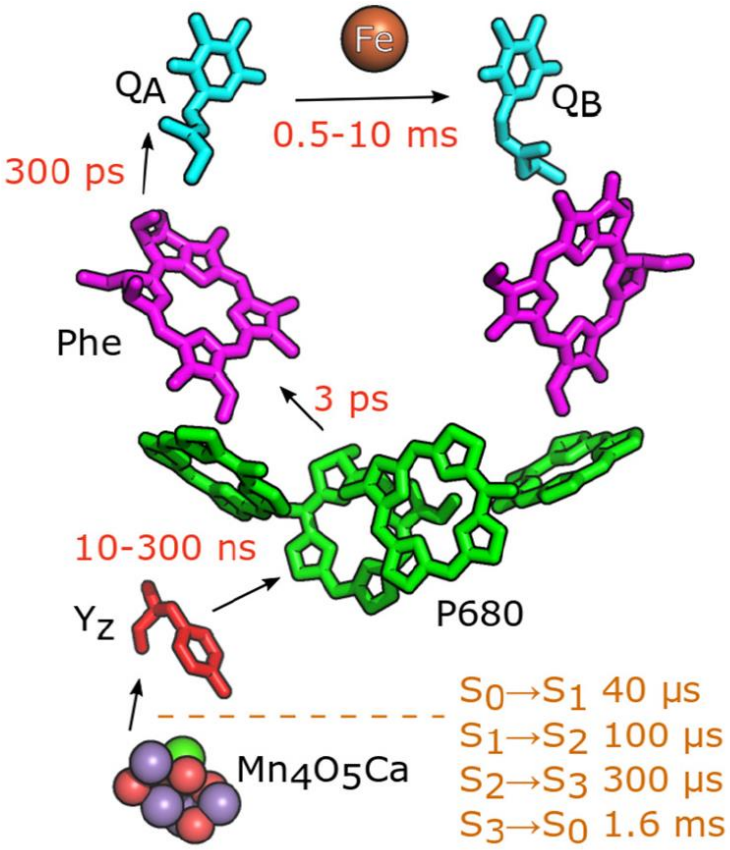

Figure 1.4 – Main cofactors in the reaction center of PSII as in the X-ray structure 3WU2 from PDB (Umena et al., 2011), with the main electron transfer pathway evidenced by the black arrows and respective time constants (Figure from Assunção et al. (2019))

1.2.3 The S-state cycle

While using a precursor of the time resolved O_2 polarography technique, primarily used during the course of this thesis work, Joliot et al. could measure on dark adapted samples of an *algae* of the genus *Chorella*, for the first time a flash induced pattern with a period of four oscillation (Joliot et al., 1969). The following year after the publishing of these results Kok and co-workers performed similar experiments and came up with a model for the reaction cycle that refuted the initial one proposed by Joliot and co-workers (Kok et al., 1970). This model became to be known as the Kok cycle or S-state cycle, which was later confirmed by both research groups in a series of independent experiments (Joliot & Kok, 1975). A historical review up to this point can be read in

(Joliot, 2003). The Kok cycle comprised of a four-step reaction cycle that included the S_0 and S_1 dark stable states, the S_2 and S_3 semi-stable states and the transient S_4 state. In dark adapted PSII a mixture of both S_0 and S_1 occurs, and the ratio depends on the preparation, however a majority of S_1 (about 75%) is often observed. This occurs because in the steady state, all states are present and mixed in about equal proportions of about 25% each, and in the dark the S_2 and S_3 states decay to the S_1 state. Moreover, the Kok's model already considered the existence of a miss factor (α) and double hits (β). The miss factor is the percentage of PSII centers that do not advance to the next S-state upon saturating light flash excitation and the double hits are the few cases where a PSII center advances two S-states with a single saturating light flash excitation (Forbush et al., 1971). Nowadays extended Kok models are commonly used to fit flash induced oxygen patterns (FIOPs) as they consider S_i dependent miss factors. An application and comparison of a few models can be seen in (Noring et al., 2008). As there is at present much more knowledge about the reaction cycle of PSII than when the S-state cycle was initially proposed, it is often referred as the "extended S-state cycle". Fig. 1.5 shows a comparison between the classical S-state cycle (inner circle) and the extended version (outer circle).

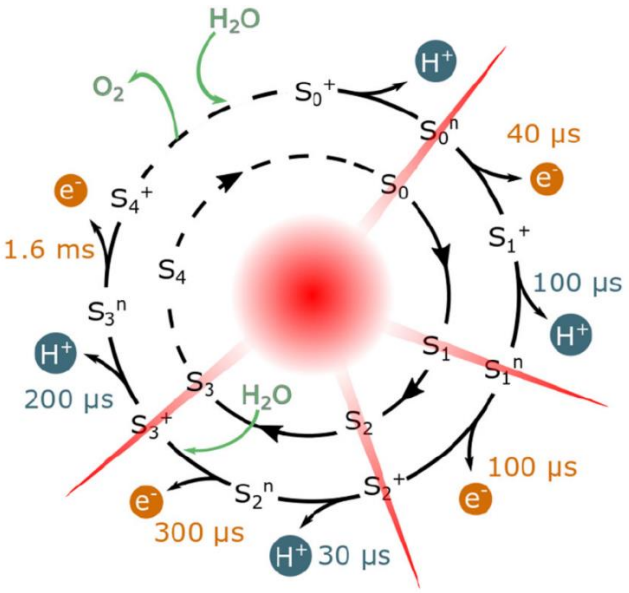

Figure 1.5 – Reaction cycle of the Mn complex in PSII. The inner circle shows the classical S-state model, and the outer circle shows the extended S-state model which includes the alternating electron and proton removal (Klauss, Haumann, et al., 2012) and the respective superscript notation n for neutral and + for positive. The know time constants for the events are shown and the H_2O uptake and oxygen release are shown in green. (Figure from Assunção et al. (2019)).

As each of the four transitions in the S-state cycle of OEC have unique features and events that makes all of them different, it is important to address them separately:

$S_1 \rightarrow S_2$ transition

In the S_1 state, the Mn cluster (Fig 1.3) is diamagnetic and has the oxidation states (III, IV, IV, III) (Koulougliotis et al., 1992), which follow the same numbering as in the picture. The transition to the S_2 state involves only an electron transfer meaning that in S_2 the OEC has a positive charge and so this transition can also be more accurately represented as $S_1^n \rightarrow S_2^+$ (Klauss, Haumann, et al., 2012). The electron transfer has a time constant of 100 µs with practically no pH dependency (at 23 °C (Gerencser & Dau, 2010) or at 20 °C (Klauss et al., 2015)). A low KIE 1.1-1.3 has also been recorded for this transition (Gerencser & Dau, 2010; Klauss et al., 2015; Zaharieva, Dau, et al., 2016). Structurally the S_2 state recorded recently at room temperature by femtosecond X-ray crystallography shows almost no difference when compared to S_1 (Kern et al., 2018) just like it has been suggested by an EXAFS study before (Yano & Yachandra, 2014). The S_2 state is paramagnetic and its possible to generate by applying continuous illumination at low temperature (140-200 K) (Casey & Sauer, 1984), as such, it has been extensively studied by EPR spectroscopy (Pokhrel & Brudvig, 2014). In these studies, clear identification of two isomers was achieved, generally referred as the low-spin open cubane with a multiline 1/2 spin $g \approx 2$ signal and the high-spin closed cubane with a 5/2 spin $g \approx 4.1$ signal, being that the isomer seen in by crystallography was the low spin one. These two isomers are interchangeable in a tautomerism manner by placement of Mn oxidation obtained by electron transfer either on the Mn1 or the Mn4 which make the O5 bond shift towards the higher oxidation Mn. As the EPR experiments were performed at low temperature the existence of the 5/2 isomer at room temperature is still in discussion but it could represent a minor fraction <20%, a transient state or have a different structure from the proposed “closed cubane” (Chatterjee et al., 2019; Pantazis, 2018).

$S_2 \rightarrow S_3$ transition

As at least a great majority of the low-spin configuration of the S_2 state is found at room temperature it is safe to assume that the transition starts from this conformation (Kern et al., 2018). The EPR study of Boussac et al. (2018) also support this idea, further suggesting that the S_2 low-spin state advances to S_3 via the S_2 high-spin state, although Kern et al. (2018) have not found any evidence for the high-spin closed cubane form on the X-ray structure taken 150 µs after the second flash. The transition involves initially a deprotonation $S_2^+ \rightarrow S_2^n$ with a time constant of 30 µs and a KIE of 5.6, which replenishes the neutrality of the Mn-cluster so that it can be oxidized by Y_Z (Gerencser & Dau, 2010; Klauss, Haumann, et al., 2012; Service et al., 2014). Other spectroscopic studies have found similar time constants and KIEs confirming the results (Klauss et al., 2015; Zaharieva, Dau, et al., 2016; Zaharieva et al., 2013). The following electron transfer $S_2^n \rightarrow S_3^+$ has a time constant of 300 µs and a high KIE of 1.7-1.9 that shows its coupled nature to the preceding proton transfer (Gerencser & Dau, 2010; Klauss, Haumann, et al., 2012; Zaharieva, Dau, et al., 2016; Zaharieva et al., 2013). The end oxidation state of the Mn-cluster in the S_3^+ (S_3 state) is (IV, IV, IV, IV) (Cox et al., 2014). In S_3 an extra bridging oxygen, generally denoted O6 (or O_X) appears between the Mn1 and Mn4. This extra oxygen was firstly encountered in the 2-Flash data crystal structure from Suga et al. (2017), although with a short 1.5 Å distance from O5 which suggested the existence of a O−O bond already (e.g. in peroxide manner). More recently, with higher resolution structures it was possible to observe a clearer picture of the S_3 state, in which the distance between O5 and O6 was about 1.9-2.1 Å that is too long for the existence of a O−O bond (Kern et al., 2018; Suga et al., 2019). The work of Suga et al. (2019) further suggests that the O5-O6 bridge to be of the oxyl/oxo type, hypothesis that was further analysed and agreed upon by Mandal et al. (2020). The pathway for the insertion of O6 is suggested to be based on the movement of W3 towards Mn1 (Ibrahim et al., 2020; Kim & Debus, 2017), which is in line with some of the S_3 formation mechanisms proposed in QM/MM studies (e.g R-pathway in Shoji et al. (2015)).

$S_3 \rightarrow S_0$ transition

Starting in the S_3^+, this transition is initiated by the release of a proton forming the S_3^n state (Klauss et al., 2015). A time constant of about 200 µs at 18 °C was previously determined for a "lag phase" that was later attributed to that deprotonation event (Haumann, Liebisch, et al., 2005). More recently, similar time constants were obtained at 23 °C (150-170 µs) with a KIE of 2.4-2.5 (Gerencser & Dau, 2010; Zaharieva, Dau, et al., 2016). Following this first step, an electron transfer ($S_3^n \rightarrow S_4^+$) occurs that enables the O−O bond formation and release of O_2. This electron transfer, mostly pH and isotope effect independent (low KIE of 1.2-1.3) has a determined time constant of 1.6-1.7 ms at 20-23 °C for plant PSII (Gerencser & Dau, 2010; Klauss et al., 2015; Zaharieva, Dau, et al., 2016). Results from membrane inlet mass spectrometry excluded earlier O−O, e.g. as peroxide formation on S_2 or S_3, by showing that in all S-states both substrate waters exchange with the bulk solvent. This was done using H_2O^{18} which was then observed in the product (O_2). Each of the two water substrates showed different rates, one with a slow exchange rate (W_s) and one faster (W_f) (Cox & Messinger, 2013; Hillier et al., 1998; Messinger et al., 1995). A combination of this technique and EPR led to the conclusion that the W_s was in the µ-oxo bridge (Navarro et al., 2013) which later was assigned to be O5 (de Lichtenberg & Messinger, 2020; Lohmiller et al., 2017), although the identity of W_f still remains a mystery (Cox et al., 2020). Several experimental and theoretical studies have suggested different pathways for the O−O bond formation which have recently mostly fallen into two categories, the oxyl/oxo radical coupling and the nucleophilic attack (Vinyard & Brudvig, 2017). The first was initially proposed by Siegbahn (2009); Siegbahn (2013) and would occur inside the cubane unit, between the two bridging oxygens positioned between Mn1 and Mn4, namely O5 and O6. On the other hand, the nucleophilic attack at the Mn4 dangler manganese would take place externally, either via a water coordinated to the Ca or to Mn4 itself (Sproviero et al., 2008), although for this mechanism, considerably higher energy barriers have been estimated (Siegbahn, 2017). Either way, the formation of O_2, ($S_4^+ \rightarrow S_0^+$) reduces the Mn cluster back to $(Mn^{III})_3Mn^{IV}$ (Haumann, Liebisch, et al., 2005; Kulik et al., 2007), with the higher oxidation most likely to be located in the Mn2 (Yamamoto et al., 2020). An H_2O

binding to the OEC and a final proton release complete the transition to S_0^n (Klauss, Haumann, et al., 2012; Klauss et al., 2015).

$S_0 \rightarrow S_1$ transition

In the S_0^n state the structure of the OEC has a motif more like S_1 (Fig 1.3), with the disappearance of O6, which either went in the released O_2 or assumed the O5 position as the previous O5 reacted to form O_2 in the S_3-S_0 transition (Kern et al., 2018). From there, transitioning to the S_1 state involves initially an electron transfer ($S_0^n \rightarrow S_1^+$) followed by a proton release ($S_1^+ \rightarrow S_1^n$) (Klauss, Haumann, et al., 2012). The electron transfer has a time constant of 30-40 μs with a low KIE of 1.3 (Dekker et al., 1984; Klauss et al., 2015), and is expected to be respective to the oxidation of Mn3 (Yamamoto et al., 2020) which changes the pK_a of a μ-hydroxo bridge (Dau et al., 2001). The following proton transfer happens with a time constant of 100 μs, has a small pH dependence and a KIE of 3.0 (Klauss, Haumann, et al., 2012; Klauss et al., 2015), most likely from the referred μ-hydroxo bridge which was suggested to be O5 (Lohmiller et al., 2017; Pal et al., 2013) although more recently contradicting results from a study combining QM/MM and FTIR difference spectra indicate that O4 could be instead the protonated bridge that gets deprotonated on the way to S_1 (Saito et al., 2015; Yamamoto et al., 2020).

1.3 Reaction kinetics and transition state theory

In reactions kinetics, the Arrhenius equation (Eq. 1.2) is widely used to model the temperature effect on the rate of reactions (Laidler, 1984; Peleg et al., 2012). The consistent application of this "empirical" relationship in 1889 by Svante Arrhenius gave physical foundation to the equation previously developed by J. H. Van 't Hoff in 1884 (Logan, 1982). In the most common expression of the Arrhenius equation (Eq. 1.2) the k is the rate constant, A is the "pre-exponential factor" which is a frequency parameter, E_a is the activation energy, k_B the Boltzmann constant and T the temperature.

$$k = Ae^{-E_a/k_BT} \quad \textbf{(Eq. 1.2)}$$

According to this model, a linear plot of Ln*k* vs. $1/k_BT$ (*T* in K) should show a straight line from whose slope the activation energy can be directly determined. Despite its simplicity and usefulness, this linear relationship has a limited validity, restricted to a certain range of temperature, given that *A* and E_a can be temperature dependant even for elementary chemical reactions (Logan, 1982; Peleg et al., 2012). However, several studies have shown the clear linear relationship of PSII processes within the biological temperature range of PSII operation (Bao & Burnap, 2015; Zaharieva & Dau, 2019). In the Arrhenius model the activation energy was referred as the energy required to convert the reactants into the "active" form, now called the transition state (or activated complex in some literature) (Fig. 1.6), characterized by being the highest energy conformation on the minimum energy path from the reactants towards the products (Truhlar et al., 1996).

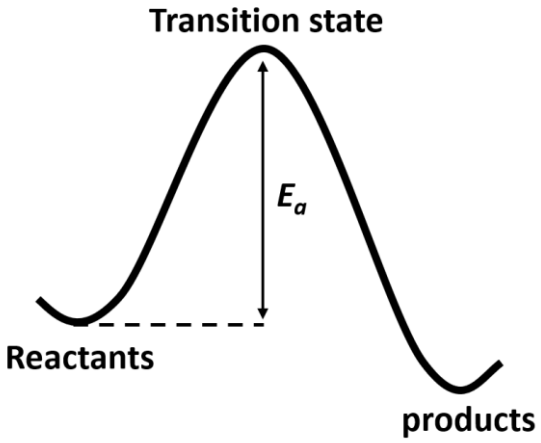

Figure 1.6 – Schematic representation of the physical meaning of activation energy as envisioned by the Arrhenius equation.

Based on the Arrhenius equation, the works of Eyring, Evans and Polanyi developed the theory of kinetics arriving in 1935 with the simultaneous formulation of the transition state theory (Evans & Polanyi, 1935; Eyring, 1935). In this theory further understanding of the parameters *A* and E_a was achieved, making possible to form a relationship between these and the enthalpy and entropy. The general form of the Eyring–Polanyi equation from this theory can be written as in Eq. 1.3 which resembles Arrhenius equation:

$$k = \frac{k_B T}{h} e^{\frac{-\Delta G^{\ddagger}}{k_B T}} = \frac{k_B T}{h} e^{\frac{\Delta S^{\ddagger}}{k_B}} . e^{\frac{-\Delta H^{\ddagger}}{k_B T}} \quad \textbf{(Eq. 1.3)}$$

where the *h* is the plank constant, $\Delta G^{\ddagger}$ is the Gibbs free energy of activation, $\Delta H^{\ddagger}$ is the activation enthalpy, $\Delta S^{\ddagger}$ the activation entropy, being that these last three thermodynamic quantities can be dependent on temperature. For a linear regime in a range of temperatures where their temperature dependence is negligible, the relationships between E_a and $\Delta H^{\ddagger}$ and between *A* and $\Delta S^{\ddagger}$ are given by Eq. 1.4 and Eq. 1.5 respectively (Guo et al., 2014):

$$\Delta H^{\ddagger} = E_a - k_B T_0 \quad \textbf{(Eq. 1.4)}$$

$$\Delta S^{\ddagger} = k_B \ln\left(\frac{hA}{k_B T_0}\right) - k_B \quad \textbf{(Eq. 1.5)}$$

1.4 Scope and organisation of the thesis

The goal of this thesis is to develop the current understanding of the dynamics of the reaction center in PSII, by employing mainly time resolve O_2 polarography which targets specifically the O_2 evolution step. It begins by an attempt at the identification of the substrate water molecules, by carrying out experiments with PSII under the influence of substrate-water analogue ammonia. Then by using X-ray absorption spectroscopy, we try to shed some light into the reasons behind the much slower than predicted (for the short distance) electron transfer from the OEC to Y_Z. This is followed-up with experiments on various PSII mutated variants to target the protonation dynamics during the S_3-S_0 transition. And lastly, the far-red photoacclimation process in organisms, where PSII Chls are replaced by red-shifted ones, was investigated in in the scope of comparing kinetics and thermodynamics. The chapters are organised as follows:

Chapter 3 investigates the activation barrier of the O_2-formation step of photosystem II under the influence of the substrate-water analogue ammonia at various concentrations.

Chapter 4 studies the protein glass transition of photosystem II through a series of temperature dependent EXAFS from 20 to 295 K.

Chapter 5 examines the O_2 evolution kinetics of several photosystem II variants from *Synechocystis* sp. PCC 6803 to better understand the protonation dynamics during the S_3-S_0 transition.

Chapter 6 compares the kinetics of the O_2 formation step in photosystem II with and without red-shifted chlorophylls, including the determination of the activation energy of a directly comparable case (*C. thermalis*).

Chapter 2 – Materials, Methods and set-up upgrades

In this section, the general experimental protocols will be presented along with the introductions to each specific measurement technique. The description of the experimental set-ups, and respective improvements done along the course of this project, will be also covered. The specific experimental details of each experiment are then presented in their respective chapter.

Buffer solutions (aqueous) were used in most experimental procedures. A detailed list containing the ingredients of each buffer solution and extra relevant information can be found in Appendix A.

2.1 Photosystem II sample preparation

For the study of photosystem II, many different types of samples can be used. Examples can be full organisms like cyanobacteria or algae, organism parts, like leaves; thylakoid membranes, plant thylakoid membrane particles (BBY), or even core complexes which would be the closest to the isolated protein. In this work, the PSII samples were prepared either from spinach or cyanobacteria (e.g. *Synechocystis* sp. PCC 6803), in the form of thylakoid membranes (for cyanobacteria) and BBY (for spinach). These have very high O_2 evolution activity and have the advantage that the PSII is embedded in its original lipid environment, even though in BBY the lumen and stroma sides are part of the same continuous liquid phase, meaning that there will be no longer a pH gradient across the membrane. In the case of spinach, like in other higher plants, the thylakoid membranes organize themselves in lamella and grana stacks, being that the second has much higher PSII concentration and so instead of full membranes, thylakoid membrane particles consisting mostly of the grana stacks are often preferred. These membrane fragment preparations (BBY) offer much higher activity and stability than the full spinach thylakoid membranes (Berthold et al., 1981; Schiller & Dau, 2000).

In full thylakoid membranes the amount of PSI present is about 60% of the total PSII (Fan et al., 2007), and through the BBY preparations it can be reduced below 25% (Danielsson et al., 2004)). This way, most of the chlorophylls in BBY samples come from PSII, which can have up to 100 on each monomer (Wei et al., 2016). The thylakoid membranes in cyanobacteria have normally a PSI/PSII ratio of about 2 (Melis & Brown, 1980) although it can vary in the range of 1 to 4 depending on the light condition (Fujimori et al., 2005). These are used as a whole, as they do not form grana stacks or any particular membrane structures that are preferred for the high PSII concentration.

2.1.1 PSII enriched membrane particles from spinach

Biologically grown Spinach (*Spinacia oleracea*) was commercially acquired from a local shop in lots of 4 kg which come in two lightproof cardboard boxes provided by us to the seller beforehand. These boxes keep the spinach in the dark to enhance further grana stacking (Anderson et al., 2012), and when they arrive at the lab are kept in a 4^{o}C cold room. To avoid unnecessary storing time, the spinach was generally obtained in the morning, just before the preparation.

The preparation, described below, goes mostly according to Schiller and Dau (2000), with slight modifications. In their work, the initial protocol to prepare PSII enriched membrane fragments from spinach, often called BBY (Berthold et al., 1981) was improved to produce samples with higher oxygen activity.

The experimental procedure is done under dim green light and the sample is always kept in the cold (4 ^{o}C). Ideally it should be done by 2-3 people to keep this process at a fast pace, avoiding extra time where unwanted enzymatic activity (especially proteases) that start once the leaf tissues are broken. These can damage the PSII centers lowering the final oxygen activity of the sample.

The spinach is prewashed at the sink to remove any excess dirt and passed to an ice-water bath. Inside the cold room (4°C), the good spinach leaves are separated from damaged leaves and the low PSII containing parts, like the stem, the petiole and

sometimes part of the bigger primary leaf veins and put into a bucket together with a bit of ice now and then to keep them cold. Along this process the ice bath keeps getting refiled with more prewashed spinach until there is enough spinach leaf parts in the bucket (about 10 l volume) to start the next step. A blender of 2 l is filled with the part of the prepared spinach leaf parts and 1 l of buffer A is added (the BSA and ascorbate in buffer A protect the sample against proteases and oxidation respectively). Now the leaves are blended with short blending cycles to keep the temperature from rising and as the blending makes room for more, the rest of the processed spinach is added. The liquid-paste is divided in two equal amounts, and each is then squeezed through a double layer of commercial gauze. The sample is further filtered through a layer of cheesecloth (Miracloth, Merck) placed in a funnel. Then, the filtrate is centrifuged for 10 min at 4 °C and 17000 g in two 1 l centrifuge tubes (Sorvall *LYNX 6000*, Thermo Scientific). The supernatant is discarded, and the pellet resuspended with a brush, in buffer B, which has a higher salt concentration (150 mM NaCl) to break the chloroplasts by osmotic pressure, and then it is centrifuged again in 6-8 40 ml centrifuge tubes for 2 min at 1100 g. this centrifugation step allows for the separation of a mixture of broken chloroplasts and thylakoid membranes, that stay in the supernatant, from the starch and other cell parts that will go to the pellet. Now, the supernatant is kept and recentrifuged at 50000 g for 12 min. To discard the lamella parts of the thylakoid membranes and keep most of the PSII rich grana stacks, a dissolution with a Triton X-100 mild detergent is used. The pellet is firstly resuspended in a limited amount of buffer C (under 100 ml) and then the chlorophyll$_{(a+b)}$ concentration is determined (see 2.2 in this chapter). The sample volume (V_0) is measured with a graduated cylinder before calculating with eq. 2.1 and 2.2 respectively the volume of buffer C (V_C) and the volume of Triton stock solution (V_T) to add. The extra buffer C is added to the sample and the in an ice-cooled beaker under slow stirring, the triton solution is added dropwise (about 2 min). After 1 min of incubation, the mixture is centrifuged at 1100 g for 2 min. Now the supernatant is collected and centrifuged for 15 min at 50000 g with a slow ramp-up acceleration (e.g. setting 6) to allow for the starch and cell debris to settle below the BBYs. The pellet is then partially resuspended in buffer D, leaving behind the starch which has a whiter colour. Up to three rewashing steps with buffer D (resuspension and re-centrifugation) follow-up, leading to the obtention of a starch free dark green sample.

Finally, the sample is collected by resuspending with a maximum of 50 ml of buffer D and then after determining the Chl concentration, which should be at least 2 mg/ml, it is stored in eppis with appropriate size (0.5-2 ml) at -80ºC. The oxygen activity of the prepared sample is determined preferably the same day and a value of 900-1400 $\mu mol_{O2}.mg_{Chl}^{-1}.h^{-1}$ (at 28 ºC, pH 6.2) should be obtained (using Buffer O_2).

$$V_C = V_0\ (\frac{2[Chl]}{5} - 1) \qquad \textbf{(Eq. 2.1)} \qquad\qquad V_T = \frac{V_0[Chl]}{10} \qquad \textbf{(Eq. 2.2)}$$

2.1.2 Thylakoid membranes from *Synechocystis* sp. PCC 6803

The preparation protocol for isolation of thylakoid membranes from *Synechocystis* sp. PCC 6803, was taught to me during my internship at the Burnap Lab at Oklahoma State University (OK, USA) where we performed it repeatedly, and although most of the *Synechocystis* sp. PCC 6803 samples used in this thesis were obtained later through collaborations with the groups of prof. Rick Debus and Prof. Robert Burnap, this protocol will be described below. Both groups collaborate and use this same protocol which was developed over the years based on the work of Burnap et al. (1989), Tang and Diner (1994) and Strickler et al. (2005).

The strain *Synechocystis* sp. PCC 6803 was originally isolated by Dr. J.G.K. Williams (DuPont, Wilmington, DE) (Mayes et al., 1993) and at the present date is likely the organism with the most available mutations of PSII, mainly because of its ability to tolerate heterotrophic growth with glucose containing media, meaning that even cells with mutations that severely impact photosynthesis, and thus non-autotrophic, can still grow. The wild-type strain and respective mutant strains were kept on solid (1.5% (w/v) agar) BG-11 media (Rippka et al., 1979) buffered with 20 mM HEPES-NaOH (pH 8.0) supplemented with 5 mM glucose, 20 mM $Na_2S_2O_3$ (Sodium thiosulfate) and 10 µM DCMU (Fig. 2.1). The later three are added from filtered solutions (pore size: 0.45 µm). For large scale cultivation, liquid BG-11 media with 5 mM glucose was inoculated with the strain of interest and grown without DCMU. This was done originally (Burnap Lab) in 7 l bottles at 30ºC, with cool white fluorescent lights and bubbling filter sterilized air,

enriched with about 3% CO_2. In our lab, instead we can use a 33 l tubular rector (Photobioreaktor PBR 25 S with xCubio control unit, bbi biotech) with automated control of several parameters like temperature, pH, light and CO_2 concentration. The growth can be controlled by measuring the optical density at 750 nm (OD_{750}) in a spectrophotometer and the cells are then harvested in the late log phase of the cell growth curve, which is the phase at which the total PSII per cell in the culture is the highest (Schuurmans et al., 2017) this happens at an OD_{750} value between 2 and 4.

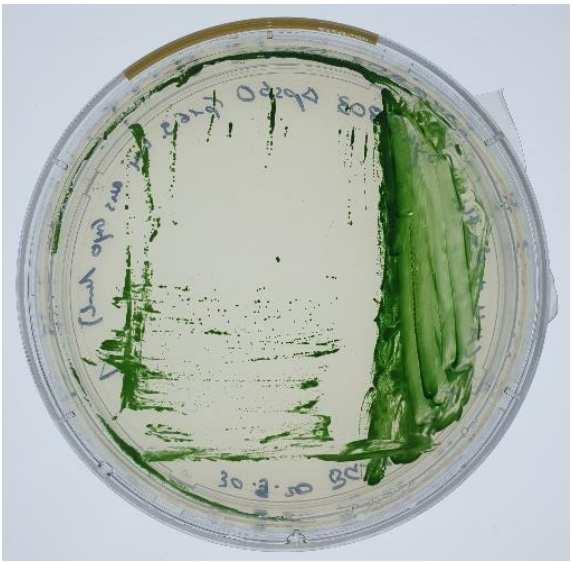

Figure 2.1 – Picture example of a *Synechocystis* sp. PCC 6803 strain in solid BG-11 media.

For this protocol, 21 l of cyanobacteria are harvested by centrifugation at 12,000 × g for 12 min at 4 °C (Sorvall *LYNX 6000*, Thermo Scientific), and then resuspended in buffer TMB (50 mM MES-NaOH (pH 6.0), 10% (vol/vol) glycerol, 1.2 M betaine, 5 mM $MgCl_2$, and 5 mM $CaCl_2$, 0.45 µm filtered) to a final volume of 600 ml. After an additional centrifugation step at 13000 x g for 15 min at 4 °C, the sample is resuspended with buffer TMB to a maximum volume of 120 ml and then left for 1h on ice in the dark. All following steps were performed in a cold room at 4°C and under dim green light. For cell breakage, 120 ml of sample at about a concentration of 1 $mg_{Chl}.ml^{-1}$ is transferred into two bead beaters (half each) and 42 ml of zirconia/silica beads with a diameter of 0.1 mm are added to each vessel. Before cell breakage, 55 µl of 1 M benzamidine, 55 µl of 1 M ε-amino-η-caproic acid and 220 µl 0.25 M phenylmethanesulfonyl fluoride (PMSF) were added. The cells were broken in the bead beaters (Bio-Spec Products) inside an ice-water

jacket, using nine cycles of 15 s on and 5 min off for the wild type cells or six cycles for the mutant cells. The resulting mixture was transferred two times from beaker to beaker using excess buffer TMB to separate all the sample containing the thylakoid membranes from the beads deposited at the bottom of the beakers. The total volume of no more than 400 ml was then centrifuged at 5000 x g for 10 min at 4 °C to remove cell debris and residual beads. The supernatant with the extracted thylakoid membranes was then ultra-centrifuged (Sorvall WX Ultra 80, Thermo Scientific) at 165000 x g for 40 min at 4 °C. The blue supernatant with red fluorescence, that contains a high amount of phycobilisomes, is discarded and the pelleted thylakoid membranes are resuspended in buffer TMS (50 mM MES-NaOH (pH 6.0), 10% (vol/vol) glycerol, 1.2 M betaine, 20 mM $CaCl_2$, and 5 mM $MgCl_2$, 0.45 µm filtered) to a chlorophyll concentration of 1-1.5 mg ml^{-1} before being snap-frozen in liquid nitrogen and stored at -80 °C.

2.1.3 Thylakoid membranes from other organisms

Even though I was only involved in the preparation of samples from Spinach (*Spinacia oleracea*) and *Synechocystis* sp. PCC 6803, during this thesis work other samples from other types of organisms were obtained from colleagues in our group.

Thermosynechococcus elongatus thylakoid membranes were provided by Janis Hantke who grew the cells culture and prepared the samples according to Schuth et al. (2017) beased on the previous protocol of Kern et al. (2005).

The samples from *Acaryochloris marina*, *Chroococcidiopsis thermalis* PCC 7203 grown in white light conditions (WL grown) and *Chroococcidiopsis thermalis* PCC 7203 grown in far-red light conditions (FRL grown) were provided by Viktor Eichmann and Dr. Dennis Nürnberg, who used a modified version of the protocol described for the preparation of thylakoid membranes from *Synechocystis* sp. PCC 6803 (Eichmann, 2021).

Thylakoid membranes from *Mastigocladus laminosus* and *Chlamydomonas nivalis* were provided by Lena Schäfer, who described the protocol in her master thesis (Schäfer, 2018).

2.2 Determination of chlorophyll concentration

To handle and do experiments with proteins in solutions, it is important to know their concentration. Although not complicated, the determination of protein concentration is not a quick and simple task (Bradford, 1976), the determination of Chl concentration for PSII can be an indirect, although fast, way of achieving that. This measurement is accurate and quantitative (Lichtenthaler, 1987), that facilitates the usage of sample in comparable amounts and in a reproducible way. Although it is generally not converted to protein amount or concentration, it can be done by knowing the ratio of PSI/PSII in the sample, about 0.25 in spinach grana cores (Danielsson et al., 2004), and the number of chlorophylls in each monomer (105 for plant PSII (Wei et al., 2016) and 167 for plant PSI (Ben-Shem et al., 2003)). For spinach BBY, the procedure starts by dissolving the sample (40 µl) in 10 ml of a solvent where chlorophylls are soluble, at least partially, for spinach BBY a mixture of 80% acetone and 20% water (v/v) was used. This is done at least in duplicate, and then both tubes are centrifuged at 1,200 x g for 4 min (Universal 320 R, Hettich) to remove particles of non-soluble material in suspension. The absorption of the supernatant is then measured at 646 nm (a max of Chl_b Absorption) and 663 nm (a max of Chl_a Absorption) in a UV-Vis spectrophotometer (Cary 50, Varian) in a cuvette with 1 cm of optical path. The chlorophyll concentration was then calculated in mg/ml with the following equations 2.3 and 2.4 (Wellburn, 1994), being the extra 0.25 factor a sample/volume ratio correction:

$$[Chl_a] = (12.21 \times A_{663} - 2.81 \times A_{646}) \times 0.25 \quad \textbf{(Eq. 2.3)}$$

$$[Chl_b] = (20.13 \times A_{646} - 5.03 \times A_{663}) \times 0.25 \quad \textbf{(Eq. 2.4)}$$

Chlorophyll concentrations for *C. thermalis* PCC 7203 were determined as described in Nürnberg et al. (2018). Small samples of thylakoid membranes were resuspended in methanol, briefly vortexed and centrifuged at 10,000 x g for 2 min. The absorption of the supernatant was measured at 665, 707 and 750 nm and the concentration calculated with the Eq. 2.5 and Eq. 2.6 (Li et al., 2014):

$$[Chl_a] = (12.52 \times (A_{665} - A_{750}) – 2.28 \times (A_{707} - A_{750}) \quad \textbf{(Eq. 2.5)}$$

$[Chl_f] = (12.78 \times (A_{707} - A_{750}) - 0.07 \times (A_{665} - A_{750})$ **(Eq. 2.6)**

The chlorophyll concentration for thylakoid membranes from A. marina was determined as described by Ritchie (2006) using methanol for the dissolution of Chls and the following equations 2.7 and 2.8 for the calculations:

$[Chl_a] = (13.0161 \times A_{665} - 3.1022 \times A_{696})$ **(Eq. 2.7)**

$[Chl_d] = (12.9376 \times A_{697} - 0.327 \times A_{665})$ **(Eq. 2.8)**

2.3 Oxygen evolution activity measurement

The oxygen evolution activity of PSII can be determined using a Clark-type electrode (van Gorkom & Gast, 1996) that was initially developed to measure oxygen in blood (Clark et al., 1953). In this method, an electrode system composed of a platinum working electrode (WE) and a silver counter electrode (CE) is adapted in a water-cooled thermostatic jacket with a sample chamber of slightly over 2 ml that is separated from the WE by an oxygen-permeable Teflon membrane. After sample injection in the chamber, saturating continuous illumination is applied and the oxygen production per Chl and unit of time can be determined by the slope of the early rise of the oxygen level recorded over time by the electrode at constant potential. The signal comes from the reduction of oxygen at the electrode which gives a current signal. (Fig. 2.2)

The experimental set-up (Fig. 2.3) is composed of a commercial oxygen monitoring system (oxygraphy+, Hansatech) which has an electronics box, one illumination lamp, one electrode and a thermostatic jacket. To ensure light saturation and homogeneity, an extra light source was added (Silent 2500 data, Kindermann). For thermostatic control, a water bath (CORIO CD-200F, Julabo) is used.

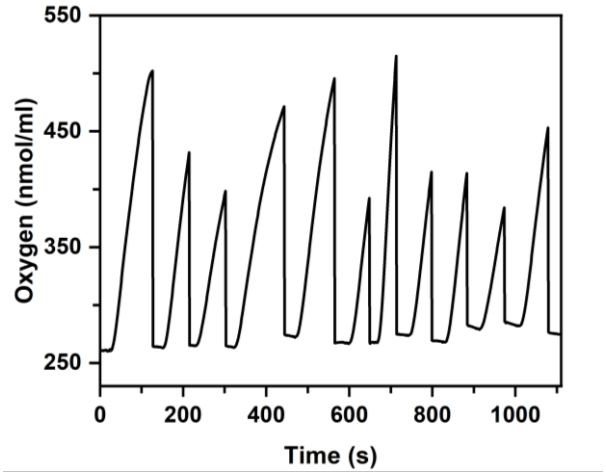

Figure 2.2 – Example of a series of eleven typical measurements of oxygen activity from different BBY samples. A sequence of light on and off events can be seen in signal. The signal recording was interrupted in between each measurement for sample exchange.

Figure 2.3 - PSII oxygen evolution activity determination set-up (Clark-type electrode). On the table the Hansatech Oxygraph+ with the thermostatic jacket, that includes the sample chamber, can be seen between the two light sources. On the right a control laptop with the O2 view software is displayed.

As the high relevance of small details to this experiment's outcome lead to very different results obtained by different users, a written protocol is needed. After extensive troubleshooting sessions with my colleague Paul Greife, one was written by me based also on some experimental knowledge passed by our predecessor Dr. Phillip Simon who worked there just before us, and so this section will have extra experimental details for the purpose of being documented.

Troubleshooting

For troubleshooting of the Hansatech Oxygraph+, one can open the O2 view software, go to the hardware dropdown menu and select “instrument test” and there select “auto test”. For this check-up, the electrode should be disconnected, and any saved calibrations must be deleted (this is done in the menu “calibration” and then “calibration details”). This instrument test is a two-stage check-up and when the device is working fine, the signal value should be 0 nAmps on stage one and about 1600-1700 nAmps on stage two (when the resistor is on).

Cleaning the electrode

For a good performance of the electrode the surfaces of both WE and CE should be of clan metal without any visible oxidation layers (which have a non-shinny dark grey colour). Also, the working electrode should have a mirror-like finish to have a homogeneous response along its area. An example of a well-kept electrode is shown in Fig. 2.4A while an example of an electrode without proper maintenance (e.g. black spots on the counter electrode due to oxidation and general salt dirtiness) is shown in Fig. 2.4B. To avoid the second example, good maintenance should be practiced by users, consisting of polishing the CE, before and after the experiment, with toothpaste and VE water using cotton buds and then rinsing with VE water, until no black spots are visible. Since the WE should not be scratched and is less susceptible to oxidation (due to higher reduction potential of platinum) it should not be polished often, passing gently with a cotton bud before the experiment with VE water is enough. Before storing in the desiccator, the electrodes should be gently dried with Kimwipes®.

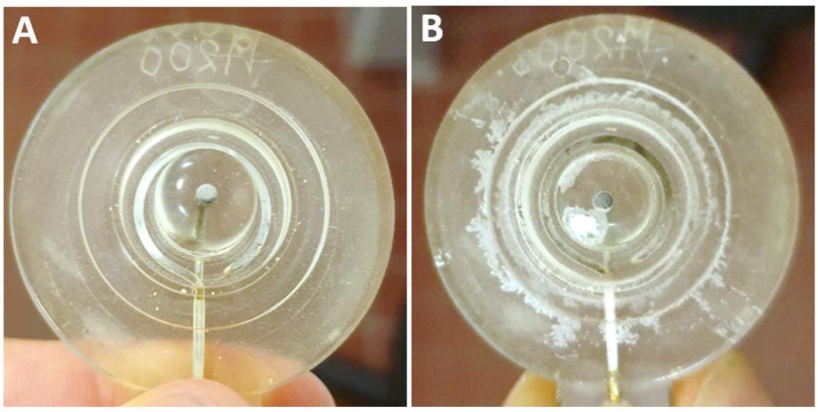

Figure 2.4 – Clean and well-kept electrode (A). Badly preserved electrode (B).

Assembling the membrane

The Teflon membrane is permeable to oxygen but not to water or ions, creating two compartments in this experiment, one below the membrane, where the electrodes can stay in a high salt concentration that promotes good conduction between the them, (KCl is used as support electrolyte) and above the membrane the sample can be probed by saturating illumination and produce oxygen in the desired buffer conditions e.g. without an excess of KCl ions. This way optimal conditions are achieved for both processes (water oxidation by the sample and O_2 reduction by the electrodes).

To assemble the membrane, 5-6 drops of KCl-solution in water are added to the dry electrode, making sure that both WE and CE are wetted. Then cigar-filter paper is cut into an appropriate square (excluding the glue part) and put on the electrode centred, the edges are bent into the CE well and 2-3 extra KCl-solution drops are added on top. The electrolyte-soaked filter paper will create a connection bridge between the WE and the CE. The membrane is cut in a bigger square and added on top of the electrode, where it is fixed using an O-ring. The excess membrane is cut away and the electrode is mounted in the thermostatic jacket and sealed with a large O-ring. While the bottom is screwed, care should be taken no to make it too tight, because this would overly stretch the membrane and widen the membranes pores. The magnetic stirrer is added and while stirring the sample chamber is rinsed twice.

Calibration

Before the measurements, the calibration must be performed to compensate for slight changes in the membrane set-up. To do so, the calibration option “air saturated water” can be selected. Here air saturated water refers to water that has been equilibrated with air, so to use VE water that was around in a wash bottle is ideal (no need to shake). 2 ml of VE water are then added to the sample chamber. The correct measuring temperature of 28°C and stirring speed of 75 rpm must be selected. The software waits for the current signal to plateau, and the respective amplitude should be noted down. After, a small spatula spoon of sodium dithionite is added to remove any oxygen dissolved in the water and then the signal will stabilize at a plateau again. The calibration finishes automatically reporting the calibration factor and the offset. If the membrane was well assembled and the electronics are working correctly, the calibration factor multiplied by the initial plateau level should be 270 ± 10 nAmps. As the sodium dithionite can interfere with the detection of oxygen, the sample chamber must be rinsed very well with VE water after the calibration (about 10 times).

Measuring the O_2 activity of PSII membrane particles from spinach (BBY)

To measure the oxygen activity of a BBY sample, 2 ml of Buffer O_2 are added to the sample chamber, the stirrer speed is set to 75 rpm and the data recording turned on. The following steps are done under dim green light. The signal is observed for a short period of time and a plateau should be reached. A sample amount equivalent to 10 µg Chl (40 µl) is added from a stock solution of 0.25 µg Chl/ml followed by the addition of 40 µl of 50 mM $K_3[Fe(CN)_6]$ in water and 10 µl of 50 mM DCBQ in DMSO. DCBQ and $K_3[Fe(CN)_6]$ act has electron acceptors instead of the natural Q_B which is in deficit in BBY preparations (Tanaka-Kitatani et al., 1990). Due to the high concentration and thus viscosity of the sample, it is better to dilute it in a stock solution. This avoids errors while pipetting the sample into the chamber, thus ensuring the right final sample concentration from which the result is dependent. The illumination is turned on and a rise in the oxygen signal should be observed. From the slope of the initial rise the oxygen

production rate is calculated and converted to $\mu mol_{O2}.mg_{Chl}^{-1}.h^{-1}$. The sample is generally measured at least 2 additional times and the results should be within ± 50 $\mu mol_{O2}.mg_{Chl}^{-1}.h^{-1}$. Between measurements, the sample chamber is rinsed with water or oxygen buffer once, but more times in case of experiments involving inhibitors. The membrane lasts for about 10 measurements, and then should be replaced, especially if drifts in the baseline signal (when only buffer is present) are observed. A sample with known oxygen activity can be measured as a control to ensure that the assembly is working as intended.

2.4 Time-resolved oxygen polarography

Although the name polarography is strongly connected to a linear sweep electrochemical technique that uses mercury-drop electrodes developed by Jaroslav Heyrovsky and led to his distinction with a Nobel prize in 1959, the present technique used is different and based instead on the Joliot electrode. This type of electrode was developed around 1968-1969 (Bennoun & Joliot, 1969; Joliot & Joliot, 1968) and was a great addition to the study of photosystem II and photosynthesis in general, enabling Kok and co-workers in 1970 to report the first time a catalytic cycle for this important enzyme (Kok et al., 1970). As the initial set-up was called a modulated polarograph, soon the name polarography started being used in different variations like oxygen polarography or flash polarography. Here the addition of “time-resolved” emphasises the higher sub-millisecond time resolution that can be achieved today in comparison with the early experimental set-ups. Another term associated with the same technique is flash-induced amperometry (Lavorel, 1992).

2.4.1 The technique

Time-resolved oxygen polarography is a technique that allows for the measurement of oxygen produced by a sample after light excitation. This is done by using a bare platinum electrode which under a continuous static polarization can reduce at its surface any oxygen arriving. The electrode used is an assembly of a platinum disk working electrode

(WE) and a silver ring counter electrode (CE) as shown in Fig. 2.5. The WE normally charged with a polarization ranging from -0.60 to -0.95 V can reduce oxygen produced by a sample directly deposited onto it. The cathodic reaction can then be represented by Eq. 2.9:

$$O_2 + 2\,H_2O + 4\,e^- \rightarrow 4\,OH^- \qquad \textbf{(Eq. 2.9)}$$

The anodic reaction happening at the CE can be summarized by Eq. 2.10:

$$Ag + Cl^- \rightarrow AgCl + e^- \qquad \textbf{(Eq. 2.10)}$$

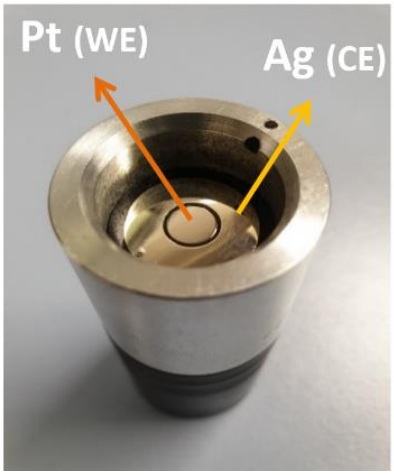

Figure 2.5 – Joliot-type electrode used for oxygen polarography.

As the reduction rate on the platinum electrode is sufficiently fast with the used potential, the oxygen yield is proportional to the accumulating electron charge (Meunier & Popovic, 1990). And so, the resulting measured signal is an oxygen diffusion curve with amplitude proportional to the current that was measured at each time point. To overcome the diffusion limitation of oxygen transfer to the electrode surface, the oxygen-evolving material is deposited directly onto the surface (Clausen et al., 2004). This improves the time resolution drastically when compared with the Clark-type electrode where the signal is strongly diffusion limited mostly by the membrane but also by the bigger electrode spacing (Renger & Hanssum, 2009). This way, the time-resolved oxygen polarography makes it possible to identify sub-millisecond reaction intermediates from the diffusion signal (Bao & Burnap, 2015).

The most common types of samples used are thylakoid membranes or membrane fragments which can produce oxygen under illumination when working PSII is present in them. These are previously dark adapted and, in our case, deposited by centrifugation (10000 x g for 10 min) directly onto the electrode creating a homogeneous and stable thin layer. The advantage of a compact thin layer is that the diffusion range from the top of the layer to the electrode is small and allows for the fast measurement of most of the signal condensed at an earlier timescale making it possible to have a higher signal to noise ratio. On the other hand, if the sample would be in a comparable non-compact form like a dispersion, the signal would be highly broadened over time, have lower maximum intensity and thus lower signal to noise ratio. The illumination is given as a sequence of short (µs range) light pulses at a convenient spacing (generally 700 ms) to promote the sequence of photochemical events that lead to oxygen evolution.

2.4.2 Experimental set-up

The experimental set-up was initially designed by Jung-Soo Kim in 2009 and apart from a few commercially available parts and devices, it was mostly constructed by the workshop of our department.

As it can be seen on the scheme on Fig. 2.6, the set-up has an electrode housing where the Joliot-type electrode is connected. This housing is made of aluminium and has two Peltier elements that are temperature controlled within a 0.1 °C precision using an electronics unit (PKE 72 A 0021, Peltron). Furthermore, since the Peltier elements rest on the outside wall of the housing, there is a temperature probe connected to a digital thermometer (GMH 3210, GREISINGER electronic), that is attached to the inside part and set at a distance so that it will touch the buffer during the experiment, to measure accurately the temperature of the sample. Both Peltier elements are water-cooled by tubes connected to an aquarium pump (Compact 1000, EHEIM) submerged in a water reservoir, that is generally at room temperature but can be changed, using ice or warm water, to help speed the temperature regulation for lower (below 10°C) or higher temperature (above 35°C) respectively. On top, the electrode housing has a hole where

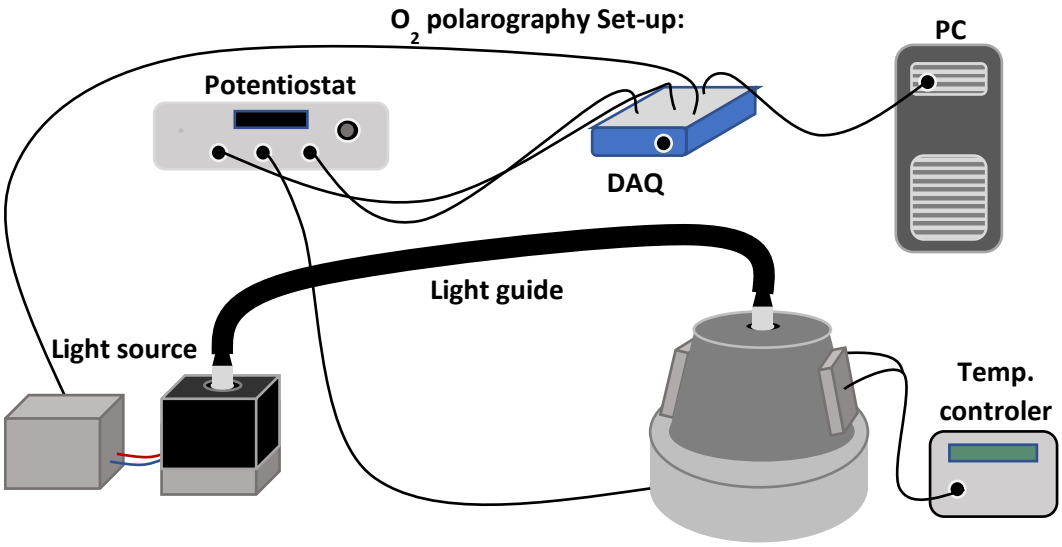

Figure 2.6 – Schematic of the time-resolved oxygen polarography set-up. In the picture the electrode cannot be seem as it is under the thermostatic jacket of the electrode housing. The light source displayed is a representation of the LED-device although the light guide can also originate from a xenon flashlamp.

a liquid light guide (Serie 380, Lumatec) can be inserted. The position is so that it aligns with the working electrode and submerges in the buffer during operation to avoid an air interface. The light guide which has about 80% transmission, connects on the other side to the light source. Initially, the only option for this was a Xeon flashlamp (FX 134, EG&G Heimann Optoelectronics) with an optical filter (OG 570, ITOS) that provided a 10 µs (FWHM) flash energy pulse of 914 µJ (at 1500 V, 538 µJ at 1000 V and 96 µJ at 400 V), measured at the end of the light guide. Now a new LED system has been developed and added to the set-up (please see 2.4.3 for details). At the current maximum operation voltage (22 V) and pulse length (40 µs) the LED pulses have an average energy of 212 µJ for the Far-red LED, 251 µJ for the green LED and 267 µJ for the red LED. A comparison between the spectrum of the flashlamp's filtered emission and the LEDs' emissions can be seen in Fig. 2.7. An in-house build potentiostat is set to apply a polarization voltage of -0.95 V and then measure the resulting current, which is treated through a high-pass filter (HPF) with a 100 ms time constant (optionally a 1 s time constant HPF is also available) and then amplified by a factor of 1 to 10 by a low-pass filter of 0.1-5 kHz. The signal was then analogue to digital converted by a multi-function data acquisition "DAQ" (USB-6251 BNC, National Instruments) and then recorded in the computer using a

Labview software at a rate on 1 MHz and 40-points averaged ending up with a time resolution of 40 µs.

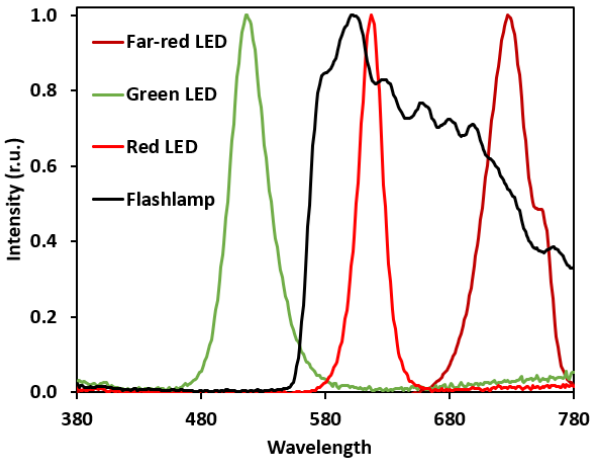

Figure 2.7 – Emission spectrums of the flashlamp and the LED- system with each of the three respective LED sources.

Because of a big enhancement of the 50 Hz noise, that happens when the temperature controller is on, and heavily compromises the quality of the data, the device was always turned off upon reaching the desired temperature, right before the start of the measurement. The resulting uncertainty on the temperature was estimated to be about ± 0.3 °C. To increase the measuring experience of the O_2 polarography user and reduce temperature uncertainty it would be great, as a future upgrade, to find a way to have the temperature controller on without interfering with the experimental signal.

2.4.3 Set-up upgrades

Although the set-up has been established in 2009 and progressively upgraded ever since, several challenges still made the experience of measuring and acquiring good data difficult. The first issue had to do with the electrical connection between the electrode and the base holder. This was made by two high-end connectors an RCA socket (WBT-0110 Ag) and an RCA plug (WBT-0210 Ag). For maximum electrical conductivity silver pins had been the obvious initial choice. The problem with those is twofold. It starts with

the fact that the pins spend much more time disconnected than connected which leave them more susceptible to oxidation. Oxide residues can be somehow cleaned but this is not an easy task given the configuration of the tight constructions, electrode and base. Secondly, while manufacturing the electrodes the plugs are cut in a way to fit the design and thus their screw tight grip, that they were intended to have, is no longer possible to apply, making it essential that the metal surfaces are clean and non-oxidized to have a good connection. The poor connection made each experiment a gamble on whether the data was going to be good, extra noisy, or not even there. The solution came when we decided to replace the socket in the base with a similar one made of gold-plated copper (WBT-0210 Cu) (Fig. 2.8 B). This one gave a good connection and although after some usage the copper starts to show up, at the time of writing this socket is still working fine. At the time we also manufactured three new electrodes with gold-plated copper plugs (WBT-0114 Cu) (Fig. 2.8 A), but soon we discovered that the electrodes with silver plugs were working just as fine. Currently there are 6 good electrodes, 3 with each type of plug, but the socket at the base, the most exposed to air and dust should keep working only with the gold-plated copper sockets.

Figure 2.8 – Gold-plated copper RCA plug (A) and socket (B). Image from www.wbt.de.

Another concern regarding this experimental set-up was the flash illumination, which was, and still can be provided by a xenon arc-discharge flashlamp. This source of illumination has high power and provides very good flash excitation to the samples tested there so far. The issue is regarding the strong flash induced artifact that appears in the data after the discharge. This can be corrected when the sample has a strong

signal, although it can engulf the early rise of the oxygen signal for samples with a weak signal. This way a more convenient light source was needed. Through conversation with our colleagues from the University of Uppsala, especially Prof. Johannes Messinger and Dr. Mun Hon Cheah from his group, we got to know that they had developed an LED system with electronics inspired in two publications (Willert et al., 2010; Wilson et al., 2015). After some discussion sessions about the implementation, I sought the help of Christian Güttler from the electronics workshop at our department who designed a new circuit according to our specific needs based also on Willert et al. (2010); Wilson et al. (2015) and then constructed the device (number 2 in Fig 2.10).

Figure 2.9 – High performance LEDs from Luminus. Red on the left, far red in the middle and green on the right side.

Meanwhile suitable LEDs from Luminus were ordered from a local supplier in three different emission colours, red (613 nm), green (520 nm) and far red (730 nm) (Fig. 2.9). By using the custom-made LED system, it is possible to flash these high-end LEDs at a very high drive current of about 150 A for a very short time (e.g. 40 µs) this way even though we are operating with about 5 times higher drive current than the maximum listed in the respective spec sheet, they still perform and do not overheat and burn due to the fact that the pulses are very short. In the LED flasher there is an out BNC port to measure the drive current, which can be done with an oscilloscope, and is regulated on the power supply of the LED flasher by changing the input voltage. 22 V and 40 µs are the current voltage and pulse length settings which should not be increased without proper testing at the risk of immediate irreversible damage to the LEDs.

The last step to incorporate the new illumination device into the polarography set-up was to design and 3D print an LED housing (see Appendix B.1-2 for dimensions). This was

needed to adapt both the LED and the liquid light guide (already in the set-up) and had to be quick to open, for LED replacement, and should have precise positioning regarding the LED-light guide alignment and distance (1 mm from the LED) so that the least light pulse energy would be lost. A picture of the LED flasher already inserted in the polarography set-up can be seen on Fig 2.10.

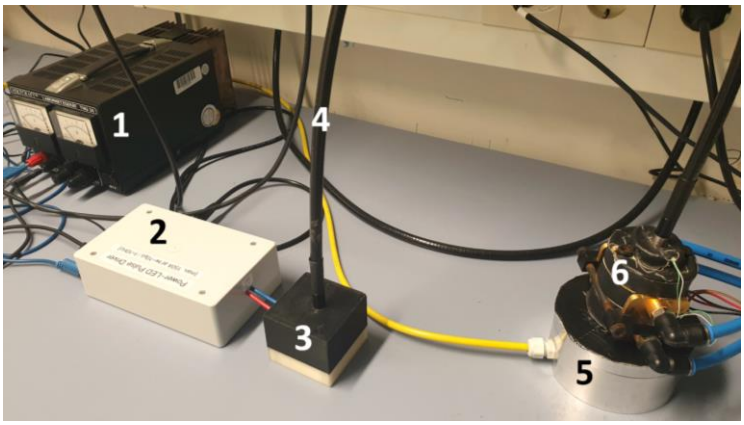

Figure 2.10 – Photography of part of the oxygen polarography set-up showing the new LED flashing system. The picture includes the LED-pulse power supply (1), the LED-system (2), the 3D printed LED housing (3), The liquid light guide (4), the base of the electrode housing (5) and the thermostatic jacket part of the electrode housing (6). On 6 it can be seen the Peltier elements in copper colour, the water-cooling tube system in blue and the wires of the temperature probe connecting on top in white and green.

2.4.4 Construction of the electrodes

Since the inception of the time resolved polarography set-up at our laboratory, many ways for constructing well performing electrodes were tested. The electrodes must be small and fitting into the adaptors of the centrifuge's rotor (TH13-6x50, Thermo Scientific). The electrode body was initially designed when the set-up was created and then upgraded slightly to further ease the electrode's construction as well as improve their resistance to centrifugal forces. The body is composed of 3 pieces of PVC (top part, middle part, and bottom cap), that can be manufactured by the department's workshop (Appendix B.3-5). A small extra modification was made during this thesis work to improve the resilience of the electrodes to high g forces. The middle part of the body is a hollow cylinder which had little roughness to create a good adhesion to the epoxy resin

fill and so a cut on the inside wall imitating a square wave was done to give extra support to the filling. The electrode itself is a ring disk assembly of a 999-platinum disk and a 999-silver ring that have a 999-silver wire soldered to the bottom side of each piece with about 4 cm length and will be used to connect them to the respective RCA plug by soldering (See Appendix B.6 for electrode dimensions). Previously it was found that less pure materials would not perform as intended (Schonbörn, 2017), so the 999-purity standard of the metals should not be overlooked. The metal rings and disks can be produced by a jeweller, being that the current provider is the nearby goldsmith store "Goldschmiede am Botanischen Garten". I leave the name of the store since was a quite hard task to find a new provider since the last one (Leihhaus Katz, Berlin) stopped being available for this task.

The assembly can be done in four gluing steps starting by gluing the metal ring and disk to the top body part, which should be done by applying a little adhesive and clicking them into position, and after a little extra adhesive should be added on top to cover all the metal parts. As before, this and all further gluing steps are made using the same two-component adhesive EPL285 and EPH285 (bacuplast, Germany) which takes about 1 day to dry. These two components should be warmed up to 50 °C, mixed in the right proportions and then applied using a 1.5 mm syringe. The heating helps to lower the viscosity that makes it flow better and release unwanted bubbles. At the workshop, the top part of the RCA plugs should be cut off at about half the threading high so that the plugs fit the electrode properly. After the first gluing step is ready and dry, the electrode is turned upside down and adhesive is inserted by the open bottom channel letting the air come out of the other channel in which the silver wire is passing through. After overflowing a little with adhesive, the RCA plug can now be placed in the center position for gluing, already aligning the correct wires to the correct connector. In this step extra care must be taken not to spread adhesive all over the contacts. After the drying on the upside-down position, the contacts of the half-assembled electrodes can be soldered (working electrode to the middle pin and counter electrode to the outer pin). It is recommended that the soldering is done in electronics workshop, Michael Schreiber could do the job with great dexterity avoiding small accidents that could occur during this step. After this step, the middle body part can be attached, and the inside part,

where the RCA plug is, can be filled with adhesive. Here the recommendation is not to add to much not to cover the connecting part of the plug and also leave a bit of space as later there might be the need to add extra resin to specific electrodes to obtain an equal weight in all of them. Before drying, the previously cut RCA plug cap is inserted and the electrode if left to dry in the upside-down position. When the drying is over, the top part of the electrode can be revealed by sanding with a sandpaper and later with diamond paste. To avoid uneven sanding, the sandpaper should lay on the workbench while sanding, and by making moves with the electrode in an infinite 8-shape. When the metal is close to reveal, a lower roughness sandpaper can be used and when the first part of the metal is revealed, it should be changed to the polishing pads while using wet diamond paste as grinding material. Now the process goes until there is no longer any resin covering the metal electrodes. Once this happens, the electrodes can be polished with toothpaste to get a mirror finish. The end step is to balance the electrodes to the same weight with a bit of extra adhesive added to the bottom part of the current assembly. Two O-rings are then added to the electrode's "neck" in the two respective places and the bottom caps can be clicked in and out any time when needed for centrifugation. Lastly, the removable metal hollow cylinder can be pushed in the electrode's neck creating the top compartment where the sample and buffer are added during the experiments.

2.4.5 Data analysis

The data obtained from the time-resolved polarography set-up is recorded as an arbitrary signal over time, proportional to the measured current. The signal is split into individual diffusion curves after each excitation flash, meaning that after applying 32 excitation flashes one should have 32 individual traces. Depending on the type of experiment, some of these traces can be discarded, for example if a dark-adapted oxygen evolving PSII (mostly in the S1 state) sample was used, generally the first two flashes are discarded as they promote, in majority, the S1-S2-S3 transitions which are non-oxygen evolving.

For the analysis of the oxygen evolution kinetics, several flash traces can be averaged for one experiment to increase the signal to noise ratio. Often repetitions of the same measurements are available and can be averaged together or analysed separately. To extract accurate information about the kinetics from the diffusion curves a model previously implemented was used (Dilbeck et al., 2012). This diffusion model divides the volume of the deposited PSII sample and buffer into layers of Δx thickness and calculates the O_2 concentration in every layer at each moment in time. To achieve this, the three following processes are described mathematically (Lavorel, 1992; Plijter et al., 1988) based on a one-dimensional diffusion of O_2 (Eqs. 2.11 and 2.12) with an O_2 production source (Eq. 2.13) and an O_2 sink process at electrode surface (Eq. 2.14), then solved by numerical integration (see below for parameters description). A schematic representation of the model can be seen of Fig. 2.11.

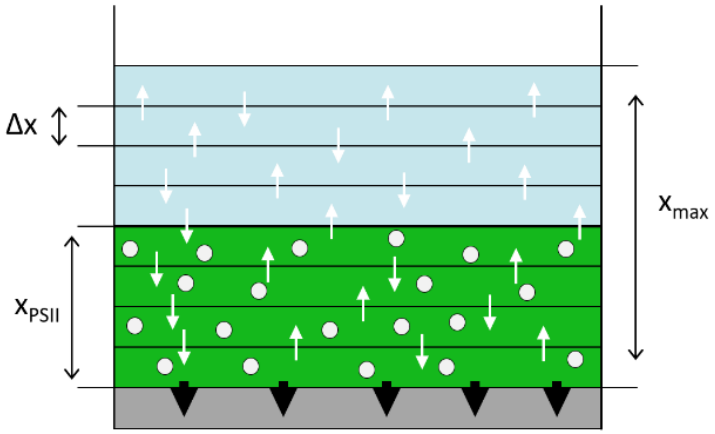

Figure 2.11 – Representation of the processes involved in the fit model. White arrows represent the diffusion of O_2 in the sample compartment; white dots the production of oxygen in the PSII layer (green); black arrowheads the consumption of oxygen at the electrode's surface (grey). Adapted from the manual of the O2-diffusion program written by Dr. Ivelina Zaharieva.

1. O_2 diffusion

1.1. For the whole bulk volume is given by:

$$[O_2]_x^{t-\Delta t} + [([O_2]_{x-\Delta x}^{t-\Delta t} - [O_2]_x^{t-\Delta t}) + ([O_2]_{x+\Delta x}^{t-\Delta t} - [O_2]_x^{t-\Delta t})] \cdot \left(\frac{D}{\Delta x}\right)^2 \cdot \Delta t \qquad \textbf{(Eq. 2.11)}$$

1.2. And for the bottom layer by:

$$[O_2]^{t-\Delta t}_{x=0} + ([O_2]^{t-\Delta t}_{x=1} - [O_2]^{t-\Delta t}_{x=0}) \cdot \left(\frac{D}{\Delta x}\right)^2 . \Delta t \qquad \textbf{(Eq. 2.12)}$$

2. O_2 production from PSII – only in the layers containing PSII, given by:

$$\frac{k_1 . k_2}{k_1 - k_2} \cdot [S_3^0] \cdot (e^{-k_2(t-t_{lag})} - e^{-k_1(t-t_{lag})}) . \Delta t \qquad \textbf{(Eq. 2.13)}$$

3. O_2 consumption from the lowest PSII-containing layer at the electrode's surface, that gives rise to the oxygen signal, is given by (only applicable for the bottom layer):

$$- R_{el} \cdot [O_2]^{t-\Delta t}_{x=0} \cdot \Delta x \qquad \textbf{(Eq. 2.14)}$$

To calculate the O_2 concentration in the layers, three cases appear: layers of buffer without PSII sample (a), PSII sample layers with buffer (b) and bottom layer at the electrode's interface composed of PSII sample and buffer (c). For the first case (a), the expression 2.11 is sufficient to calculate the oxygen concentration in these layers as there is no production or consumption. For the second case (b) where there is both diffusion and production, the oxygen concentration is given by the sum of expression 2.11 and 2.13:

$$[O_2]^t_x = [O_2]^{t-\Delta t}_x + [([O_2]^{t-\Delta t}_{x-\Delta x} - [O_2]^{t-\Delta t}_x) + ([O_2]^{t-\Delta t}_{x+\Delta x} - [O_2]^{t-\Delta t}_x)] \cdot \left(\frac{D}{\Delta x}\right)^2 . \Delta t + \frac{k_1 . k_2}{k_1 - k_2} \cdot [S_3^0] \cdot (e^{-k_2(t-t_{lag})} - e^{-k_1(t-t_{lag})}) . \Delta t \qquad \textbf{(Eq. 2.15)}$$

The last case (c), at the electrode´s interface, the diffusion part is simplified (Eq. 2.12) as it is limited to the upwards direction and the term for consumption at the electrode is added (Eq. 2.14):

$$[O_2]^{t}_{x=0} = [O_2]^{t-\Delta t}_{x=0} + ([O_2]^{t-\Delta t}_{x=1} - [O_2]^{t-\Delta t}_{x=0}) \cdot \left(\frac{D}{\Delta x}\right)^2 . \Delta t + \frac{k_1 . k_2}{k_1 - k_2} . [S_3^0] . (e^{-k_2(t-\tau_{lag})} - e^{-k_1(t-\tau_{lag})}) . \Delta t - R_{el} . [O_2]^{t-\Delta t}_{x=0} . \Delta x$$ **(Eq. 2.16)**

Parameter description:

- D is the O_2 diffusion constant.
- k_1 is the rate constant of the step preceding the O_2 evolution step, with the formation of the intermediate known as S_3^n or S_4.
- k_2 is the rate constant of the O_2 evolution step.
- $[S_3^0]$ corresponds to the initial (t=0) population of PSII in S_3 state.
- τ_{lag} is the time delay relative to the oxygen reduction reaction by the electrode.
- R_{el} represents the oxygen reduction rate at the electrode.
- Δt represents the simulated time steps that were set to 40 μs.

The numerical integration starts with t = 0 and $[O_2]_x = 0$ in all Δx layers.

To facilitate the frequent application of the described model to fit the polarography transients and extract the time constants of the two main steps involved in the S_3-S_0 transition, the 'O2 diffusion' program was previously written and subsequently upgraded by Dr. Ivelina Zaharieva. This program uses an iterative method to minimize the fit errors based either on the Simplex algorithm or alternatively the Levenberg–Marquardt algorithm. The interface can be seen in Fig. 2.12 and shows the parameter and fit section and the graphical part for visualization of the data and the fit results. This fit method was able to reproduce previously obtained results for different samples like spinach BBY and thylakoid membranes from WT *Synechocystis* sp. PCC 6803 like shown in the Fig. 2.12 (Dilbeck et al., 2012). There, among other parameters and options, the six parameters to be fit are also displayed:

- τ_{lag} and R_{el} that were previously introduced.
- R_{ox}, that is equivalent to the initial population of PSII in S_3 state concentration $[S_3^0]$.
- τ_{pre} that corresponds to $1/k_1$.

- τ_{ox} that corresponds to $1/k_2$.
- PS2 layer that corresponds to the thickness of the PSII layer.

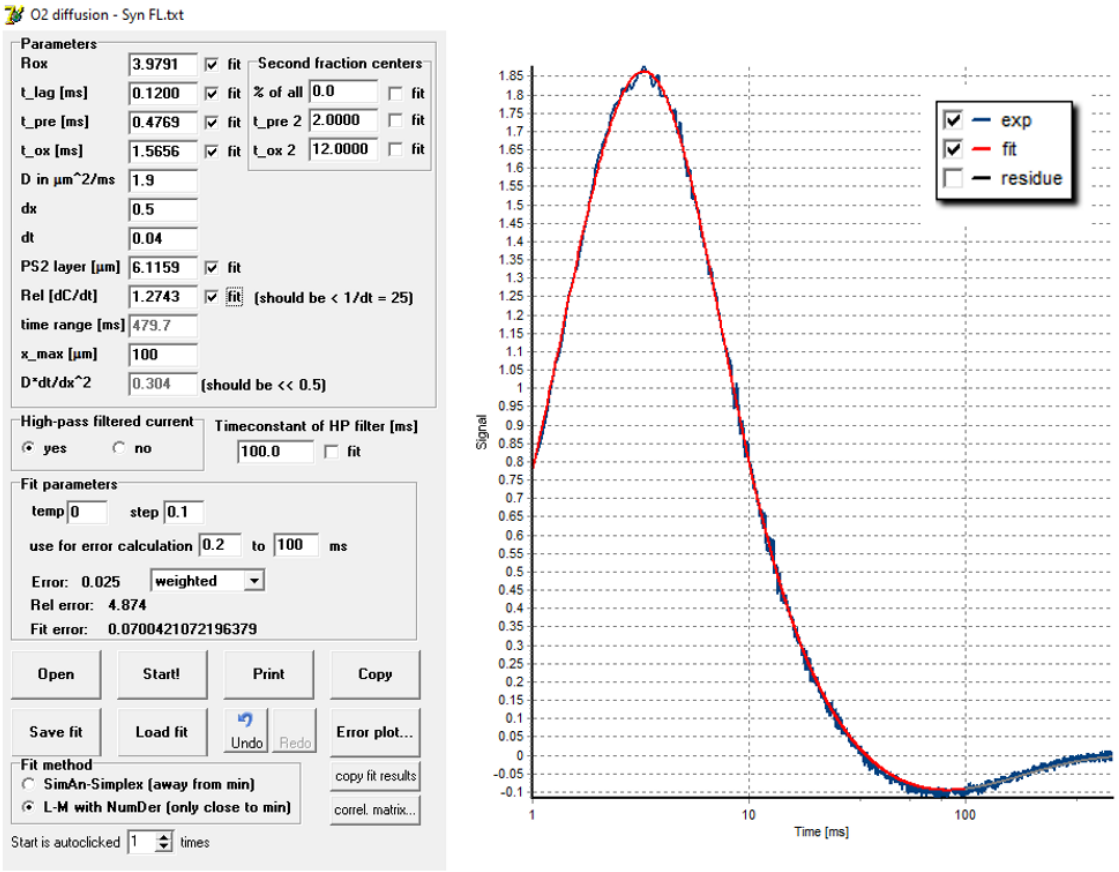

Figure 2.12 – Interface of the O2 diffusion program used for fitting the O_2 polarography transients. In the pot area, a typical time resolved O_2 transient from WT *Synechocystis* sp. PCC 6803 can be observed in blue, and the respective fit is shown in red.

Apart from these six fit parameters, another parameter that changes according to the temperature of the measurement is the diffusion coefficient of O_2, for which we use different coefficients for each of the temperature steps commonly used. These were obtained by extrapolation from known diffusion coefficients of O_2 in pure water (Xing et al., 2014), and can be seen in table 2.1. In previous work, and also on the early work of this thesis (Chapter 3), a constant O_2 diffusion coefficient, generally 2.2 $\mu m^2/ms$, was used and although it did not affect the end fit results in terms of time constants, it made the parameter PS2 layer vary highly with temperature. With the new use of temperature adapted O_2 diffusion coefficients we can get the same kinetic results while maintaining the PS2 layer thickness fit result quite constant throughout the whole temperature

range (0-45 °C), which should be closer to reality as the layer thickness is not expected to vary highly with the change in temperature. Important to note is that the use of O_2 diffusion coefficients in pure water is an approximation, as it is known that in aqueous mixtures, for example with the presence of salts, lipids or other substances that our sample is composed of, the O_2 diffusion coefficients can be slightly different (Jamnongwong et al., 2010).

Table 2.1 – O_2 diffusion coefficients in pure water obtained by extrapolation from experimental points collected by different authors (Xing et al., 2014).

	Calculated
T (°C)	O_2 Diffusion Coefficients in Pure Water ($\mu m^2 ms^{-1}$)
0	1.2
2.5	1.3
5	1.3
7.5	1.4
10	1.5
12.5	1.6
15	1.7
17.5	1.8
20	1.9
22.5	2.0
25	2.2
27.5	2.3
30	2.5
32.5	2.6
35	2.8
37.5	3.0
40	3.1
42.5	3.3
45	3.4

2.5 Chlorophyll fluorescence

As chlorophylls (Chl) are the mostly widely distributed natural fluorophores that occur in the photosystems (I and II) of plants and other photosynthetic organisms, chlorophyll fluorescence methods became one of the most common ways used since many years to study photosynthesis (Humphrey, 1979; Maxwell & Johnson, 2000).

Even though Chl fluorescence did not make part of my main research work, two Chl fluorescence methods, known as Prompt fluorescence (PF) and delayed fluorescence (DF) (Buchta et al., 2007) will be shortly described. These were used mostly as a support role for the work of other colleagues, like in Chernev et al. (2020), and it is important to write about them here since a considerable upgrade to the set-up was performed, motivated by the need of a laser safety improvement (see 2.5.3 in this chapter). Also, these methods were the main part of the work of two students that were at our group, Bruno Serrano (Bsc) (Serrano, 2018) and Boram Yu (Msc) (Yu, 2021), and it was also my responsibility to tutor them whilst using the experimental set-up.

2.5.1 Prompt fluorescence

Three possible pathways can be taken when light energy is absorbed by chlorophyll molecules in PSII. The first is to be used to induce the photochemistry and drive photosynthesis, the second and third, which apply to the excess energy, are thermal dissipation or re-emission of light as fluorescence, respectively (Maxwell & Johnson, 2000). When an absorbed photon promotes charge separation at the Chl complex P680, the first two electron transfer steps (P680-Phe and Phe-Q_A) occur in the ps range and the third Q_A-Q_B take a bit longer, already in the ms range (Dau, 1994). During the time at which the electron sits on the quinone Q_A, the reaction center is considered to be "closed" as any new photon absorbed would quickly (ps-ns range) recombine at the P680 and produce chlorophyll fluorescence (Grabolle & Dau, 2005). This specific fluorescence is called prompt fluorescence as it occurs within the ns range after the

excitation, differing from the delayed fluorescence which can be emitted at later times (ms range).

The prompt fluorescence is measured in a pump-probe manner, starting with a saturating light flash that initiates the PSII photochemistry, followed by a sequence of low intensity probe-LED light flashes which provoke the outcoming fluorescence that is measured. Initially, the fluorescence level is high and reaches its maximum when the concentration of the radical pair $Y_Z^{\bullet+}\ Q_A^-$ is maximal, this occurs when most of the PSII centers are closed and bounce back any arriving photon as fluorescence. As the electron transfer from Q_A to Q_B start to take place, the fluorescence level after the probe flashes starts to decrease, eventually reaching very low levels where most of the Q_A^- are re-oxidized and the PSII centers are "open" again.

General experimental conditions and set-up

In the standard measurement, the sample is added to a 4-window cuvette (normally made of polystyrene) with 4 ml of volume, generally mixing 895 µl of buffer D, 100µl of 1 mgChl /ml PSII sample and 5 µl of 50 µM DCBQ in DMSO as electron acceptor, added in the listed order, making up to a total of 1 ml. The dark-adapted sample is then put in the sample holder (part of the fluorometer FL-3000, PSI instruments) and then the temperature can be set with a thermostatic bath (Haake DC50, Thermo Fisher Scientific) and controlled by a temperature sensor with precision of 0.1 °C inserted directly in the cuvette. Attached to the sample holder are two weak source LEDs that will flash five times with 200 µs spacing before the arrival of the excitation flash. These first flashes serve to determine the level of fluorescence of the sample in the dark-adapted state called F_0, that corresponds to when all Q_A are still fully oxidized. The 5 ns excitation pulse with wavelength of 532 nm arrives from a laser (Minilite II, Continuum) guided by five mirrors and passing through a set of two lenses, that wides the beam up to almost 3 cm in diameter, hitting the sample from the top with an intensity of 2 mJ/cm2, measured with a power meter (PE25-C, Ophir Photonics). After, a train of 23 weak LED probe pulses hit the sample, logarithmically spaced, being that the first one is coming 100 µs after the

excitation flash and the last after 700 ms. Then this cycle of excitation flash and probe pulses can be repeated as needed. The level of the fluorescence signal after each probe flash is measured by the fluorometer (FL-3000, PSI instruments). The Fig. 2.13 shows a schematic representation of the set-up and beam path. The set-up is sharing parts with the delayed fluorescence set-up (like the laser, part of the beam path, fluorometer, etc.) and both are enclosed inside a large box for increased laser safety.

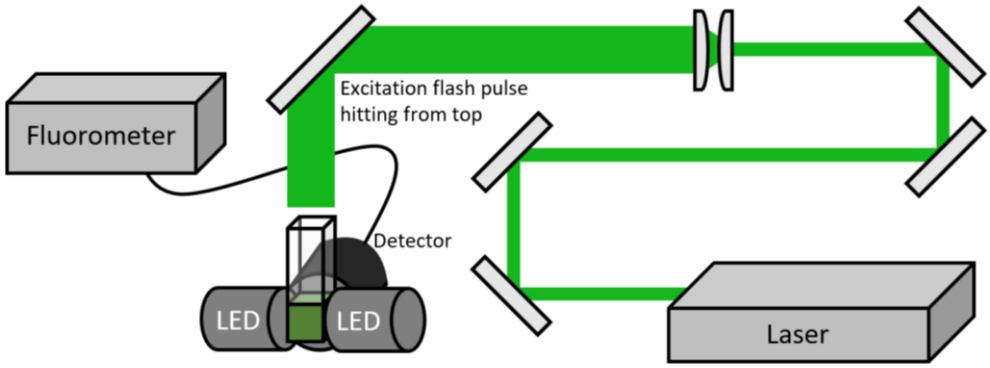

Figure 2.13 – Schematic of the main part of the prompt fluorescence set-up. Apart from what is shown, a case that encloses the set-up, a thermostatic bath, a power meter, a computer, and a temperature sensor also make part of the experimental set-up.

The data obtained for the fluorescence decays after each flash can be fitted with a sum of three exponential functions (de Wijn & van Gorkom, 2001), allowing for the determination of the time constants of electron transfer from Q_A to Q_B. Also, from the continuous function given by the fit, it is possible to correct for the Q_A^- decay contribution to the delayed fluorescence (DF) signal, which can be calculated with Eq. 2.17 (Buchta et al., 2007), and will be further discussed in the respective DF section:

$$[Q_A^-](t) = \left(\frac{F_P(t) - F_0}{F_M - F_0}\right) \qquad \textbf{(Eq. 2.17)}$$

2.5.2 Delayed fluorescence

The delayed fluorescence (DF) emission is delayed from 20 ns up to seconds from the photon absorption whereas the prompt fluorescent happens before 20 ns, but

nonetheless both have a very similar spectrum with a peak at about 685 nm (for plant PSII), indicating that both originate from the same excited state of the PSII Chl antenna. The repopulation of the initial Chl excited state can take three pathways: it can follow the forward reaction direction and reform the primary and secondary radical-pair states, the energy can be dissipated thermally or lastly, it can decay by emission of delayed fluorescence (Buchta et al., 2007).

Experimental set-up

As the delayed fluorescence originates from low probability recombination reactions, the measurement of DF has other challenges not seen in PF measurements, being the most crucial the fact that the DF has a signal several orders of magnitude smaller than the PF. For this reason, the DF set-up uses a gated photomultiplier tube (PMT) (R928, Hamamatsu) that records the data from 10 μs to 60 ms after the sample is hit by a saturating laser flash of 5 ns and wavelength of 532 nm (Minilite II, Continuum), generally with intensity of 2 mJ/cm^2, adjusted with the help of a power meter (PE25-C, Ophir Photonics). To drive the photomultiplier a voltage of 500 V is applied with a direct current power supply, and to avoid the initial stronger signal from the PF and scattered light from the excitation light pulse, a 250 V gating counter voltage is applied to the detector 7 μs before the flash arrives and turned off 3 μs after, to allow for the recording of the delayed fluorescence signal. Extra protection from unwanted photons is achieved by using two optical filters (DT-red and DT-magenta, LINOS Photonics) with cut-off wavelength at 600 and 632 nm (Fig. 2.14) between the detector and the sample. Because the delayed fluorescence signal has in itself 3-4 orders of magnitude difference from the start to end of the decay (Buchta et al., 2007), the signal from the PM is split into two channels that differ only in an extra 30x preamplifier that is applied to one of them. From the amplifier the signal is recorded by the computer with the help of an interface card (PCI 9812, Adlink). For the standard measurement, a sequence of 32 flashes is generally employed, during which the respective signal after each flash is recorded. A representation of the experimental set-up can be seen bellow in Fig 2.15.

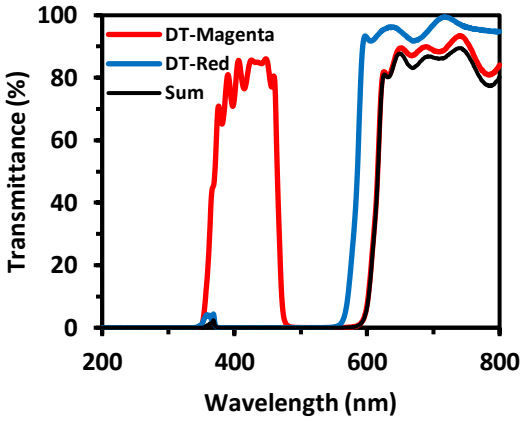

Figure 2.14 – Recorded transmission spectrum of the filters DT-red and DT-magenta used in the DF set-up. The combination of both filters blocks incoming photons below 600 nm where chlorophyll fluorescence is practically non-existent (Krause & Weis, 1984).

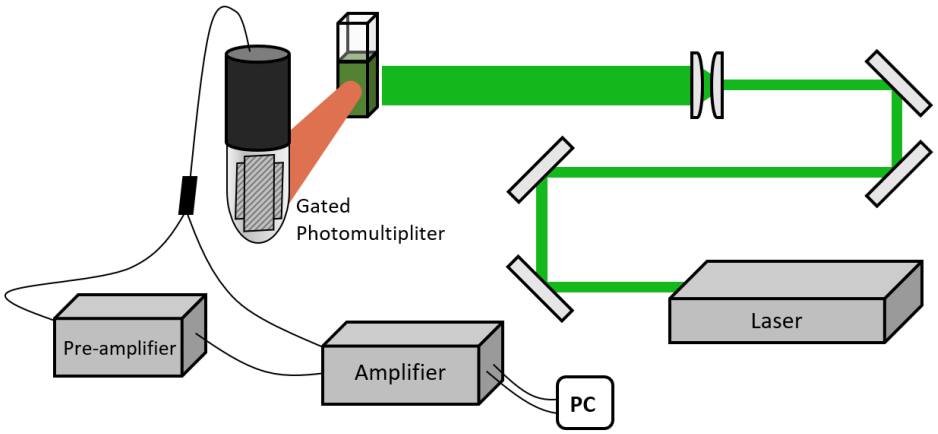

Figure 2.15 – Schematic of the main part of the delayed fluorescence set-up. Apart from what is shown, a case that encloses the set-up, a thermostatic bath, a power meter, an oscilloscope, two power supplies, a PM gater, and a temperature sensor also make part of the set-up.

The recorded signal can be corrected to eliminate additional fluorescence signals, called the flash artifact, which comes from the prompt fluorescence or from the glass of the cathode material from the detector induced by strong scattering of light. For that, an additional measurement at double the laser intensity (assuming that both are saturating) is recorded. The flash artifact (FA) is calculated by subtracting the data from the first flash of the regular measurement (F_D^{exp}) to the data from the first flash of the double laser intensity measurement (F_D^{double}), like shown in Eq. 2.18. One can then

correct the data from a measurement by subtracting FA from all flash induced data (Eq. 2.19) (Buchta et al., 2007).

$$FA = F_D^{double}(1) - F_D^{exp}(1) \quad \textbf{(Eq. 2.18)}$$

$$F_D^{\exp\, corr}(t) = F_D^{exp}(t) - FA \quad \textbf{(Eq. 2.19)}$$

An additional correction to account for the multiplicative influence of the Q_A^- concentration to the DF signal ($F_D(t)$) can also be done. To do so, PF signal can be recorded and the Q_A^- concentration decay over time determined with Eq. 2.20 (Buchta et al., 2007; Dau, 1994):

$$[Q_A^-] = \left(\frac{F_P(t) - F_0}{F_M - F_0}\right) \quad \textbf{(Eq. 2.20)}$$

being that F_M is the maximum PF signal and F_0 is the PF signal before the laser flash. Then the DF signal can be corrected with Eq. 2.21 to obtain $F_D^{corr}(t)$ signal that decays according to the population of $P680^+$ over time without the small $[Q_A^-]$ contribution.

$$F_D^{corr}(t) = \frac{F_D(t)}{[Q_A^-]} \quad \textbf{(Eq. 2.21)}$$

The corrected signal can be simulated (least squares) by a sum of (3-4) exponential functions, being that the best agreement is achieved when four exponential functions are used and one of which describes the millisecond phase (Buchta et al., 2007).

2.5.3 Chlorophyll fluorescence set-up upgrades

Motivated by the need for improvement of the laser safety of the PF and DF set-up some changes in the set-up had to be made. The solution came with the enclosure of the laser beam path inside a large bottomless case which has three removable top covers that allows for easy access to the inside during experimental work. The case was laid on top of the same laser table and the optics, including the laser head, were moved inside. To

achieve this, three mirrors were added to form the beam path as shown in Figs. 2.13 and 2.15. A removable mirror can be rotated into the widened laser path to make it hit the PF sample holder from the top instead of continuing towards the DF sample holder, like it was done before. The sample holder, detector and LED modules for the PF were kept the same. For the DF, a new PMT detector (R928, Hamamatsu) was installed, and a new sample holder was designed and constructed at the department workshop. Even though the previous detector was working, the change was done as it would massively help with mounting the experiment since the old PMT detector (7102, Hamamatsu) was of the head-on type and took up much more table space compared to the new one which is side-on type. It was also possible to achieve an improvement in the signal by using the new photomultiplier either because the older one may have suffered from light induced damage over time or because the noise coming from photons from other tiny light sources in the room was reduced by lowering the driving voltage for the PMT to 500 V (down from 1000 V, used previously). The new photomultiplier has a housing with a window where the same two optical filters can be attached (Fig. 2.14), and the new sample holder was designed so it screws directly in the PMT housing. A manual shutter to block light was also designed in the sample holder, to protect the PMT from residual room light when the set-up is not under operation.

Chapter 3 – Activation barrier of the O_2-formation step under the influence of the substrate-water analogue Ammonia.

This chapter was published as:

Assunção, R., Zaharieva, I., & Dau, H. (2019). Ammonia as a substrate-water analogue in photosynthetic water oxidation: Influence on activation barrier of the O_2-formation step. *Biochimica et Biophysica Acta (BBA)-Bioenergetics, 1860(7)*, 533-540.

DOI: https://doi.org/10.1016/j.bbabio.2019.04.005

Author contributions:

R. Assunção prepared the samples, conducted all time resolved O_2 polarography measurements and evaluated the data. Prepared the presented figures and wrote the initial manuscript

I. Zaharieva wrote the software for data evaluation and was involved in the revision of the manuscript

H. Dau supervised the work and was involved in the revision of the manuscript

The water oxidation reaction in Photosystem II has a particular detail that makes the investigation of this reaction's mechanism more challenging, namely the fact that the solvent of the reaction, water, is also the substrate of the reaction. One approach to overcome the problem has been to use ammonia (NH_3/NH_4^+) as a substrate water analogue as it is sufficiently similar, chemically and in size, to be able replace some water molecules in the vicinity of the manganese cluster (Mandal et al., 2017; Vinyard et al., 2016). Moreover, one binding spot has been shown to be directly to the Mn4 on the W1 position (Fig. 3.1) (Navarro et al., 2013; Schraut & Kaupp, 2014), and a second binding position to the Mn-cluster has been suggested but not confirmed (Schuth et al., 2017; Young et al., 2016). The presence of ammonia during the water oxidation by PSII has been reported to create a certain degree of inhibition (40-60% (Schuth et al., 2017; Tsuno et al., 2011)), which has generally led to the conclusion that ammonia was not replacing a substrate water, and thus ruling out W1 as a substrate water (Marchiori et al., 2018; Oyala et al., 2015).

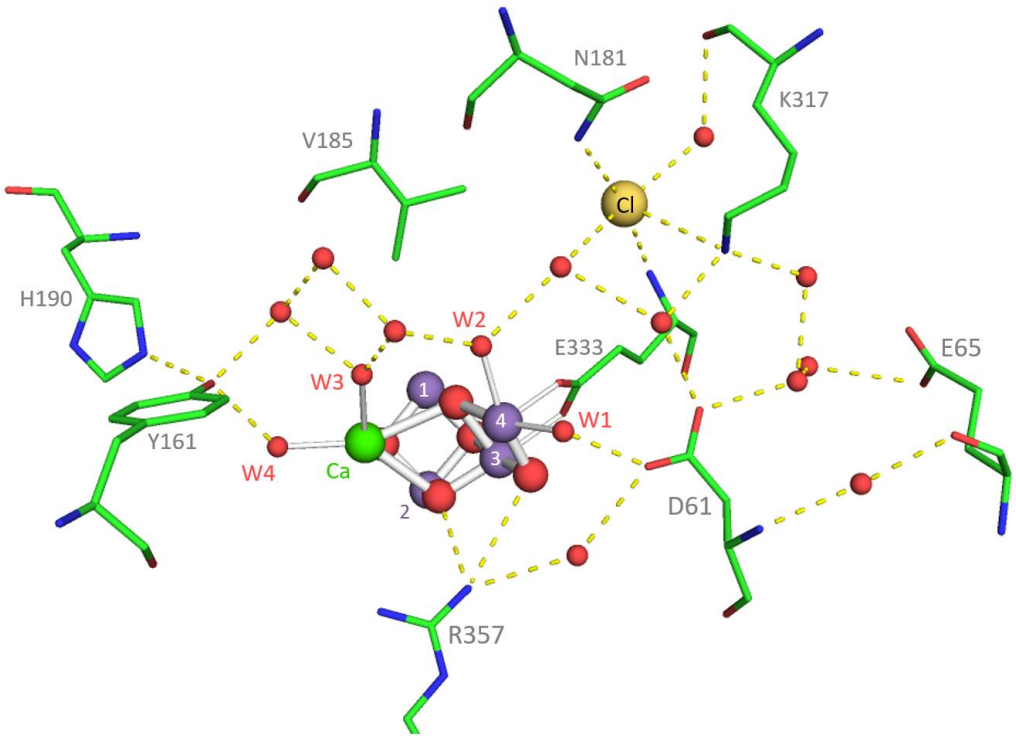

Fig. 3.1 – Partial representation of the hydrogen bond network around the OEC (Kern et al., 2018). Key amino acids and water molecules are shown along with the nearby Cl^-. Mn ions are shown in purple and oxygen atoms in red, while the smaller red spheres represent waters. The OEC-bound waters are labelled as W1, W2, W3 and W4.

Recently, it was shown that the (partial) inhibition of PSII oxygen evolution in the presence of NH_4Cl is largely due to an on/off effect of the O_2 activity (Schuth et al., 2017) and cannot be explained exclusively by slowed oxygen evolution (Boussac et al., 1990). Depending on the NH_4Cl concentration, a fraction of about 50% of the PSII cores were fully inhibited, for spinach as well as cyanobacterial PSII. In the major fraction of the O_2-active PSII, the rate constant of O_2 formation was found to be independent of the ammonium concentration in the buffer solution. To explain the experimental results, it was proposed that an anti-cooperative binding could occur at two sites, either to the inhibitory site or to the non-inhibitory site. The two binding sites would correspond to the W1 and W2 water molecules coordinated to Mn4, the "dangler manganese" (Fig. 3.1), but possibly also involving the carousel mechanism of water and ammonia binding proposed by Brudvig, Batista and co-workers (Askerka et al., 2017; Vinyard et al., 2016). However, among the O_2-producing PSII centers, PSII centers with O_2 evolution kinetics unaffected by ammonia binding are coexisting with a fraction of "slow" PSII, which could be explained by a third ammonia binding site (Schuth et al., 2017).

In the work presented in this chapter, we use time-resolved O_2 polarography for analysis of the temperature-dependence of ammonia inhibition, with a focus on determination of thermal activation energies of O_2 formation in the presence of ammonia. Using Eyring's transition-state treatment (Mortimer & Eyring, 1980), we also analyse the thermodynamic parameters of the O_2 evolution reaction in ammonia-treated PSII. Ammonia binding was induced by addition of various concentrations of NH_4Cl to the buffer solution.

3.1 Experimental details

3.1.1 Preparation of plant-PSII membrane particles

High-activity PSII-enriched membrane particles were prepared from spinach leaves, as described in Schiller and Dau (2000). Before storage at −80 °C, the chlorophyll concentration was determined spectroscopically according to a protocol from Wellburn (Wellburn, 1994). Using a Clark-type electrode (Hansatech Instruments) (Clark et al.,

1953), an O_2-evolution activity of 860 ± 20 μmol_{O2} $mgChl^{-1}$ h^{-1} was determined at 25 °C for the PSII membrane particles illuminated with continuous white light of saturating intensity. The measurements were done in buffer containing 15 mM NaCl, 5 mM $CaCl_2$, 1 M glycine betaine, 25 mM of 2-morpholinoethanesulfonic acid (MES - pH 6.3) with additional 0.25 mM 2,6-dichloro-1,4-benzoquinone (DCBQ) and 1 mM $K_3[Fe(CN)_6]$ as artificial electron acceptors (Schiller & Dau, 2000).

3.1.2 Time-resolved oxygen polarography

Time-resolved oxygen evolution measurements were performed using a centrifugable custom- made bare platinum electrode as described earlier (Dilbeck et al., 2012; Schuth et al., 2017). Before use, the frozen PSII suspension was thawed on ice (for 60 min, in the dark) and resuspended in Buffer NC [150 mM NaCl, 25 mM MES (pKa = 6.15), 25 mM HEPES (pKa = 7.55), 25 mM HEPES (pKa = 8.0), 1 M glycine betaine, 5 mM $MgCl_2$, and 5 mM $CaCl_2$, pH 7.5 (NaOH)]. The protein sample was then centrifuged at 50,000 × g for 12 min, the supernatant discarded, and the resulting pellet resuspended again in Buffer NC and kept on ice. For each measurement a sample containing 75 µg chlorophyll and a combination of Buffer NC and Buffer NH were added to the electrode. The Buffer NH had the same composition as Buffer NC but with 150mM NH_4Cl instead of 150 mM NaCl, and so using a mixture of the two buffers the NH_4Cl concentration (0–100 mM) could be controlled. Thereby the total chloride concentration was kept constant at the level of 170 mM. Fig. 3.2 shows that at this salt level the yield and reaction kinetics of O_2 formation were not negatively affected (no inhibition up to 330 mM). The total volume of the PSII suspension over the electrode was adjusted to be 750 µL, followed by centrifugation of the electrode assembly in a swing-out rotor at 10,000 × g for 10 min (at 4 °C).

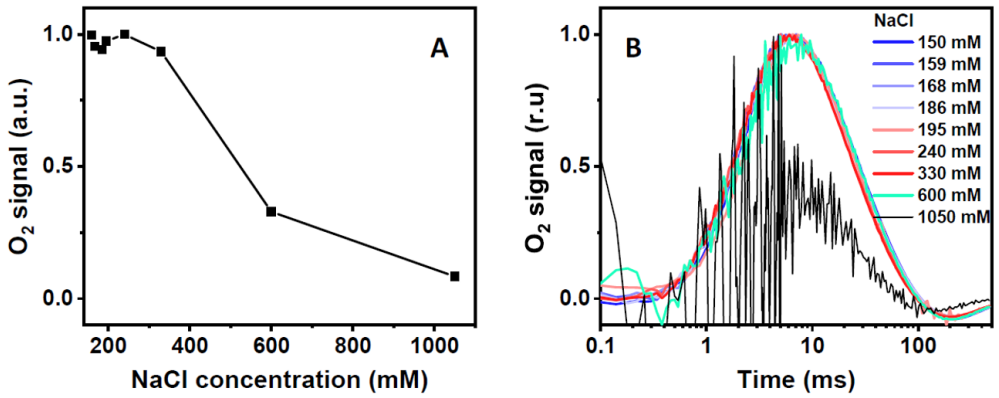

Figure 3.2 – NaCl influence on the yield and time course of O_2-formation by PSII. (A) signal amplitude (which here is proportional to the overall yield of O_2 production) versus the NaCl concentration. (B) Corresponding O_2 production transients normalized to 1. This figure illustrates that no deleterious salt effect is observed up to a NaCl concentration of 330 mM. Figure from SI of Assunção et al. (2019).

S-state transitions were excited in the dark-adapted PSII using saturating light flashes of about 10 µs duration (Xenon flash lamp, EG&G Optoelectronics, 4.5 J of electrical energy per discharge which corresponds to about 1 J measured at the sample (after filtering and light guide), an orange glass filter with a 570 nm cut-off was used to eliminate photoelectric flash artefacts induced by blue light. The final excitation spectrum is presented in Chapter 2. The individual oxygen-evolution transients were measured with a flash spacing of 900 ms for 20 flashes and an electrode potential of −0.95 V at the central Pt electrode vs the Ag ring electrode; the potential was switched on 15 s prior to the first flash. A home-built potentiostat was used for electrode polarization and detection of the O_2-reduction currents, the latter involving a high-pass filter with a time constant of 100 ms. The high-pass filter separates the light-induced O_2-transients from an approximately linear decrease in the O_2- signal. The latter results from detection and consumption (by the polarized platinum electrode) of dioxygen dissolved in the buffer solution. The simulations in Fig. 3.3 illustrate how the high-pass filter affects the O_2 signal. Its influence was considered in the fit algorithm used for simulation of the O_2 transients (using a fixed value for the filter time constant of 100 ms). The temperature (0–35 °C) was controlled by Peltier elements and monitored during the measurement by a miniature sensor immersed in the buffer solution of the O_2 flash experiment.

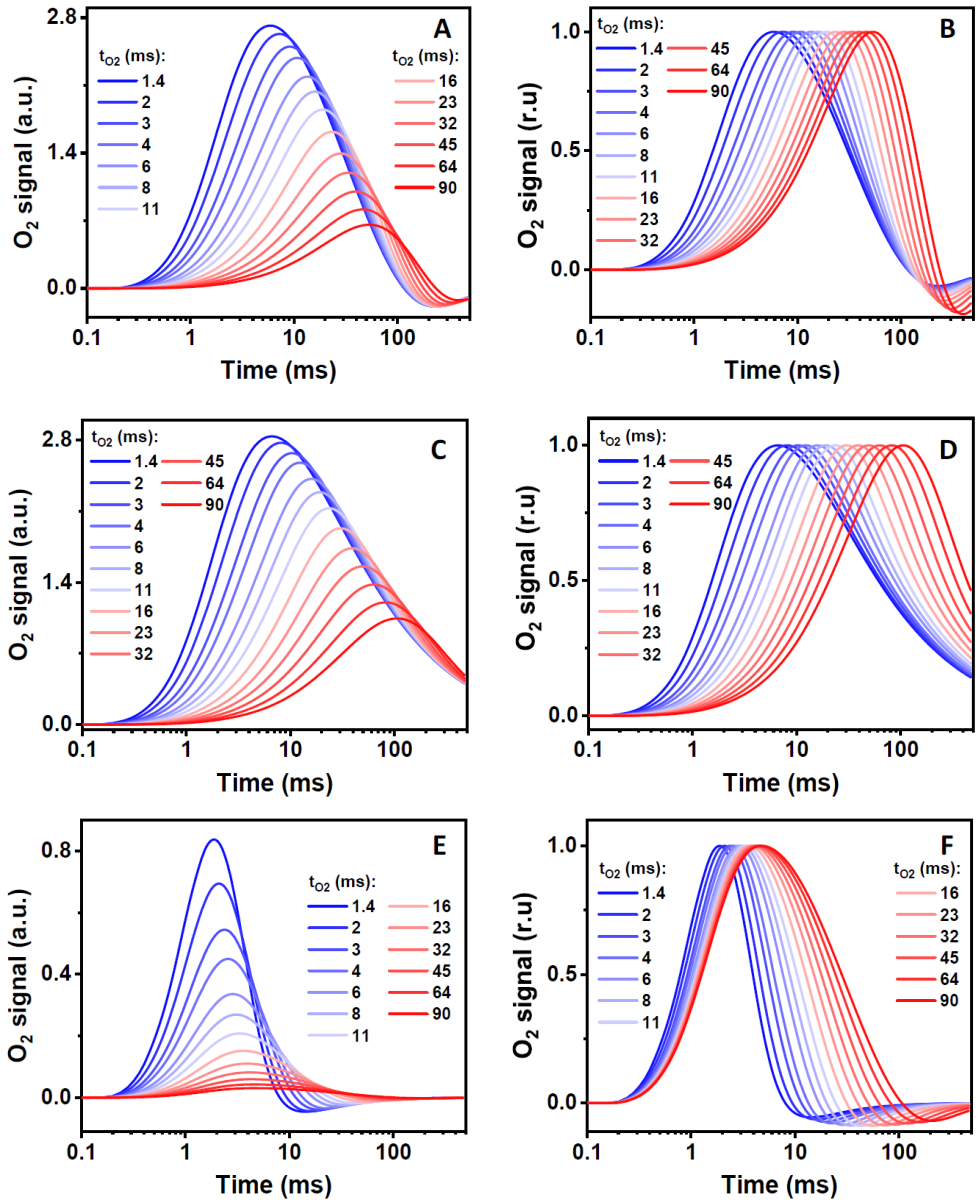

Figure 3.3 – Influence of high-pass filtering in the detection electronics illustrated by simulations using the same physical diffusion model and software implementation as used for curve-fitting of experimental transients. In the shown simulations, only the time constant of O_2-formation by PSII (τ_{O2}) was varied; all other parameters were kept constant at typical values. Panels (A) and (B) show the signals for a high-pass filter with a time constant of 100 ms, as used in this study. Panels (C) and (D) show the signal predicted for detection without any high-pass filter. Panels (E) and (F) show the simulated signals for a high-pass filter with a time constant of 1 ms. Panels (B), (D) and (F) are the normalized versions of the panels (A), (B) and (E). For detection without any high-pass filter, the integral of the O_2-transients (area below the curves for a linear time axis) corresponds to the total amount of produced O_2; this integral (area) is the same for all curves shown in panel C. We note that detection with a filter time constant of 1 ms results in O_2-transients with strongly reduced amplitudes (see (E)); this variant is shown for illustrative purpose only. Figure from SI of Assunção et al. (2019).

The O_2-evolution transients were simulated based on a reaction–diffusion model first described in Dilbeck et al. (2012). This numerical model takes into account the oxygen production from the PSII layer, the O_2 diffusion within the PSII layers (towards electrode surface and into the buffer solution), and the O_2 reduction reaction at the electrode surface using a minimum of adjustable parameters (Dilbeck et al., 2012). In addition, the simulations covered two populations of O_2-producing PSII, as introduced in Schuth et al. (2017), each with two individual time constants (τ_{lag} and τ_{O2}), but with identical electrode and diffusion parameters (effective layer thickness) for both PSII fractions (Fig. 3.4). The total O_2 signal was simulated as a linear combination of the O_2 transients calculated for the two PSII fractions with the percentage of the slow PSII fraction being a fit parameter. In all simulated O_2 transients, also the influence of the high-pass filter was part of the computational model.

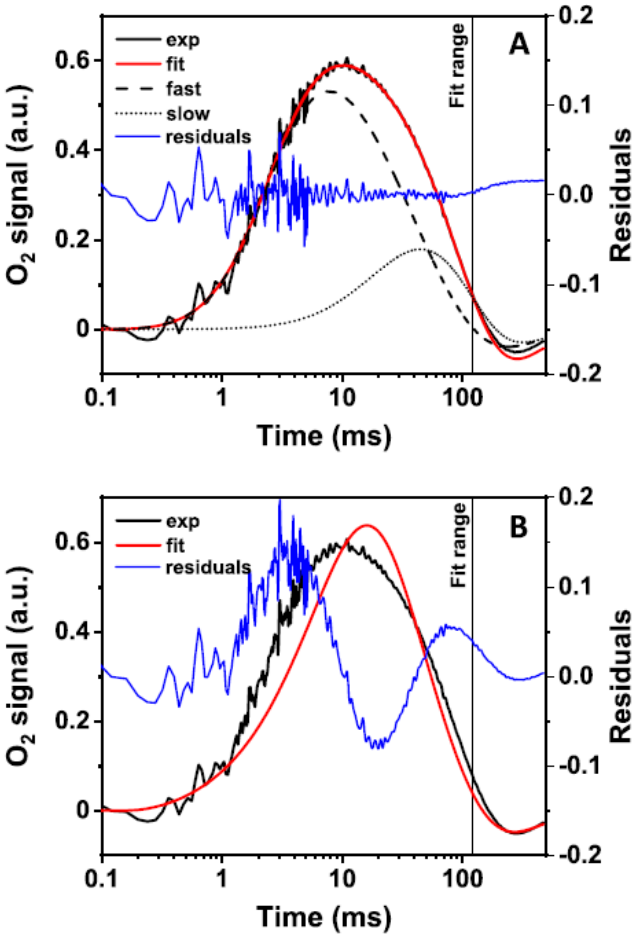

Figure 3.4 – Example of an experimental O_2 transient (exp) with simulated curves (fit). In A, curve-fitting for two fractions of O_2-producing PSII (Fast-PSII and Slow-PSII) is shown. In B, curve-fitting for a single PSII fraction is displayed. Only the PSII-layer thickness was kept at the same

level in the otherwise fully independent fits in A and B. The shown data was collected at 15 °C in the presence of 100 mM NH_4Cl and the O_2-formation for three reaction cycles of water oxidation by PSII were averaged (12 transients induced by saturating flashes of visible light sequentially applied to the same PSII sample). In A, the time constants of O_2 formation (τ_{ox}) and the relative fractions of PSII with fast and slow oxygen evolution were 2.0 ms (55%) and 46 ms (45%). In (B), only a single fraction was used (100%) and the fit algorithm provided a value of 7.2 ms. In A and B, the negative currents at times exceeding 100 ms resulted from the use of a high-pass filter in the detection electronics (Fig. 3.3), which was appropriately considered in the numerical simulation of the O_2 transients. Figure from Assunção et al. (2019).

3.1.3 Reversibility of NH_4Cl treatment

For evaluation of the reversibility of NH_4Cl treatment, after thawing, the PSII sample was divided into three portions, which were resuspended and centrifuged twice. The first portion was two times resuspended in Buffer NC (no NH_4Cl) and the third portion was two times resuspended in a buffer containing 100 mM NH_4Cl (appropriate Buffer NC/NH mix). The second portion was first centrifuged in 100 mM NH_4Cl (with an appropriate Buffer NC/NH mix) and then resuspended and centrifuged in Buffer NC (no NH_4Cl). Subsequently each portion was investigated at 15 °C using the O_2 polarography procedure described above, using the buffer of the second resuspension step (first and second portion in Buffer NC without NH_4Cl; third portion with 100 mM NH_4Cl).

3.2 Results

To verify the absence of irreversible modifications of PSII by NH_4Cl exposure in the dark, we exposed PSII for 20 min to 100 mM NH_4Cl and then exchanged the buffer against NH_4Cl-free buffer. By exchanging the buffer twice, the O_2 evolution activity was completely restored (Fig. 3.5). This control experiment shows that also prolonged dark-exposure of PSII to 100 mM NH_4Cl does not result in any specific deleterious effect on O_2-evolution by PSII.

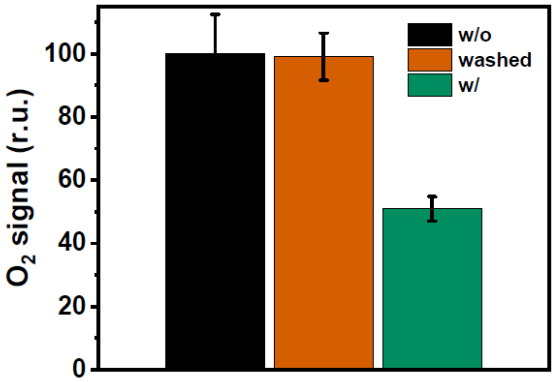

Figure 3.5 – Reversibility of NH_4Cl treatment. In black (left), magnitude of the O_2 signal for PSII in NH_4Cl-free buffer and normalized to 100%. In orange (middle), O_2 signal for PSII incubated with 100 mM NH_4Cl for about 20 min, and then washed (by centrifugation) in NH_4Cl-free buffer. In green (right), O_2 signal for PSII incubated and measured in 100 mM NH_4Cl Buffer. For each bar, the average of three experiments is shown; the error bars indicate standard deviations. Figure from SI of Assunção et al. (2019).

Aiming at testing the NH_4Cl influence on the thermal activation energy of the water oxidation reaction, we investigated O_2-release kinetics of plant PSII membrane particles (BBY prepared from spinach) by time-resolved O_2 polarography at different temperatures. The time-resolved O_2 detection after excitation of dark-adapted PSII membrane particles by sequences of saturating microsecond flashes of visible light (flashes spaced by 900 ms) allows us to discriminate between the NH_4Cl influence on the rate constant of the O_2 formation step, the efficiency of the S-state transitions, and the fraction of PSII with complete inhibition of the O_2-formation step; the influence of reactions at the PSII acceptor side can be safely ignored (Schuth et al., 2017). Therefore, analysis of these transients provides a clearly more differentiated picture than obtainable by the conventional detection of the rate of O_2-formation for continuous illumination of PSII in the presence of artificial electron acceptors.

In order to address the activation energy of the O_2-formation step in the presence of bound NH_4^+/NH_3, we measured O_2-release transients at eight temperatures ranging from 0 °C to 35 °C. For each temperature, measurements were performed in the presence of 0, 20, 60 and 100 mM NH_4Cl, while keeping the chloride concentration and ionic strength constant by addition of complementary amounts of NaCl. The temperature modified the oxygen evolution traces by affecting both, the electrode

response and the rate constants related to water oxidation reaction in PSII. As a result, the total amplitude of the O_2-release signal increases with temperature (Fig. 3.6), resulting in especially favourable signal-to-noise ratios at higher temperatures.

From the O_2 transients, we determined the O_2-forming fraction of PSII at various NH_4Cl concentrations (Fig. 3.7). At 35 °C, the inhibitory effect of NH_4Cl is especially pronounced (close to 60% inhibition at 100 mM NH_4Cl); at 0 °C it is especially weak (close to 30% inhibition). Its magnitude is in reasonably good agreement with values reported previously for data collection at 10 °C, for oxygen evolution by PSII from spinach and from various cyanobacteria (Schuth et al., 2017). Noteworthily, there are no indications for a pronounced temperature dependence of the K_M of NH_4^+/NH_3 binding suggesting that the previously determined K_M of about 25 mM (Schuth et al., 2017) could describe the behaviour at all investigated temperatures (with a caveat for the 0 °C data, where the seeming lack of inhibition at 20 mM NH_4Cl may be explainable by comparably high noise contributions).

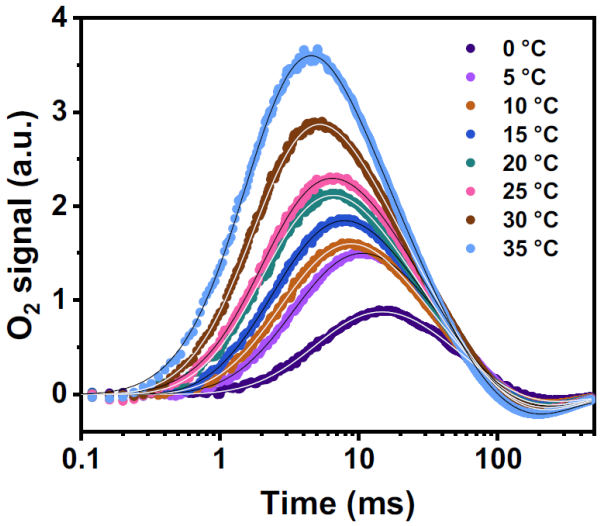

Figure 3.6 – O_2-evolution transients of PSII membrane particles at various temperatures. The PSII membrane particles were deposited on a bare platinum electrode by joined centrifugation of a PSII solution and the Pt/Ag electrode assembly. Here the temperature dependence of the O_2 transients is shown for PSII membrane particles without NH_4Cl in the buffer system. The white and black lines were obtained by simulations based on a numerical model that takes into account the O_2-formation and diffusion in the PSII layer as well as the O_2 reduction at the bare platinum electrode. The simulation parameters were determined by a fit procedure; the high fit quality is visible when comparing the simulated curves (smooth white and black lines) and experimental transients (coloured data points). Figure from Assunção et al. (2019).

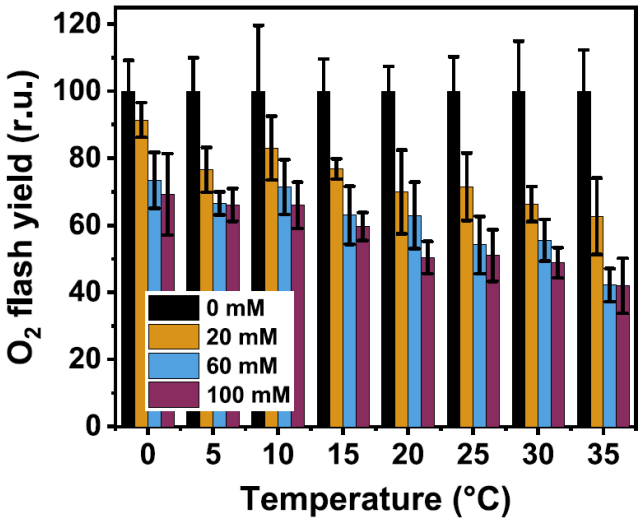

Figure 3.7 – Influence of NH_4Cl on the O_2-production per saturating light flash. The shown O_2-flash yield provides a relative measure of the total amount of produced dioxygen, independent of the rate constants of the O_2-formation step. It corresponds to the integral of the O_2-electrode signal as determined by the simulation approach detailed further below. All measurements were done at pH 7.5. The filled bars indicate the mean value of minimally three repetitions (with averaging of 12 O_2 transients each). The error bars indicate standard deviations, which are predicted to exceed the 1σ-uncertainty range of the mean value. Figure from Assunção et al. (2019).

As shown previously (Schuth et al., 2017), NH_4Cl does not only inhibit a major fraction of PSII completely, but it also slows down drastically the O_2-evolution rate constant in another fraction of PSII centers. We simulated the O_2 transients by employing a one-dimensional diffusion model that covers light-induced O_2 production (by PSII), O_2 diffusion (within the PSII film and in the bulk solvent), and O_2 reduction (at the bare Pt electrode), as described elsewhere (Dilbeck et al., 2012; Schuth et al., 2017). The slowing down in the decay of the polarographic signal observed with increasing NH_4Cl concentration (Fig. 3.8A), is well explained by assuming the coexistence of two O_2-producing PSII populations: (i) a PSII fraction with fast oxygen evolution (1.7 ms at 20 °C) and (ii) a PSII fraction with slow oxygen evolution (36 ms at 20 °C) (Schuth et al., 2017). The temperature dependence of the relative contributions of the three PSII fractions at various NH_4Cl concentrations are shown in Fig. 3.8B–D; further simulation parameters can be seen on Fig. 3.9 and the corresponding time constants of the O_2-formation step are shown in the form of Arrhenius plots in Fig. 3.10.

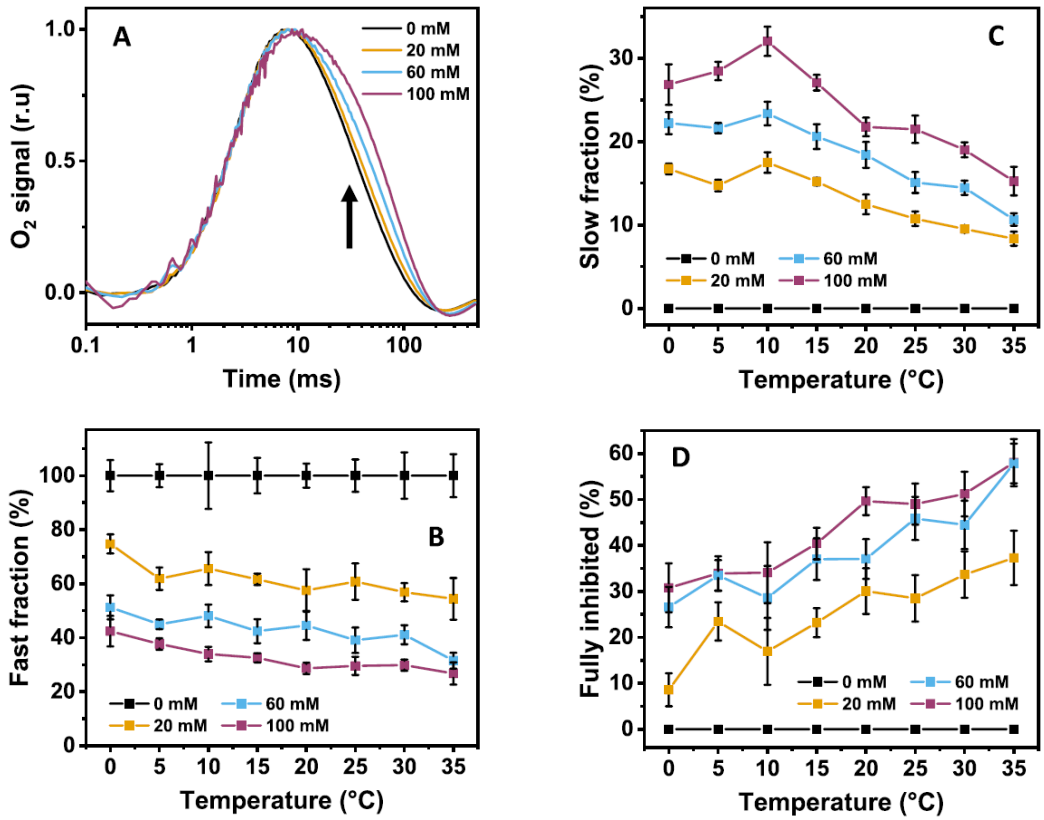

Figure 3.8 – Relative fractions of PSII centers with fast, slow and fully inhibited O_2-formation. (A) Normalized O_2 release kinetics recorded at 15 °C. The signature of a slow PSII fraction at higher NH_4Cl concentration is indicated by an arrow. (B) Fraction of PSII with fast O_2-formation (1.7 ms at 20 °C). (C) Fraction of PSII with slow O_2-formation (35 ms at 20 °C). (D) Fraction of fully inhibited PSII. The quantification is based on simulation (fitting) the O_2-transients with the reaction-diffusion model described elsewhere (Dilbeck et al., 2012; Schuth et al., 2017). The simulated O_2-transients were obtained by averaging the O_2-transients detected for the 3rd to 14th flash of a flash sequence applied to dark-adapted PSII. For each data point, the fit results of three experiments were averaged; the error bars indicate the corresponding standard deviation. Figure from Assunção et al. (2019).

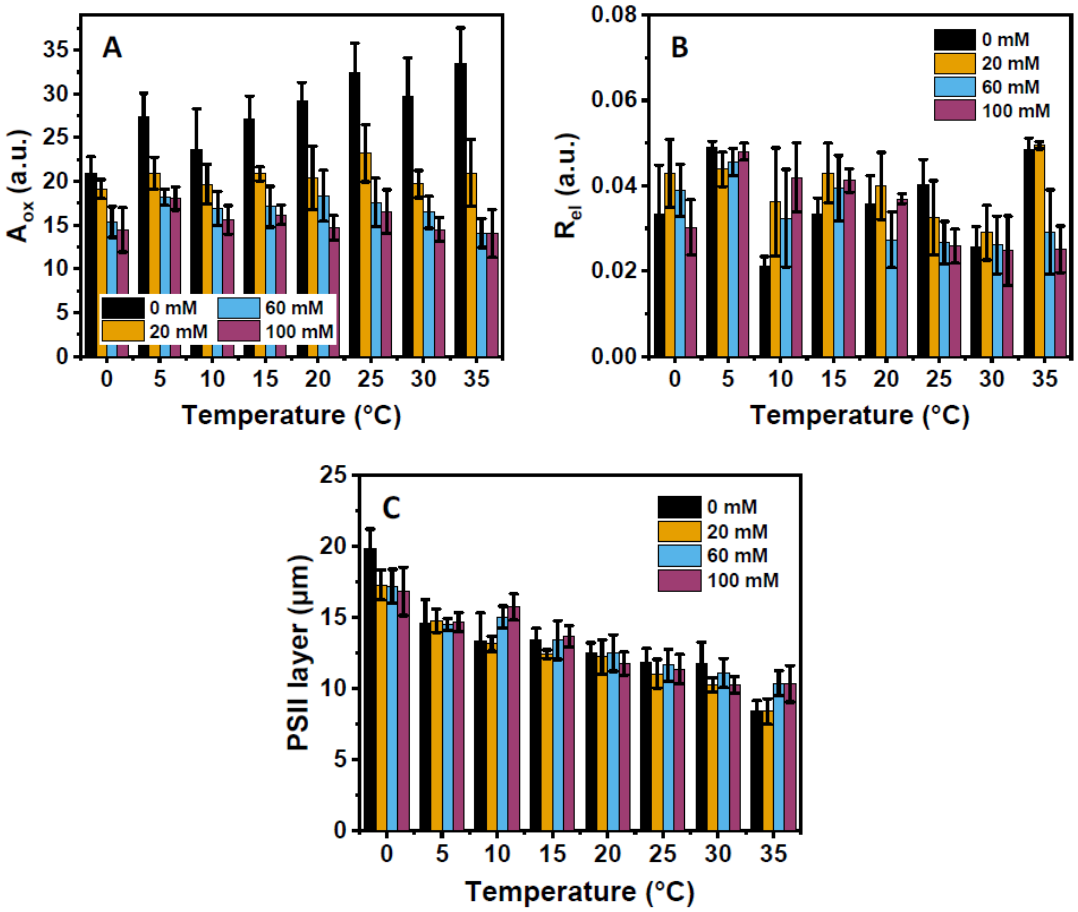

Figure 3.9 – Further simulation parameters for the time-resolved O_2-evolution traces simulated according to the reaction-diffusion model. In A, the scaling parameter relating to the amount of O_2 molecules formed by PSII (A_{ox}) is shown. In B, rate-constant parameter for O_2 reduction at the bare platinum electrode is displayed. In C, apparent thickness of the PSII layer obtained for a diffusion constant of 2.2 μm^2/ms is shown. The apparent layer thickness changes with temperature because of the temperature dependence of the O_2 diffusion constant that was not considered. Figure from SI of Assunção et al. (2019).

The time constant for O_2 release (τ_{O2}) by PSII in the absence of NH_4Cl is found to be about 1.7 ms at 20 °C. This value agrees well with time constants for PSII oxygen evolution reported before (see, e.g., Buchta et al. (2007)) and is not modified by the presence of NH_4Cl in the Fast-PSII fraction (Fig. 3.10A). On the other hand, the O_2 evolution time constant for the Slow-PSII fraction is about 36 ms. This value is similar to the time constants reported for PSII mutants with point mutations at amino acid residues that interact with the water cluster surrounding the Mn_4CaO_5 core of the OEC (e.g. D1-D61, D1-V185, D2-K317 and CP43-R357) (Bao & Burnap, 2015; Dilbeck et al., 2012; Hwang et al., 2007; Pokhrel et al., 2013). Similar to the Fast-PSII fraction, at all investigated temperatures the O_2-evolution time constant of the Slow-PSII does not depend on the

NH_4Cl concentration (Fig. 3.10B). To extract the activation energies (E_a) for the O_2-evolution reaction, the time constants were plotted as a function of the temperature (Fig. 3.10) and fitted using the standard Arrhenius equation (Eq. 3.1):

$$ln(\tau) = -ln(A) + E_a/K_BT \quad \textbf{(Eq. 3.1)}$$

The thereby obtained activation energies (E_a) and the pre-exponential factors (A) are presented in Table 3.1. We find that the activation energies for both O_2-producing PSII fractions are independent of the NH_4Cl concentration. The activation energy for the Fast-PSII fraction is 248 ± 11 meV and for the Slow-PSII fraction it is 348 ± 14 meV (see Table 1 for the individual values). The plots for the time constants related to the proton-release step (τ_{lag}) preceding the O–O bond formation are shown in Fig. 3.11. Unlike the O_2 formation step, a slight NH_4Cl dependence may be present, but it is below the uncertainty range of the experimental data and is thus not further discussed. Based on Eyring's transition state theory (Åqvist et al., 2017; Mortimer & Eyring, 1980), we determined activation enthalpy, $\Delta H^{\ddagger}$, and activation entropy, $\Delta S^{\ddagger}$, of the O_2-evolution reaction according to Eq. 3.2 and Eq. 3.3, respectively (Table 3.1).

$$\Delta H^{\ddagger} = E_a - k_BT_0 \quad \textbf{(Eq. 3.2)}$$

$$\Delta S^{\ddagger} = k_B\, ln(hA/k_BT) - k_B \quad \textbf{(Eq. 3.3)}$$

In the above equations, k_B is the Boltzmann constant, h is the Planck constant, T refers to the absolute temperature in Kelvin, and T_0 is a temperature in center of the investigated temperature range (here 20 °C).

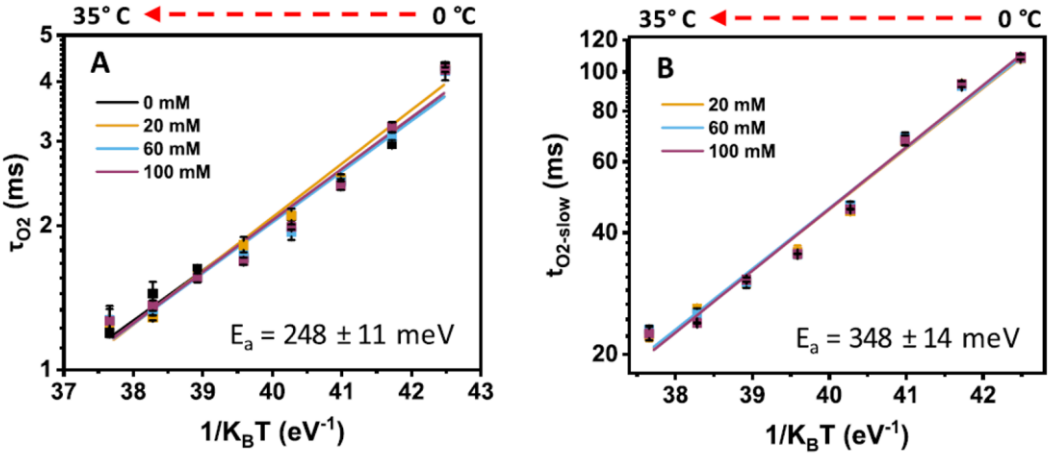

Figure 3.10 – Arrhenius plots for the O_2-release step at different NH_4Cl concentrations. The plots for the O_2 release (τ_{O2}) are shown for the PSII fraction with fast O_2 formation (A) and for the PSII fraction with slow O_2 formation (B). In (A) and (B), average E_a-values are indicated, for individual E_a values see Table 3.1. The values for the time constant of O_2 formation, τ_{O2}, were obtained from simulation (fit) of the averaged O_2-transients of the 3rd to 14th flash applied to dark-adapted PSII. For each data point, the fit results of three experiments were averaged; the error bars indicate the corresponding standard deviations. Figure from Assunção et al. (2019).

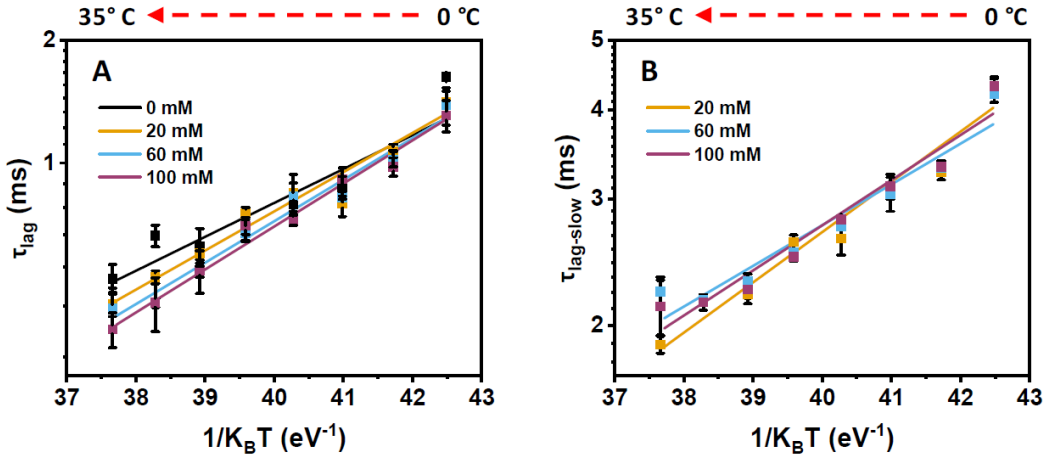

Figure 3.11 – NH_4Cl influence on the 'lag phase' (delayed onset) of the O_2 release step of PSII. The time constant is partially assignable to proton release in the $Y_Z^{ox}S_3^+ \rightarrow Y_Z^0S_3^n$ transitions, but also includes a contribution from the O_2 electrode response. This is shown for the Fast-PSII (A) and Slow-PSII (B) fractions. The results are obtained from the fit of the average of three catalytic cycles (averaged O_2 traces from the 3rd flash to the 14th), and for each point, at least three experiments were performed. Figure from Assunção et al. (2019).

Table 3.1 – Time constants at 20 °C (τ_{O2}), the Arrhenius activation parameters (E_a and A, Eq. 3.1) and Eyring's activation enthalpy and activation entropy ($\Delta H^{\ddagger}$ and $-T\Delta S^{\ddagger}$; Eq. 3.2 and Eq. 3.3). The values of $\Delta H^{\ddagger}$ and $-T\Delta S^{\ddagger}$ are provided for 20 °C (293 K). The error ranges provided for E_a apply also for to the activation enthalpy and entropy. Table from Assunção et al. (2019).

	$[NH_4Cl]$ (mM)	τ_{O2} (ms) at 20 °C	E_a (meV)	A (s^{-1})	$\Delta H^{\ddagger}$ (meV)	$-T\Delta S^{\ddagger}$ (meV)
Fast PSII fraction	0	1.71	241 ± 10	7.6×10^6	216	369
	20	1.82	258 ± 8	1.5×10^7	233	352
	60	1.74	244 ± 11	8.7×10^6	219	365
	100	1.69	248 ± 11	9.8×10^6	223	362
Slow PSII fraction	20	35.9	346 ± 12	2.2×10^7	321	342
	60	35.4	346 ± 14	2.2×10^7	321	342
	100	35.5	352 ± 13	2.9×10^7	327	335

The quantum yield of the tertiary light-driven reactions at the PSII donor side is lower than unity, largely due to charge recombination processes that compete with forward electron transfer (Dau & Zaharieva, 2009; Grabolle & Dau, 2007). This reduction in quantum yield (φ) can be viewed as resulting from 'miss events', which are described by the miss factor, m (φ = 100% - m); typical m-values for intact PSII range from 7 to 15% (Dau & Haumann, 2007; Kok et al., 1970). The miss events desynchronize cycling through the S-state cycle and thus result in deviations from the perfect flash number dependence with maximal O_2-yield on the 3rd, 7th, and 11th saturating flash of light applied to dark-adapted PSII. The extent of these deviations thus is informative regarding the miss-factor magnitude. Fig. 3.12 shows the flash-number dependence of the O_2 yield at 0 °C and 30 °C for control-PSII without NH_4Cl (black curves) and with 100 mM NH_4Cl. Visual inspection facilitates an informative qualitative comparison of the miss-factor magnitude. Upon addition of 100 mM NH_4Cl, there is a fraction of Fast- PSII (orange curves) and Slow-PSII (blue curves), for which we determined the respective O_2-flash yield for each of the first 10 flashes individually, by simulation of the O_2 transients as described above. The control PSII (without NH_4Cl) exhibits a reasonably low miss factor at 0 °C (Fig. 3.12A), which is moderately increased at 30 °C (Fig. 3.12B). For the Fast-PSII, in the presence of NH_4Cl, we observe a significantly more pronounced de-synchronization (in comparison to the control PSII) indicative of an increased miss factor at both temperatures (strongly damped period-of-four oscillations) at both temperatures. For the Slow-PSII, the de-synchronization is increased further. Especially

the increased miss factor of the Fast-PSII is informative. In the absence of any clear effect of NH_4Cl exposure on rate constant and activation energy of the O_2-formation step, the modified miss factor detected for the Fast-PSII fraction provides important support to NH_4^+/NH_3 binding to the Fast-PSII fraction.

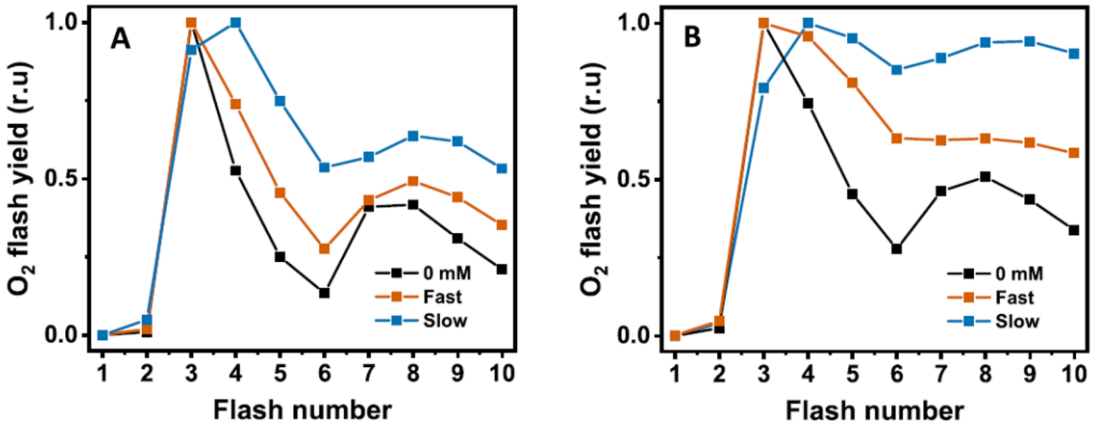

Figure 3.12 – Oxygen yield per flash for control PSII without NH_4Cl (black), Fast-PSII in the presence of 100 mM NH_4Cl (orange), and Slow-PSII in the presence of 100 mM NH_4Cl (blue). The O_2 transients were collected at 0 °C (A) and 30 °C (B). A sequence of saturating flashes of visible light (spaced by 900 ms) was applied to dark-adapted PSII. For each flash, the respective O_2-transient was recorded and analysed. The shown O_2-flash-yield patterns are normalized to unity at the maximal O_2-yield. Figure from Assunção et al. (2019).

3.3 Discussion

3.3.1 Three NH_4^+/NH_3 binding sites with distinctly different relations to the O_2-formation chemistry

Time-resolved detection of O_2 formation after light-flash excitation facilitated discrimination of NH_4^+/NH_3 binding at three sites resulting in three PSII fractions with distinct functional properties, in line with previous findings (Schuth et al., 2017). The K_M value for binding has been found to be around 20–30 mM (referring to the NH_4^+ concentration in the buffer solution) (Schuth et al., 2017), without obvious differences in the K_M value when comparing the three sites. Also, the data shown in Fig. 3.7 does not provide evidence for distinctly different K_M values, at least not in the temperature range from 5 °C to 30 °C, even though more minor differences cannot be excluded. We

can only speculate on possible reasons for identical K_M values. Previously, we have suggested that identical K_M values could result from mutually exclusive, anti-cooperative NH_3 binding (Schuth et al., 2017). An alternative option is binding of NH_4^+/NH_3 in the S_1 state at a single binding site with a K_M value close to 25 mM followed by relocation in the S_2 state to different binding sites with similar affinities, possibly associated with NH_4^+ deprotonation and NH_3 binding to a manganese ion of the catalytic Mn_4CaO_5 cluster. At largely saturating NH_4^+ concentration of 100 mM, we observe three PSII fractions distinguished by the following functional properties: (1) complete inhibition of O_2-formation, (2) fast O_2-formation with a time constant of 1.7 ms at 20 °C (Fast-PSII), and (3) slow O_2-formation with a time constant of 36 ms at 20 °C (Slow-PSII). For the Fast-PSII, we now determined an activation enthalpy of 223 ± 11 meV. Activation enthalpy and entropy of the Fast-PSII are essentially identical to the corresponding figures in the absence NH_4^+/NH_3 binding determined herein and elsewhere (Buchta et al., 2007). For the Slow-PSII, the activation enthalpy is 323 ± 11 meV and is thus significantly increased, whereas the activation entropy remains essentially unchanged. The completely unchanged properties of the O_2-formation step raise the question whether detection of the Fast-PSII fraction could result from an NH_4Cl concentration that was too low to allow for binding at all Slow-PSII and at all fully-inhibitory sites. However, the experimentally determined K_M values of 20–30 mM strongly suggest that NH_4^+/NH_3 binding at 100 mM NH_4Cl should be largely complete. In the present investigation, additional evidence for binding to the Fast-PSII fraction comes from the data of Fig. 3.11, which indicates that the Fast-PSII fraction at 100 mM NH_4Cl differs clearly in its miss factor from the PSII in NH_4Cl-free buffer. Thus, we consider NH_4^+/NH_3 binding to the Fast-PSII fraction as likely and see two basic options to explain the unchanged properties of the O_2-formation step: Either (i) NH_4^+/NH_3 binding indeed occurs at a site without any influence on the O_2-formation step, excluding not only that the Fast-PSII site is a substrate water site, but also any relevant modification of the H-bonded network formed by the water molecules, amino-acid residues and the nearby chloride ion. Or (ii) NH_4^+/NH_3 binding occurs in the S_2-state followed by unbinding before onset of the O–O bond formation step, in the $Y_Z^0S_3^+$ or $Y_Z^{ox}S_3^+$ or $Y_Z^{ox}S_3^n$ state. In line with the second option, the absence of bound ammonia in the S_3-state recently has been suggested based on EPR and kinetic UV–vis experiments (Boussac et al., 2018). We note that the second scenario does not exclude

that in the S_2-state, the NH_4^+/NH_3 binding site of the Fast-PSII corresponds to a substrate-water site. The fully inhibitory binding site could very well correspond to the binding site of a substrate-water molecule, whereas the lack of complete inhibition suggests that the Slow-PSII binding site is not identical with a water-binding site. We believe NH_4^+/NH_3 binding at the Slow-PSII site relates to disturbances of the H-bonded protein-water cluster(s) neighbouring the Mn_4Ca-oxo core of the catalytic site. Evidence for this conjecture comes from comparison to genetic PSII variants. The time constant of the O_2-formation step in the Slow-PSII is 36 ms at 20 °C and is thus very similar to time constants determined in mutants where the hydrogen-bonding network coupled to the Mn_4CaO_5 center was modified by point mutations, e.g. D1-D61, D1-V185, D2-K317 and CP43-R357 (Bao & Burnap, 2015; Dilbeck et al., 2012; Hwang et al., 2007; Pokhrel et al., 2013). However, here we find in the Slow-PSII a pronounced increase of the activation enthalpy, without major changes in the activation entropy (Table 3.1). In clear contrast, for PSII variants with severely retarded O_2-formation, a surprising decrease in activation enthalpy has been reported, which is overcompensated by less favourable entropic contribution to the total activation energy (Bao & Burnap, 2015). The clear increase in the activation enthalpy of the O_2-formation step implies that NH_4^+/NH_3 binding at the Slow-PSII site increases the energetic (enthalpic) barrier of the rate-determining step in O–O bond formation. The increased energetic barrier may be viewed as destabilization of the transition state or stabilization of an unfavourable active-site conformation before onset of the O–O bond formation step, where the active site comprises not only the catalytic metal-oxo complex and its first-sphere ligands, but also the surrounding protein-water environment.

3.3.2 Identification of the NH_4^+/NH_3 binding sites?

Recently, non-inhibitory ammonia binding to the water ligand of Mn4 denoted as W1 and inhibitory binding at the W2 site was suggested (Schuth et al., 2017). For these two sites, similar ammonia-binding energies are plausible as is mutually exclusive (anti-cooperative) binding, thereby explaining that a single K_M value describes the formation of an inhibited PSII fraction and an uninhibited PSII fraction. FTIR S-state difference

spectra indicated that the uninhibited PSII fraction is associated with spectral changes that exhibit clear similarities to spectral changes observed for mutation of the D61 residue (of the D1 protein of PSII), which is an H-bonding partner of W1, thereby providing support to assignment of the non-inhibitory ammonia-binding site to W1. However, similar spectral changes are also observed for other genetic modifications that affect the H-bonded protein-water network surrounding W1 and W2. On these grounds, also non-inhibitory binding at different sites in vicinity of W1 cannot be excluded. A recent computational investigation evaluated six putative binding positions in the second coordination sphere of the Mn_4Ca-oxo cluster. Two of these were judged as being of possible relevance; one involves the NH_4^+- $K317^0$ - $D61^-$ ion pairing (Mandal et al., 2017).

The suggestion of non-inhibitory binding at the W1 site (Schuth et al., 2017) was motivated by experimental evidence obtained by means of advanced EPR investigations on PSII in its S_2-state combined with detection of substrate-water exchange rates and computational methods (Navarro et al., 2013). Ammonia binding to Mn4 with strong H-bonding to D61 was later confirmed by other investigators (Oyala et al., 2015). It was concluded that non-inhibitory ammonia binding occurs at the W1 site of PSII, thereby rendering a role of W1 as a substrate-water molecule unlikely (Navarro et al., 2013). Although not necessarily in conflict with this conclusion, the present results suggest that also other scenarios are conceivable that do not exclude W1 as a substrate water molecule:

(1) There exists a fully inhibitory NH_4^+/NH_3 binding site which could relate to bound NH_3 replacing one of the two substrate-water molecules. Here ammonia might replace the W2 ligand of Mn4, but solid evidence for this conjecture is still lacking.

(2) There exists a NH_4^+/NH_3 binding site, for which the average quantum yield of the S-state transitions is significantly lowered (higher miss factor) but the kinetics of the O_2-formation steps are not at all affected (unchanged activation enthalpy and entropy). This binding site could correspond to the W1 ligand of Mn4. However, it is unlikely that ammonia still bound at the W1 site in the O_2-formation step (and thus affecting the surrounding H-bond network) would leave the kinetic characteristics completely

unaffected. To explain fully non-inhibitory ammonia binding at the W1 site, we tentatively propose that NH_3/NH_4^+ binding in the S_2-state of PSII is followed by unbinding before onset of the O–O bond formation step. This scenario is not easily reconciled with the carousel mechanism (Askerka et al., 2017; Vinyard et al., 2016). It implies that assignment of W1 to a substrate-water molecule cannot be ruled out (in contrast to a conclusion in Navarro et al. (2013)). We note that, based on DFT calculations, recently Siegbahn ruled out pivot or carousel mechanisms because the involved 5-coordinated Mn(IV) complex would be too high in energy (Siegbahn, 2018).

(3) There exists a site where NH_3/NH_4^+ binding increases the energetic barrier of the O–O bond formation step significantly. This site is not a substrate-water site. It likely is within the H-bonded protein-water cluster in vicinity of the Mn_4Ca-oxo cluster that comprises also W1 and W2. Binding by replacement of W1 or W2 cannot be excluded, but a location outside the first coordination sphere of Mn4 might be more likely.

Chapter 4 – Glass-transition in structural dynamics of the water-oxidizing complex of photosynthesis

Complemented by additional experiments this chapter is part of a manuscript by:

Assunção, R., Oliver, N., Nürnberg, D., Zaharieva, I., Haumann, M., Dau, H. (2022).

Author contributions:

R. Assunção prepared the samples, performed XAS experiments and evaluated the data

N. Oliver, D. Nürnberg, I. Zaharieva supported the synchrotron measurements

M. Haumann supported the synchrotron measurements, performed extra XAS measurements on non-biological samples (not shown in this chapter) and evaluated the data

H. Dau supervised the work and was involved in the revision of the manuscript

In PSII, the kinetics of OEC → $Y_Z^{\bullet+}$ electron transfer (ET) are well known and the time constants (τ) increase from ~40 µs in S_0 → S_1 to ~1.5 ms for the O_2-releasing step S_3 → S_0 at room temperature. The τ increase was related to up-charging of the OEC that diminishes the redox potential difference to $Y_Z^{\bullet+}$, to proton-coupled electron transfer, e.g., in the S_2 → S_3 transition, as well as to O=O bond formation, substrate water binding, and further structural changes (Cox & Messinger, 2013; Dau & Haumann, 2008; Renger, 2011). However, the absolute ET rate constants have remained enigmatic. The classical theory of Marcus and coworkers for thermally activated, non-adiabatic ET in electronically weakly coupled systems predicts that the rate decreases exponentially with increasing edge-to-edge distance between donor and acceptor (Marcus & Sutin, 1985). Seminal studies by Dutton and colleagues demonstrated that such a distance-dependence is indeed observed for many biological ET reactions including in photosynthetic proteins (Moser et al., 1992). Since the distance between the closest Mn ion of the OEC and Y_Z is only ~7.5 Å (Ibrahim et al., 2020; Kern et al., 2018; Suga et al., 2017), for a "pure" ET reaction a rate of at least 10^{10} s^{-1} or a τ-value of <1 ns thus may be expected (Moser et al., 1992), which is minimally 5 orders of magnitude smaller than experimentally observed. This gap is getting smaller because of the activation energy term in Electron transfer theory, but still remains sizeable. Therefore, the OEC → $Y_Z^{\bullet+}$ ET seems not to be well described by the Marcus formalism, even for S_1 → S_2 where the ET is not coupled to proton release. We here approached identification of factors that are crucial for the water oxidation reactions by studying temperature effects on the OEC.

X-ray absorption spectroscopy (XAS) provides direct access to the metrical parameters of coordination complexes (interatomic distances, R, at ~0.02 Å accuracy) and to the mobility of atoms via the Debye-Waller parameter (σ^2) (Dau et al., 2003; Strange & Feiters, 2008; Yano & Yachandra, 2009). σ^2 reflects the mean atomic position displacement, similar to the root-mean-square displacement from crystallography, including static and dynamic disorder, i.e., due to superposition of structures with slight coordinate variations and vibrational motions (Fornasini & Grisenti, 2015; Sevillano et al., 1979; Vila et al., 2007). Earlier XAS and crystallographic studies showed a similar OEC structure at cryogenic and ambient temperatures at least in S_1 (Haumann, Müller, et al., 2005; Kern et al., 2012). Here, we used XAS to determine the R and σ^2 values for the OEC

from cryogenic to ambient temperatures (20-295 K). The obtained biphasic σ^2 increase with temperature for the interatomic distances in the OEC indicated that the atomic mobility was determined by the so-called protein-glass transition with a "breakpoint" around 200 K (Doster, 2010; Ringe & Petsko, 2003). This behavior is commonly attributed to the onset of coupled protein/water motions above the transition temperature (Doster, 2010; Jansson & Swenson, 2010; Ringe & Petsko, 2003; Tournier et al., 2003; Yang et al., 2015). We propose that the ET reactions are largely limited by reaching specific conformations of the hydrogen-bonded network that prime and facilitate the OEC oxidation.

4.1 Materials and Methods

4.1.1 Preparation of PSII samples

PSII-enriched membrane particles with high O_2 evolution activity (≥1000 µmol O_2 mg chl^{-1} h^{-1} at 28 °C) were prepared from market spinach and stored at ~2 mM chlorophyll (chl) in a -80 °C freezer, as described earlier (Schiller & Dau, 2000). Preparation of PSII samples for XAS was done under dim green light or in darkness. PSII preparations were thawed on ice (60 min), washed with a buffer containing 15 mM NaCl, 1 M glycinebetaine, 5 mM $MgCl_2$, 5 mM $CaCl_2$, and 25 mM MES (pH 6.3), collected by centrifugation (12 min, 50000xg), and 200 µl of the pellet (~10 mM chl) was loaded into transparent polycarbonate holders (dimensions of 2x10x10 mm^3) covered on one side by 25 µm thick Kapton tape. The samples were partly dehydrated (loss of ~25 % of the initial water content) in a desiccator over silica gel at 0.2 bar air pressure in a cold room at 4 °C in darkness for 1.5 h (Haumann, Liebisch, et al., 2005). After this, the open side of the samples was covered also with Kapton tape and samples were immediately frozen in liquid nitrogen until use. This procedure provided PSII membrane particle samples with a manganese concentration of about 0.5 mM and the OEC practically 100 % synchronized in the dark-stable S_1 state, as reported earlier (Haumann, Liebisch, et al., 2005; Haumann, Müller, et al., 2005).

4.1.2 X-ray absorption spectroscopy

XAS at the Mn K-edge was performed at beamline KMC-3 at the BESSY-II synchrotron (Helmholtz Center Berlin, Germany; 300 mA top-up mode of the storage ring), using a set-up including a Si[111] double-crystal monochromator, a 13-element energy-resolving Si-drift detector (RaySpec) for X-ray fluorescence detection and an ion chamber for transmission detection, and DXP-XMAP pulse-processing electronics (XIA) (Abrashev et al., 2019; González-Flores et al., 2016). Samples were held in a liquid-helium cryostat (Oxford) at temperatures ranging between about 20-300 K in a ~0.2 bar heat-exchange He gas atmosphere. The sample temperature was adjusted via the He-flow/heating control system of the cryostat and was measured via a sensor close to the holder on the cryostat rod. Sample mounting on the cryostat rod during sample changes was carried out in the experimental hutch of the beamline under dim green light. The energy axis of the monochromator was calibrated (accuracy ±0.1 eV) using the sharp pre-edge peak in the K-edge spectrum of a $KMnO_4$ powder sample (fitted reference energy of 6543.3 eV). The spot size on the samples was ca. 0.6 x 4 mm (vertical x horizontal) as set by a focusing mirror and slits. Several non-overlapping spots of the samples were moved into the X-ray beam by computerized positioning of the rod (vertical) and X-ray fluorescence spectra were collected using a continuous monochromator scan mode (scan duration ~6.5 min). Up to 20 scans per temperature to k = 12.2 $Å^{-1}$ were averaged (1-2 scans per sample spot) for signal-to-noise ratio improvement. XAS data were processed (dead-time correction, background subtraction, normalization) to yield XANES and EXAFS spectra using established procedures and in-house software (Dau et al., 2003). k^3-weighted EXAFS spectra were simulated with in-house software and phase functions from FEFF9 (S_0^2 = 0.75) (Jorissen & Rehr, 2013; Rehr et al., 2010).

4.2 Results

PSII membrane particle samples with high O_2-evolution activity were prepared with the oxygen-evolving Mn_4CaO_5 complex (OEC) in the dark-stable S_1 state. XAS spectra at the Mn K-edge were collected in a temperature range of about 20-295 K. Earlier XAS studies on PSII showed that the X-ray photoreduction (xpr) velocity of the manganese ions in the OEC depends on X-ray flux, sample temperature, and S-state (Grabolle et al., 2006; Haumann, Liebisch, et al., 2005; Haumann, Müller, et al., 2005). Here, the X-ray dose per area was minimized by employing a low-flux bending-magnet beamline (ca. 1010 photons s-1) and irradiating a large sample area (~2.5 mm^2). We assayed xpr under these conditions, for determining the "safe" time-period for collection of unperturbed S_1 XAS spectra (Figs. 4.1, 4.2). To monitor Mn K-edge shifts to lower energies due to xpr, either a series of XAS spectra were collected on a single sample spot or X-ray fluorescence time traces were recorded at a fixed incident energy (6551.5 eV) (Grabolle et al., 2006; Haumann, Liebisch, et al., 2005; Haumann, Müller, et al., 2005). The data revealed a pronouncedly temperature-dependent xpr rate, which was about 10-fold larger at 295 K vs. 20 K, as observed earlier (Grabolle et al., 2006; Haumann, Müller, et al., 2005). However, negligible xpr during at least 15 min of X-ray exposure even at room temperature allowed for two XAS scans of ~6.5 min each per PSII sample spot (Figs. 4.1, 4.2), as used below.

A series of about fifty XAS spectra in a 20-295 K range were collected for dark-adapted PSII membrane particles (Fig. 4.3). The XANES spectra were similar to earlier reported S_1 spectra (Dau et al., 2001; Haumann, Müller, et al., 2005). Negligible K-edge shifts for 1 vs. 2 scans per sample spot in the whole temperature range further established the absence of xpr. From suitable data averaging, a set of 15 XAS spectra at mean temperatures in the 20-295 K range with similar signal quality was derived for in-depth analysis (Figs. 4.3 and 4.4). The temperature dependence of EXAFS spectra of the OEC is shown in Fig. 4.4. Visual inspection revealed significant changes in the Fourier-transform (FT) peaks for increasing temperature. In particular, a minor amplitude decrease of peak 1 due to manganese-ligand (Mn-N/O) bonds as well as a more pronounced decrease of peak 2 and smaller amplitude changes of peak 3, both mostly reflecting metal-metal (Mn-Mn/Ca) distances (Haumann, Müller, et al., 2005; Yano et al., 2008). The three main

FT features revealed an amplitude decrease of up to ~25 % primarily above ~200 K so that the protein-glass transition behavior could well be identified (Fig. 4.4). A quantitative description of the EXAFS spectra was achieved by simulations, which included mainly two manganese-ligand and three metal-metal interactions. This approach yielded metrical parameters (~1.85 Å and ~2.05 Å Mn-N/O bond lengths and ~2.7 Å, ~3.3 Å, and ~3.7 Å Mn-Mn/Ca distances) in good agreement with S_1-state crystal structures of the OEC (Table 1). A similarly good description of the EXAFS spectra at all (mean) temperatures indicated that coordination changes at the manganese ions did not occur (Fig. 4.4).

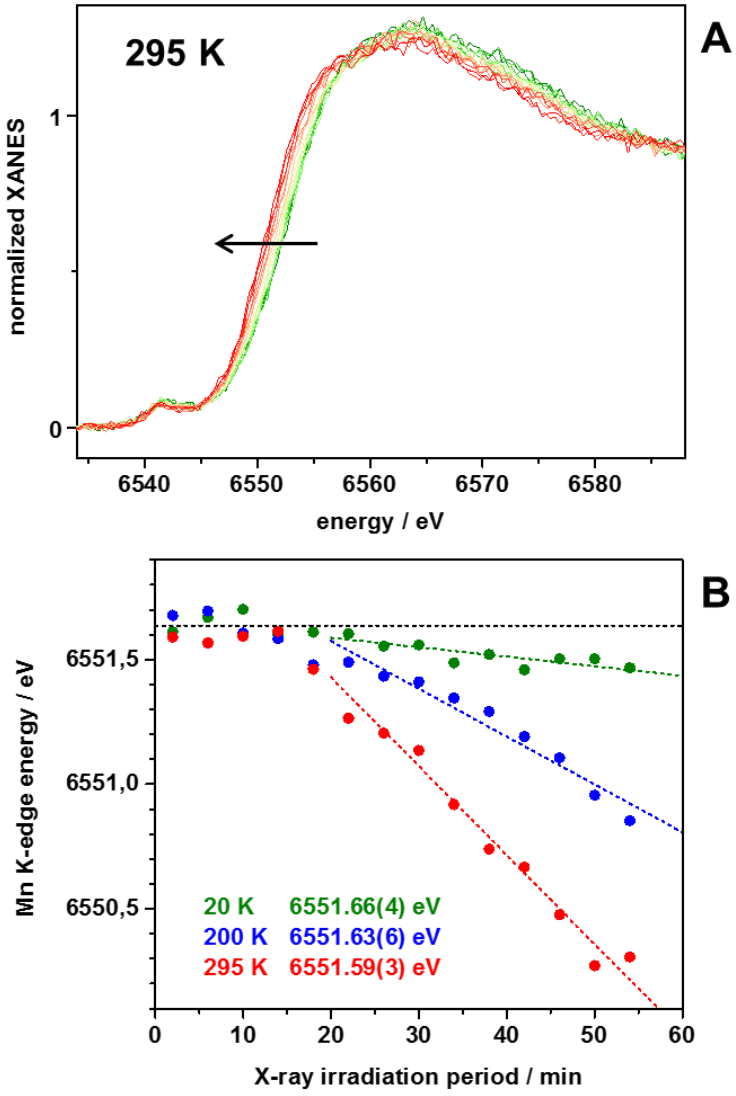

Figure 4.1 – X-ray photoreduction (xpr) of the OEC in the S_1-state. (A) Example of a series of 14 single-scan Mn K-edge XANES spectra, collected on the same sample spot, for the OEC of PSII in the S_1-state close to room temperature (295 K). The arrow marks the shift of the K-edge to lower

energies during prolonged X-ray exposure due to xpr of the manganese ions in the OEC. (B) Mn K-edge energies (from the "integral method" (Kristina N Ferreira et al., 2004) in a 10-100 % K-edge amplitude range). The first 4 scans at each temperature show similar and about constant K-edge energies (as indicated) and the following K-edge downshifts reveal rates (from linear fits to the data points) of 0.004(1), 0.018(2), and 0.037(3) eV min^{-1} at 20 K, 200 K, and 295 K. The data reveals that xpr was negligible in the whole studied temperature range during the first 2 scans (~13 min) on a single sample spot.

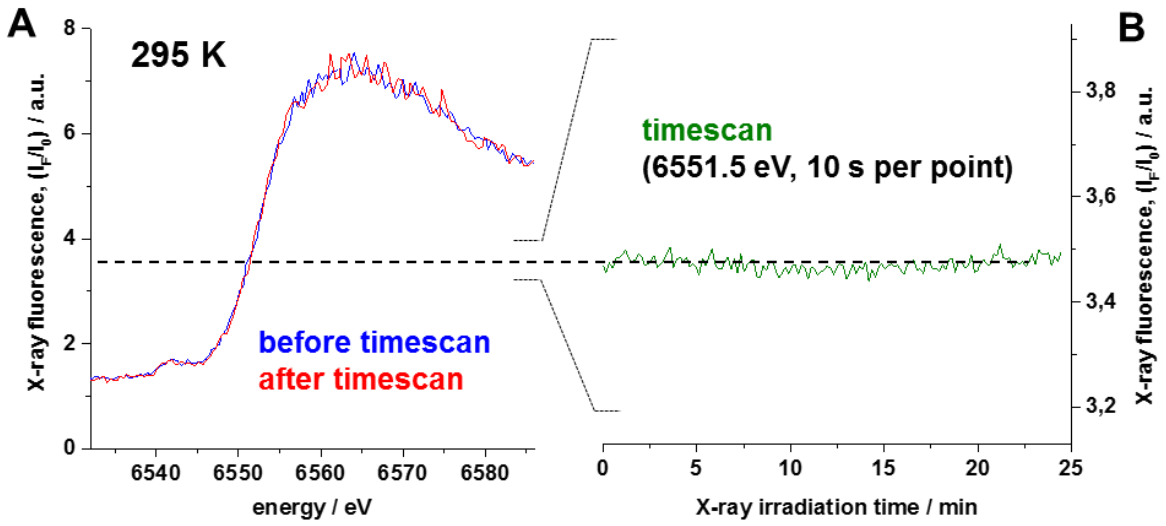

Figure 4.2 – X-ray photoreduction in a timescan. Panel A shows Mn XANES spectra for the OEC of PSII in the S_1-state at 295 K as obtained prior to or after the X-ray irradiation timescan for ca. 25 min in panel B (note the expanded y-scale). The data reveal an X-ray fluorescence intensity change of not more than 0.03 units, translating into a K-edge downshift of not more than 0.04 eV (assuming a downshift of 0.75 eV for the 1-electron reduction of 1 out of the 4 Mn ions in the OEC), which means that not more than 5 % of Mn ions had become reduced by 1 electron in 25 min of X-ray irradiation at 295 K. Because the duration of 1 EXAFS scan was ~6.5 min, 1-2 scans per sample spot did not cause any significant xpr even at room temperature under the conditions at the beamline KMC-3.

The EXAFS analysis revealed that all discernable interatomic distances in the OEC are temperature-independent below and above 200 K (Fig. 4.5). This finding further supports that the low and room temperature structures of the OEC are identical, in agreement with earlier XAS and crystallographic studies (Haumann, Müller, et al., 2005; Kern et al., 2012). In contrast, the Debye-Waller parameters (σ^2) showed a significant temperature dependence, being almost constant below 200 K, but increasing in particular above 200 K by up to a factor of 2, i.e., for the Mn-Mn distance of ~2.7 Å (Fig. 4.5). Clear "breakpoint" behavior of σ^2 around 200 K hence was observed for the Mn-

N/O bonds and, more pronouncedly, for the longer Mn-Mn/Ca distances. Because the XAS Debye-Waller parameter indicates the atomic coordinate dispersion, the observed temperature dependence for the OEC suggests that specific vibrational motions that affect the longer interatomic distances are frozen out below ~200 K while the manganese-ligand vibrations are less affected by the temperature sensitivity of the environment.

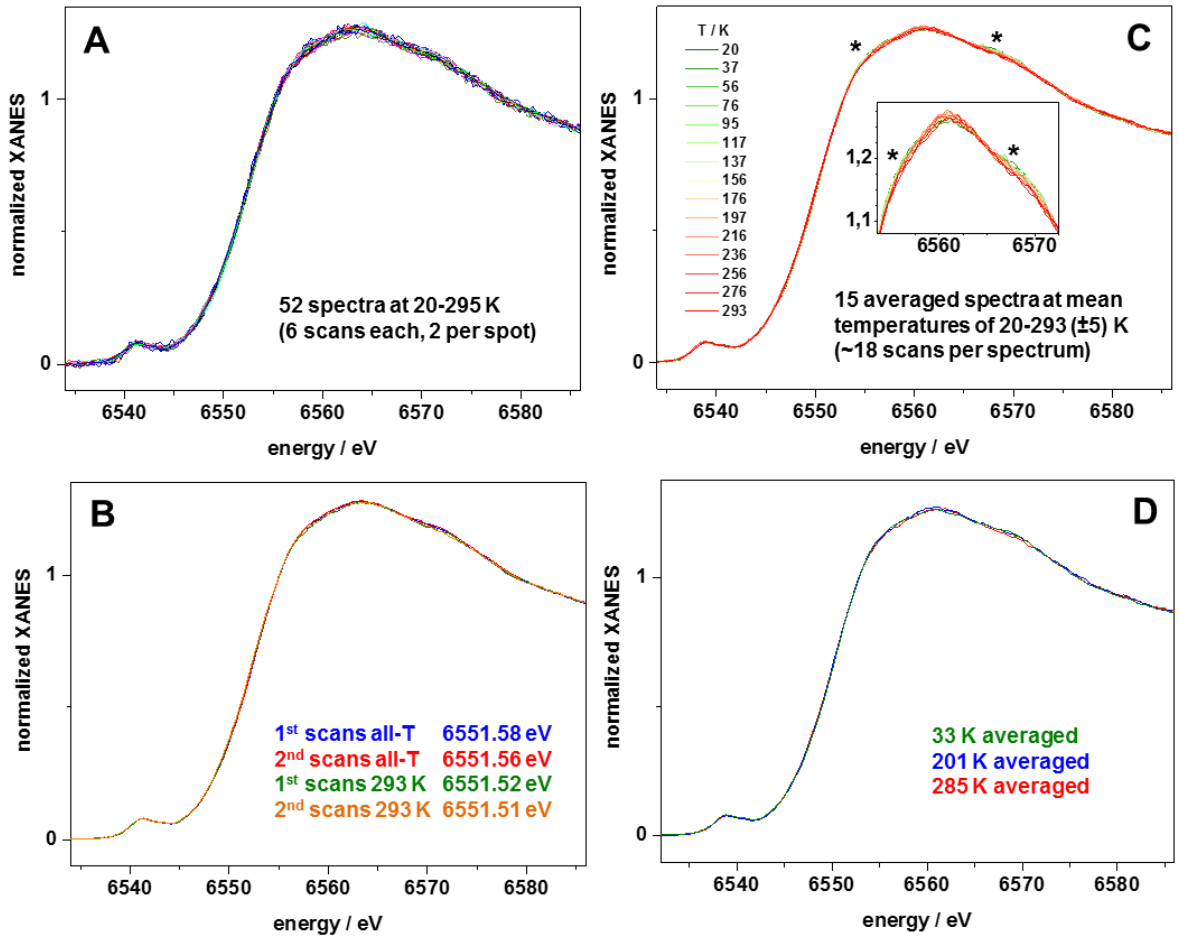

Figure 4.3 – Mn XANES spectra of PSII in the S_1 state. (A) 52 spectra at 20-295 K. (B) Comparison of spectra from the first or second scan on the same sample spot (for averaged spectra at all temperatures or at 293±3 K). The maximal K-edge downshift of 0.02 eV corresponds to <3 % of 1-electron reduction of 1 out of 4 Mn ions in the OEC. The slightly lower K-edge energy at 293 K likely reflects minor temperature-dependent XANES shape changes (rather than xpr). (C) 15 averaged spectra (mean K-edge energy 6551.61(6) eV) and magnified edge maximum in the inset (asterisks mark temperature-dependent features). (D) Averaged spectra (at T ±10 K) at cryogenic, "breakpoint", and ambient temperatures, which are very similar.

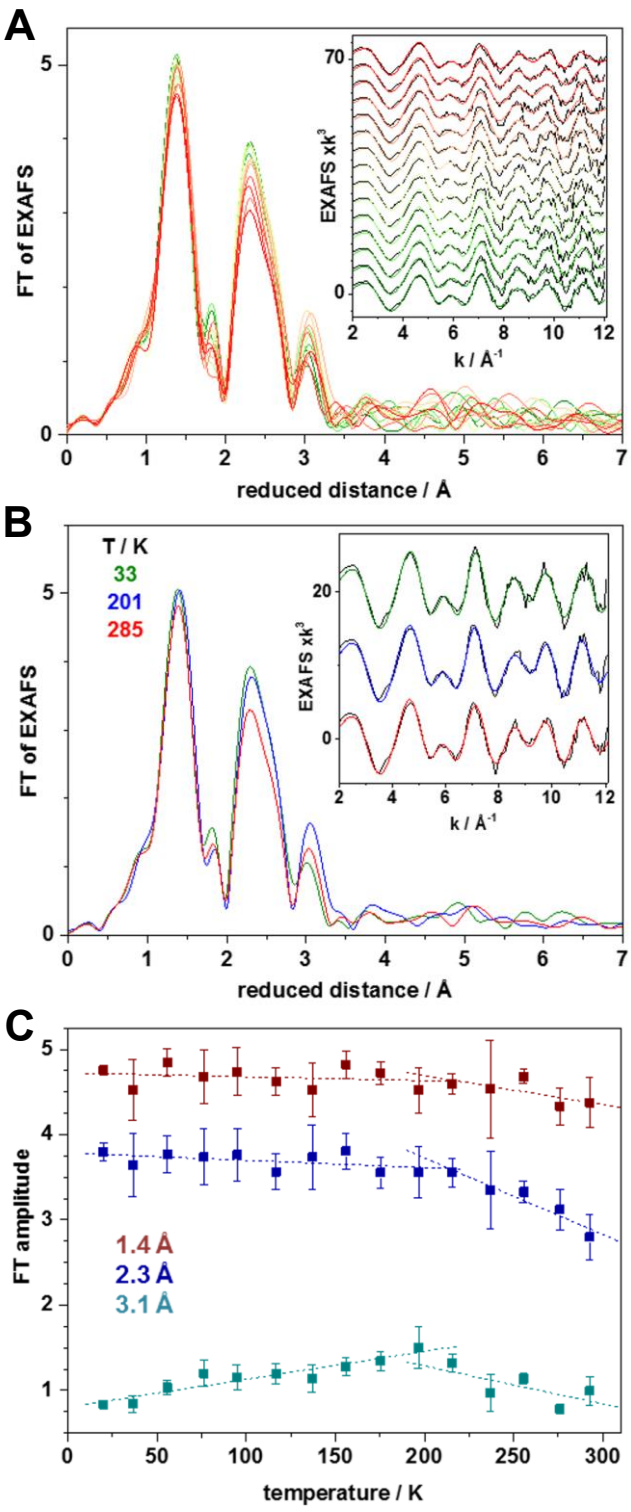

Figure 4.4 – Temperature-dependent XAS of the OEC in PSII in the S_1-state. (A) Fourier-transform (experimental data) of EXAFS spectra in the inset (vertically stacked; black lines, experimental data; colored lines, simulations. See Table 1, Appendix C and Fig. 4.5 for simulation results). (B) same as in (A) but at three mean temperatures (±10 K). (C) FT amplitude changes at indicated (reduced) distances (±0.1 Å) reveal apparent "breakpoint" behavior at ~200 K (lines show fit curves for data below or above 200 K).

Table 1 – EXAFS simulation parameters.[a]

shell	N [per Mn]	R [Å]	σ^2 x10^3 [Å^2]
Mn-O	3.75*	1.83±0.02	4.5±1.5#
Mn-N/O	2.00*	2.00±0.03	4.5±1.5#
Mn--Mn	1.50*	2.74±0.01	2.0±1.0
Mn--C/N/O	2.00*	2.98±0.06	7.5±4.0&
Mn--Mn/Ca	1.00*	3.26±0.04	7.5±4.0&
Mn--Mn/Ca	0.50*	3.73±0.09	7.5±4.0&

[a]Fit results are for the mean Mn EXAFS spectrum of PSII in the S_1 state (20-295 K data averaged). N, coordination number; R, interatomic distance; σ^2, Debye-Waller parameter. Fit restraints: *, fixed N-values resembling the crystallographic metrics (Tanaka et al., 2017); #,&, coupled to yield equal values. The fit error sum (R_F, deviation in % between the fit curve and the Fourier-backtransformed k-space spectrum in a 1-3.5 Å reduced distance range) was 8.4 % for the mean spectrum and 8-12 % for the 15 spectra at 20-293 K. See Appendix C for individual fit results.

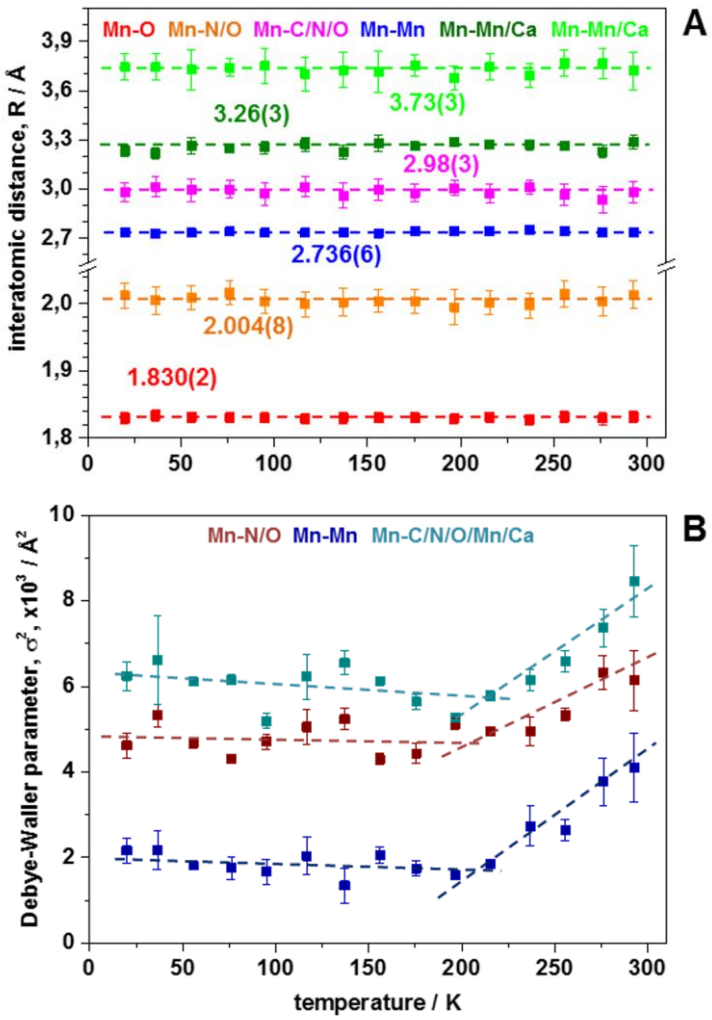

Figure 4.5 – Temperature behavior of EXAFS simulation parameters. Data for the OEC (colored symbols) refer to spectra in Fig. 4.4 and a fit approach as in Table 1. (A) Interatomic distances, R (± standard deviation). (B) Debye-Waller parameter, σ^2 (fit error in brackets, values in dark-cyan smoothed over 2 adjacent data points). Straight lines highlight constant R values in (A) and the protein-glass transition for σ^2 at ~200 K in (B).

4.3 Discussion

We evaluated the temperature dependence of the Debye-Waller parameter to study the nuclear dynamics of the water oxidizing catalyst in PSII. We could focus exclusively on the inorganic core of the metal cluster by analysis of EXAFS spectra detected at the Mn K-edge. The structural flexibility of the OEC in PSII is governed by the typical glass-transition behavior of the protein/water environment (Doster, 2010; Ringe & Petsko, 2003). The observed breakpoint behavior at about 200 K is characteristic for

(presumably all) proteins in their aqueous solvent and has been noted before also for structural and functional properties of PSII (Gorka et al., 2020; Grabolle et al., 2006; Pieper et al., 2007; Pieper et al., 2012; Reifarth & Renger, 1998; Renge et al., 2007; Schlodder et al., 2015). For example, a similar breakpoint was found for the mean square displacement of the single metal ions in the cytochrome-b_{559} (Fe^{III}) and the non-heme site (Fe^{II}) of PSII (Garbers et al., 1998). We show here that also the dynamics of the multi-nuclear OEC is tightly coupled to the non-harmonic nuclear dynamics of the PSII protein.

The character of the metal cluster dynamics is important because it is assumed to relate directly to the ET yield and rate. The Marcus theory of ET explicitly assumes that harmonic vibrations govern the reorganization processes and determine the rate (Eq. 4.1) (Marcus & Sutin, 1985), yielding the following equation for non-adiabatic ET:

$$k_{ET} = \frac{2\pi}{\hbar} V_0^2 e^{-\beta R} \frac{1}{\sqrt{4\pi\lambda k_B T}} e^{\frac{-(\triangle G+\lambda)^2}{4\lambda k_B T}} \qquad \textbf{(Eq. 4.1)}$$

$\hbar$ = 6.582x10^{-16} eV s (Planck´s constant h / 2π); V_0, maximal electronic coupling at van-der Waals distance; β, damping factor depending on the medium between donor and acceptor; R, edge-to-edge donor-acceptor distance in Å; k_B, 8.617x10^{-5} eV K^{-1} (Boltzmann´s constant); ΔG, Gibbs free energy change ("driving force"); λ, reorganization energy; T, temperature in K.

Assuming that electron-tunneling is not a major determinant of the rate constant (e.g. in the adiabatic limit), general transitions state theory may be applicable. Based on the Eyring equation (Mortimer & Eyring, 1980) and assuming unity transfer coefficient, the following equation relates the rate constant to the enthalpy and entropy of activation:

$$k_{TST} = \frac{k_B T}{h} e^{\frac{\triangle S^{\ddagger}}{k_B}} e^{\frac{-\triangle H^{\ddagger}}{k_B T}} \qquad \textbf{(Eq. 4.2)}$$

with $\Delta H^{\ddagger} = E_a - k_B T$ and $\Delta S^{\ddagger} = k_B \ln(Ah / k_B T) - k_B$ (A and E_a, Arrhenius´ pre-factor and activation energy) being the enthalpy and entropy contributions to the free energy change for reaching the transition state (i.e., $\Delta G^{\ddagger} = \Delta H^{\ddagger} - T\Delta S^{\ddagger}$).

Both rate-constant theories predict a direct relation between the logarithmic ET rate and the inverse temperature (i.e., similar to the Arrhenius equation). A discontinuity, meaning a breakpoint at ~200 K in the yield or rate of ET, is not included in these theories.

The S-transitions at the OEC clearly reveal a more complex picture. The yield decrease to zero around 200 K was found for all S-transitions except $S_1 \rightarrow S_2$ (Brudvig et al., 1983; Demeter et al., 1985; Inoue & Shibata, 1978; Koike et al., 1987; Styring & Rutherford, 1988). In contrast, for the $S_1 \rightarrow S_2$ transition formation of the multiline (g ~ 2) EPR signal of the normal S_2 state (Dismukes & Siderer, 1981) is quantitative down to ~200 K and decreases to zero at ~130 K, while the (g ~ 4) EPR signal of a second S_2 species (Boussac & Rutherford, 2000) increases below ~200 K to a maximum at ~130 K and decreases to zero at ~80 K, so that S_2 is not detectable at lower temperatures (Brudvig et al., 1983; De Paula et al., 1985; Styring & Rutherford, 1988). The lower vanishing temperature of $S_1 \rightarrow S_2$ corresponds to the absence of proton release from the OEC only during this transition, while proton release and/or water binding occurs during the other transitions (Ibrahim et al., 2020; Junge et al., 2002; Kern et al., 2018; Lavergne & Junge, 1993; Schlodder & Witt, 1999; Suga et al., 2017). The importance of water particularly in the higher S-transitions is emphasized by their vanishing at lower hydration levels of the PSII protein than $S_1 \rightarrow S_2$ (Noguchi & Sugiura, 2002). Neutron scattering revealed that the average atomic displacement of natively hydrated PSII membranes shows glass-transition behavior, whereas dried material does not (Pieper et al., 2008; Pieper et al., 2012). Interestingly, even two slope changes at ~120 K (weak) and around 220 K (strong) of the atomic displacements were observed for hydrated PSII, similar to the yield of the $S_1 \rightarrow S_2$ transition (Pieper et al., 2012). This finding was attributed to the onset of anharmonic protein or protein/water motions (with different relaxation times) at the lower- or higher-temperature points, in contrast to only harmonic motions below ~120 K (Doster, 2010; Pieper et al., 2007; Ringe & Petsko, 2003; Tournier et al., 2003; Vitkup et al., 2000). For the relatively small Debye-Waller parameter changes, we resolved only one clear breakpoint at ~200 K in the σ^2 temperature dependence of the OEC in the S_1 state.

In the following, we have a closer look at the $S_1 \rightarrow S_2$ transition, for which the most extensive experimental data is available. The redox potential difference ΔE ~ 50 mV of the $Y_Z^{\bullet+}/Y_Z$ and S_2/S_1 pairs (Vass & Styring, 1991; Vos et al., 1991) yields a free energy change ΔG ~ -50 meV (Renger & Hanssum, 1992), whereas an enthalpy change ΔH of about -150 meV was directly determined by photothermal beam deflection (Klauss, Haumann, et al., 2012). Whether the discrepancy suggests a major entropy change associated with the $S_1 \rightarrow S_2$ transition (-TΔS of about 100 meV) or results from methodical problems possibly related to relaxation dynamics of the $Y_Z^{\bullet+}$ state (Christen et al., 1998; Eckert & Renger, 1988; Klauss, Sikora, et al., 2012; Schilstra et al., 1998; Schlodder et al., 1985), still represents an open question. Using transition-state theory (Eq. 4.2), the activation energy E_a ~ 100 meV and a pre-exponential factor A_0 ~ $4x10^6$ s^{-1} (Haumann et al., 1997; Klauss, Haumann, et al., 2012; Renger & Hanssum, 1992) yield $\Delta G^{\ddagger}$ ~ 475 meV with $\Delta H^{\ddagger}$ ~ 75 meV and $-T\Delta S^{\ddagger}$ ~ 400 meV.

Application of the Marcus theory to the experimental ET rate (k ~ 10^4 s^{-1} (Klauss, Haumann, et al., 2012)) in $S_1 \rightarrow S_2$ by Renger et al. (Renger et al., 1998; Renger & Hanssum, 1992) suggests an at least 2-fold larger distance (≥ 15 Å) between tyrosine Y_Z (hydroxo oxygen) and the nuclei of Mn ions than found in the crystal structures (7-8 Å, see Fig. 4.6). Using the parameters displayed in Table 2, an expected reaction rate constant about 3 x 10^4 times faster than experimentally observed could be calculated with eq. 4.1.

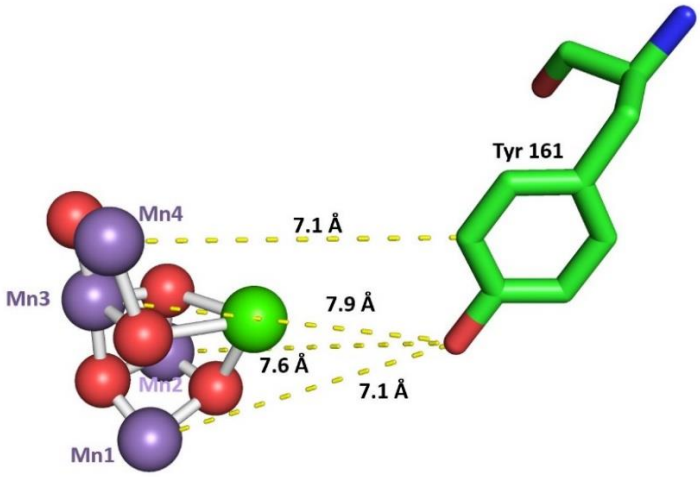

Figure 4.6 – Distances between tyrosine Y_Z and the nuclei of the Mn ions in the OEC. Figure based on the 0 Flash (0F) structure data (6DHE) from of Kern et al. (2018).

Table 2 – Parameters* used for determination of the ET rate according to Marcus theory and results in rate ($k_{ET\ (calc.)}$) and time constant ($\tau_{ET\ (calc.)}$).

	Value	***Units***	***note***
ħ	6.582×10^{-16}	eV.s	
V_0	4.89	eV	*(Marcus & Sutin, 1985)*
β	1.4	$Å^{-1}$	*(Moser et al., 1992; Moser et al., 1995; Renger et al., 1998)*
R	7.5	Å	*(Kern et al., 2018)*
$E_{a(S1-S2)}$	160	meV	*(Klauss, Haumann, et al., 2012)*
$\Delta G_{(S1-S2)}$	-0.05	eV	*(Renger & Hanssum, 1992)*
T	293.15	K	
k_B	8.617×10^{-5}	$eV.K^{-1}$	
λ	0.736	eV	*Calculated with Eq. 4.3*
$k_{ET\ (calc.)}$	3.17×10^{8}	s^{-1}	*Calculated with Eq. 4.1*
$\tau_{ET\ (calc.)}$	3.15	ns	*$1/k_{ET}$*

*Where ħ is the Planck´s constant (h / 2π); V_0 is the maximal electronic coupling at van-der Waals distance; β is the damping factor depending on the medium between donor and acceptor; R is the edge-to-edge donor-acceptor distance; $E_{a(S1-S2)}$ is the activation energy of the ET step in the $S_1 \rightarrow S_2$ transition; $\Delta G_{(S1-S2)}$ is the Gibbs free energy change in the $S_1 \rightarrow S_2$ transition; T is the temperature; k_B is the Boltzmann´s constant; λ is the reorganization energy. $k_{ET\ (calc.)}$ is the calculated electron transfer rate and $\tau_{ET\ (calc.)}$ is the respective time constant calculated as the inverse of $k_{ET\ (calc.)}$.

$$E_{a,ET} = \frac{(\triangle G + \lambda)^2}{4\lambda} \qquad \textbf{(Eq. 4.3)}$$

The application of the approach developed for biological ET reactions by Moser et al. (1992); (Moser et al., 2005) to the $S_1 \rightarrow S_2$ transition predicts a similar 10^5-fold larger rate than experimentally observed. This was calculated with Eq. 4.4 (Moser et al., 2005) that is only valid for room temperature, using the parameters displayed in table 3. It should be noted that Moser et al. (2005) did not use the semi-classical ET theory of Marcus. Whereas Marcus describes the nuclear motions exclusively in a classical framework, Moser et al. also include the coupling to non-classical vibrational modes using empirically determined coupling factors and frequencies.

$$log_{10}k_{ET} = 13 - (1.2 - 0.8\rho)(R - 3.6) - 3.1\frac{(\triangle G+\lambda)^2}{\lambda} \qquad \textbf{(Eq. 4.4)}$$

Where R is edge-to-edge donor-acceptor distance in Å, the λ is the reorganization energy in eV, the ΔG is the Gibbs free energy change in eV and ρ is the packing density. For simplicity the units are dropped following Moser et al. (2005). Furthermore in this equation (Eq. 4.4), the 3.6 represents the van der Waals contact and the intersection of 13 was determined in Moser et al. (1992) by studying a range of electron tunneling reactions in purple photosynthetic reaction centers at different distances. The coefficient of 3.1 in the last term differs from the 4.2 coefficient expected in a classical Marcus treatment. This difference reflects the non-classical coupling of typical electron tunneling reactions in proteins to high energy vibrational modes (Moser et al., 2005).

Table 3 – Parameters** used for determination of the ET rate according to Moser et al. (2005) and results in rate ($k_{ET\ (calc.)}$) and time constant ($\tau_{ET\ (calc.)}$).

	Value	***Units***	***note***
ρ	0.82	$Å^{-1}$	*(Moser et al., 2005)*
R	7.5	Å	*(Kern et al., 2018)*
$\Delta G_{(S1\text{-}S2)}$	-0.05	eV	*(Renger & Hanssum, 1992)*
λ	0.7	eV	*(Moser et al., 2005)*
$k_{ET\ (calc.)}$	$1.02x10^9$	s^{-1}	*Calculated with Eq. 4.4*
$\tau_{ET\ (calc.)}$	0.983	ns	*$1/k_{ET}$*

**Where ρ is the packing density of atoms between the donor and acceptor; R is the edge-to-edge donor-acceptor distance; $\Delta G_{(S1\text{-}S2)}$ is the Gibbs free energy change in the $S_1 \rightarrow S_2$ transition; λ is the reorganization energy. $k_{ET\ (calc.)}$ is the calculated electron transfer rate and $\tau_{ET\ (calc.)}$ is the respective time constant calculated as the inverse of $k_{ET\ (calc.)}$.

Above the ET step is discussed in terms of electron transfer theory, as developed by Marcus (Marcus & Sutin, 1985) and a variant applied by Moser et al. to a variety of biological ET reactions (Moser et al., 1992; Moser et al., 2005). Both ET-theory variants yield rate constant values that are by orders of magnitude smaller than the experimentally determined values, suggesting that these ET theories are not directly applicable. Could the need for simultaneous electron and proton transfer (Parada et al.,

2019) determine the rate of the $S_1 \rightarrow S_2$ transition? It seems unlikely that the $S_1 \rightarrow S_2$ ET step is slowed down strongly by the coupled motion of the Tyr_Z proton, inter alia because the proton-coupled ET step of Tyr_Z oxidation is a fast process (around 100 ns (Klauss, Sikora, et al., 2012; Renger, 2004). More importantly, the absence of any sizeable H/D kinetic isotope effect (Gerencser & Dau, 2010; Klauss et al., 2015; Zaharieva, Dau, et al., 2016), confirms that proton-tunneling probabilities are not a determinant of the ET rate constant.

In the light of the here described results on the Debye-Waller parameter, the non-applicability ET theories does not come as a surprise, as best discussed for the semi-classical Marcus theory (Marcus & Sutin, 1985). Marcus explicitly assumes nuclear motions describable by quadratic potentials, which is a pivotal foundation of Marcus theory and inter alia leads to the well-known Marcus parabola's. For the S-state transitions of PSII, the relevant nuclear motions include the motions of the nuclei of the manganese ions and ligated (oxygen) atoms. The analysis of the temperature dependence of the EXAFS Debye-Waller parameter now reveals that these motions are governed by a protein-specific type of mobility which rather than being harmonic motions in quadratic potentials may be seen as a diffusive motion along a rough (multitude of minima), but overall, comparably flat multidimensional potential energy surface (Doster, 2010; Frauenfelder et al., 1988; Parak et al., 1982; Parak & Nienhaus, 1991).

Neglecting the role of electron tunneling probabilities, general transition-state theory provides an alternative description (Eyring equation, Eq. 4.2). Complete neglect of rate-limiting electron tunneling probabilities represents an approximation which may be in order because of the short donor-acceptor distance between the Mn complex and the TyrZ residue so that the limit of adiabatic electron transfer is approached. Irrespective of the potentially approximative character, application of Eq. 4.2 clearly implies a large entropy of activation. It is plausible that the flat potential energy surface with a multitude of minima (substates), which correspond to the protein-specific nuclear motions of the catalytic metal cluster, relate to the entropic contribution free energy of activation in the S-state transitions of PSII. Noting that the entropic contribution to the

free energy of activation represents an “entropic slow-down” of the reaction, we assume that only a minor fraction of the numerous conformational sub-states represents an active conformation that facilitates the respective S-state transition suggesting that the $S_1 \rightarrow S_2$ transition (and likely in all other steps in the S-state cycle) is determined by non-harmonic nuclear mobility and reorganizations in the protein/water environment of the catalytic metal cluster (Frauenfelder et al., 1991; Gorka et al., 2020; Henzler-Wildman & Kern, 2007).

The role of the protein-water environment of the OEC is corroborated by amino acid substitutions affecting the Mn ligands and the H-bonded network that cause slowing or even abolishment of the higher S-transitions and/or of water oxidation (Dilbeck et al., 2012; Ghosh, Khan, et al., 2019; Hundelt et al., 1998; Nagao et al., 2017; Service et al., 2010; Strickler et al., 2008). Time-resolved X-ray crystallography and spectroscopy studies, which revealed, e.g., additional water binding at the manganese (Ibrahim et al., 2020; Kern et al., 2018; Schuth et al., 2018; Suga et al., 2017; Wang et al., 2017; Zaharieva, Chernev, et al., 2016), as well as molecular dynamics simulations (Nakamura et al., 2020; Ogata et al., 2013; Vassiliev et al., 2012) support the importance of protein/water and metal core reorganization in the catalytic cycle. Determination of the specific molecular conformations that facilitate the reactions at the OEC remains an important future task for understanding water oxidation by PSII.

Chapter 5 – Mutagenesis of hydrogen-bonding amino acid sidechains around the manganese cluster of PSII affect the O_2 evolution kinetics and activation barrier of the O_2-formation step

Along the reaction cycle of the donor side of PSII, four protons and four electrons are removed from the OEC-bound water molecules, culminating into the oxidation of two H_2O molecules into O_2 (Klauss, Haumann, et al., 2012). During this process, the substrate waters must be supplied to the catalytic center and the products, O_2 and protons, must be conducted away from it (Gabdulkhakov et al., 2009). Although pathways remain not established, a huge water-filled hydrogen bonding network around the Mn-cluster can be seen in the crystal structures (e.g. Kern et al. (2018); Umena et al. (2011)) which include the narrow, broad and large channels that may serve these exact purposes (Ishikita et al., 2006; Vassiliev et al., 2012). These water-filled channels can most likely facilitate water diffusion from the lumen (Ibrahim et al., 2020; Reiss et al., 2019), while protons can make use of the Grotthuss mechanism to travel through the chains of waters and key polar amino acids that compose them (De Grotthuss, 2006). Moreover, O_2 diffusion could easily happen through such channels or occur along less hydrophilic paths (Cai et al., 2018; Wikstrom et al., 2015).

The broad channel begins nearby the Mn4 and O5 bridge of the OEC (see Fig. 5.1), including the D1-D61 region and extending all the way to the PsbO subunit (Bondar & Dau, 2012). Similarly, the narrow channel extends towards the PsbO subunit's interface with the PsbU subunit and starts on the other side of Mn4, including the O4 and W1. Although this channel could support proton transfer, a case can be made for its purpose as a substrate water delivery pathway as small molecules, also known as substrate water analogues, like ammonia (Navarro et al., 2013; Oyala et al., 2015) and methanol have been shown to bind at the end of this channel (Oyala et al., 2014; Retegan & Pantazis, 2016). The large channel is more separated from the other two, starting at O1 and continuing towards the lumen via the PsbV subunit. It has been proposed to be a O_2

release channel as it has more hydrophobic residues, but other functions like water delivery or proton release could also take place through there (Vassiliev et al., 2012).

The three channels separate as they stretch towards the lumen but start very entangled nearby the Mn-cluster (Kaur et al., 2021), which makes it important to understand which specific amino acids are key in the proton transfer process nearby the OEC. A partial representation of the hydrogen bond network around the OEC can be seen in Fig. 5.1, where the initial part of the three channels can be seen. We know that the amino acid residues that ligate directly to the Mn-cluster, and the hydrogen bond sharing pair D1-Y161/D1-H190, are required for efficient photoassembly of the OEC and O_2 evolution (Debus, 2008; Diner, 2001). However, second shell amino acids (non-ligating amino acids within ca. 10 Å of the OEC), or at least some, can be replaced through mutations without completely compromising O_2 production, allowing for the use of more direct experimental investigation methods that measure the released O_2. In a study from Ghosh, Khan, et al. (2019) a steady state Clark-type electrode was used to measure the O_2 evolution rate of several point mutated PSII, from which they could identify a high KIE in the D61A and N317A mutants, leading them to conclude their involvement in the proton release from the Mn-cluster during the S_3-S_0 transition. Another example is the study from Bao and Burnap (2015), where they investigated the kinetics of V185 and D61 mutants of PSII and could find a huge slowdown of the O_2 release of about 20-30 times (depending on the exact mutation) when compared to the wild type. Furthermore, they could also relate an increase in a kinetic phase related to reactions that precede the O_2 evolution with structural rearrangements that lead to the ideal configuration for dioxygen formation. This was also evidence for the S-state stabilization function of the hydrogen bond network around the OEC (Vogt et al., 2015).

In this section we use a similar approach as in Bao and Burnap (2015). By carrying out temperature dependant O_2 polarography measurements in several different mutants with point mutations of second shell amino acids around the OEC, we aim at observing alterations in the O_2 release kinetics to further assess the activation enthalpy ($\Delta H^{\ddagger}$) and entropy ($T\Delta S^{\ddagger}$) of the reaction. We will target mostly amino acids with carboxylate side chains, namely glutamates (E) and aspartates (D), within 12 Å of the OEC in the S_3-state

(Fig 5.1), hoping to better understand their individual role in the proton release from the OEC right before O_2 release.

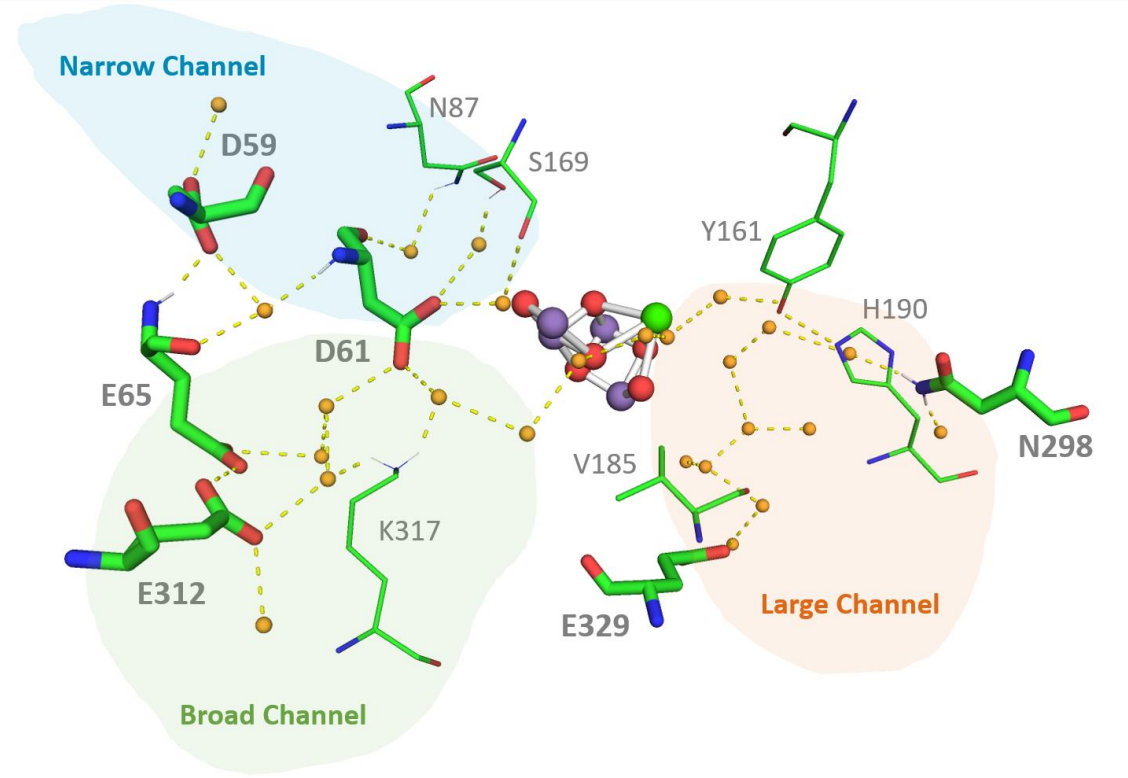

Figure 5.1 – Partial representation of the second shell hydrogen bond network around the OEC in the S_3-state as in the structure 6HDO from Kern et al. (2018). The cut-off for the hydrogen bonds shown was 3 Å. The three channels, large, broad, and narrow, can be seen marked and include some key amino acids and water molecules forming the hydrogen bond networks. Waters are represented as orange spheres. Point mutations of the highlighted amino acids are investigated in this chapter.

5.1 Experimental details

Thylakoid membranes from *Synechocystis* sp. PCC 6803, including wild type and several single point mutations: D59A, E65A, E312A, E329A and N298A were provided by Prof. Dr. Richard J. Debus, from the Biochemistry Department of the University of California in Riverside, CA (USA) and thylakoid membranes also from *Synechocystis* sp. PCC 6803 with the D61K point mutation were provided by Prof. Dr. Robert Burnap, from the Department of Microbiology & Molecular Genetics of the Oklahoma State University in

Stillwater, OK (USA). The protocol presented in Chapter 2 of this thesis for the preparation of thylakoid membranes from *Synechocystis* sp. PCC 6803 is the same used by the collaboration partners in the preparation of the samples we received. The samples had been previously stored at -80 °C and transported appropriately in a N_2 dewar. Before use they were thawed on ice for 60 min in the dark.

5.1.1 Time-resolved oxygen polarography

The measurements of time-resolved oxygen evolution were performed on thylakoid membrane samples from *Synechocystis* sp. PCC 6803, including the wild-type and variants with the following single point mutations: D59A, D61K, E65A, E312A, E329A N298A. A custom-made centrifugable static ring-disk electrode assembly of a bare platinum working electrode and silver-ring counter electrode, was used to perform the measurements as described before (Dilbeck et al., 2012; Schuth et al., 2017), and in Chapter 2 of this thesis. Each measurement was prepared by adding an aliquot of the thylakoid membrane suspension equivalent to 10 µg of total chlorophyll onto the electrode complemented with Buffer D-NaCl [150 mM NaCl, 25 mM MES (pKa = 6.15), 1 M glycine betaine, 5 mM $MgCl_2$, and 5 mM $CaCl_2$, pH 6.2 (NaOH)] to a total volume of 750 µl. The electrode assembly was then centrifuged in a swing-out rotor at 10,000 × g for 10 min (at 4 °C). Using a home-built potentiostat that also provided an electrode polarization of -0.95 V, switched on 15 s before the first excitation flash, the current signal was recorded for 500 ms, 20 ms before and 480 ms after each flash, for a total of 80 flashes with 900 ms spacing. A custom-made LED flashing device with a high-performance red (613 nm) LED (Luminus) was used as light source to induce S-state transitions. The samples were measured in a temperature-dependent manner, measuring in triplicate every temperature point in 5 °C steps in the ranges of 0-35 °C, except for the E65A mutant where 2.5 °C temperature steps were used in the range of 10-35 °C due to the extremely low signal it had at lower temperatures. During the data acquisition the sample was brought to the desired temperature using Peltier elements, which was then monitored by a miniature temperature sensor immersed in the sample buffer. The O_2 transients were then fit with the diffusion model (Dilbeck et al., 2012),

also presented in Chapter 2 of this thesis, with which the time-constants of oxygen evolution could be determined and compared. After fitting, the obtained time constants were used to make the Arrhenius plots from which the activation energy (E_a) and the pre-exponential frequency factor (A) were determined. These parameters were then both used to calculate the enthalpic ($\Delta H^{\ddagger}$) and entropic ($\Delta S^{\ddagger}$) contributions by applying the Eyring treatment (Guo et al., 2014).

5.2 Results and discussion

We employed time resolved O_2 polarography to measure a series of O_2 evolution kinetic traces from several *Synechocystis* sp. PCC 6803 samples in a temperature dependent manner. Apart from the WT *Synechocystis* sp. PCC 6803, other samples were from variants containing point mutations in the second sphere amino acids around the OEC, that may have important roles in the proton transfer process away from the Mn-cluster (Kaur et al., 2021), namely the aspartates D59A and D61K, the glutamates E312A, E65A and E329A and the asparagine N298A. The alanine mutations are typical substitutions as they replace the side chain by a methyl group that is smaller and not prone to specific interactions. In the case of the aspartate D61, the alanine mutation had been studied before by O_2 polarography along with the D61N (Bao & Burnap, 2015; Dilbeck et al., 2012), and so we decided to study another available point mutation of the same residue, the D61K.

The averaged transients obtained for each sample at each temperate point were fitted by simulation with the diffusion model described in Chapter 2 and in Dilbeck et al. (2012), to obtain the time constants respective to the O_2 evolution (τ_{ox}) and the phase that precedes that event (τ_{pre}) and like before, good agreement with the experimental data have been found as shown in Fig. 5.2. The τ_{lag} parameter that regards the O_2 reduction rection at the electrode's surface, showed very similar temperature dependencies for the different samples (Fig. 5.3). This way the determined PSII time constants were not significantly influenced by the small differences in the τ_{lag} among

different samples, and so a proper comparison of the PSII time constants between samples could be achieved.

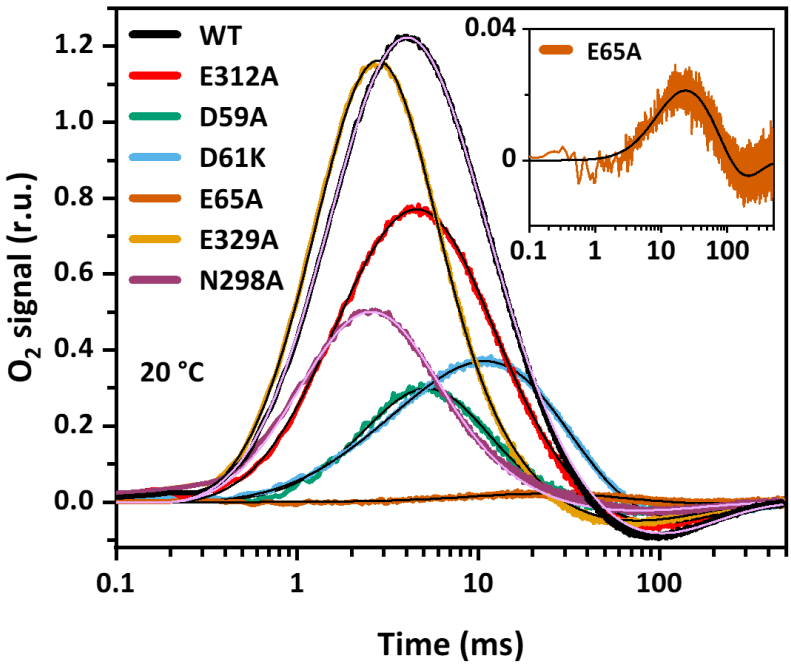

Figure 5.2 – O_2-evolution transients measured at 20 °C on thylakoid membranes from *Synechocystis* sp. PCC 6803 in the wild-type form and the tested variants. Here the fit results can be seen in good agreement with the experimental data. The indicated color coding is respective to the experimental data. The fit curves are displayed in black, except for WT and N298A where light purple was used for better contrast.

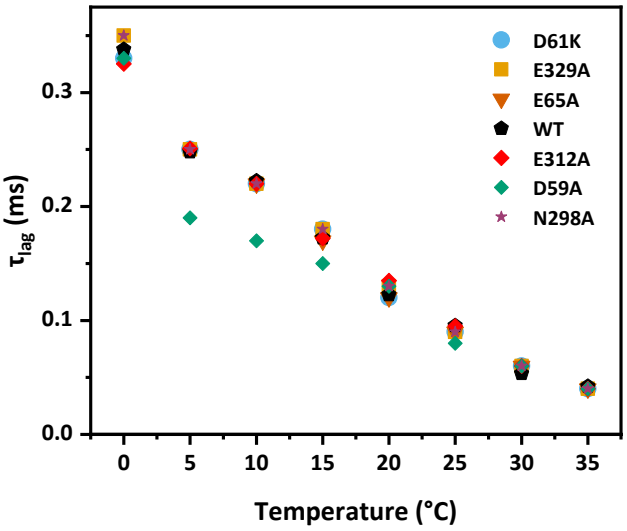

Figure 5.3 – Determined τ_{lag} by simulation with the diffusion model (Bao & Burnap, 2015; Dilbeck et al., 2012) for the different samples at the various temperatures. This plot illustrates that the temperature dependencies of the τ_{lag} were similar for each sample.

In the next figure (Fig. 5.4), it is possible to see the kinetic traces at 0 °C and 30 °C of the WT and the variants E312A, D59A and D61K, that were normalized for an easier comparison. The kinetics obtained for the WT sample were quite reproducible from previous results (Bao & Burnap, 2015), as we obtained time constants for the O_2 evolution of 3.7 ms at 5 °C and 1.0 ms at 30 °C while in the mentioned study they got 3.7 ms at 6 °C and 1.1 ms at 27 °C using a similar experimental set-up and the same simulation model. The results D61K showed a significant slowdown of the O_2 evolution as it had been seen before in preliminary unpublished results from the Burnap Lab, where the samples were produced. In our case, the fit showed a time constant for the oxygen phase of 22.6 ms at 5 °C. The O_2 release kinetics of the mutations E312A, D59A and E65A are shown here for the first time. In both temperatures, the E312A appeared to be just slightly slower than the WT samples whereas the D59A mutation was highly slowed down at 0 °C but not that much at 30 °C, indicating already a significant increase in the activation energy of this mutated sample. As the E65A sample showed very low signal at temperatures below 10 °C, in Fig. 5.5, a separate comparison between the kinetics from WT, D59A and D61K with the E65A at 10 °C and 30 °C can be seen. The E65A, apart from being the sample with the lowest signal from all the measured samples, was also the mutation with the slowest O_2 evolution kinetics. For the E329A

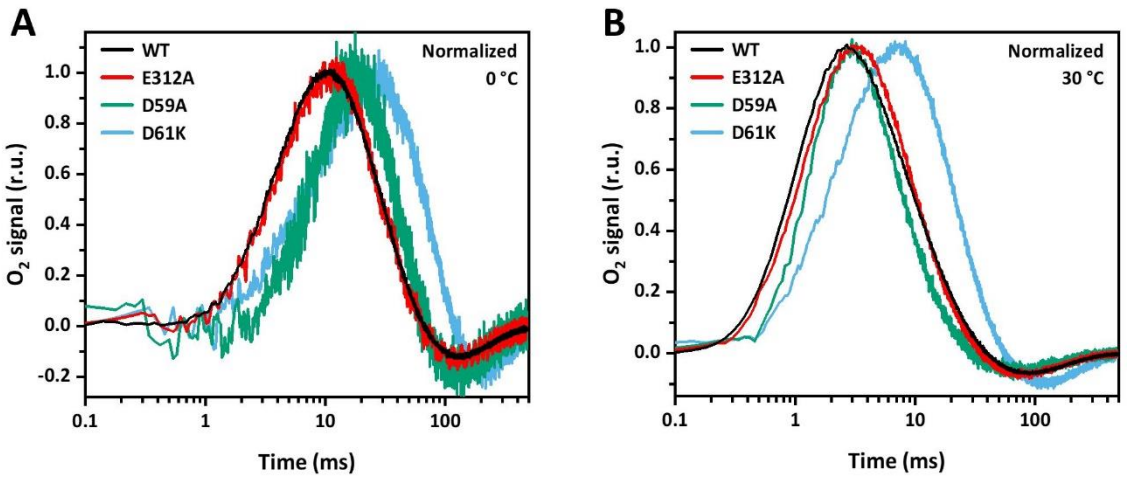

Figure 5.4 – O_2-evolution transients measured at 0 °C (A) and 30 °C (B) on thylakoid membranes from *Synechocystis* sp. PCC 6803 in the wild-type form and the variants E312A, D59A and D61K. The membranes were deposited on a bare platinum electrode by joined centrifugation of a PSII solution and the Pt/Ag electrode assembly. The kinetics are the average of 230 individual transients measured after each flash, summed up from three independent experiments on each condition.

and N298A point mutations the comparison of their O_2 transients to the WT can be seen on Fig. 5.6. In this figure we can see that the kinetics for both these mutants were slightly faster than the WT, which is surprising, although our colleagues at the University of California, Riverside, checked the genome of all the samples from the same batch that was sent to confirm the absence of back-mutation to WT, which was the first suspicion after obtaining such results.

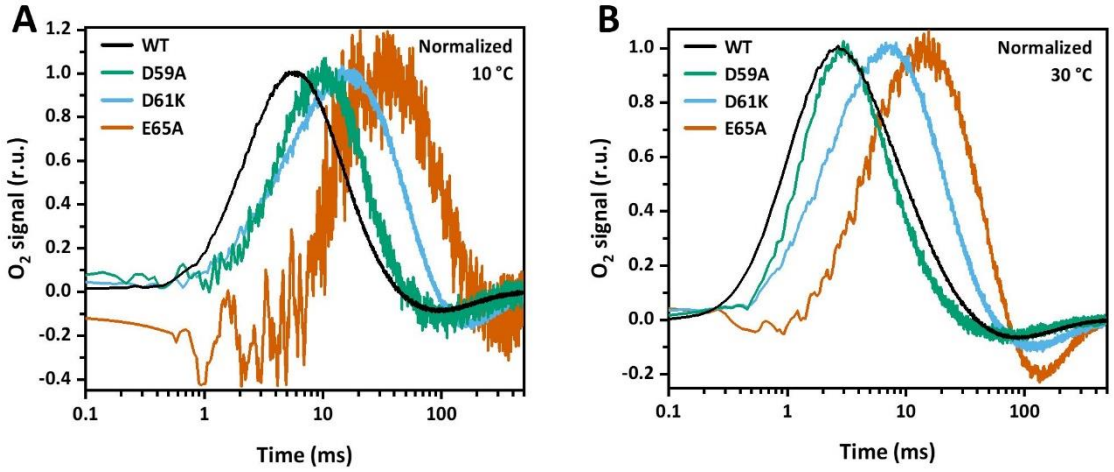

Figure 5.5 – O_2-evolution transients measured at 10 °C (A) and 30 °C (B) on thylakoid membranes from *Synechocystis* sp. PCC 6803 in the wild-type form and the variants D59A, D61K and E65A. The membranes were deposited on a bare platinum electrode by joined centrifugation of a PSII solution and the Pt/Ag electrode assembly. The kinetics are the average of 230 individual transients measured after each flash, summed up from three independent experiments on each condition. Due to low signal of the E65A sample, it was measured twice as much as the other samples.

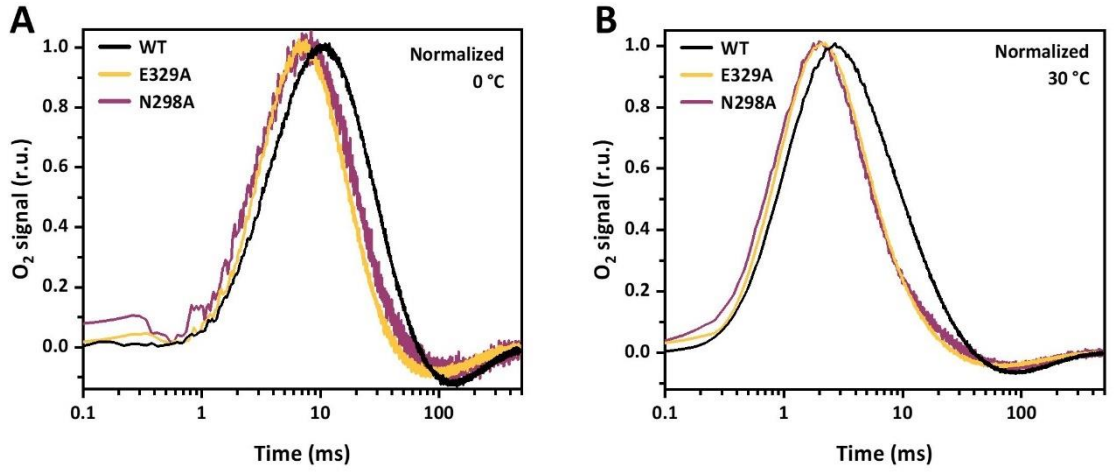

Figure 5.6 – O_2-evolution transients measured at 0 °C (A) and 30 °C (B) on thylakoid membranes from *Synechocystis* sp. PCC 6803 in the wild-type form and the variants E329A and N298A. The membranes were deposited on a bare platinum electrode by joined centrifugation of a PSII solution and the Pt/Ag electrode assembly. The kinetics are the average of 230 individual transients measured after each flash, summed up from three independent experiments on each condition.

With the obtained time constants respective to the O_2 evolution (τ_{ox}) and the phase that precedes that event (τ_{pre}), Arrhenius plots for both phases were created, τ vs $1/k_BT$ in a logarithmic scale, which resulted in linear behaviours from which the activation energy (E_a) and the pre-exponential factor (A) could be determined. The long Fig. 5.7 shows a list of plots for each sample, where the temperature dependant kinetics can be seen on the left side and the respective Arrhenius plots can be seen on the right side.

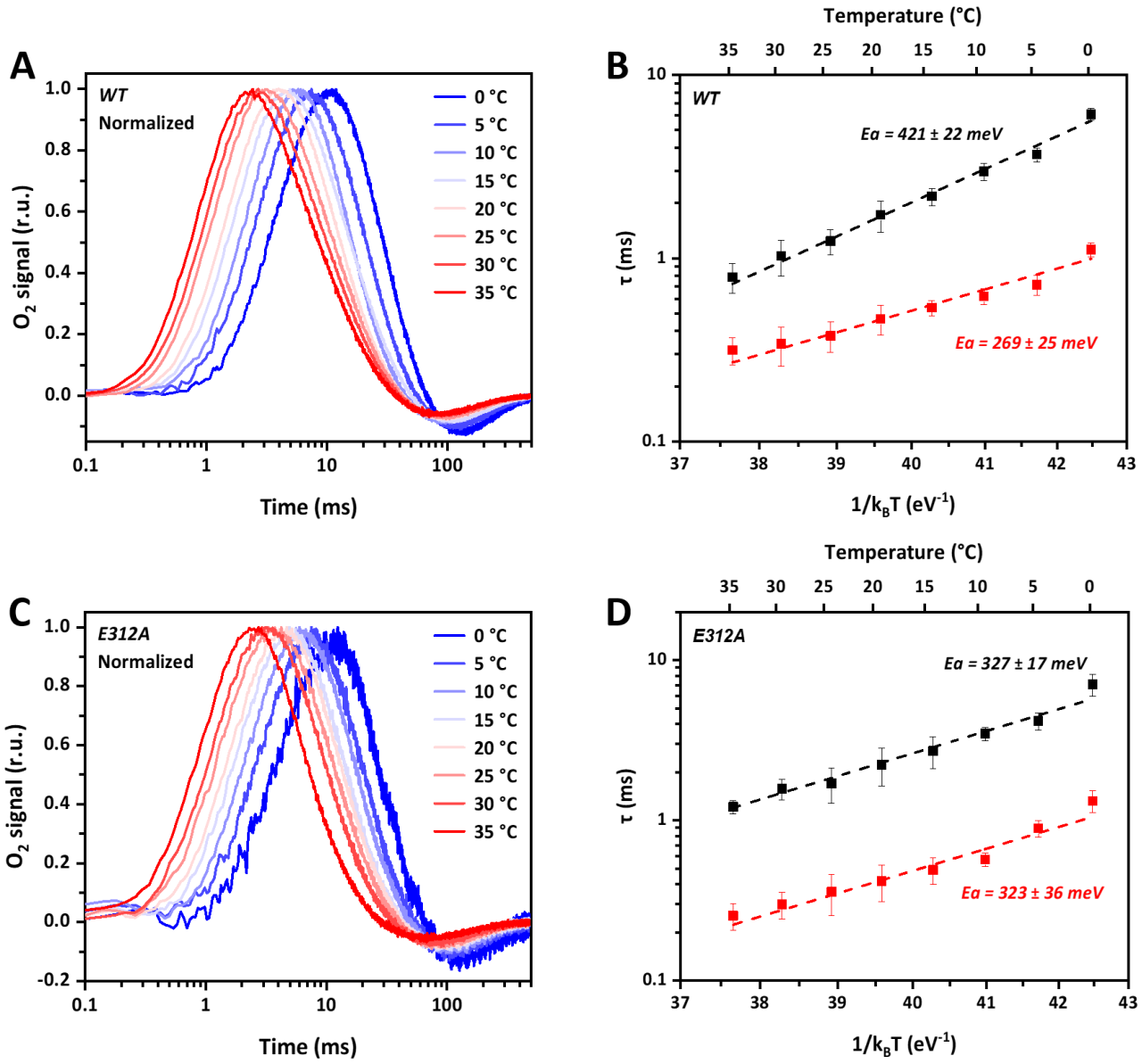

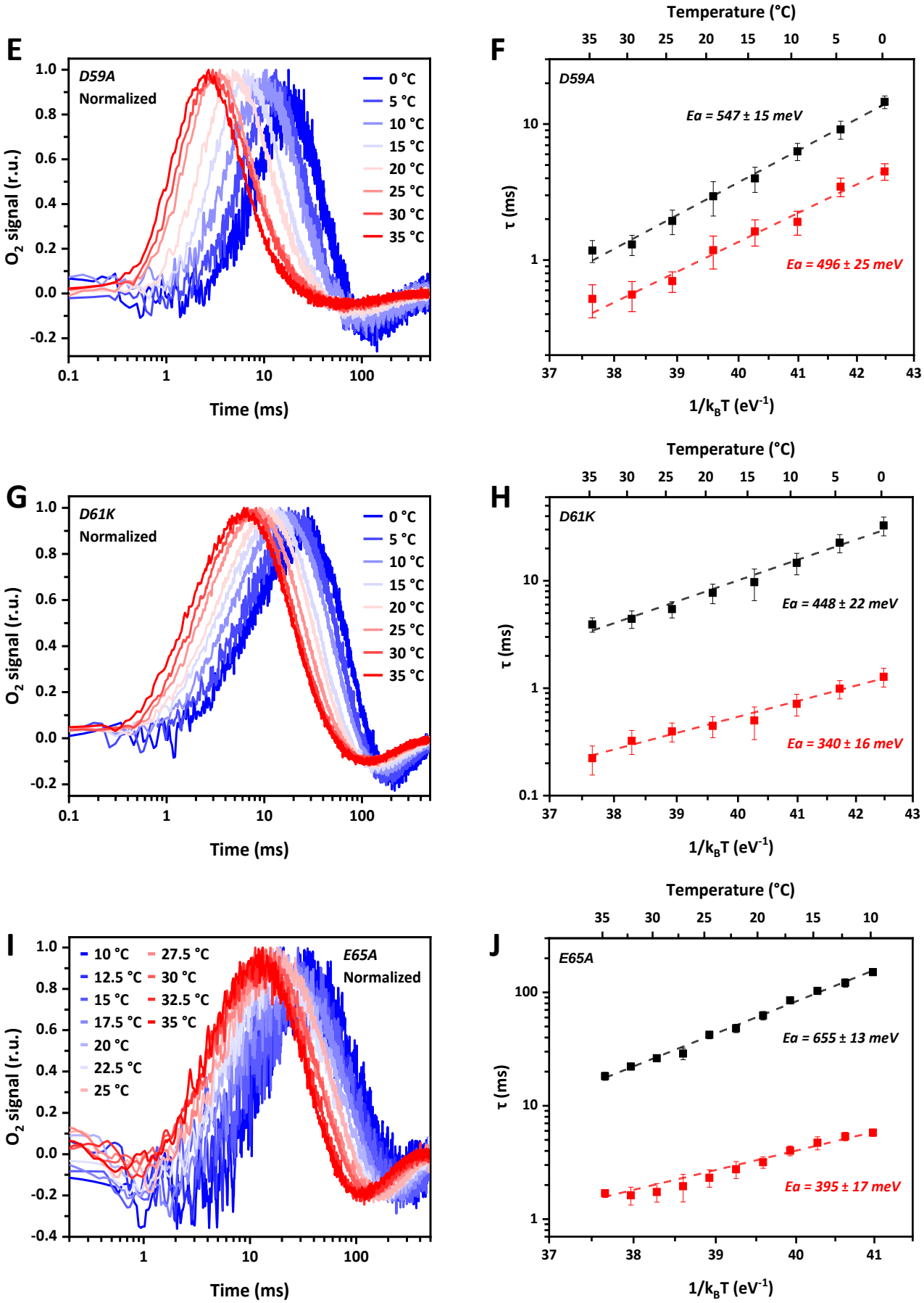
E
D59A
Normalized
0 °C
5 °C
10 °C
15 °C
20 °C
25 °C
30 °C
35 °C
O2 signal (r.u.)
Time (ms)
F
Temperature (°C)
D59A
Ea = 547 ± 15 meV
Ea = 496 ± 25 meV
τ (ms)
1/kBT (eV-1)
G
D61K
Normalized
H
D61K
Ea = 448 ± 22 meV
Ea = 340 ± 16 meV
I
10 °C
12.5 °C
15 °C
17.5 °C
20 °C
22.5 °C
25 °C
27.5 °C
30 °C
32.5 °C
35 °C
E65A
Normalized
J
E65A
Ea = 655 ± 13 meV
Ea = 395 ± 17 meV

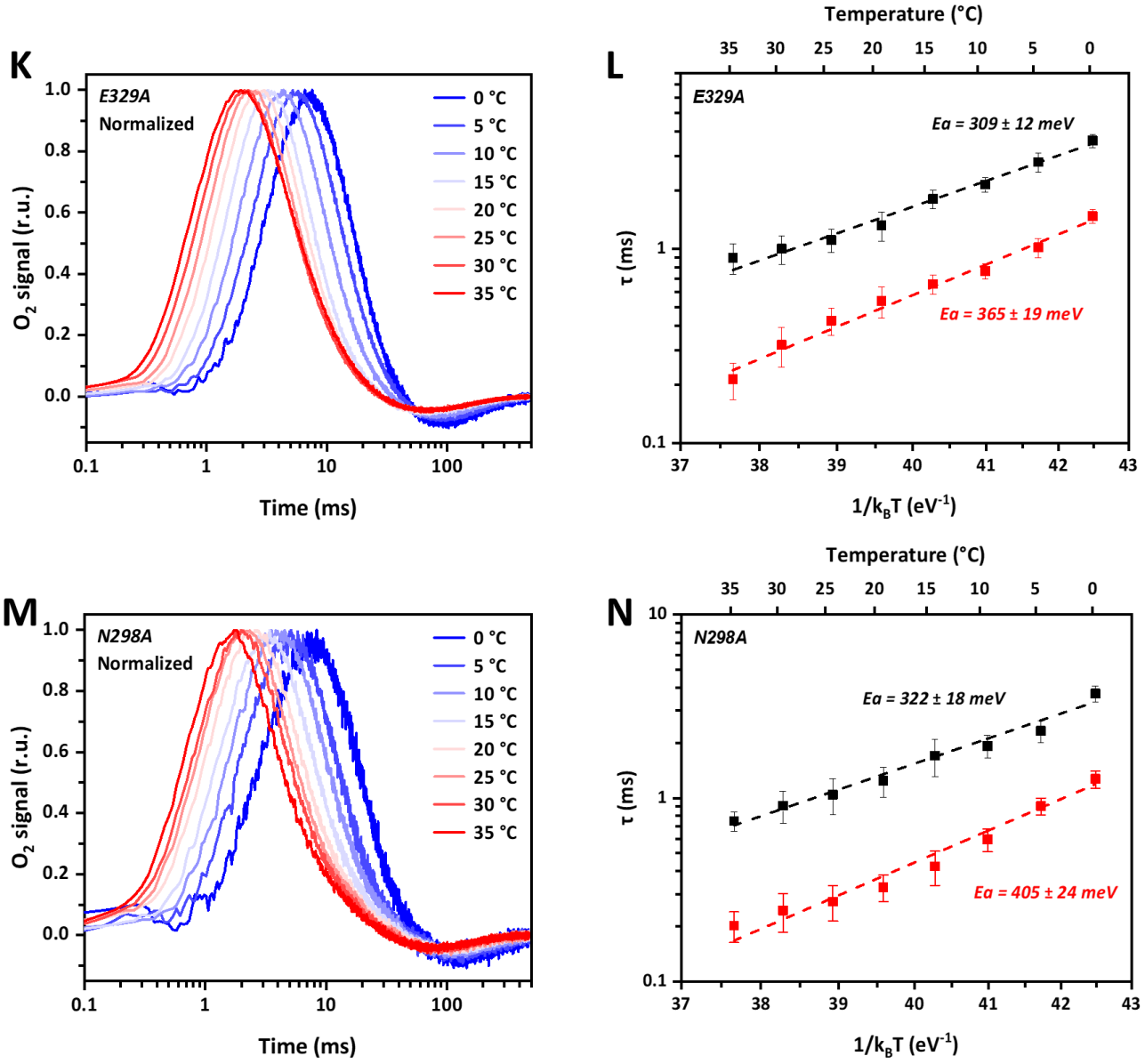

Figure 5.7 – On the left side (A, C, E, G, I, K, M), temperature dependant O_2-evolution transients measured for each of the *Synechocystis* sp. PCC 6803 variants can be seen, while on the right side (B, D, F, H, J, L, N) the respective Arrhenius plots can be seen for both phases, the O_2 evolution (τ_{ox} in black) and the phase that precedes it (τ_{pre} in red). The obtained activation energy for each line fit is displayed. The membranes were deposited on a bare platinum electrode by joined centrifugation of a PSII solution and the Pt/Ag electrode assembly. The kinetics are the average of 230 individual transients measured after each flash, summed up from three independent experiments on each condition. Due to low signal of the E65A sample, it was measured twice as much as the other samples.

Using an Eyring treatment, the activation enthalpy, $\Delta H^{\ddagger}$, and activation entropy, $\Delta S^{\ddagger}$, for both phases of the S_3-S_0 transition were determined. The equations used were respectively Eq. 5.1 and Eq. 5.2 (Mortimer & Eyring, 1980).

$$\Delta H^{\ddagger} = E_a - k_B T_0 \qquad \textbf{(Eq. 5.1)}$$

$$\Delta S^{\ddagger} = k_B \ln(hA/k_B T) - k_B \qquad \textbf{(Eq. 5.2)}$$

In the above equations, k_B is the Boltzmann constant, h is the Planck constant, T refers to the absolute temperature in Kelvin, and T_0 is a temperature in center of the investigated temperature range (here 20 °C).

For the first phase τ_{pre}, that accounts for the proton transfer ($S_3^+ \rightarrow S_3^n$) and structural rearrangements that may occur prior to the electron transfer (Haumann, Liebisch, et al., 2005), the results obtained are shown in table 5.1. By comparing the wild-type time constants at 20 °C to the ones obtained for the variants, two mutations stand out by showing a significant slow-down, namely the D59A with 1.18 ms and E65A with 3.17 ms. These mutations also appeared to have a higher $\Delta G^{\ddagger}$ than the wild-type, which was quite significant in the case of E65A, being higher by 50 meV, and the enthalpic component was quite dominant for both of them. This increase in $\Delta H^{\ddagger}$ may not be related to extra stabilization of the reactive conformation but rather an energy increment on the transition state, as the absence of one of these amino acids may force the proton transfer to take an alternative path as as indicated in computational work from Guerra et al. (2018). Guerra et al. (2018) suggest that the D61 residue that would normally transfer a proton to E65, through a single water molecule with high occupancy between both amino acids, would instead transfer through a water wire to E312 in the E65A mutation. In the same work, they also found profound changes in the H-bond network towards PsbO, including for example the reorientation of D2-E310 away from D1-E312. These results are in line with other works suggesting that the E65 residue is a core piece in the proton transfer pathway prior to the O_2 evolution in the S_3-S_0 transition. Our results further suggest that the D59 residue may also be involved in this proton transfer, directly or indirectly by being hydrogen bonded to the backbone of E65A (Ishikita et al., 2006; Kaur et al., 2021).

Table 5.1 – Fit parameters (A and E_a) obtained from the Arrhenius plots of the first phase (τ_{pre}) of the WT and the six variants of *Synechocystis* sp. PCC 6803 studied here. The thermodynamic parameters $\Delta H^{\ddagger}$, $-T\Delta S^{\ddagger}$ and $\Delta G^{\ddagger}$, calculated using Eqs. 5.1 and 5.2 are also displayed. The time constant τ_{pre} at 20° C is shown for comparison.

***Synechocystis* sp. PCC 6803 Variant**	**τ_{pre} at 20° C (ms)**	**Ln(A) (s^{-1})**	**E_a (meV)**	**$\Delta H^{\ddagger}$ (meV)**	**$-T\Delta S^{\ddagger}$ (meV)**	**$\Delta G^{\ddagger}$ (meV)**
Wild-type	0.47 ±0.02	18.3 ±1.6	269 ±25	244 ±23	306 ±27	550 ±35
E312A	0.42 ±0.02	20.5 ±2.3	323 ±37	298 ±34	251 ±27	549 ±44
D59A	1.18 ±0.04	26.4 ±1.4	496 ±25	471 ±24	102 ±5	573 ±24
D61K	0.45 ±0.02	21.1 ±1.0	340 ±16	315 ±15	236 ±11	550 ±18
E65A	3.17 ±0.05	21.3 ±1.0	395 ±17	370 ±16	231 ±11	600 ±19
E329A	0.54 ±0.02	22.0 ±1.1	365 ±19	340 ±18	213 ±11	553 ±21
N298A	0.33 ±0.01	23.9 ±1.4	405 ±24	380 ±22	165 ±9	545 ±24

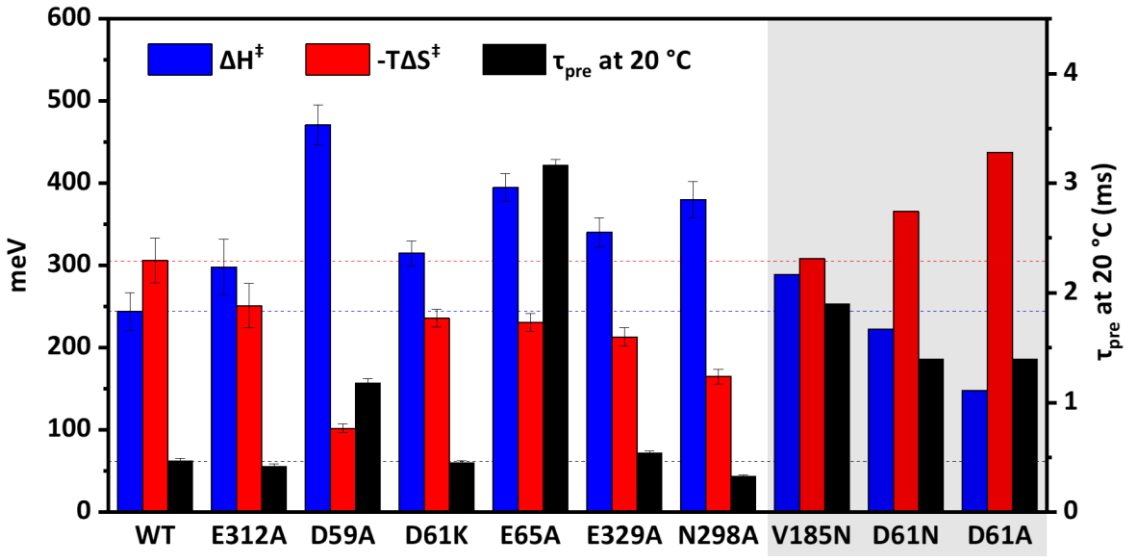

Figure 5.8 – Thermodynamic parameters determined for first phase (τ_{pre}) of the wild-type and variants of *Synechocystis* sp. PCC 6803. Dashed lines with the $\Delta H^{\ddagger}$, $-T\Delta S^{\ddagger}$ and τ_{pre} for the wild type can be seen for easier comparison with the variants. The results for three mutants previously studied in a similar way by Bao and Burnap (2015) were also presented and highlighted in grey, those are namely the V185N, D61N and D61A.

Apart from a slight enthalpy-entropy rebalance, that can be seen in table 5.1 or better perceived in Figure 5.8, the mutations E312A and D61K did not alter much the kinetics or thermodynamics of the first phase associated with $\tau_{pre.}$ The D61 residue is almost unanimously accepted as a crucial amino acid in the H-bond network around the Mn-cluster that mediates the proton transfer away from it. Experimental evidence for such can be found in the works of (Bao & Burnap, 2015; Dilbeck et al., 2012), and more recently (Ghosh, Khan, et al., 2019) where they have observed a significant enhancement in the kinetic solvent isotope effect in the D61A mutant when measuring oxygen evolution rates at different pL (L = H or D). In the first two works, they have showed by time-resolved O_2 polarography a significant slow-down in both phases, of other D61 mutants, like the D61A and D61N. For the D61K mutant we have found only significant changes in the O_2 evolution phase (Table 5.2), where an average of a slowdown by a factor of 5 was seen across the temperature range (0-35 °C), although it is a small effect when compared to the slowdown by factors of about 20 and 30 for the D61N and D61A, respectively observed in those works. In the Burnap lab, where the D61K samples were prepared, there were some preliminary measurements indicating already that the D61K would not be as slow as the D61A and D61N tested by them before. Even though 5 times slower O_2 evolution and 40 meV increase in $\Delta G^{\ddagger}$ (Table 5.2, Fig 5.7) is considerable, the fact that this mutation had a weaker effect in the S_3-S_0 transition may be because it can still participate in proton transfer or may attract nearby carboxylates e.g. the E65 and E312, just like K317 does to D61 in the absence of the nearby Cl^- (Rivalta et al., 2011).

The glutamate E312 is in close range of E65, and both form a dyad that share a proton, according to several theoretical studies (Guerra et al., 2018; Kaur et al., 2021; Sakashita et al., 2017). Even though that may be the case, it seems that these amino acids have slightly different involvement with the first proton transfer from the OEC during the S_3-S_0. For the first phase we showed that the E65A mutation had a severe impact, although the E312A mutation had a much milder effect on the first phase, where only a small increase in $\Delta H^{\ddagger}$, compensated by a small decrease in $-T\Delta S^{\ddagger}$ could be observed. For the O_2 evolution phase, the E312A slowed the reaction from 1.7 ms, in the wild type, to 2.2

ms and the $\Delta G^{\ddagger}$ was kept almost the same, however it included a decrease in $\Delta H^{\ddagger}$, that was compensated by about the same amount in a in $-T\Delta S^{\ddagger}$ increase (Table 5.2, Fig 5.7).

Table 5.2 – Fit parameters (A and E_a) obtained from the Arrhenius plots of the O_2 evolution phase (τ_{ox}) of the WT and the six variants of S*ynechocystis* sp. PCC 6803 studied here. The thermodynamic parameters $\Delta H^{\ddagger}$, $-T\Delta S^{\ddagger}$ and $\Delta G^{\ddagger}$, calculated using Eqs. 5.1 and 5.2 are also displayed. The time constant τ_{ox} at 20° C is shown for comparison.

***Synechocystis* sp. PCC 6803 Variant**	**τ_{Ox} at 20° C (ms)**	**Ln(A) (s^{-1})**	**E_a (meV)**	**$\Delta H^{\ddagger}$ (meV)**	**$-T\Delta S^{\ddagger}$ (meV)**	**$\Delta G^{\ddagger}$ (meV)**
Wild Type	1.72 ±0.07	23.0 ±1.3	421 ±22	396 ±21	188 ±10	584 ±23
E312A	2.2 ±0.09	19.0 ±1.1	327 ±17	302 ±16	289 ±16	591 ±22
D59A	2.9 ±0.10	27.5 ±0.8	547 ±14	522 ±13	74 ±2	596 ±13
D61K	7.7 ±0.22	22.5 ±1.2	448 ±22	423 ±21	200 ±11	623 ±23
E65A	62.4 ±0.74	28.7 ±0.7	655 ±13	630 ±13	44 ±1	674 ±13
E329A	1.3 ±0.04	18.8 ±0.8	309 ±12	284 ±11	294 ±13	578 ±17
N298A	1.2 ±0.04	19.3 ±1.1	321 ±18	296 ±17	281 ±16	577 ±23

Even though theoretical studies attribute high importance to the glutamate E312 in the proton transport around the OEC, these results show otherwise, indicating that a severe mutation like the E312A does not substantially impair the Mn-cluster from evolving O_2. Similar conclusions came from the recent study of (Kuroda et al., 2021), where they performed extensive mutations of several amino acids around the OEC in *Chlamydomonas reinhardtii*, and then analyzed cell growth and O_2 evolution rates. Among others, the study included 19 mutations of each of the following amino acid residues: D2-E312, D1-D61 and D1-E65, and in their work they clearly showed that the E312 residue was much more resilient to mutations than the E65 or the D61. Specifically in the case of their alanine mutation, the E65A had a much lower cell growth and O_2 evolution rate than the E312A. For the E65A mutation in our study, the O_2 phase was also greatly affected, with 36 times slower O_2 release, and an increase in $\Delta G^{\ddagger}$, this time by 90 meV which was justified by a great increase in $\Delta H^{\ddagger}$ (Table 5.2, Fig. 5.7). Similarly slow O_2 evolution phases were previously observed in the V185N, D61N and D61A

mutants studied by Bao and Burnap (2015) (Fig. 5.7). Apart from the study of Kuroda et al. (2021) and our results presented here, other experimental studies already had shown significant effects of this mutation. For example Chu et al. (1994) observed that the O_2 evolution rate for the E65A mutant was only a fifth of the Wild type´s, and in the study of Service et al. (2010) they showed by FTIR difference spectroscopy that the E65A mutation significantly decreased the S-state turnover on the S_3-S_0 transition.

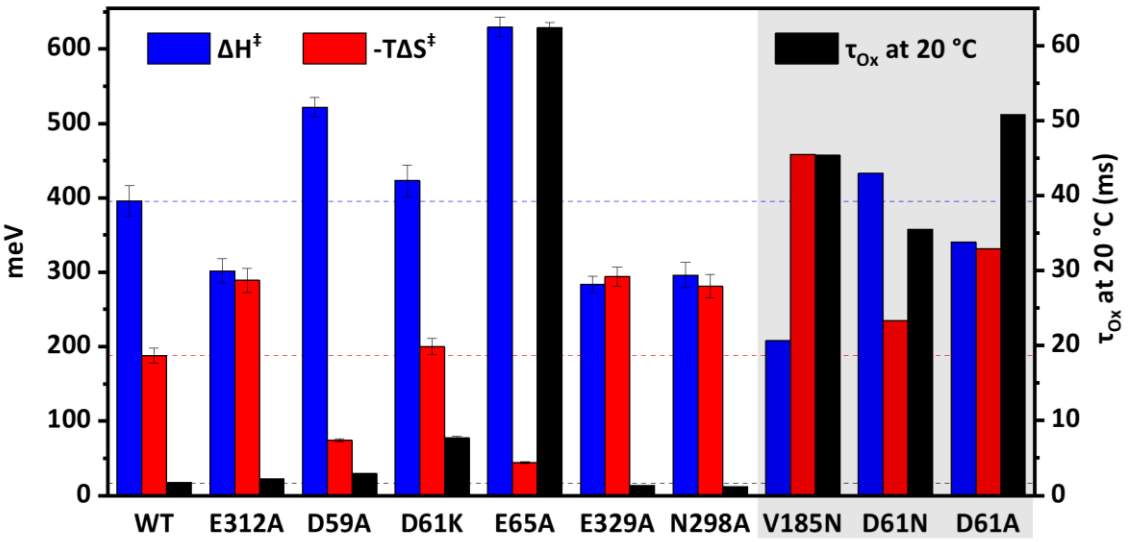

Figure 5.7 – Thermodynamic parameters determined for O_2 evolution phase (τ_{ox}) of the wild-type and variants of *Synechocystis* sp. PCC 6803. Dashed lines with the $\Delta H^{\ddagger}$, $-T\Delta S^{\ddagger}$ and τ_{ox} for the wild type can be seen for easier comparison with the variants. The results for three mutants previously studied by Bao and Burnap (2015) in a similar way as done in the present work were also presented and highlighted in grey, those are namely the V185N, D61N and D61A.

In the D59A mutant, the O_2 evolution phase showed also a significantly higher activation energy than the WT, of about 520 meV, which can be even perceived in the temperature dependance of the kinetic transients (Figs. 5.4 and 5.5). In this mutation the average time constant for the O_2 evolution across the temperature range was 3 times slower as in the wild type, although the $\Delta G^{\ddagger}$ of the reaction was about the same. As indicated by the high activation energy, the $\Delta H^{\ddagger}$ was also predominat in this mutation, that in turn showed a very small $-T\Delta S^{\ddagger}$ (Table 5.2, Fig. 5.7). Even though other experimental work targeting D59 is quite scarce, results from (Qian et al., 1999) showed that another mutation of this glutamate, the D59N, showed slightly slower O_2 release kinetics than

the wild type, and in the same study it was concluded from the faster S_2 and S_3 decays, that the mutation could be altering slightly the redox properties of the OEC. Their suggestion could explain the difference in thermodynamic parameters found here between the D59A and the wild type, indicating that D59 may not be only relevant for the hydrogen bond network around the Mn-cluster but also help to regulate its redox potential, at least during the S_3-S_0 transition.

The S*ynechocystis* sp. PCC 6803 variants discussed so far were from point mutations of amino acids that are mostly part of the broad channel, with D59 being in the border between the broad and narrow channels. The E329 and N298 residues are both located on the other side of the OEC closer to O1 and make part of the large channel. In our study, the variants with replacement of these amino acids by alanine, E329A and N298A, showed very similar results. Both had a slightly faster O_2 evolution, and similar $\Delta G^{\ddagger}$ in both phases when compared to the wild type. The difference from the wild type was mostly related to the shifts between enthalpy and entropy which can be seen for both phases in Figs. 5.6 and 5.7. These were almost the same for both variants, for the first phase (τ_{pre}), there was an increase in $\Delta H^{\ddagger}$ and decrease of $-T\Delta S^{\ddagger}$, which may be related to the fact that in the absence of these amino acids, there may be a fewer number of possible conformations of the hydrogen bond network around the OEC for the release of the proton, since alanines would not participate. On the other hand, for the O_2 evolution phase, the absence of these amino acids may affect the perfect conformation of the OEC for the electron transfer reaction and so destabilize the reactive conformation leading to a decrease in $\Delta H^{\ddagger}$ and increase in $-T\Delta S^{\ddagger}$ as in these cases it has to compete with more non-reactive substates of similar energy. In the case of the N298A variant, our results may be contradicting previous conclusions from FTIR and transient IR measurements in PSII core particles from the same species and mutation. In (Nagao et al., 2017), they showed by FTIR difference spectroscopy that the N298A mutation highly affected the turnover in the S_2-S_3 and S_3-S_0 transitions leading to the conclusion that the entrance of the large channel, namely the Y_Z H-bond network, could be a functional proton transfer pathway away from the OEC during those transitions. In (Okamoto et al., 2021), they measured kinetics by transient IR spectroscopy for the S_1-S_2 and S_2-S_3 transitions in the N298A and found that the dominant time constants were

respectively 4 and 7 times slower with a low KIE (1.2-1.4). This way, it was concluded that the slow-down in the S_2-S_3 transition was related to a delayed water insertion (which they propose to happen through the large channel) that becomes the rate limiting step instead of the proton transfer. Since there is no water insertion before O_2 release in the S_3-S_0 transition, this would not contradict our findings, although water insertion doesn't occur during the S_1-S_2, and (Okamoto et al., 2021) have observed a slowdown in that transition. In the S_1-S_2 transition, which mainly consists of an electron transfer event, a possible explanation for the slowdown could be an alteration of the redox properties of the OEC or more likely of Y_Z, since the histidine H190 in close relation with Y_Z, hydrogen bonds to the N298 residue (Kawashima et al., 2018). If this would be true for the S_1-S_2 transition, we believe that a similar effect might take place in the S_3-S_0 transition and would be visible in our measurements unless it would not alter the rate limiting steps. In the case of the E329A mutation the experimental data available is from FTIR difference spectroscopy. In the spectra acquired in those works, it can be seen that the E329A mutation does not significantly alter the specific vibrations that take place during the S-state cycle (Kim & Debus, 2020; Service et al., 2010), which is consistent with the very mild effect we observe in the kinetics of this variant when compared to the wild type.

5.3 Conclusion

In this chapter we carry out a temperature series of time resolved O_2 polarography measurements using thylakoid membranes from *Synechocystis* sp. PCC 6803 wild type and the variants D59A, D61K, E65A, E312A, E329A and N298A. With this we obtained temperature dependant kinetics that we used to produce Arrhenius plots to extract the respective E_a and the pre-exponential factor that by using an Eyring treatment could be converted into $\Delta H^{\ddagger}$ and $-T\Delta S^{\ddagger}$, the two parameters that compose the $\Delta G^{\ddagger}$. This kinetic and thermodynamic study of these variants from mutated amino acids located within 12 Å of the OEC allowed us to better understand their role during the S_3-S_0 transition. Our results show that the D61K mutation had a smaller effect in this transition than previously studied mutations like the D61A and D61N (Bao & Burnap, 2015), showing

that the lysine may still be able to participate in the proton transfer process or at least adapt the local H-bond network, and does not exclude the D61 aspartate as a primary proton acceptor from the OEC in the S_3-S_0 transition prior to the O_2 evolution. Regarding the E65A variant, we showed the importance of this amino acid in the proton transfer away from the OEC that may happen through a water molecule positioned between the D61 and the E65 residues just like described in (Guerra et al., 2018). Furthermore, we believe that by the large increase in $\Delta H^{\ddagger}$ observed in the mutant, the E65 residue is also important for the stabilization of the transition state of the rate limiting step during the O_2 formation. Also, we conclude that the overall function of E65 cannot be replaced by the nearby D2-E312 glutamate. The E312A mutation of this amino acid that appears very close to the E65, did not significantly affect the kinetics or thermodynamics of both phases, with a mere 20% reduction in O_2 evolution and some enthalpy-entropy adjustments that did not reflect any changes in the overall $\Delta G^{\ddagger}$. This led us to exclude E312 as an essential participant in the proton release that precedes O_2 evolution. The D59A mutation substantially increased the activation energy of both phases of the S_3-S_0 transition which may be related to the hydrogen bonding this amino acid has with the backbone of E65. The D59A mutation may increase the distance between E65 and D61 affecting in this way the proton transfer process, although another explanation for our results could relate to the participation of this aspartate in the proton transfer pathway, which could happen mainly at lower temperatures, being progressively replaced by another pathway at higher temperatures for which we found much lower kinetic disparities when comparing to the wild type. The similar results obtained for the E329A and N298A mutations, that only showed weak perturbations for the kinetics and thermodynamics of the reaction for both variants, suggest that these amino acid residues are not involved in the first proton transfer away from the OEC in the S_3-S_0 transition. This hypothesis may even be extended to defend that the large channel, where these residues are located, is not serving as a proton pathway for the deprotonation that immediately precedes the O_2 evolution. Combining with the experimental evidence gathered from the measurements on the other variants, we can strongly support the hypothesis that the first deprotonation in the S_3-S_0 transition happens through the broad channel, without excluding the possible participation of part of the narrow channel for the proton movement nearby the Mn-cluster.

Chapter 6 – O_2 evolution kinetics and activation barrier of the O_2-formation step in red-shifted Photosystem II

The chlorophylls (Fig. 6.1) in the reaction center of Photosystem II define the energy level of the initial excited state from where the subsequent photochemistry can happen (Dau & Zaharieva, 2009; Rutherford et al., 2012). Generally, this chlorophyll complex contains chlorophyll (Chl) *a* exclusively and is denoted as P680. However, there exist a few exceptions. One case occurs in the cyanobacterium *Acaryochloris marina* which contains photosystems containing mainly Chlorophyll *d* (~97%) and only one or two Chorophyll *a* molecures in a few key positions (Miyashita et al., 2014; Renger & Schlodder, 2008). For this strain, the PSII reaction centers contain Chl *d*, and whether or not Chl *a* is also present there is still under discussion (Miyashita et al., 2014; Tomo et al., 2007). Another example is *Chroococcidiopsis thermalis,* a cyanobacterium which was found to also produce red-shifted chlorophylls when grown under far-red light illumination, while it produces only chlorophyll *a* under white light (Itoh et al., 2015; Nürnberg et al., 2018). The red-shifted chlorophyll content was estimated to be about 10% for Chl *f* and <1% for Chl *d* (Nürnberg et al., 2018). Even though these chlorophylls were thought to have an exclusively light-harvesting role (Trampe & Kühl, 2016), recently it has been suggested that they would be also present in the reaction centers of both photosystems as primary electron donors (Nürnberg et al., 2018). For PSII, cryo-EM data supports the existence of a red-shifted Chl (*d* or *f*) in the Chl_{D1} position (Gisriel, Huang, et al., 2021; Gisriel, Shen, et al., 2021). However, for PSI recent studies showed contradicting evidence (Cherepanov et al., 2020; Gisriel, Flesher, et al., 2021; Kato et al., 2020). Furthermore in (Nürnberg et al., 2018), evidence was presented supporting that the energy of the primary excited state P727* had 110 meV less energy than P680* in PSIIs from white light grown cyanobacteria. Having a PSII that changes the Chl content of its reaction center depending on the illumination and adapts to the lower photochemical driving energy is a very special situation, that brings up a great opportunity to learn more about the water oxidation mechanism in PSII.

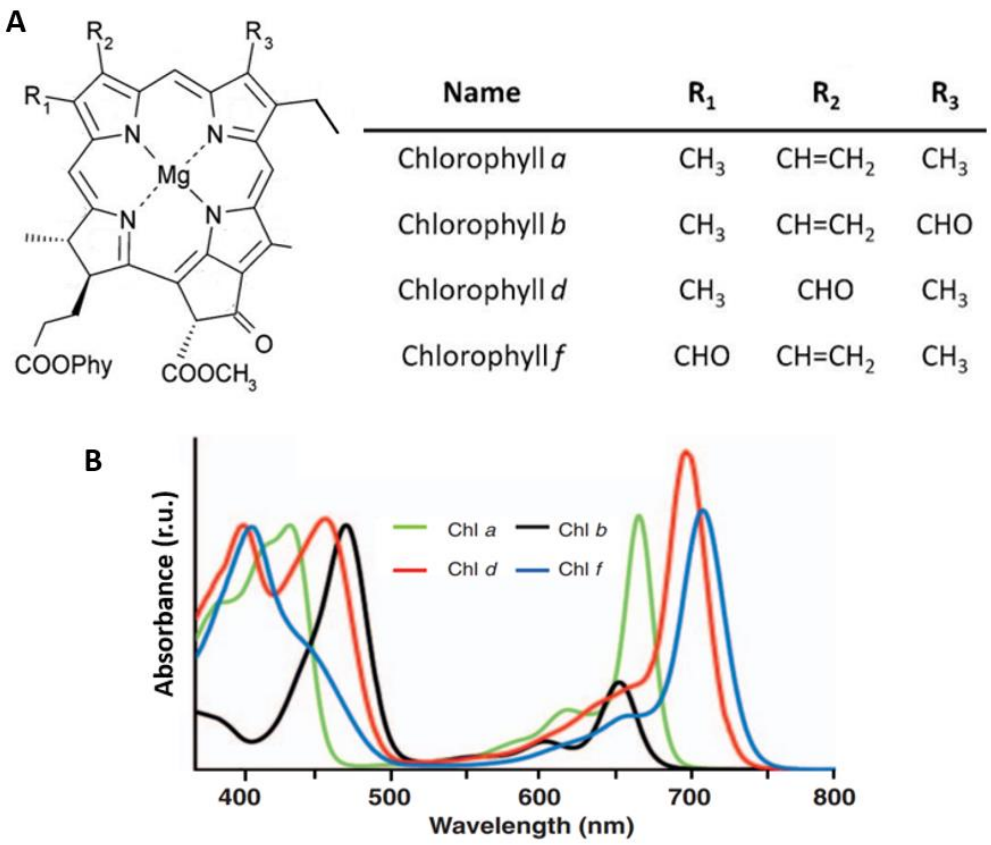

Name	R_1	R_2	R_3
Chlorophyll *a*	CH_3	$CH{=}CH_2$	CH_3
Chlorophyll *b*	CH_3	$CH{=}CH_2$	CHO
Chlorophyll *d*	CH_3	CHO	CH_3
Chlorophyll *f*	CHO	$CH{=}CH_2$	CH_3

Figure 6.1 – Molecular structure of a generic Chl molecule with the terminal group changes for each specific Chl *a*, *b*, *d*, *f* molecules (A). The respective absorption spectrum for each of the represented Chls (B). Adapted from (Chen & Blankenship, 2011).

The work presented in this chapter, aims to show how photosystem II with red-shifted chlorophylls works under various excitation lights relative to samples containing chlorophyll *a* only. For this approach, time-resolved O_2 polarography was used to measure O_2 evolution transients, from which kinetic information relative to the oxygen release and the respective flash-induced oxygen-evolution patterns (FIOPs) can be extracted. These provide insight on how efficiently each sample can make use of the excitation energy to go through the S-state cycle. Furthermore, we extended the measurements on *C. thermalis*, both WL and RL grown, to a wider temperature range, in order to assess the thermal activation energy by means of an Arrhenius treatment.

6.1 Experimental details

6.1.1 Preparation of thylakoid membranes

Thylakoid membranes from white-light and far-red light grown *Chroococcidiopsis thermalis* PCC 7203 and from *Acaryochloris marina* cells were provided by Viktor Eichmann and Dr. Dennis Nürnberg (Eichmann, 2021). The protocol is based on the protocol for the preparation of thylakoid membranes from S*ynechocystis* sp. PCC 6803 presented in Chapter 2 but with a few modifications (Eichmann, 2021). The samples had been previously stored at -80 °C and, before use, were thawed on ice for 60 min in the dark.

6.1.2 Time-resolved oxygen polarography

The measurements of time-resolved oxygen evolution were performed on thylakoid membrane samples from *A. marina*, *Synechocystis* sp. PCC 6803, and *C. thermalis* grown in white and far-red light. A custom-made centrifugable static ring-disk electrode assembly consisting of a bare platinum working electrode and silver-ring counter electrode, was used to perform the measurements as described before (Dilbeck et al., 2012; Schuth et al., 2017), and in Chapter 2. Each measurement was prepared by adding an aliquot of the thylakoid membrane suspension equivalent to 10 µg of total chlorophyll onto the electrode complemented with Buffer D-NaCl [150 mM NaCl, 25 mM MES (pKa = 6.15), 1 M glycine betaine, 5 mM $MgCl_2$, and 5 mM $CaCl_2$, pH 6.2 (NaOH)] to a total volume of 750 µl. The electrode assembly was then centrifuged in a swing-out rotor at 10,000 × g for 10 min (at 4 °C). Using a home-built potentiostat that also provided an electrode polarization of -0.95 V, switched on 15 s before the first excitation flash, the current signal was recorded for 500 ms, 20 ms before and 480 ms after each flash, for a total of 40 flashes with 900 ms spacing. Three different light sources were used to induce the S-state transitions: a custom-made LED flashing device with two changeable high-performance LEDs (Luminus) and a Xenon flashlamp (EG&G Optoelectronics). The LEDs had emission peaks in the red and far-red (613 nm and 730 nm respectively) and the flashlamp was equipped with 570 nm cut-off filter supressing

the shorter wavelengths. The total energy per light flash was determined with a 1 cm^2 power meter (Ophir Photonics) at the exit of the liquid light guide, which conveyed the light to the sample. The LED flash length was 40 µs, powered by a maximum voltage of 22 V, whereas the voltage applied for the discharge of the flashlamp was 1000 V (see Chapter 2 for the exact energy per flash pulse and respective spectrums). During the data acquisition the sample was brought to a temperature of 20 °C, controlled by Peltier elements and monitored by a miniature temperature sensor immersed in the sample buffer. The O_2 transients were then fit with the diffusion model (Dilbeck et al., 2012), also presented in Chapter 2 of this thesis, with which the time-constants of oxygen evolution could be determined and compared. From the maximal O_2 signal of each recorded flash transient, flash-induced oxygen-evolution patterns (FIOPs) were plotted and then fitted with an extended Kok model as described in Kebekus et al. (1995); Noring et al. (2008).

Similarly, extra measurements were made with both *C. thermalis* thylakoid membrane samples (white and far-red light grown), in a temperature-dependent manner, measuring in triplicate every temperature point in a 5 °C step in the ranges of 0-35 °C (WL) and 0-45 °C (FRL), respectively. For this experiment only the red LED was used, as it provided a good O_2 signal amplitude for both samples. After fitting the kinetic transients with the same oxygen diffusion model (Dilbeck et al., 2012), the time constants were used to make the Arrhenius plots from which the activation energy (E_a) and the pre-exponential frequency factor (A) was determined. These parameters were then both used to calculate the enthalpic ($\Delta H^{\ddagger}$) and entropic ($\Delta S^{\ddagger}$) contributions by applying the Eyring treatment (Guo et al., 2014).

6.2 Results

6.2.1 O_2 evolution kinetics

To estimate how the excitation light could affect either the kinetics or the cycling ability of the S-state cycle, O_2 polarography was measured in four different thylakoid membrane samples, namely from S*ynechocystis* sp. PCC 6803, *A. marina and C.*

thermalis WL grown and FRL grown. For each three different light excitations were used: the red LED, the far-red LED and the flashlamp (see Chapter 2 for details). The results measured at 20 °C are shown in Fig. 6.2, and there, different changes in the signal amplitude can be seen depending on the excitation light. For *C. thermalis* grown under WL (Fig. 6.2 A) the amplitude of the transient relative to the far-red LED excitation was much lower. A similar effect can be seen for S*ynechocystis* sp. PCC 6803 (Fig. 6.2 B). This relates to the fact that these two samples have no red-shifted chlorophylls, and the far-red excitation with a peak at 730 nm was already mostly out of the absorption range of the chlorophyll a, only overlapping with a tail in the emission spectrum between 660-700 nm. This small overlap still made it possible for S*ynechocystis* sp. PCC 6803 to evolve oxygen, allowing for the detection of the kinetics under these conditions (Fig. 6.2 B). When comparing to the samples with red-shifted chlorophylls (Fig. 6.2 C and D), it is possible to see a more homogeneous amplitude response from the system excited with different sources, but for *C. thermalis* grown with FRL a higher amplitude was achieved when exciting with the far-red LED, even though this was the slightly weaker source (see Chapter 2). For *A. marina*, the amplitudes were constant independently of the excitation light most probably because of the absorption peak of Chl *d*, which has been determined to be at 695 nm for Chl *d* extracted from several species (Gan et al., 2015). The absorption peak at 695 nm is located in between the emission peaks of both excitation LEDs (615 nm and 730 nm) making it so that it only partially overlaps with both, which may justify the similar amplitudes observed (Fig. 6.2 D).

The simulation curves fitted according to the diffusion model (Dilbeck et al., 2012), can be seen in great agreement with the experimental data in Fig. 6.2. For all the four samples, the oxygen release kinetics did not significantly change with the application of different light excitations, indicating that the PSIIs from these samples release oxygen at their intrinsic rate, independently of the wavelength applied, as long as it is within the spectral range that can drive the photochemistry in that particular PSII. For a better visual comparison, the data is shown normalized in Fig. 6.3. The simulated time constants for the oxygen evolution step (τ_{ox}) obtained are shown in Fig. 6.4 A and a comparison of the kinetics at 20 °C for each sample can be seen Fig. 6.4 B. For S*ynechocystis* sp. PCC 6803 the O_2 release time constants obtained by the fit, 1.6 ms at

20 °C, reproduce well the values that were previously reported (Bao & Burnap, 2015; Dilbeck et al., 2012).

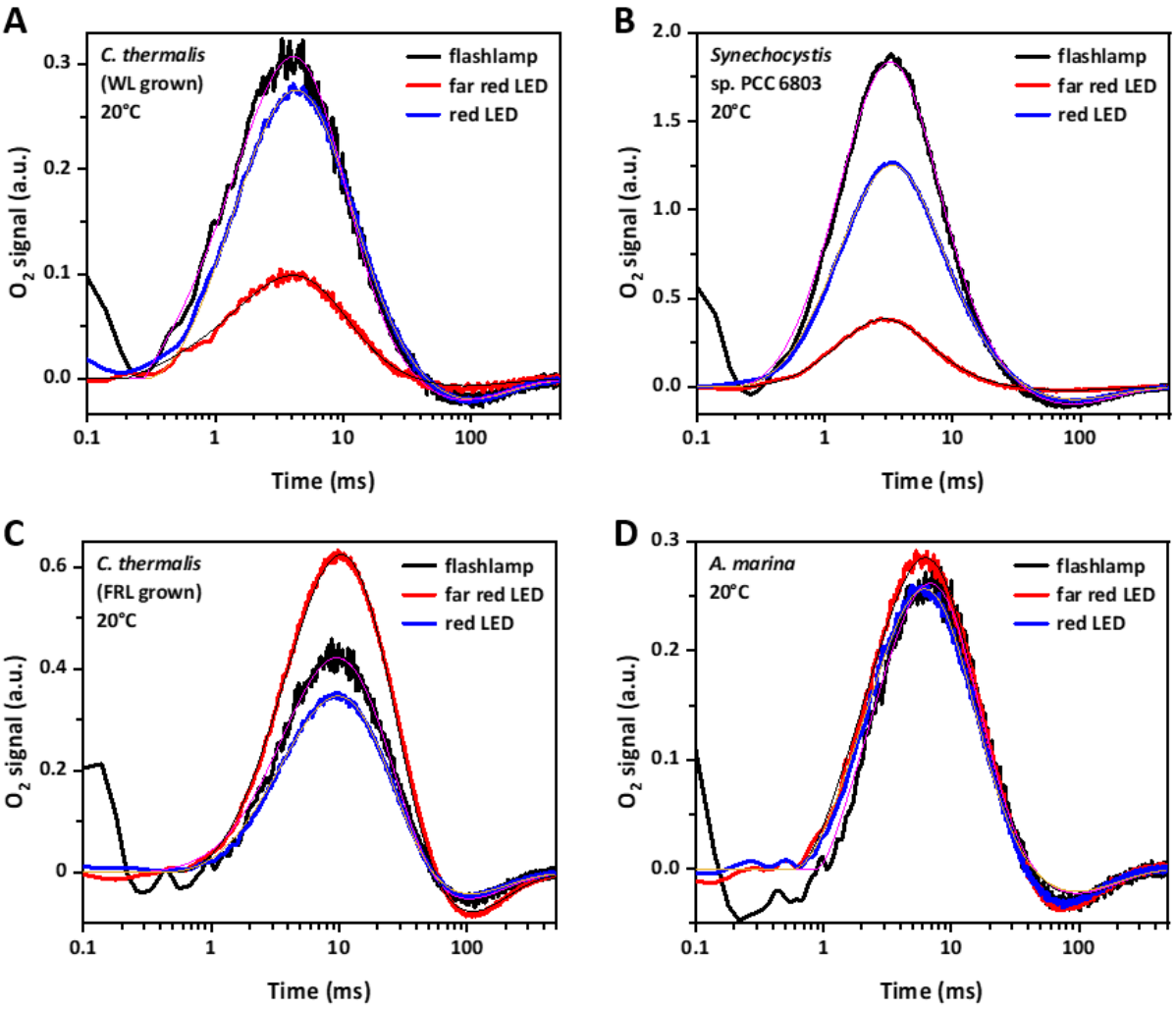

Figure 6.2 – O_2-evolution transients of thylakoid membranes excited by different light sources. The membranes were deposited on a bare platinum electrode by joined centrifugation of a thylakoid membrane dispersion and the Pt/Ag electrode assembly. On the left side the transients obtained from *C. thermalis* membranes grown in white (A) and far-red light (C) can be seen. On the right side, it is shown the results relative to *Synechocystis* sp. PCC 6803 (B) and *A. marina* (D). The kinetics are the average of 230 individual transients measured after each flash, averaged from three independent experiments on each condition. Thin lines represent the respective fits obtained by simulations based on a numerical model that considers the O_2-formation and diffusion in the PSII layer as well as the O_2 reduction at the bare platinum electrode. The simulated time constants are presented in Fig. 6.4 A.

The other samples were during this work measured with time resolved oxygen polarography for the first time. While membranes from *C. thermalis* (WL grown) have an O_2 evolution time constant of about 2.2 ms at 20 °C, which is slightly slower, when compared to *Synechocystis* sp. PCC 6803, the τ_{ox} in *A. maria* is significantly slower (4.6

ms at 20 °C). While this is likely to be related to the high Chl *d* content in the PSII centers of this organism, other explanations cannot be completely ruled out since in this work O_2 evolution transients were also measured for *Chlamydomonas nivalis*, obtaining for this alga, that has no red-shifted Chls, a similar τ_{ox} of 4.1 ms at 20 °C (Table 6.1 and Appendix E.3). However, other factors like the unique thylakoid lipid composition (Lukeš et al., 2014) or other low temperature photosynthetic regulatory processes (Zheng et al., 2020) may justify the τ_{ox} observed for *C. nivalis.* More significant was the much slower 10.3 ms at 20 °C τ_{ox} observed in *C. thermalis* (FRL grown), which is almost five times higher than the same species grown is WL conditions, making this FRL grown

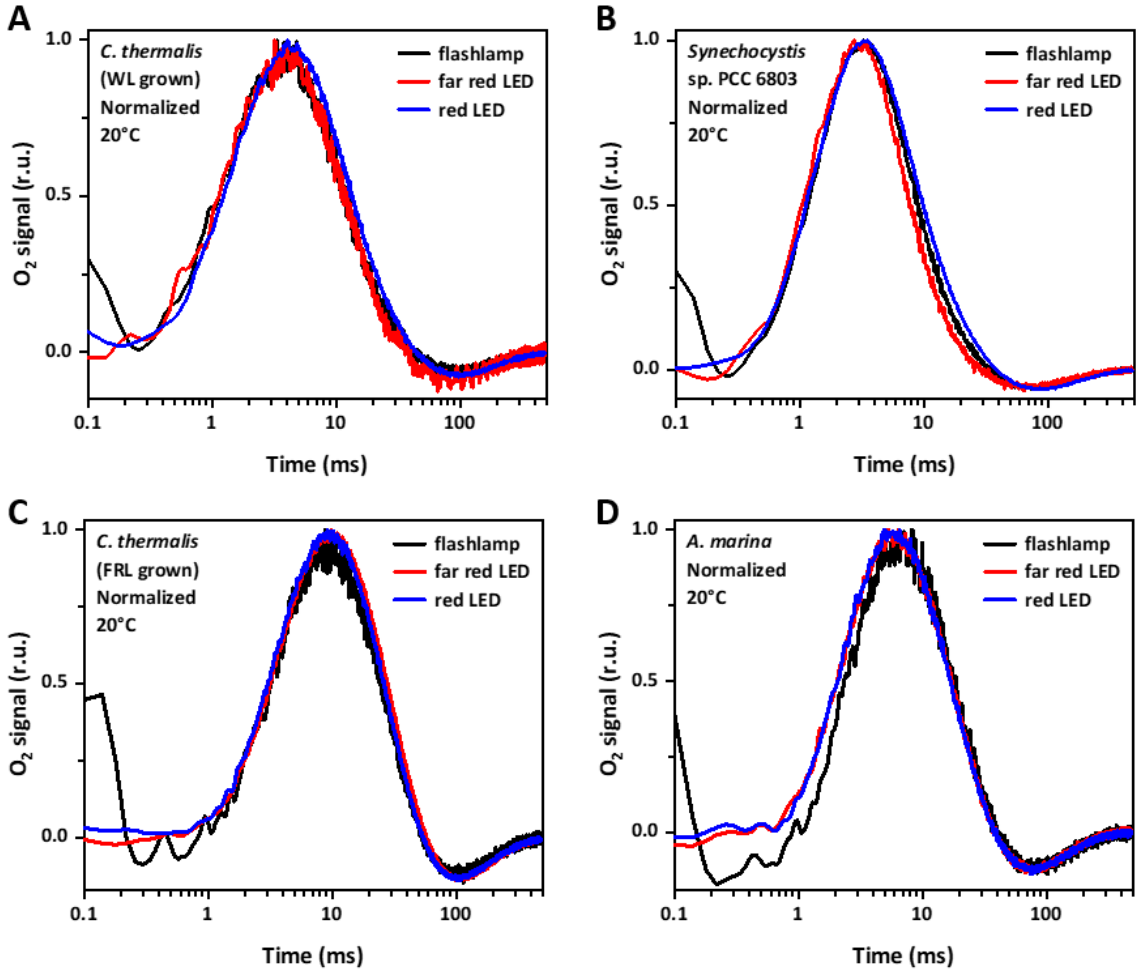

Figure 6.3 – Same data as presented in Fig. 6.2 but with the maximum normalized to unity for better visual comparison of the O_2-evolution transients from thylakoid membranes excited by different light sources. On the left side the transients obtained from *C. thermalis* membranes grown in white (A) and far-red light (C) can be seen. On the right side, it is shown the results relative to *Synechocystis* sp. PCC 6803 (B) and *A. marina* (D). The kinetics are the average of 230 individual transients measured after each flash, summed up from three independent experiments on each condition.

cyanobacterium the slowest O_2 evolving non-mutant photosynthetic organism reported so far. This shows that the Far-Red Light Photoacclimation (FaRLiP) comes at a cost of making PSII less efficient but letting it to work under far-red light conditions, and thus allowing for photosynthetic life in places where only longer wavelength light can penetrate like in the Shark Bay stromatolites in Australia or in sediments of Lake Biwa in Japan (Akutsu et al., 2011; Chen et al., 2010).

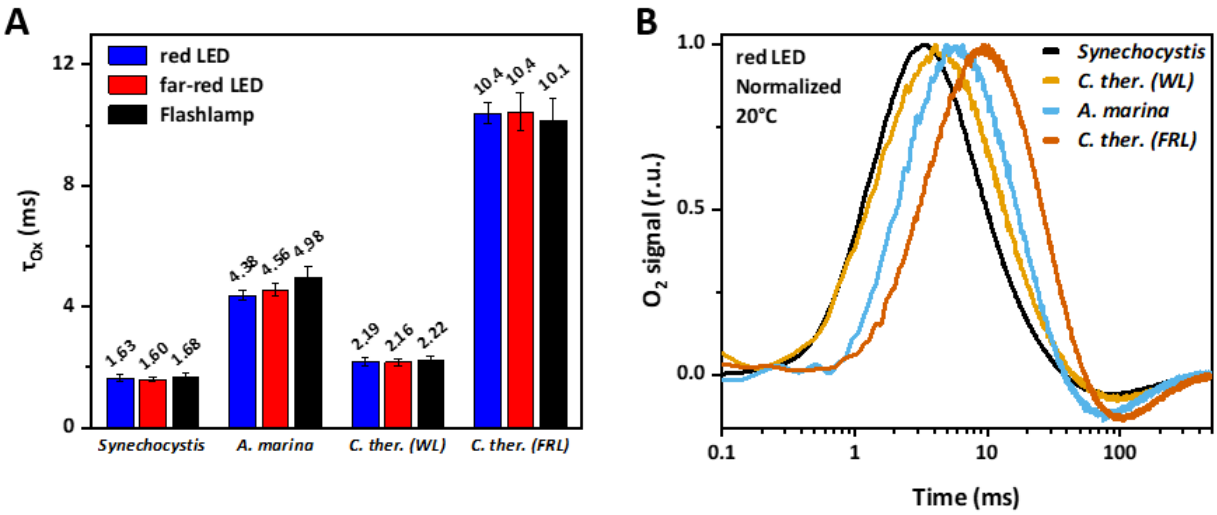

Figure 6.4 – On the left, bar plot comparing the fitted O_2 evolution time constants (τ_{ox}) for every sample at 20 °C for each light excitation (A). On the right side it is shown a comparison of the normalized O_2 evolution kinetics obtained at 20 °C using the red LED presented in Fig. 6.3 (B). The kinetics are the average of 230 individual transients measured after each flash, averaged from three independent experiments on each condition.

6.2.2 Flash-induced oxygen evolution patterns and miss factor analysis

Apart from kinetic information, the transients obtained can provide insight into the ability of PSII to cycle through the S-state cycle. As the transients are recorded independently after each flash, the maximum amplitude of the signal is proportional to the overall O_2 production induced by that excitation flash. By plotting these amplitudes versus the flash number, the flash-induced oxygen-evolution patterns (FIOPs) are obtained which show the proportional amount of PSII centers that had the $S_3 \rightarrow S_0$ transition after the excitation. In Fig. 6.5, the flash patterns for each of the four samples is shown for the different light excitations. Note that for proper comparison the amplitudes have been normalized to the amplitude of the 40th flash where it is expected

to have already fully mixed S-states (about 25% each). By employing suitable light excitation, such as the emissions from the red LED (613 nm) and the flashlamp used here, active PSII thylakoid samples without red-shifted chlorophylls should show a flash pattern where the period of four oscillation characteristic of the S-state cycle can be seen (Kok et al., 1970).

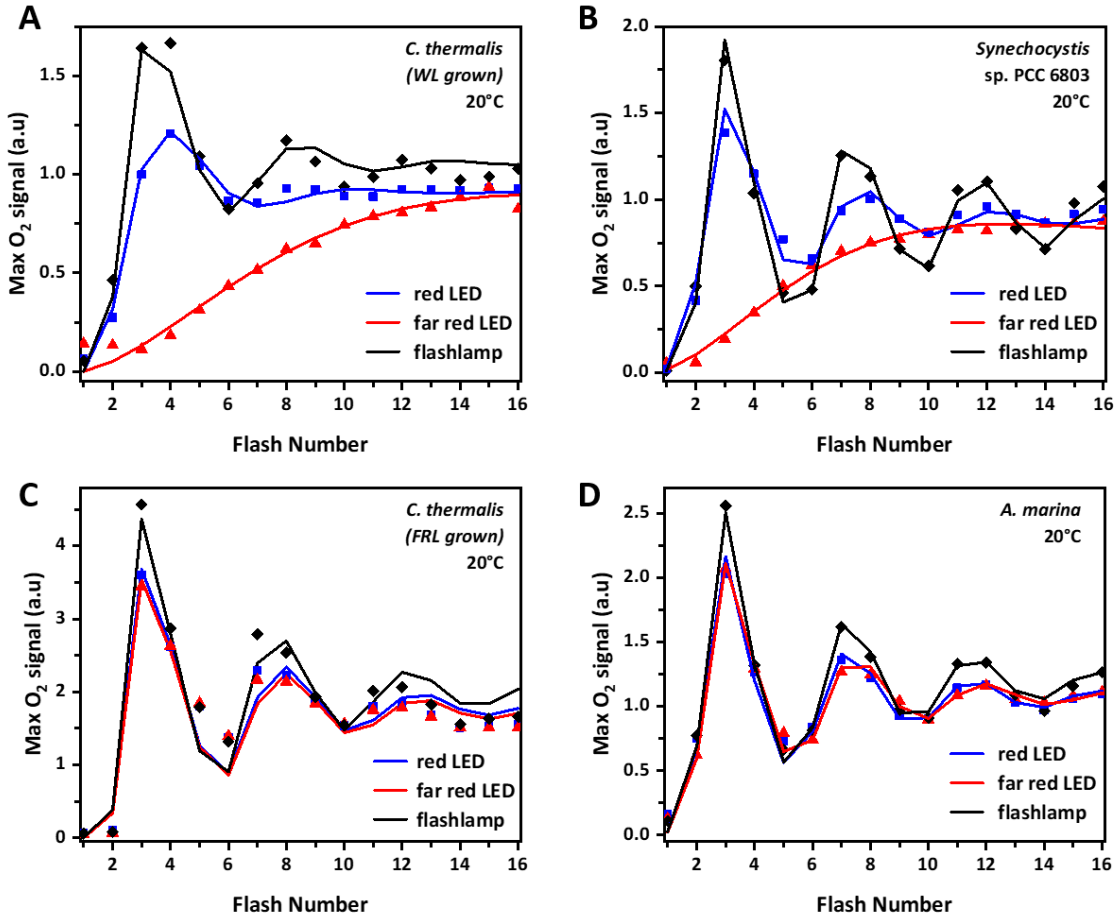

Figure 6.5 – Flash-induced oxygen-evolution patterns (FIOPs) of thylakoid membranes excited by three different light sources. On the left side the patterns obtained for *C. thermalis* membranes grown in white (WL) and far-red light (FRL) can be seen. On the right side, it is shown the same for *Synechocystis* sp. PCC 6803 and *A. marina*. The FIOPs were normalized to the amplitude of the 40th flash. The experimental data is presented as points and is the average of three independent experiments on each condition. Continuous lines represent the respective fits according to the extended Kok cycle model (Kebekus et al., 1995; Noring et al., 2008). The simulation parameters are presented in the Fig. 6.6.

This characteristic oscillation could be observed for *C. thermalis* (WL grown) and *Synechocystis* sp. PCC 6803, however the pattern vanished when the far-red LED was used for excitation instead (Fig. 6.5 A-B). This implies a very high miss probability that is

only apparent in this case due to the inefficient ability of these samples to absorb far-red light, as it can also be seen in Fig. 6.2 A-B, where a major reduction on the transient signal amplitude is evident when the far-red LED was the excitation source. In the case of the red-shifted Chl containing samples*, A. marina* and *C. thermalis* (FRL grown), Fig. 6.5 C-D shows that their FIOPs feature a pronounced period of four oscillation that was very similar, independently of the light excitation, even for the far-red LED. For all samples in Fig. 6.5, the more pronounced oscillations were observed when the flashlamp was used for excitation due to its higher pulse energy (540 μJ) then the red LED (270 μJ). The red LED was flashed at maximum intensity although it seemed to be slightly undersaturating, making it so that for every sample the lowest miss factor was achieved when using the flashlamp for light excitation. The miss factors, double hits and initial S-state populations were estimated by fitting the experimental data with an extended Kok cycle model (Kebekus et al., 1995; Noring et al., 2008). The fits could describe well the data and can be seen in Fig 6.5 as continuous lines and the fit parameters, that include initial S-state populations, miss factor and double hits, can be seen on Fig. 6.6. Although there is a gap in pulse energy between the flashlamp and the LEDs, for the red-shifted samples the miss factors were only slightly smaller when the flashlamp was used, meaning that the LEDs were close to delivering saturating flash pulses. The apparent very high miss factor (>80%) obtained for the PSIIs from *C. thermalis* (WL grown) and S*ynechocystis* sp. PCC 6803 when excited with the far-red LED matches well with the vanishing of the period of four oscillation (Fig 6.5 A-B).

For the *C. thermalis* (WL grown) membranes, the flash patterns are dampened and show a comparably high miss parameter when the red LED or the flashlamp were used, even though the period of four oscillation can still be seen (Fig 6.5 A). This may result from the fact that the data here reported come from measurements done with the first active *C. thermalis* WL grown membranes and the preparation may have not yet been optimal. However, this analysis will focus on the major differences between WL to FR light grown *C. thermalis* and so the conclusions here discussed later will not be affected.

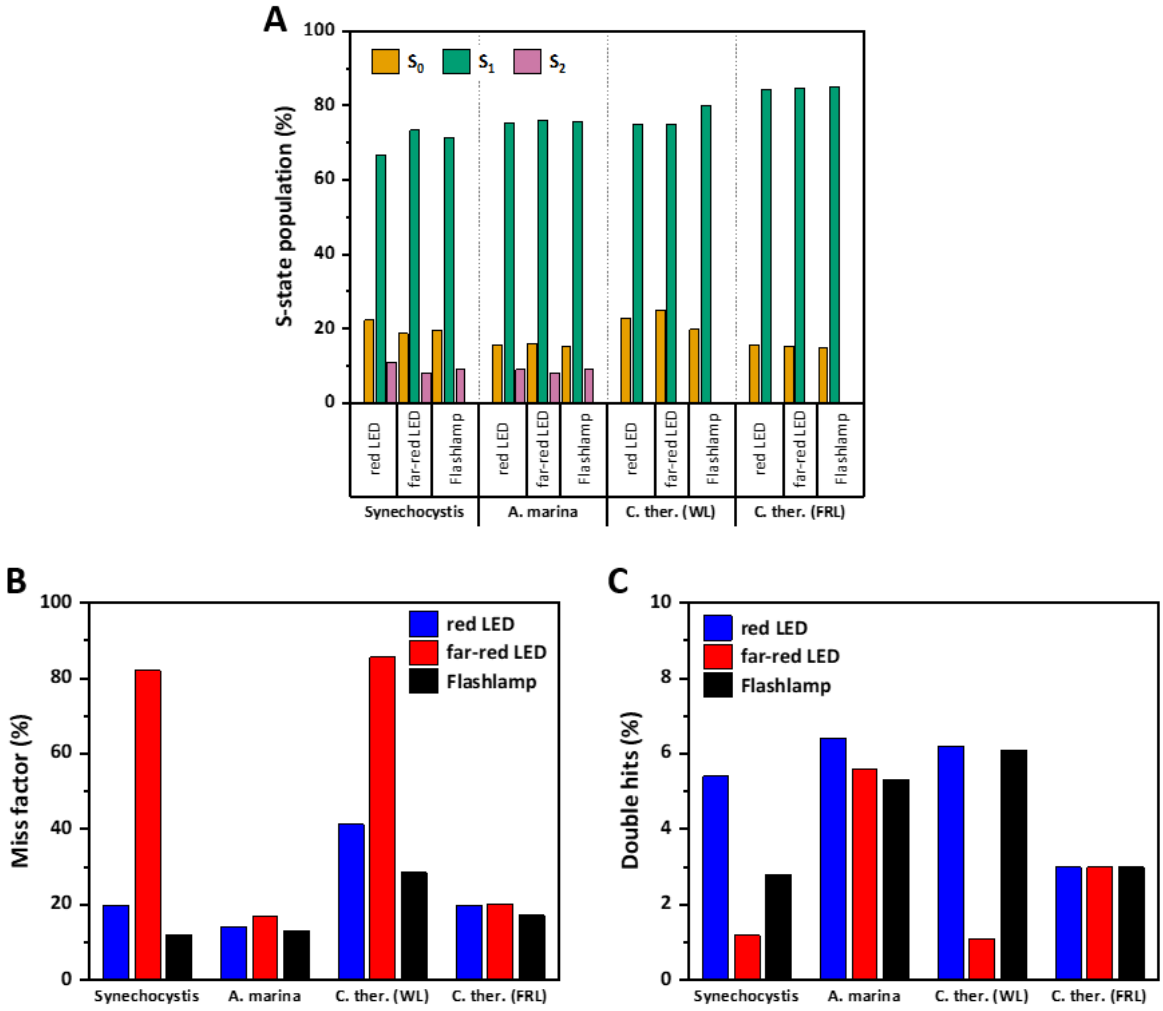

Figure 6.6 – Fit parameters for the flash-induced oxygen-evolution patterns (FIOPs) presented in Fig. 6.5. The initial S-state population are displayed in panel A, the obtained miss factor in panel B and the double hit parameter in panel C. The fits were performed according to the extended Kok cycle model (Kebekus et al., 1995).

6.2.3 Activation energy

As an attempt to comprehend the slow-down in oxygen release in membranes from far-red light (FRL) adapted *C. thermalis* when compared to the ones grown in white light (WL), O_2 release kinetics were measured the same way, this time for different temperatures, aiming at the determination of the thermal activation energy for the two main reaction phases of the S_3-S_0 transition in membranes grown in both conditions. The temperature series had the range 0-45 °C for the FRL membranes and 0-35 °C for the WL membranes, as the WL membranes lost activity at higher temperatures. This effect can be seen in the data presented in Appendix D.2 where the transients at 45 °C and

35°C for the FRL and WL grown, respectively, lost already quite some amplitude. The obtained O_2 transients are presented normalized in Fig. 6.7, and the non-normalized data can also be seen in Appendix D.2. In Fig. 6.7, the gradual speed-up of the reaction with the rise of the temperature can be seen clearly for both samples. At 20 °C the data was very reproducible to what had been measured for the experiment presented earlier in this chapter (Fig. 6.3 A and C). Here the same diffusion model to fit the data and extract the respective time constants was used and the other outcoming fit parameters are displayed in Appendix E.2. For further determination of the thermodynamic parameters, we used the Arrhenius treatment by plotting the time constants (τ) as a function of $1/K_BT$ and by means of a linear fit we quantified the activation energy E_a from the slope and the frequency factor A from the intersection with the Y axis. The respective Arrhenius plot for the τ_{ox} can be seen in Fig. 6.8 alongside the Arrhenius plot for the τ_{pre}. The τ_{pre} time constant was determined simultaneously in the same fit and represents the rate of the initially called lag phase of the O_2 evolution, as it was shown that the O_2 evolution was not immediate after the flash excitation (Bao & Burnap, 2015; Haumann, Liebisch, et al., 2005). This phase preceding the electron transfer in the S_3-S_0 transition comprises mainly of a proton release from one of the bound waters in the OEC and some subsequent structural rearrangements (Gerencser & Dau, 2010; Kern et al., 2018). In Fig. 6.8 A, the slow-down of the τ_{ox} observed is evident just like it was seen before for the FRL membranes, although the slow-down is not constant for the whole temperature range. At 0 °C the reaction slowed down about 9 times when compared to the WL membranes, whereas at 35 °C the comparative slowdown was closer to a factor of 4. This resulted in a change in activation energy, from 307 ± 13 meV in the WL membranes to 460 ± 10 meV in the FRL membranes. Furthermore, in Fig. 6.8 B, the slow-down for the τ_{pre}, of about 30%, was much more modest. For this reaction, activation energies of 418 ± 10 meV for the WL membranes and 297 ± 30 meV for the FRL membranes were determined. From the E_a and the pre-exponential factor A, which was also determined with the Arrhenius plots, the activation enthalpy, $\Delta H^{\ddagger}$, and activation entropy, $\Delta S^{\ddagger}$, for the O_2-evolution reaction were determined according to the Eyring's transition state theory (Mortimer & Eyring, 1980), using Eq. 6.1 and Eq. 6.2, respectively.

$$\Delta H^{\ddagger} = E_a - k_B T_0 \qquad \textbf{(Eq. 6.1)}$$

$$\Delta S^{\ddagger} = k_B \ln(hA/k_BT) - k_B \qquad \textbf{(Eq. 6.2)}$$

In the above equations, k_B is the Boltzmann constant, h is the Planck constant, T refers to the absolute temperature in Kelvin, and T_0 is the average temperature of the investigated temperature range (here 20 °C).

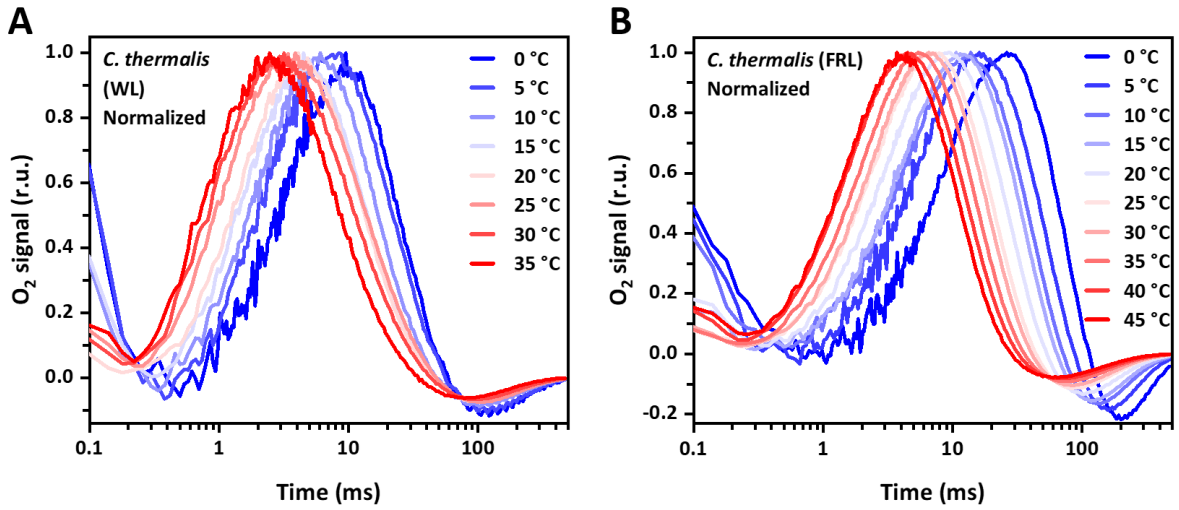

Figure 6.7 – O_2-evolution transients obtained at various temperatures for thylakoid membranes from *C. thermalis* membranes grown in WL (A) and FRL (B). The temperature range was 0-35 °C for the WL membranes and 0-45 °C for FRL ones. All of them were measured with time resolved O_2 polarography using the red LED for excitation. The kinetics are the average of 230 individual transients measured after each flash, averaged from three independent experiments on each condition. The parameters obtained from the fit made to the experimental curves are shown in Appendix E.2.

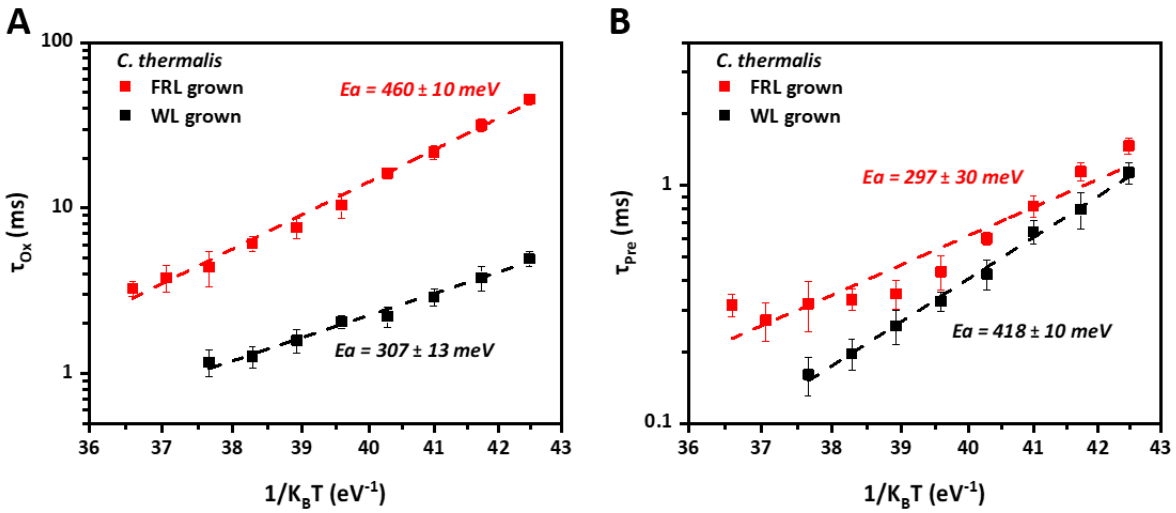

Figure 6.8 – Arrhenius plots for the time constants of the reactions involved in the S_3-S_0 transition of Photosystem II. On the left plot (A) the O_2 evolution time constant τ_{ox} can be seen. On the right (B), the time constant for the preceding reaction τ_{pre} is shown. The time constants were obtained by fitting the data presented in Fig. 6.7.

The obtained values for $\Delta H^{\ddagger}$ were 282 ± 12 meV for the WL *C. thermalis* membranes and 435 ± 10 meV for the FRL ones. For the entropic component, $-T\Delta S^{\ddagger}$, the values obtained were 305 ± 14 meV for the WL membranes and 197 ± 5 meV for the FRL sample. Here a hint of an enthalpy-entropy compensation can be seen as the higher $\Delta H^{\ddagger}$ in the FRL membranes is paired with a lower entropic component. Generally, such compensations maintain the overall $\Delta G^{\ddagger}$ of a reaction constant, although this compensation was not complete, meaning that the $\Delta G^{\ddagger}$ values obtained for the O_2-evolution reaction were not the same for both samples. In WL membranes the ΔG was 587 ± 31 meV which matched well the general ΔG range so far determined for various photosynthetic organisms (580-600 meV) (Liang, 2018). The same did not occur for the FRL membranes that had a bigger $\Delta G^{\ddagger}$ of 632 ± 10 meV, which was significantly outside of that range.

The same way these parameters were determined for *C. thermalis* thylakoid membranes, they were also determined for membranes from different photosynthetic species including *Spinacia oleracea* (Spinach) and S*ynechocystis* sp. PCC 6803, which were measured in the scope of the work presented in Chapters 3 and 5, respectively, and *Thermosynechococcus elongatus*, measured to provide experimental confirmation of the outcome of the theoretical simulations (manuscript submitted). In addition, thylakoid membranes from the thermophilic cyanobacterium *Mastigocladus laminosus* and the cryogenic green alga *Chlamydomonas nivalis* were measured to expand on the initial work of Dr. Zhiyong Liang (Liang, 2018) and the following work of Anna Lena Schäfer (Schäfer, 2018) where a linear compensatory relationship between the enthalpy ($\Delta H^{\ddagger}$) and entropy ($-T\Delta S^{\ddagger}$) of the O_2 evolution step was found for different photosynthetic species meaning that the final $\Delta G^{\ddagger}$ for the reaction was constant. In their work a relation between the extent of the compensation and the temperature range of the respective natural habitat of the organism was suggested, meaning that in hotter environments the $\Delta H^{\ddagger}$ for the O_2 evolution step would be higher and the $-T\Delta S^{\ddagger}$ would be lower, whereas the opposite would be true for the organisms from colder environments. Aiming to achieve a better understanding of this phenomenon, here the data for the species referred to will be presented in Fig. 6.9 (for the data on Spinach and S*ynechocystis* sp. PCC 6803 see chapters 3 and 5 respectively). All the samples were

measured as described for *C. thermalis* in this chapter. Further determined thermodynamic parameters are presented in Table 6.1.

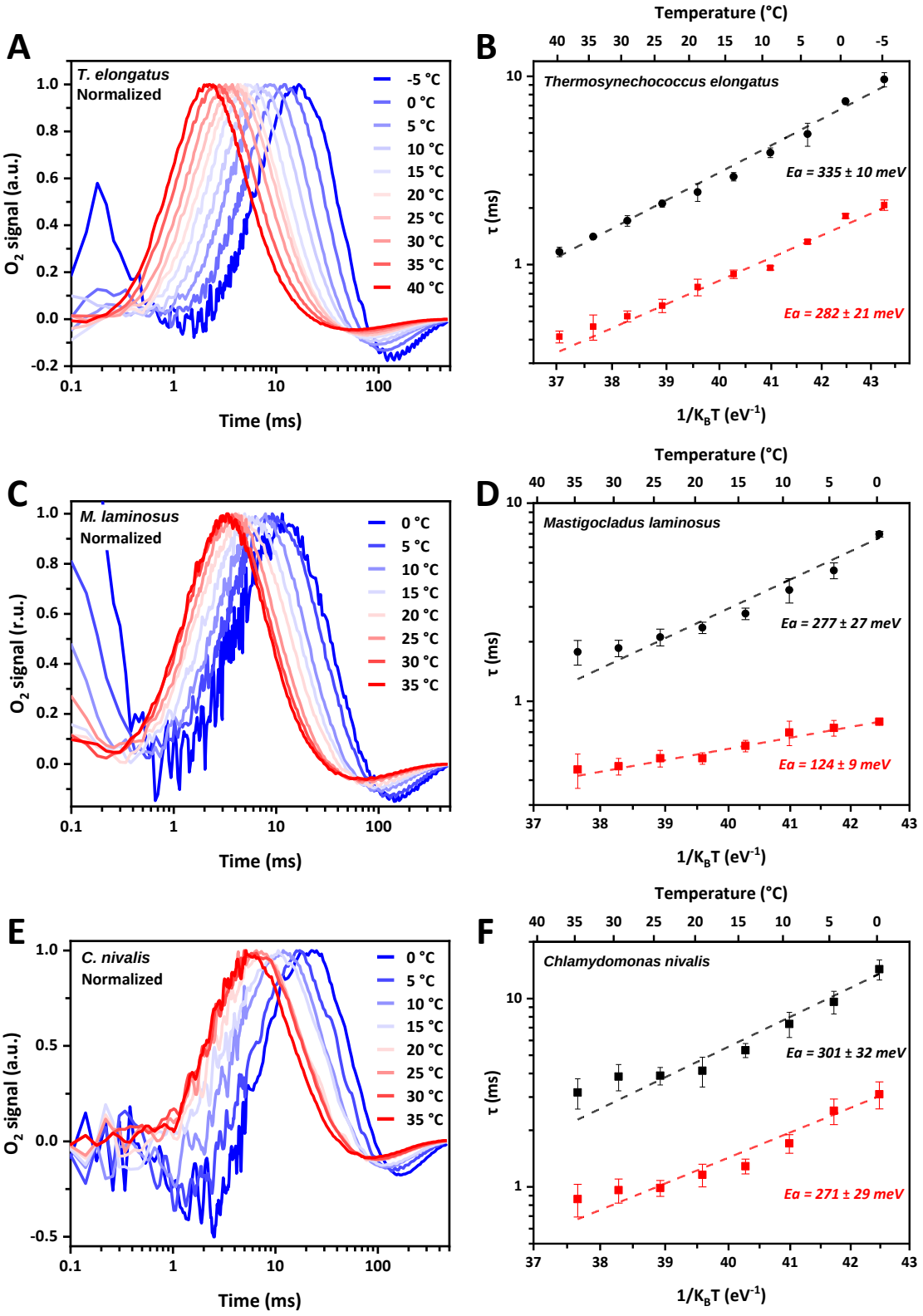

Figure 6.9 – On the left, O_2-evolution transients obtained at various temperatures for thylakoid membranes from *T. elongatus (A*), *M. laminosus* (C) and *C. nivalis (E)*. The temperature range was -5-40 °C for *T. elongatus* and 0-35°C for the other two. The measurements were performed using the red LED from the time resolved O_2 polarography set-up. The kinetics are the average of 230 individual transients measured after each flash, summed up from three independent experiments on each condition. The non-normalized data can be seen on Appendix D.1 and the parameters obtained by fitting the data can be seen on Appendix E.3. On the right (B, D, F), it is displayed the respective Arrhenius plots for the time constants of the reactions involved in the S_3-S_0 transition of Photosystem II. In black for the O_2 evolution time constant τ_{ox} and in red for the time constant for the preceding reaction τ_{pre}.

Table 6.1 – Kinetic and thermodynamic parameters for the oxygen evolution reaction in thylakoid membranes from different organisms. The activation energy (Ea) and the frequency parameter (A) were determined from the respective Arrhenius plots, from which the formation enthalpy ($\Delta H^{\ddagger}$) and entropic component ($-T\Delta S^{\ddagger}$) were respectively calculated using equations 6.1 and 6.2. When needed, a midrange temperature of 20 °C was used in the calculations.

Organism	τ_{Ox} at 20 °C (ms)	A (s^{-1})	E_a (meV)	$\Delta H^{\ddagger}$ (meV)	$-T\Delta S^{\ddagger}$ (meV)	$\Delta G^{\ddagger}$ (meV)
Spinacia oleracea (Spinach)	1.71	7.6×10^6	241 ± 10	216 ± 9	369 ± 14	585 ± 17
Synechocystis sp. PCC 6803	1.72	9.8×10^9	421 ± 22	396 ± 21	188 ± 11	584 ± 23
Chroococcidiopsis thermalis (WL grown)	2.1	9.5×10^7	307 ± 13	282 ± 12	305 ± 14	587 ± 19
Chroococcidiopsis thermalis (FRL grown)	10.4	6.9×10^9	460 ± 10	435 ± 10	197 ± 5	632 ± 11
Thermosynechococcus elongatus	2.43	2.2×10^8	335 ± 10	310 ± 9	284 ± 9	593 ± 13
Mastigocladus laminosus	2.35	2.2×10^7	277 ± 27	251 ± 25	342 ± 37	593 ± 44
Chlamydomonas nivalis	4.14	3.0×10^7	301 ± 32	276 ± 30	334 ± 42	610 ± 52

6.3 Discussion

The first experiment aimed at understanding the relation between the light excitation wavelength and both the rate of the O_2 release step in the catalytic cycle of PSII and its cycling ability. For this time-resolved oxygen polarography was used which can in an

almost direct way measure the O_2 release kinetics of PSII. Also, in our custom-made experimental step-up, three possible excitation light conditions were available, the standard xenon flashlamp and the LED flasher with a red LED and a far-red LED that was developed for the purpose of this experiment and other future O_2 polarography experiments involving different light excitations. In this way O_2 evolution transients at 20 °C from thylakoid membranes were measured from three cyanobacterial species: S*ynechocystis* sp. PCC 6803, *A. marina* and *C. thermalis*, the latter having two distinct samples as it was grown in WL and FRL conditions. The collected data is presented in Fig. 6.2, where changes in the amplitude of the transient signals were immediately visible. For the *C. thermalis* (WL) and S*ynechocystis* sp. PCC 6803 samples (Fig 6.2 A and B), the most relevant effect from changing the excitation pulse was the great decrease in the max signal amplitude of about 70% when flashing with the far-red LED versus the red LED, both with a very similar energy per flash. This shows that these samples have no mechanism to enable them to use far-red light and barely can achieve water oxidation by just relying on a spectral tail overlap between the absorption spectrum of Chl *a* and the far-red LED's emission. This justifies the small signal observed but still allows for the analysis of the reaction's kinetics in this condition. The systems with red-shifted Chls could produce oxygen well with the three light excitations tested, showing that both *C. thermalis* (FRL grown) and *A. marina*, could harvest light better under far-red light conditions than *C. thermalis* (WL) and S*ynechocystis* sp. PCC 6803. Specifically for *C. thermalis* (FRL grown) a higher amplitude in the oxygen signal was observed when the far-red LED was used (Fig. 6.2 C). Further confirmation of these last two points could be achieved by analysing the respective FIOPs shown in Fig. 6.5. Here the flash patterns consolidated the idea that both far-red shifted PSIIs, from *C. thermalis* (FRL grown) and *A. marina* could use the far-red light as well as the other light excitations without significant changes in the miss factor (Fig. 6.6 B), meaning that these samples proceed with the water oxidation reaction the same way they do when using the other two light sources. On the other hand, a very high miss factor can be observed, as expected by now, in the FIOPs of *C. thermalis* (WL) and S*ynechocystis* sp. PCC 6803 shown in Fig. 6.5 A-B and quantified by our fit approach (Fig. 6.6 B), when the far-red LED was employed.

The period of four oscillation characteristic of the S-state cycle can be observed in the FIOPs of active PSII, previously dark-adapted and suspended in a suitable buffer (like buffer D-NaCl), when excited with saturating light pulses (Schuth et al., 2017). When testing PSII samples with different absorption ranges, some light excitations like the far-red LED fall outside the absorption range of some samples, such as *C. thermalis* (WL) and S*ynechocystis* sp. PCC 6803 (Fig. 6.5 A-B). This does not necessarily mean that the >80% miss factor determined by the fit (Fig. 6.6 B) for these two cases is a result of higher recombination of the excited states, but it rather comes from the poor ability to gather far-red light, which in turn makes the LED light pulse sub-saturating. In non-far-red adapted PSII the O_2 evolution rate was never reported to be dependent on the excitation wavelength and the same was observed here for S*ynechocystis* sp. PCC 6803 and *C. thermalis* (WL grown) as seen in Fig. 6.3 A-B and Fig 6.4 A. This is of course only true for the wavelengths that match the specific PSII's light harvesting absorption range and are not too energetic to cause photodamage. Whether there would be changes in the reaction's rate due to the excitation by far-red light, for the case of PSII samples containing red-shifted Chls, like *C. thermalis* (FRL grown) and *A. marina*, is of core importance to the understanding of this red-shifted water oxidation reaction. Comparing the kinetic data (Fig. 6.3 C-D) we could demonstrate that the incident wavelength had no influence over the rate of the reaction for both red-shifted samples, which we also observed in the other samples. Fitting the referred data with the diffusion model (Dilbeck et al., 2012) could further support this conclusion by determining O_2 evolution time constants (τ_{ox}) for the different light excitations that were statistically equal (Fig. 6.4 A). This supports the hypothesis that the photochemistry in the reaction center of PSII doesn't change depending on the excitation wavelength, meaning that for *C. thermalis* the FaRLiP process doesn't create an alternative reaction pathway but rather changes or replaces part of the original one. Although seemingly trivial, this point will be important for further discussion of the O_2 evolution reaction in red-shifted PSII.

The 1.6 ms (at 20 °C) value for τ_{ox} obtained for S*ynechocystis* sp. PCC 6803 (Fig. 6.4 A) is in good agreement with the results from previous measurements on the same organism (Dilbeck et al., 2012) and the 2.2 ms (at 20 °C) value obtained for the first time for *C. thermalis* (WL grown) matched well the general range for τ_{ox} at 20 °C, which can be as

fast as 1.2 ms for *Synechococcus* sp. PCC 7002 but often not slower than 3 ms (Liang, 2018). However, it can be as slow as 4.1 ms in organisms like *C. nivalis* (Table 6.1), which should not be taken as a rule since this *alga* is native to very cold environments, like polar regions and may have intrinsic adaptations to allow for its life in those hash conditions (Lukeš et al., 2014). Along this slow side, a similarly slow O_2 evolution time constant of 4.6 ms was obtained for *A. marina* (Fig 6.4 A). This slow O_2 evolution kinetic may result from a unique adaptation of this *cyanobacterium.* Generally, Chl *a* in organisms that do oxygenic photosynthesis is considered a main pigment generally appearing as a great majority of total Chl, if not 100% as is true for many cyanobacteria. Chl *a* is often complemented by accessory Chls that appear as a minority like Chl *b* in the case of plants and some cyanobateria, Chl *c* in chromophyte *algae* from marine environments (Zapata et al., 2006) and Chl *d* and *f* appearing in cyanobateria that have undergone FaRLiP like *Synechococcus* sp. PCC 7335 and *C. thermalis* used also in this work (Ho et al., 2020; Nürnberg et al., 2018). This makes *A. marina* special as it has this the other way around, with a majority of Chl *d* and a minority of Chl *a* (1-2 molecules per PSII) (Miyashita et al., 2014), which occurs even when the strain is grown under WL, meaning that this Chl content is not due to a photoacclimation process (Miyashita et al., 1997). The type of Chls present in *A. marina*'s reaction center (Chls P_{D1} and P_{D2}) is still being discussed but it is either with two Chl *d* molecules or one Chl *d* and one Chl *a*, although the Chl_{D1} and Chl_{D2} positions should be both occupied by Chl *d* molecules (Miyashita et al., 2014). Either way, such changes in the reaction center's Chl content, where the primary charge separation occurs, may be enough to justify a larger O_2 evolution time constant. However, further investigation into the specific details of why the rection is slower in this organism will not be conducted here and we will now focus our investigations on the comparison between *C. thermalis* grown in WL and FRL. This allows for a direct characterization of effects related to changes in PSII relative to the FaRLiP adaptation, and the respective conclusions may also help us to understand what happens in the case of *A. marina*. Also, another reason that pushed for further investigation and comparison of the two distinct *C. thermalis* samples was the difference in the O_2 evolution time constant. From the 2.2 ms obtained for *C. thermalis* (WL grown), the reaction slowed down almost five times to 10.3 ms at 20 °C for the *C. thermalis* (FRL grown) membranes. Although the result was surprising at first, the continuous

improvement of the thylakoid membrane preparations that indeed increased the activity of the samples, did not result in changes in the kinetics. Four different preparations were in total tested for PSII activity, and the measurements were then performed with the samples with the highest activity, yielding the experimental data presented here.

Additional time resolved O_2 polarography measurements were performed for both *C. thermalis* samples, at different temperatures, in the ranges of 0-35 °C for the WL and 0-45 °C for FRL, to access their respective activation energy as described before (Fig. 6.7). Furthermore, the transients were fitted with a diffusion model (Dilbeck et al., 2012) and the respective time constants were used to make the respective Arrhenius plots (Ln τ vs $1/K_BT$), from where we extracted the activation energy and the frequency parameter A. The results for the oxygen evolution step using the obtained time constants τ_{Ox} were an activation energy of 307 ± 13 meV with the pre-exponential factor A of 9.5 x 10^7 ± 4 x 10^6 S^{-1} for WL membranes and for the FRL membranes the values obtained were 460 ± 10 meV and 6.8 x 10^9 ± 2 x 10^8 S^{-1}, respectively. For all points in the tested temperature range, the O_2 evolution reaction speed was highly slowed down for the FRL PSII like observed initially at 20 °C (Fig. 6.8). Like stated, this resulted in an increase in activation energy and frequency parameter A, which in turn reflects in a higher enthalpy ($\Delta H^{\ddagger}$), and lower entropic component ($-T\Delta S^{\ddagger}$). As previous work suggests (Liang, 2018), the O_2 evolution reaction in PSII from different species has an enthalpy-entropy compensation behaviour (Low & Somero, 1974), which was observed when Liang (2018) compared the thermodynamic parameters from different organisms, showing that when the reaction had a lower $\Delta H^{\ddagger}$, it would compensate with a higher $-T\Delta S^{\ddagger}$, and vice versa, keeping the overall $\Delta G^{\ddagger}$ constant at about 590 meV. This type of phenomenon was also studied for different enzymes before and was generally discussed to have a high correlation to an adaptation to native environmental temperature (Siddiqui & Cavicchioli, 2006; Somero, 2004). Furthermore, the type of environment, terrestrial versus aquatic, was also discussed in Liang (2018) as a possible shifting factor of the enthalpy-entropy compensation. In Fig. 6.10, a similar analysis of the thermodynamics of the O_2 evolution reaction in different photosynthetic species was performed, but we do not see any trend in the data that would favour a specific explanation for the lower or higher enthalpy (or

entropy) for each case. Perhaps, the enthalpy-entropy compensation in PSII is not dependent on a single factor.

To have a better chance at understanding the thermodynamic changes in the O_2 evolution reaction in PSII from *C. thermalis* due to the FaRLiP process, the Eyring's transition state theory was used to determine the reaction's $\Delta H^{\ddagger}$, and $-T\Delta S^{\ddagger}$ (Eq. 6.1 and Eq. 6.2) (Mortimer & Eyring, 1980). From the WL membranes to the FRL ones, the $\Delta H^{\ddagger}$ increased from 282 meV to 435 meV and the $-T\Delta S^{\ddagger}$ decreased from 305 meV to 197 meV. Although these are big changes, one could argue that an already seen before, enthalpy-entropy compensation, could explain it. However, that is not the case here, as the total $\Delta G^{\ddagger}$ was considerably higher for the FRL membranes, at 632 meV, when compared to the WL membranes that had a $\Delta G^{\ddagger}$ of 587 meV, consistent with previously determined values for various PSII samples from different species like spinach, *Synechocystis* sp. PCC 6803 and *Synechococcus* sp. PCC 7002, among others (Bao & Burnap, 2015; Liang, 2018). To further enhance this point, data from all different photosynthetic species that had their O_2 evolution activation energy measured the same way as *C. thermalis*, during this thesis work, were gathered in this chapter. These included data from spinach, which was presented in Chapter 3, *Synechocystis* sp. PCC 6803 that was presented in Chapter 5, and data from *T. elongatus*, *Mastigocladus laminosus* and *Chlamydomonas nivalis*, all presented in Fig. 6.9 in this chapter. A summary from all the measured and calculated parameters from all the seven samples (including both *C. thermalis* samples) is presented in Table 6.1. For spinach, *Synechocystis* sp. PCC 6803, and *Thermosynechococcus elongatus*, the activation energy and further calculated parameters confirm the results from previous studies (Bao & Burnap, 2015; Liang, 2018) and for *M. laminosus* and *C. nivalis*, whose activation energy was here determined for the first time, their calculated $\Delta G^{\ddagger}$ was 593 and 610 meV, respectively. For *M. laminosus* the new value matched well the average $\Delta G^{\ddagger}$ obtained for WT samples from different species measured here or in the studies just mentioned. The value for *C. nivalis* was still statistically within the range for $\Delta G^{\ddagger}$ observed so far but with a high uncertainty of ± 52 meV that originates from the lower oxygen signal and higher noise in the data we acquired (Fig. 6.9), which leaves open the possibility of this algae having a higher $\Delta G^{\ddagger}$ than most PSII. As *C. nivalis* is native from very cold environments, a special adaptation

that affects the O_2 evolution reaction and could also justify the slow τ_{Ox} time constant at 20° C of 4.14 ms, is not so unreasonable to suggest (Lukeš et al., 2014).

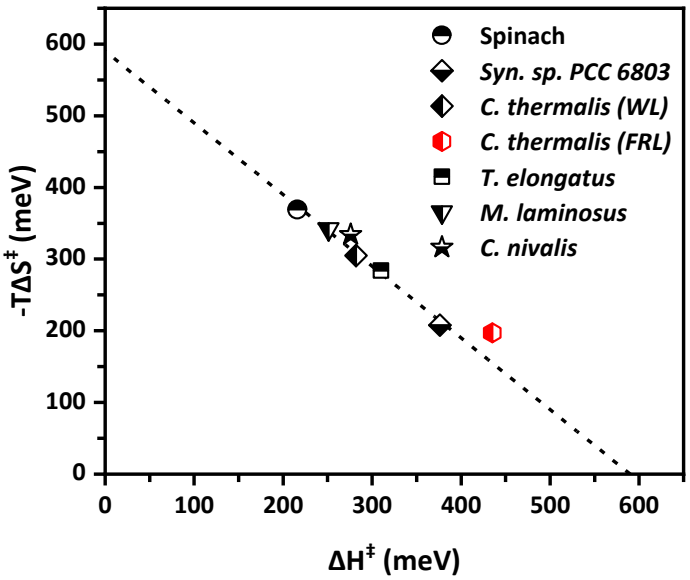

Figure 6.10 – Comparison of the thermodynamic contribution from the parameters $\Delta H^{\ddagger}$ and $-T\Delta S^{\ddagger}$ to the $\Delta G^{\ddagger}$ of the oxygen evolution reaction in PSII. The data presented was measured from seven different thylakoid membranes samples (BBY in the case spinach) from six distinct organisms. Plotted values are shown in Table 6.1 and the dotted line represents a $\Delta G^{\ddagger}$ of 590 meV.

By potting the determined $-T\Delta S^{\ddagger}$ as a function of $\Delta H^{\ddagger}$ for each of the seven samples, one can easily visualize that six of those data points sit on a $\Delta G^{\ddagger}$ isoenergetic line ($\Delta G^{\ddagger} = 590$ meV) that shows the enthalpy-entropy compensation behaviour (Fig. 6.10), as seen before (Liang, 2018). One of the samples, *C. thermalis* (FRL grown) has a higher $\Delta G^{\ddagger}$ of 632 meV and can be seen deviating from this isoenergetic line. This is a significant change and previously such changes in $\Delta G^{\ddagger}$ were only observed for lab-modified PSII like the Sr-Ca exchanged PSII from *T. elongatus* which had a $\Delta G^{\ddagger}$ of 619 meV (Kim & Debus, 2019; Rappaport et al., 2011), and the *Synechocystis* sp. PCC 6803 PsbA mutants: V185N, D61N and D61A, having all three essentially the same a $\Delta G^{\ddagger}$ of 669 meV (Bao & Burnap, 2015). As significant changes had been done to these four modified PSII examples near the reaction center we would also suspect a significant change to be present in the *C. thermalis* (FRL grown) when compared to the WL grown. As studied before by Nürnberg et al. (2018), it is very likely that the FaRLiP process in *C. thermalis* involves the inclusion of a Chl *f* in the recation center made by the four Chl positions, P_{D1}, P_{D2}, Chl_{D1}, Chl_{D2} (Fig.

6.11). The replacement of the Chl *a* for the Chl *f* most likely occurs at the position Chl_{D1} as suggested by Nürnberg et al. (2018) who looked at amino acid changes occurring around the Chl_{D1} position to find new replacements that would help to accommodate for a Chl *f* molecule, like the F119Y and A154T that are featured in Fig. 6.11. Specifically, the OH-group of this Tyrosine can hydrogen bond with the formyl-O from a Chl *f*. We also looked for changes closer to the Mn-cluster and we found two amino acid replacements worth considering, the L184F and the S85M. The first essentially occupies more space than the Leucine in the WL version and is prone to π-stacking. In the latter,

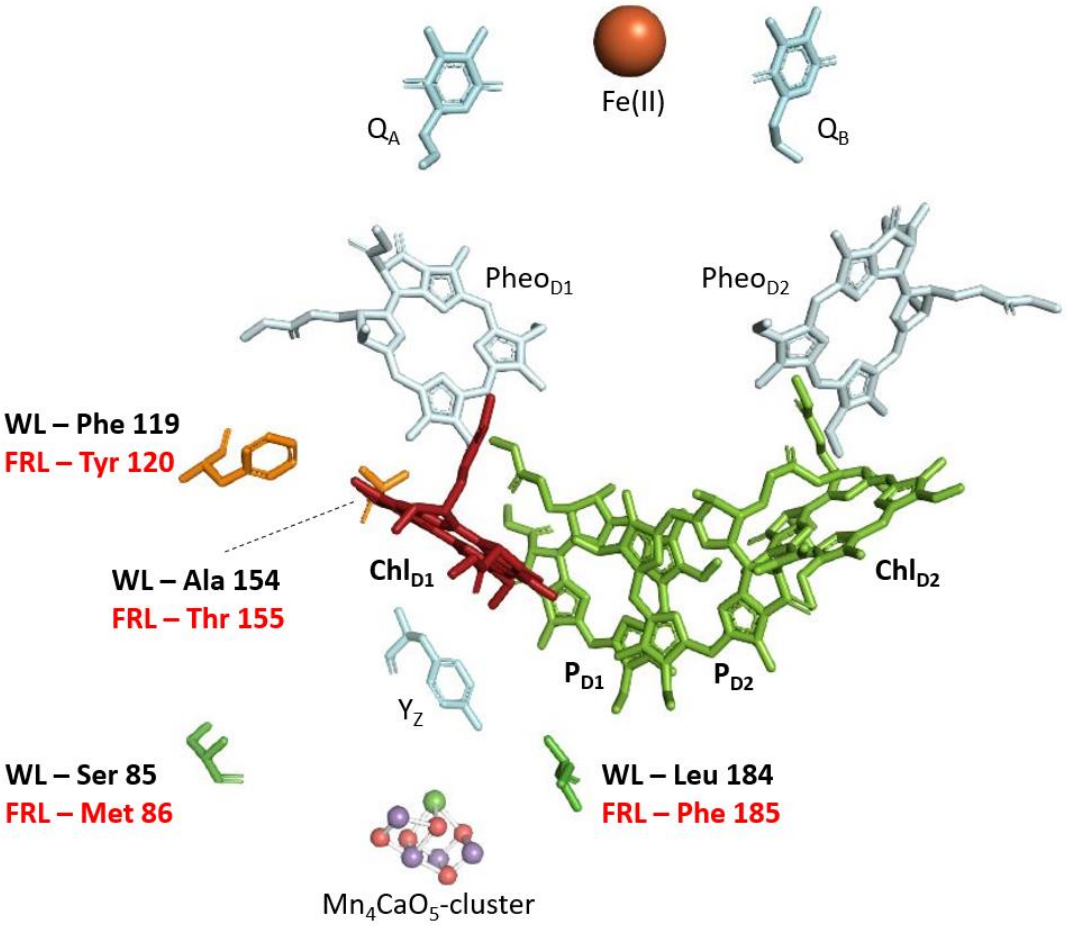

Figure 6.11 – PSII reaction center based on the structure 3WU2 from *Thermosynechococcus vulcanus* (Umena et al., 2011). The most important cofactors are shown: the Mn_4CaO_5-Cluster, the chlorophyll complex P680 (P_{D1} and P_{D2}) and the other two adjacent chlorophylls Chl_{D1} and Chl_{D2}; both pheophytins (Phe_{D1} and Phe_{D2}), the quinones A and B (Q_A and Q_B, respectively), and the non-heme Iron(II). The redox active tyrosine (Y_Z) is present along with four amino acids: Ser 85, Phe 119, Ala 154, and Leu 184, all of which are present in *C. thermalis* but are replaced by other amino acids when undergoing FaRLiP process. The Chl *a* in position Chl_{D1} is shown with a dark red colour to highlight its highly likely replacement by a Chl *f* in *C. thermalis* (FRL grown) as suggested in Nürnberg et al. (2018).

methionine replaces a serine that is a neighbour to Serine 169 which is an important residue in the H-bonding network around OEC (Ghosh, Banerjee, et al., 2019), and even though they do not hydrogen bond between themselves, they both share a water molecule as a hydrogen bond partner. The change to methionine may not leave much space for this water molecule to exist there and so this change may have an effect on Serine 169. Nonetheless, we believe that these changes alone would not justify the scale of this slow-down and increase in $\Delta G^{\ddagger}$ and so the replacement of Chl_{D1} for a Chl *f* may have the greater contribution.

Summary

The aim of this work was to gain a better understanding of the water oxidation reaction by PSII. Different samples from various photosynthetic species were tested either by time resolved O_2 polarography or X-ray absorption spectroscopy targeting several open questions regarding the function of this enzyme mostly during the $S_3 \rightarrow S_0$ transition.

In chapter 3, the investigation of the effect of ammonia, a substrate water analogue, on the catalytic cycle of PSII was presented. From the results obtained by time resolved O_2 polarography it was possible to confirm a degree of full inhibition of the O_2 evolution which affected up to about 50% of the PSII centers. Furthermore, in the presence of ammonia, two O_2 evolving PSII fractions were identified, one with unaltered kinetics and another with significantly slower O_2 evolution (~20 times). These two fractions showed different activation energies which were independent of the ammonia concentration. This way, three binding spots directly to or in the vicinity of the OEC were suggested, one of which may unbind before the O_2 release, and another which might be one of the substrate water molecules.

The following chapter 4 shows an EXAFS study on dark adapted PSII that could show a clear breakpoint in the temperature dependence of the Debye-Waller factor at around 200 K. This suggests that ET in all S-state transitions does not just rely on harmonic vibrations but is instead facilitated by mobility and molecular reorganizations in the protein/water environment that affect the dynamics of the OEC. This could explain the much slower than theoretically predicted τ-value for the OEC $\rightarrow Y_Z^{\bullet+}$ ET, even for the simplest $S_1 \rightarrow S_2$ transition, and why the further S-state transitions are frozen out bellow 200 K.

In chapter 5, an extensive study on various point mutations of H-bonding active amino acids close to the OEC was performed. For this, time-resolved O_2 polarography which targets the $S_3 \rightarrow S_0$, transition was used. The results suggest that the E65 might be involved in the proton transfer away from the OEC most likely receiving this proton from D61. Although E312 forms a dyad with E65, we only observed a small effect for the

alanine substitution, suggesting that the E312 might not be directly involved in the main proton pathway. For the D59A, a high activation energy was obtained even though the O_2 evolution kinetics were mostly slower at lower temperatures. This could be explained either by the H-bond interaction between D59 and the backbone of E65 or by direct involvement in the H-transfer pathway, at least at lower temperatures. The similar results obtained for both the E329A and N298A variants, that make up part of the large channel, led to the hypothesis that this channel may not be used as a proton pathway during the $S_3 \rightarrow S_0$ transition. In summary, this chapter's results are in line with the idea that the proton transfer right before O_2 formation happens mostly through the broad channel.

Lastly in chapter 6, PSII with far-red shifted Chls was studied by using time-resolved O_2 polarography, employing different light excitations. This way, slow O_2 evolution kinetics could be observed for *A. marina* and FRL grown *C. thermalis,* both containing far-red shifted Chls. Although it should be noted that higher photon absorption efficiency was seen for these photosystems when illuminated by far-red light. In the last part of chapter 6, gathered data from different species was used to compare their overall $\Delta G^{\ddagger}$ and respective enthalpic and entropic components for the O_2 evolution reaction. The distribution of $\Delta H^{\ddagger}$ and $-T\Delta S^{\ddagger}$ did not show a specific trend. However, like observed for PSII from other species, the $\Delta G^{\ddagger}$ results for the species studied here were very similar except for FRL grown *C. thermalis*, which had a significantly higher value. This last point supports that in *C. thermalis*, during FaRLiP a red-shifted Chl replaces one of the four Chls in the reaction center of PSII, lowering the energy of the chlorophyll radical that serves as the primary oxidant in PSII water oxidation.

References

Abrashev, M. V., Chernev, P., Kubella, P., Mohammadi, M. R., Pasquini, C., Dau, H., & Zaharieva, I. (2019). Origin of the heat-induced improvement of catalytic activity and stability of MnOx electrocatalysts for water oxidation. *Journal of Materials Chemistry A*, *7*(28), 17022-17036.

Akutsu, S., Fujinuma, D., Furukawa, H., Watanabe, T., Ohnishi-Kameyama, M., Ono, H., Ohkubo, S., Miyashita, H., & Kobayashi, M. (2011). Pigment analysis of a chlorophyll f-containing cyanobacterium strain KC1 isolated from Lake Biwa. *Photomed. Photobiol*, *33*, 35-40.

Anderson, J. M., Horton, P., Kim, E.-H., & Chow, W. S. (2012). Towards elucidation of dynamic structural changes of plant thylakoid architecture. *Philosophical Transactions of the Royal Society B: Biological Sciences*, *367*(1608), 3515-3524.

Åqvist, J., Kazemi, M., Isaksen, G. V., & Brandsdal, B. O. (2017). Entropy and enzyme catalysis. *Accounts of chemical research*, *50*(2), 199-207.

Askerka, M., Brudvig, G. W., & Batista, V. S. (2017). The O_2-evolving complex of photosystem II: Recent insights from quantum mechanics/molecular mechanics (QM/MM), extended X-ray absorption fine structure (EXAFS), and femtosecond X-ray crystallography data. *Accounts of chemical research*, *50*(1), 41-48.

Assunção, R., Zaharieva, I., & Dau, H. (2019). Ammonia as a substrate-water analogue in photosynthetic water oxidation: Influence on activation barrier of the O-2-formation step. *Biochimica et Biophysica Acta*, *1860*(7), 533-540.

Bao, H., & Burnap, R. L. (2015). Structural rearrangements preceding dioxygen formation by the water oxidation complex of photosystem II. *Proceedings of the National Academy of Sciences of the United States of America*, *112*(45), E6139-E6147.

Barber, J. (2002). Photosystem II: a multisubunit membrane protein that oxidises water. *Current opinion in structural biology*, *12*(4), 523-530.

Ben-Shem, A., Frolow, F., & Nelson, N. (2003). Crystal structure of plant photosystem I. *Nature*, *426*(630-635).

Bennoun, P., & Joliot, A. (1969). Etude de la photooxydation de l'hydroxylamine par les chloroplastes d'epinards. *Biochimica et Biophysica Acta (BBA)-Bioenergetics*, *189*(1), 85-94.

Berthold, D. A., Babcock, G. T., & Yocum, C. F. (1981). A Highly Resolved, Oxygen-Evolving Photosystem-II Preparation from Spinach Thylakoid Membranes - Electron-Paramagnetic-Res and Electron-Transport Properties. *FEBS letters*, *134*(2), 231-234.

Blankenship, R. E. (2021). *Molecular Mechanisms of Photosynthesis*. John Wiley & Sons.

Bondar, A. N., & Dau, H. (2012). Extended protein/water H-bond networks in photosynthetic water oxidation. *Biochim Biophys Acta*, *1817*, 1177-1190.

Boussac, A., & Rutherford, A. W. (2000). Comparative study of the g= 4.1 EPR signals in the S2 state of photosystem II. *Biochimica et Biophysica Acta (BBA)-Bioenergetics*, *1457*(3), 145-156.

Boussac, A., Rutherford, A. W., & Styring, S. (1990). Interaction of ammonia with the water splitting enzyme of photosystem II. *Biochemistry*, *29*(1), 24-32.

Boussac, A., Ugur, I., Marion, A., Sugiura, M., Kaila, V. R., & Rutherford, A. W. (2018). The low spin-high spin equilibrium in the S_2-state of the water oxidizing enzyme. *Biochimica Et Biophysica Acta-Bioenergetics*, *1859*(5), 342-356.

Bradford, M. M. (1976). A rapid and sensitive method for the quantitation of microgram quantities of protein utilizing the principle of protein-dye binding. *Analytical biochemistry*, *72*(1-2), 248-254.

Brudvig, G. W., Casey, J. L., & Sauer, K. (1983). The effect of temperature on the formation and decay of the multiline EPR signal species associated with photosynthetic oxygen evolution. *Biochimica et Biophysica Acta (BBA)-Bioenergetics*, *723*(3), 366-371.

Buchta, J., Grabolle, M., & Dau, H. (2007). Photosynthetic dioxygen formation studied by time-resolved delayed fluorescence measurements--method, rationale, and results on the activation energy of dioxygen formation. *Biochimica et Biophysica Acta*, *1767*, 565-574.

Burnap, R., Koike, H., Sotiropoulou, G., Sherman, L., & Inoue, Y. (1989). Oxygen evolving membranes and particles from the transformable cyanobacterium Synechocystis sp. PCC6803. *Photosynthesis research*, *22*(2), 123-130.

Cai, X., Haider, K., Lu, J., Radic, S., Son, C. Y., Cui, Q., & Gunner, M. (2018). Network analysis of a proposed exit pathway for protons to the P-side of cytochrome c oxidase. *Biochimica et Biophysica Acta (BBA)-Bioenergetics*, *1859*(10), 997-1005.

Casey, J. L., & Sauer, K. (1984). EPR detection of a cryogenically photogenerated intermediate in photosynthetic oxygen evolution. *Biochimica et Biophysica Acta (BBA)-Bioenergetics*, *767*(1), 21-28.

Chatterjee, R., Lassalle, L., Gul, S., Fuller, F. D., Young, I. D., Ibrahim, M., de Lichtenberg, C., Cheah, M. H., Zouni, A., & Messinger, J. (2019). Structural isomers of the S2 state in photosystem II: do they exist at room temperature and are they important for function? *Physiologia plantarum*, *166*(1), 60-72.

Chen, M., & Blankenship, R. E. (2011). Expanding the solar spectrum used by photosynthesis. *Trends in plant science*, *16*(8), 427-431.

Chen, M., Schliep, M., Willows, R. D., Cai, Z.-L., Neilan, B. A., & Scheer, H. (2010). A red-shifted chlorophyll. *Science*, *329*(5997), 1318-1319.

Cherepanov, D. A., Shelaev, I. V., Gostev, F. E., Aybush, A. V., Mamedov, M. D., Shen, G., Nadtochenko, V. A., Bryant, D. A., Semenov, A. Y., & Golbeck, J. H. (2020). Evidence that chlorophyll f functions solely as an antenna pigment in far-red-light photosystem I from Fischerella thermalis PCC 7521. *Biochimica et Biophysica Acta (BBA)-Bioenergetics*, *1861*(5-6), 148184.

Chernev, P., Fischer, S., Hoffmann, J., Oliver, N., Assunção, R., Yu, B., Burnap, R. L., Zaharieva, I., Nurnberg, D. J., Haumann, M., & Dau, H. (2020). Light-driven formation of manganese oxide by today's photosystem II supports evolutionarily ancient manganese-oxidizing photosynthesis. *Nature communications*, *11*(1).

Christen, G., Reifarth, F., & Renger, G. (1998). On the origin of the `35-µs kinetics' of P680+· reduction in photosystem II with an intact water oxidising complex. *FEBS letters*, *429*(1), 49-52.

Chu, H.-A., Nguyen, A. P., & Debus, R. J. (1994). Site-directed photosystem II mutants with perturbed oxygen-evolving properties. 1. Instability or inefficient assembly of the manganese cluster in vivo. *Biochemistry*, *33*(20), 6137-6149.

Clark, L. C., Wolf, R., Granger, D., & Taylor, Z. (1953). Continuous recording of blood oxygen tensions by polarography. *Journal of applied physiology*, *6*(3), 189-193.

Clausen, J., Debus, R. J., & Junge, W. (2004). Time-resolved oxygen production by PSII: Chasing chemical intermediates. *Biochimica et Biophysica Acta*, *1655*(1-3), 184-194.

Cox, N., & Messinger, J. (2013). Reflections on substrate water and dioxygen formation. *Biochim Biophys Acta*, *1827*(8-9), 1020-1030.

Cox, N., Pantazis, D. A., & Lubitz, W. (2020). Current Understanding of the Mechanism of Water Oxidation in Photosystem II and Its Relation to XFEL Data. *Annu Rev Biochem*, *89*, 795-820.

Cox, N., Retegan, M., Neese, F., Pantazis, D. A., Boussac, A., & Lubitz, W. (2014). Photosynthesis. Electronic structure of the oxygen-evolving complex in photosystem II prior to O-O bond formation. *Science*, *345*(6198), 804-808.

Danielsson, R., Albertsson, P.-Å., Mamedov, F., & Styring, S. (2004). Quantification of photosystem I and II in different parts of the thylakoid membrane from spinach. *Biochimica et Biophysica Acta (BBA)-Bioenergetics*, *1608*(1), 53-61.

Dau, H. (1994). Molecular mechanisms and quantitative models of variable photosystem II fluorescence. *Photochemistry and Photobiology*, *60*(1), 1-23.

Dau, H., & Haumann, M. (2007). Time-resolved X-ray spectroscopy leads to an extension of the classical S-state cycle model of photosynthetic oxygen evolution. *Photosynthesis research*, *92*, 327-343.

Dau, H., & Haumann, M. (2008). The manganese complex of photosystem II in its reaction cycle—basic framework and possible realization at the atomic level. *Coordination Chemistry Reviews*, *252*(3-4), 273-295.

Dau, H., Iuzzolino, L., & Dittmer, J. (2001). The tetra-manganese complex of photosystem II during its redox cycle: X-ray absorption results and mechanistic implications. *Biochimica et Biophysica Acta*, *1503*(1-2), 24-39.

Dau, H., Liebisch, P., & Haumann, M. (2003). X-ray absorption spectroscopy to analyze nuclear geometry and electronic structure of biological metal centers - potential and questions examined with special focus on the tetra-nuclear manganese complex of oxygenic photosynthesis. *Analytical and Bioanalytical Chemistry*, *376*(5), 562-583.

Dau, H., Limberg, C., Reier, T., Risch, M., Roggan, S., & Strasser, P. (2010). The mechanism of water oxidation: from electrolysis via homogeneous to biological catalysis. *ChemCatChem*, *2*(7), 724-761.

Dau, H., & Zaharieva, I. (2009). Principles, efficiency, and blueprint character of solar-energy conversion in photosynthetic water oxidation. *Accounts of chemical research*, *42*(12), 1861-1870.

De Grotthuss, C. (2006). Memoir on the decomposition of water and of the bodies that it holds in solution by means of galvanic electricity. *Biochimica et Biophysica Acta (BBA)-Bioenergetics*, *1757*(8), 871-875.

de Lichtenberg, C., & Messinger, J. (2020). Substrate water exchange in the S2 state of photosystem II is dependent on the conformation of the Mn4Ca cluster. *Phys Chem Chem Phys*, *22*(23), 12894-12908.

De Paula, J. C., Innes, J. B., & Brudvig, G. W. (1985). Electron transfer in photosystem II at cryogenic temperatures. *Biochemistry*, *24*(27), 8114-8120.

de Wijn, R., & van Gorkom, H. J. (2001). Kinetics of electron transfer from Q_a to Q_b in photosystem II. *Biochemistry*, *40*(39), 11912-11922.

Debus, R. J. (2008). Protein Ligation of the Photosynthetic Oxygen-Evolving Center. *Coordination Chemistry Reviews*, *252*(3-4), 244-258.

Dekker, J. P., & Boekema, E. J. (2005). Supramolecular organization of thylakoid membrane proteins in green plants. *Biochimica et Biophysica Acta (BBA)-Bioenergetics*, *1706*(1-2), 12-39.

Dekker, J. P., Plijter, J. J., Ouwehand, L., & van Gorkom, H. J. (1984). Kinetics of manganese redox transitions in the oxygen evolving apparatus of photosynthesis. *Biochimica et Biophysica Acta*, *767*, 176-179.

Demeter, S., Rozsa, Z., Vass, I., & Hideg, E. (1985). Thermoluminescence study of charge recombination in Photosystem II at low temperatures. II. Oscillatory properties of the Zv and A thermoluminescence bands in chloroplasts dark-adapted for various time periods. *Biochimica et Biophysica Acta (BBA)-Bioenergetics*, *809*(3), 379-387.

Dilbeck, P. L., Hwang, H. J., Zaharieva, I., Gerencser, L., Dau, H., & Burnap, R. L. (2012). The mutation D1-D61N in Synechocystis sp. PCC 6803 allows the observation of

pH-sensitive intermediates in the formation and release of O_2 from Photosystem II. *Biochemistry*, *51*(6), 1079–1091.

Diner, B. A. (2001). Amino acid residues involved in the coordination and assembly of the manganese cluster of photosystem II. Proton-coupled electron transport of the redox-active tyrosines and its relationship to water oxidation. *Biochimica et Biophysica Acta (BBA) - Bioenergetics*, *1503*(1-2), 147-163.

Dismukes, G. C., & Siderer, Y. (1981). Intermediates of a polynuclear manganese center involved in photosynthetic oxidation of water. *Proceedings of the National Academy of Sciences of the United States of America*, *78*(1), 274-278.

Doster, W. (2010). The protein-solvent glass transition. *Biochimica et Biophysica Acta (BBA)-Proteins and Proteomics*, *1804*(1), 3-14.

Eckert, H. J., & Renger, G. (1988). Temperature dependence of P680+ reduction in O2-evolving PS II membrane fragments at different redox states Si of the water oxidizing system. *FEBS letters*, *236*(2), 425-431.

Eichmann, V. (2021). Characterization of photosystem I variants by FTIR spectroscopy. *Masterthesis*, *Freie Universität Berlin*.

Evans, M. G., & Polanyi, M. (1935). Some applications of the transition state method to the calculation of reaction velocities, especially in solution. *Transactions of the Faraday Society*, *31*, 875-894.

Eyring, H. (1935). The activated complex in chemical reactions. *The Journal of Chemical Physics*, *3*(2), 107-115.

Fan, D.-Y., Hope, A. B., Smith, P. J., Jia, H., Pace, R. J., Anderson, J. M., & Chow, W. S. (2007). The stoichiometry of the two photosystems in higher plants revisited. *Biochimica et Biophysica Acta (BBA)-Bioenergetics*, *1767*(8), 1064-1072.

Faunce, T., Styring, S., Wasielewski, M. R., Brudvig, G. W., Rutherford, A. W., Messinger, J., Lee, A. F., Hill, C. L., deGroot, H., Fontecave, M., MacFarlane, D. R., Hankamer, B., Nocera, D. G., Tiede, D. M., Dau, H., Hillier, W., Wang, L. Z., & Amal, R. (2013). Artificial photosynthesis as a frontier technology for energy sustainability. *Energy & Environmental Science*, *6*(4), 1074-1076.

Ferreira, K. N., Iverson, T. M., Maghlaoui, K., Barber, J., & Iwata, S. (2004). Architecture of the photosynthetic oxygen-evolving center. *Science*, *303*(5665), 1831-1838.

Ferreira, K. N., Iverson, T. M., Maghlaoui, K., Barber, J., & Iwata, S. (2004). Architecture of the photosynthetic oxygen-evolving center. *Science*, *303*, 1831-1838.

Forbush, B., Kok, B., & McGloin, M. P. (1971). Cooperation of charges in photosynthetic O2 evolution-II. damping of flash yield oscillation, deactivation. *Photochemistry and Photobiology*, *14*(3), 307-321.

Fornasini, P., & Grisenti, R. (2015). On EXAFS Debye-Waller factor and recent advances. *Journal of synchrotron radiation*, *22*(5), 1242-1257.

Frauenfelder, H., Parak, F., & Young, R. D. (1988). Conformational Substates in Proteins. *Annual Review of Biophysics and Biophysical Chemistry*, *17*(1), 451-479.

Frauenfelder, H., Sligar, S. G., & Wolynes, P. G. (1991). The energy landscapes and motions of proteins. *Science*, *254*(5038), 1598-1603.

Fujimori, T., Higuchi, M., Sato, H., Aiba, H., Muramatsu, M., Hihara, Y., & Sonoike, K. (2005). The mutant of sll1961, which encodes a putative transcriptional regulator, has a defect in regulation of photosystem stoichiometry in the cyanobacterium Synechocystis sp. PCC 6803. *Plant physiology*, *139*(1), 408-416.

Gabdulkhakov, A., Guskov, A., Broser, M., Kern, J., Muh, F., Saenger, W., & Zouni, A. (2009). Probing the accessibility of the Mn(4)Ca cluster in photosystem II: channels calculation, noble gas derivatization, and cocrystallization with DMSO. *Structure*, *17*(9), 1223-1234.

Gan, F., Shen, G., & Bryant, D. A. (2015). Occurrence of far-red light photoacclimation (FaRLiP) in diverse cyanobacteria. *Life*, *5*(1), 4-24.

Garbers, A., Reifarth, F., Kurreck, J., Renger, G., & Parak, F. (1998). Correlation between protein flexibility and electron transfer from QA-* to QB in PSII membrane fragments from spinach. *Biochemistry*, *37*(33), 11399-11404.

Gerencser, L., & Dau, H. (2010). Water oxidation by Photosystem II: H_2O–D_2O Exchange and the influence of pH support formation of an intermediate by removal of a proton before dioxygen creation. *Biochemistry*, *49*(47), 10098-10106.

Ghosh, I., Banerjee, G., Kim, C. J., Reiss, K., Batista, V. S., Debus, R. J., & Brudvig, G. W. (2019). D1-S169A substitution of photosystem II perturbs water oxidation. *Biochemistry*, *58*(10), 1379-1387.

Ghosh, I., Khan, S., Banerjee, G., Dziarski, A., Vinyard, D. J., Debus, R. J., & Brudvig, G. W. (2019). Insights into proton-transfer pathways during water oxidation in photosystem II. *The Journal of Physical Chemistry B*, *123*(39), 8195-8202.

Gisriel, C. J., Flesher, D. A., Shen, G., Wang, J., Ho, M.-Y., Brudvig, G. W., & Bryant, D. A. (2021). Structure of a photosystem I-ferredoxin complex from a marine cyanobacterium provides insights into far-red light photoacclimation. *Journal of Biological Chemistry*, 101408.

Gisriel, C. J., Huang, H.-L., Reiss, K. M., Flesher, D. A., Batista, V. S., Bryant, D. A., Brudvig, G. W., & Wang, J. (2021). Quantitative assessment of chlorophyll types in cryo-EM maps of photosystem I acclimated to far-red light. *BBA Advances*, *1*, 100019.

Gisriel, C. J., Shen, G., Ho, M.-Y., Kurashov, V., Flesher, D. A., Wang, J., Armstrong, W. H., Golbeck, J. H., Gunner, M., & Vinyard, D. J. (2021). Structure of a monomeric photosystem II core complex from a cyanobacterium acclimated to far-red light reveals the functions of chlorophylls d and f. *Journal of Biological Chemistry*, 101424.

González-Flores, D., Zaharieva, I., Heidkamp, J., Chernev, P., Martinez-Moreno, E., Pasquini, C., Mohammadi, M. R., Klingan, K., Gernet, U., Fischer, A., & Dau, H. (2016). Electrosynthesis of biomimetic manganese-calcium oxides for water oxidation catalysis - atomic structure and functionality. *ChemSusChem*, *9*(4), 379-387.

Gorka, M., Cherepanov, D. A., Semenov, A. Y., & Golbeck, J. H. (2020). Control of electron transfer by protein dynamics in photosynthetic reaction centers. *Critical Reviews in Biochemistry and Molecular Biology*, *55*(5), 425-468.

Grabolle, M., & Dau, H. (2005). Energetics of primary and secondary electron transfer in Photosystem II membrane particles of spinach revisited on basis of recombination-fluorescence measurements. *Biochimica et Biophysica Acta*, *1708*(2), 209-218.

Grabolle, M., & Dau, H. (2007). Efficiency and role of loss processes in light-driven water oxidation by PSII. *Physiologia plantarum*, *131*, 50-63.

Grabolle, M., Haumann, M., Müller, C., Liebisch, P., & Dau, H. (2006). Rapid loss of structural motifs in the manganese complex of oxygenic photosynthesis by X-ray irradiation at 10-300 K. *Journal of Biological Chemistry*, *281*(8), 4580-4588.

Guerra, F., Siemers, M., Mielack, C., & Bondar, A. N. (2018). Dynamics of Long-Distance Hydrogen-Bond Networks in Photosystem II. *Journal of Physical Chemistry B*, *122*(17), 4625-4641.

Guo, Y., Sekharan, S., Liu, J., Batista, V. S., Tully, J. C., & Yan, E. C. (2014). Unusual kinetics of thermal decay of dim-light photoreceptors in vertebrate vision. *Proceedings of the National Academy of Sciences*, *111*(29), 10438-10443.

Gust, D., Moore, T. A., & Moore, A. L. (2009). Solar fuels via artificial photosynthesis. *Accounts of chemical research*, *42*(12), 1890-1898.

Hankamer, B., Nield, J., Zheleva, D., Boekema, E., Jansson, S., & Barber, J. (1997). Isolation and biochemical characterization of monomeric and dimeric photosystem II complexes from spinach and their relevance to the organisation of photosystem II in vivo. *European journal of biochemistry*, *243*(1-2), 422-429.

Haumann, M., Bögershausen, O., Cherepanov, D., Ahlbrink, R., & Junge, W. (1997). Photosynthetic oxygen evolution: H/D isotope effects and the coupling between electron and proton transfer during the redox reactions at the oxidizing side of Photosystem II. *Photosynthesis research*, *51*(3), 193-208.

Haumann, M., Liebisch, P., Muller, C., Barra, M., Grabolle, M., & Dau, H. (2005). Photosynthetic O_2 formation tracked by time-resolved x-ray experiments. *Science*, *310*(5750), 1019-1021.

Haumann, M., Müller, C., Liebisch, P., Iuzzolino, L., Dittmer, J., Grabolle, M., Neisius, T., Meyer-Klaucke, W., & Dau, H. (2005). Structural and oxidation state changes of the photosystem II manganese complex in four transitions of the water oxidation

cycle ($S_0 \rightarrow S_1$, $S_1 \rightarrow S_2$, $S_2 \rightarrow S_3$, and $S_{3,4} \rightarrow S_0$) characterized by X-ray absorption spectroscopy at 20 K and room temperature. *Biochemistry*, *44*(6), 1894-1908.

Henzler-Wildman, K., & Kern, D. (2007). Dynamic personalities of proteins. *Nature*, *450*(7172), 964-972.

Hillier, W., Messinger, J., & Wydrzynski, T. (1998). Kinetic determination of the fast exchanging substrate water molecule in the S_3 state of photosystem II. *Biochemistry*, *37*(48), 16908-16914.

Ho, M.-Y., Niedzwiedzki, D. M., MacGregor-Chatwin, C., Gerstenecker, G., Hunter, C. N., Blankenship, R. E., & Bryant, D. A. (2020). Extensive remodeling of the photosynthetic apparatus alters energy transfer among photosynthetic complexes when cyanobacteria acclimate to far-red light. *Biochimica et Biophysica Acta (BBA)-Bioenergetics*, *1861*(4), 148064.

Humphrey, G. (1979). Photosynthetic characteristics of algae grown under constant illumination and light-dark regimes. *Journal of Experimental Marine Biology and Ecology*, *40*(1), 63-70.

Hundelt, M., Hays, A. M., Debus, R. J., & Junge, W. (1998). Oxygenic photosystem II: the mutation D1-D61N in Synechocystis sp. PCC 6803 retards S-state transitions without affecting electron transfer from YZ to P680+. *Biochemistry*, *37*(41), 14450-14456.

Hwang, H. J., Dilbeck, P., Debus, R. J., & Burnap, R. L. (2007). Mutation of arginine 357 of the CP43 protein of photosystem II severely impairs the catalytic S-state cycle of the H2O oxidation complex. *Biochemistry*, *46*(43), 11987-11997.

Ibrahim, M., Fransson, T., Chatterjee, R., Cheah, M. H., Hussein, R., Lassalle, L., Sutherlin, K. D., Young, I. D., Fuller, F. D., & Gul, S. (2020). Untangling the sequence of events during the S2→ S3 transition in photosystem II and implications for the water oxidation mechanism. *Proceedings of the National Academy of Sciences*, *117*(23), 12624-12635.

Inoue, Y., & Shibata, K. (1978). Oscillation of thermoluminescence at medium-low temperature. *FEBS letters*, *85*, 193-197.

Ishikita, H., Saenger, W., Loll, B., Biesiadka, J., & Knapp, E. W. (2006). Energetics of a possible proton exit pathway for water oxidation in photosystem II. *Biochemistry*, *45*(7), 2063-2071.

Itoh, S., Ohno, T., Noji, T., Yamakawa, H., Komatsu, H., Wada, K., Kobayashi, M., & Miyashita, H. (2015). Harvesting far-red light by chlorophyll f in photosystems I and II of unicellular cyanobacterium strain KC1. *Plant and cell physiology*, *56*(10), 2024-2034.

Jamnongwong, M., Loubiere, K., Dietrich, N., & Hébrard, G. (2010). Experimental study of oxygen diffusion coefficients in clean water containing salt, glucose or surfactant: Consequences on the liquid-side mass transfer coefficients. *Chemical Engineering Journal*, *165*(3), 758-768.

Jansson, H., & Swenson, J. (2010). The protein glass transition as measured by dielectric spectroscopy and differential scanning calorimetry. *Biochimica et Biophysica Acta (BBA)-Proteins and Proteomics*, *1804*(1), 20-26.

Joliot, P. (2003). Period-four oscillations of the flash-induced oxygen formation in photosynthesis. *Photosynthesis research*, *76*(1), 65-72.

Joliot, P., Barbieri, G., & Chabaud, R. (1969). Un nouveau modele des centres photochimiques du systeme II*. *Photochemistry and Photobiology*, *10*(5), 309-329.

Joliot, P., & Joliot, A. (1968). A polarographic method for detection of oxygen production and reduction of Hill reagent by isolated chloroplasts. *Biochimica et Biophysica Acta*, *153*, 625-634.

Joliot, P., & Kok, B. (1975). Oxygen evolution in photosynthesis. In *Energetics of Photosynthesis* (pp. 387-412). Elsevier.

Jorissen, K., & Rehr, J. J. (2013). New developments in FEFF: FEFF9 and JFEFF. Journal of Physics: Conference Series.

Junge, W., Haumann, M., Ahlbrink, R., Mulkidjanian, A., & Clausen, J. (2002). Electrostatics and proton transfer in photosynthetic water oxidation. *Philosophical Transactions of the Royal Society B-Biological Sciences*, *357*(1426), 1407 - 1418.

Kato, K., Shinoda, T., Nagao, R., Akimoto, S., Suzuki, T., Dohmae, N., Chen, M., Allakhverdiev, S. I., Shen, J.-R., & Akita, F. (2020). Structural basis for the adaptation and function of chlorophyll f in photosystem I. *Nature communications*, *11*(1), 1-10.

Kaur, D., Zhang, Y., Reiss, K. M., Mandal, M., Brudvig, G. W., Batista, V. S., & Gunner, M. (2021). Proton exit pathways surrounding the oxygen evolving complex of photosystem II. *Biochimica et Biophysica Acta (BBA)-Bioenergetics*, *1862*(8), 148446.

Kawashima, K., Saito, K., & Ishikita, H. (2018). Mechanism of radical formation in the H-bond network of D1-Asn298 in photosystem II. *Biochemistry*, *57*(33), 4997-5004.

Kebekus, U., Messinger, J., & Renger, G. (1995). Structural changes in the water-oxidizing complex monitored via the pH dependence of the reduction rate of redox state S1 by hydrazine and hydroxylamine in isolated spinach thylakoids. *Biochemistry*, *34*(18), 6175-6182.

Kern, J., Alonso-Mori, R., Hellmich, J., Tran, R., Hattne, J., Laksmono, H., Glockner, C., Echols, N., Sierra, R. G., Sellberg, J., Lassalle-Kaiser, B., Gildea, R. J., Glatzel, P., Grosse-Kunstleve, R. W., Latimer, M. J., McQueen, T. A., DiFiore, D., Fry, A. R., Messerschmidt, M., . . . Yachandra, V. K. (2012). Room temperature femtosecond X-ray diffraction of photosystem II microcrystals. *Proceedings of the National Academy of Sciences of the United States of America*, *109*(25), 9721-9726.

Kern, J., Chatterjee, R., Young, I. D., Fuller, F. D., Lassalle, L., Ibrahim, M., Gul, S., Fransson, T., Brewster, A. S., Alonso-Mori, R., Hussein, R., Zhang, M., Douthit, L., de Lichtenberg, C., Cheah, M. H., Shevela, D., Wersig, J., Seuffert, I., Sokaras, D., . . . Yachandra, V. K. (2018). Structures of the intermediates of Kok's photosynthetic water oxidation clock. *Nature*, *563*(7731), 421-425.

Kern, J., Loll, B., Lüneberg, C., DiFiore, D., Biesiadka, J., Irrgang, K.-D., & Zouni, A. (2005). Purification, characterization, and crystallization of photosystem II from Thermosynechococcus elongatus cultivated in a new type of photobioreactor. *Biochimica et Biophysica Acta*, *1706*, 147-157.

Kiang, N. Y., Segura, A., Tinetti, G., Blankenship, R. E., Cohen, M., Siefert, J., Crisp, D., & Meadows, V. S. (2007). Spectral Signatures of Photosynthesis. II. Coevolution with Other Stars and the Atmosphere on Extrasolar Worlds. *Astrobiology*, *7*(1), 252-274.

Kim, C. J., & Debus, R. J. (2017). Evidence from FTIR Difference Spectroscopy That a Substrate H2O Molecule for O-2 Formation in Photosystem II Is Provided by the Ca Ion of the Catalytic Mn4CaO5 Cluster. *Biochemistry*, *56*(20), 2558-2570.

Kim, C. J., & Debus, R. J. (2019). One of the substrate waters for O2 formation in photosystem II is provided by the water-splitting Mn4CaO5 cluster's Ca2+ Ion. *Biochemistry*, *58*(29), 3185-3192.

Kim, C. J., & Debus, R. J. (2020). Roles of D1-Glu189 and D1-Glu329 in O2 formation by the water-splitting Mn4Ca cluster in Photosystem II. *Biochemistry*, *59*(40), 3902-3917.

Klauss, A., Haumann, M., & Dau, H. (2012). Alternating electron and proton transfer steps in photosynthetic water oxidation. *Proceedings of the National Academy of Sciences of the United States of America*, *109*(40), 16035-16040.

Klauss, A., Haumann, M., & Dau, H. (2015). Seven steps of alternating electron and proton transfer in photosystem II water oxidation traced by time-resolved photothermal beam deflection at improved sensitivity. *J Phys Chem B*, *119*(6), 2677-2689.

Klauss, A., Sikora, T., Suss, B., & Dau, H. (2012). Fast structural changes (200-900ns) may prepare the photosynthetic manganese complex for oxidation by the adjacent tyrosine radical. *Biochim Biophys Acta*, *1817*, 1196-1207.

Koike, H., Hanssum, B., Inoue, Y., & Renger, G. (1987). Temperature dependence of S-state transition in a thermophilic cyanobacterium, *Synechococcus vulcanus* Copeland measured by absorption changes in the ultraviolet region. *Biochimica et Biophysica Acta*, *893*, 524-533.

Kok, B., Forbush, B., & McGloin, M. (1970). Cooperation of charges in photosynthetic O_2 evolution - I. A linear four-step mechanism. *Photochemistry and Photobiology*, *11*, 457-475.

Koulougliotis, D., Hirsh, D. J., & Brudvig, G. W. (1992). The O_2-evolving center of photosystem II is diamagnetic in the S_1 resting state. *Journal of the American Chemical Society*, *114*(21), 8322-8323.

Krause, G. H., & Weis, E. (1984). Chlorophyll fluorescence as a tool in plant physiology. *Photosynthesis research*, *5*(2), 139-157.

Kulik, L. V., Epel, B., Lubitz, W., & Messinger, J. (2007). Electronic structure of the Mn4O x Ca cluster in the S0 and S2 states of the oxygen-evolving complex of photosystem II based on pulse 55Mn-ENDOR and EPR spectroscopy. *Journal of the American Chemical Society*, *129*(44), 13421-13435.

Kuroda, H., Kawashima, K., Ueda, K., Ikeda, T., Saito, K., Ninomiya, R., Hida, C., Takahashi, Y., & Ishikita, H. (2021). Proton transfer pathway from the oxygen-evolving complex in photosystem II substantiated by extensive mutagenesis. *Biochim Biophys Acta Bioenerg*, *1862*(1), 148329.

Laidler, K. J. (1984). The development of the Arrhenius equation. *Journal of chemical Education*, *61*(6), 494.

Lavergne, J., & Junge, W. (1993). Proton release during the redox cycle of the water oxidase. *Photosynthesis research*, *38*, 279-296.

Lavorel, J. (1992). Determination of the Photosynthetic Oxygen Release Time by Amperometry. *Biochimica Et Biophysica Acta*, *1101*(1), 33-40.

Lewis, N. S., & Nocera, D. G. (2006). Powering the planet: chemical challenges in solar energy utilization. *Proceedings of the National Academy of Sciences of the United States of America*, *103*(43), 15729-15735.

Li, Y., Lin, Y., Loughlin, P. C., & Chen, M. (2014). Optimization and effects of different culture conditions on growth of Halomicronema hongdechloris–a filamentous cyanobacterium containing chlorophyll f. *Frontiers in Plant Science*, *5*, 67.

Liang, Z. (2018). Photosynthetic Water Oxidation in Plants and Cyanobacteria - Activation Energy of the O-O Bond Formation Step and Substrate Analogue NH3. *Dissertation Freie Univ. Berlin,* https://refubium.fu-berlin.de/handle/fub188/4210.

Lichtenthaler, H. K. (1987). Chlorophylls and Carotenoids - Pigments of Photosynthetic Biomembranes. *Methods in Enzymology*, *148*, 350-382.

Logan, S. (1982). The origin and status of the Arrhenius equation. *Journal of chemical Education*, *59*(4), 279.

Lohmiller, T., Krewald, V., Sedoud, A., Rutherford, A. W., Neese, F., Lubitz, W., Pantazis, D. A., & Cox, N. (2017). The first state in the catalytic cycle of the water-oxidizing enzyme: Identification of a water-derived μ-hydroxo bridge. *Journal of the American Chemical Society*, *139*(41), 14412-14424.

Loll, B., Kern, J., Saenger, W., Zouni, A., & Biesiadka, J. (2005). Towards complete cofactor arrangement in the 3.0 A resolution structure of photosystem II. *Nature*, *438*(7070), 1040-1044.

Lonergan, T. A. (2000). The photosynthetic dark reactions do not operate in the dark. *The American Biology Teacher*, *62*(3), 166-170.

Low, P., & Somero, G. N. (1974). Temperature adaptation of enzymes: a proposed molecular basis for the different catalytic efficiencies of enzymes from ectotherms and endotherms. *Comparative Biochemistry and Physiology--Part B: Biochemistry and*, *49*(2), 307-312.

Lukeš, M., Procházková, L., Shmidt, V., Nedbalová, L., & Kaftan, D. (2014). Temperature dependence of photosynthesis and thylakoid lipid composition in the red snow alga Chlamydomonas cf. nivalis (Chlorophyceae). *FEMS microbiology ecology*, *89*(2), 303-315.

Mandal, M., Askerka, M., Banerjee, G., Amin, M., Brudvig, G. W., Batista, V. S., & Gunner, M. (2017). Characterization of ammonia binding to the second coordination shell of the oxygen-evolving complex of photosystem II. *Dalton Transactions*, *46*(46), 16089-16095.

Mandal, M., Saito, K., & Ishikita, H. (2020). The Nature of the Short Oxygen–Oxygen Distance in the Mn4CaO6 Complex of Photosystem II Crystals. *The Journal of Physical Chemistry Letters*, *11*(23), 10262-10268.

Marchiori, D. A., Oyala, P. H., Debus, R. J., Stich, T. A., & Britt, R. D. (2018). Structural effects of ammonia binding to the Mn_4CaO_5 cluster of Photosystem II. *The Journal of Physical Chemistry B*, *122*(5), 1588-1599.

Marcus, R. A., & Sutin, N. (1985). Electron transfers in chemistry and biology. *Biochimica et Biophysica Acta (BBA)-Reviews on Bioenergetics*, *811*(3), 265-322.

Maxwell, K., & Johnson, G. N. (2000). Chlorophyll fluorescence—a practical guide. *Journal of experimental botany*, *51*(345), 659-668.

Mayes, S. R., Dubbs, J. M., Vass, I., Hideg, E., Nagy, L., & Barber, J. (1993). Further characterization of the psbH locus of Synechocystis sp. PCC 6803: inactivation of psbH impairs QA to QB electron transport in photosystem 2. *Biochemistry*, *32*(6), 1454-1465.

Melis, A., & Brown, J. S. (1980). Stoichiometry of system I and system II reaction centers and of plastoquinone in different photosynthetic membranes. *Proceedings of the National Academy of Sciences*, *77*(8), 4712-4716.

Messinger, J., Badger, M., & Wydrzynski, T. (1995). Detection of *one* slowly exchanging substrate water molecule in the S_3 state of photosystem II. *Proceedings of the National Academy of Sciences of the United States of America*, *92*(8), 3209-3213.

Meunier, P. C., & Popovic, R. (1990). Control of misses in oxygen evolution by the oxido-reduction state of plastoquinone in Dunaliella tertiolecta. *Photosynthesis research*, *23*(2), 213-221.

Miyashita, H., Adachi, K., Kurano, N., Ikemot, H., Chihara, M., & Miyach, S. (1997). Pigment composition of a novel oxygenic photosynthetic prokaryote containing chlorophyll d as the major chlorophyll. *Plant and cell physiology*, *38*(3), 274-281.

Miyashita, H., Ohkubo, S., Komatsu, H., Sorimachi, Y., Fukayama, D., Fujinuma, D., Akutsu, S., & Kobayashi, M. (2014). Discovery of chlorophyll d in Acaryochloris marina and chlorophyll f in a unicellular cyanobacterium, strain KC1, isolated from Lake Biwa. *Journal of Physical Chemistry & Biophysics*, *4*(4), 1.

Mortimer, R. G., & Eyring, H. (1980). Elementary Transition-State Theory of the Soret and Dufour Effects. *Proceedings of the National Academy of Sciences of the United States of America*, *77*(4), 1728-1731.

Moser, C. C., Keske, J. M., Warncke, K., Farid, R. S., & Dutton, P. L. (1992). Nature of biological electron transfer. *Nature*, *355*(6363), 796-802.

Moser, C. C., Page, C. C., & Dutton, P. L. (2005). Tunneling in PSII. *Photochemical & Photobiological Sciences*, *4*(12), 933-939.

Moser, C. C., Page, C. C., Farid, R., & Dutton, P. L. (1995). Biological electron transfer. *Journal of Bioenergetics and Biomembranes*, *27*(3), 263-274.

Muh, F., Glockner, C., Hellmich, J., & Zouni, A. (2012). Light-induced quinone reduction in photosystem II. *Biochim Biophys Acta*, *1817*(1), 44-65.

Nagao, R., Ueoka-Nakanishi, H., & Noguchi, T. (2017). D1-Asn-298 in photosystem II is involved in a hydrogen-bond network near the redox-active tyrosine YZ for proton exit during water oxidation. *Journal of Biological Chemistry*, *292*(49), 20046-20057.

Nakamura, S., Capone, M., Narzi, D., & Guidoni, L. (2020). Pivotal role of the redox-active tyrosine in driving the water splitting catalyzed by photosystem II. *Physical Chemistry Chemical Physics*, *22*(1), 273-285.

Navarro, M. P., Ames, W. M., Nilsson, H., Lohmiller, T., Pantazis, D. A., Rapatskiy, L., Nowaczyk, M. M., Neese, F., Boussac, A., Messinger, J., Lubitz, W., & Cox, N. (2013). Ammonia binding to the oxygen-evolving complex of photosystem II identifies the solvent-exchangeable oxygen bridge (m-oxo) of the manganese tetramer. *Proceedings of the National Academy of Sciences of the United States of America*, *110*(39), 15561-15566.

Nield, J., Kruse, O., Ruprecht, J., da Fonseca, P., Buchel, C., & Barber, J. (2000). Three-dimensional structure of Chlamydomonas reinhardtii and Synechococcus elongatus photosystem II complexes allows for comparison of their oxygen-evolving complex organization. *Journal of Biological Chemistry*, *275*(36), 27940-27946.

Noguchi, T., & Sugiura, M. (2002). Flash-induced FTIR difference spectra of the water oxidizing complex in moderately hydrated photosystem II core films: Effect of hydration extent on S-state transitions. *Biochemistry*, *41*(7), 2322-2330.

Noring, B., Shevela, D., Renger, G., & Messinger, J. (2008). Effects of methanol on the Si-state transitions in photosynthetic water-splitting. *Photosynth Res*, *98*(1-3), 251-260.

Nürnberg, D. J., Morton, J., Santabarbara, S., Telfer, A., Joliot, P., Antonaru, L. A., Ruban, A. V., Cardona, T., Krausz, E., & Boussac, A. (2018). Photochemistry beyond the red limit in chlorophyll f–containing photosystems. *Science*, *360*(6394), 1210-1213.

Ogata, K., Yuki, T., Hatakeyama, M., Uchida, W., & Nakamura, S. (2013). All-atom molecular dynamics simulation of photosystem II embedded in thylakoid membrane. *Journal of the American Chemical Society*, *135*(42), 15670-15673.

Okamoto, Y., Shimada, Y., Nagao, R., & Noguchi, T. (2021). Proton and Water Transfer Pathways in the S2→ S3 Transition of the Water-Oxidizing Complex in Photosystem II: Time-Resolved Infrared Analysis of the Effects of D1-N298A Mutation and NO3–Substitution. *The Journal of Physical Chemistry B*.

Oyala, P. H., Stich, T. A., Debus, R. J., & Britt, R. D. (2015). Ammonia binds to the dangler manganese of the photosystem II oxygen-evolving complex. *Journal of the American Chemical Society*, *137*(27), 8829-8837.

Oyala, P. H., Stich, T. A., Stull, J. A., Yu, F., Pecoraro, V. L., & Britt, R. D. (2014). Pulse electron paramagnetic resonance studies of the interaction of methanol with the S2 state of the Mn4O5Ca cluster of photosystem II. *Biochemistry*, *53*(50), 7914-7928.

Pal, R., Negre, C. F. A., Vogt, L., Pokhrel, R., Ertem, M. Z., Brudvig, G. W., & Batista, V. S. (2013). S-0-State Model of the Oxygen-Evolving Complex of Photosystem II. *Biochemistry*, *52*(44), 7703-7706.

Pantazis, D. A. (2018). Missing pieces in the puzzle of biological water oxidation. *ACS Catalysis*, *8*(10), 9477-9507.

Parada, G. A., Goldsmith, Z. K., Kolmar, S., Rimgard, B. P., Mercado, B. Q., Hammarström, L., Hammes-Schiffer, S., & Mayer, J. M. (2019). Concerted proton-electron transfer reactions in the Marcus inverted region. *Science*, *364*(6439), 471-475.

Parak, F., Knapp, E. W., & Kucheida, D. (1982). Protein dynamics - Mössbauer spectroscopy on deoxymyoglobin crystals. *Journal of Molecular Biology*, *161*(1), 177-194.

Parak, F., & Nienhaus, G. U. (1991). Glass-like behaviour of proteins as seen by Mössbauer spectroscopy. *Journal of Non-Crystalline Solids*, *131-133*, 362-368.

Peleg, M., Normand, M. D., & Corradini, M. G. (2012). The Arrhenius equation revisited. *Critical reviews in food science and nutrition*, *52*(9), 830-851.

Pieper, J., Hauss, T., Buchsteiner, A., Baczynski, K., Adamiak, K., Lechner, R. E., & Renger, G. (2007). Temperature- and hydration-dependent protein dynamics in photosystem II of green plants studied by quasielastic neutron scattering. *Biochemistry*, *46*(40), 11398-11409.

Pieper, J., Hauss, T., Buchsteiner, A., & Renger, G. (2008). The effect of hydration on protein flexibility in photosystem II of green plants studied by quasielastic neutron scattering. *European Biophysics Journal*, *37*(5), 657-663.

Pieper, J., Trapp, M., Skomorokhov, A., Natkaniec, I., Peters, J., & Renger, G. (2012). Temperature-dependent vibrational and conformational dynamics of photosystem II membrane fragments from spinach investigated by elastic and inelastic neutron scattering. *Biochimica et Biophysica Acta (BBA) - Bioenergetics*, *1817*(8), 1213-1219.

Plijter, J. J., Aalbers, S. E., Barends, J.-P. F., Vos, M. H., & van Gorkom, H. J. (1988). Oxygen release may limit the rate of photosynthetic electron transport; the use of a weakly polarized oxygen cathode. *Biochimica et Biophysica Acta (BBA)-Bioenergetics*, *935*(3), 299-311.

Pokhrel, R., & Brudvig, G. W. (2014). Oxygen-evolving complex of photosystem II: correlating structure with spectroscopy. *Phys Chem Chem Phys*, *16*(24), 11812-11821.

Pokhrel, R., Service, R. J., Debus, R. J., & Brudvig, G. W. (2013). Mutation of lysine 317 in the D2 subunit of Photosystem II alters chloride binding and proton transport. *Biochemistry*, *52*(28), 4758-4773.

Qian, M., Dao, L., Debus, R. J., & Burnap, R. L. (1999). Impact of Mutations within the Putative Ca2+-Binding Lumenal Interhelical a− b Loop of the Photosystem II D1 Protein on the Kinetics of Photoactivation and H2O-Oxidation in Synechocystis sp. PCC6803. *Biochemistry*, *38*(19), 6070-6081.

Raines, C. A. (2003). The Calvin cycle revisited. *Photosynthesis research*, *75*(1), 1-10.

Rappaport, F., Ishida, N., Sugiura, M., & Boussac, A. (2011). Ca^{2+} determines the entropy changes associated with the formation of transition states during water oxidation by Photosystem II. *Energy & Environmental Science*, *4*(7), 2520-2524.

Rehr, J. J., Kas, J. J., Vila, F. D., Prange, M. P., & Jorissen, K. (2010). Parameter-free calculations of X-ray spectra with FEFF9. *Physical Chemistry Chemical Physics*, *12*(21), 5503-5513.

Reifarth, F., & Renger, G. (1998). Indirect evidence for structural changes coupled with $Q_{B}^{-\cdot}$ formation in photosystem II. *FEBS letters*, *428*(3), 123-126.

Reiss, K., Morzan, U. N., Grigas, A. T., & Batista, V. S. (2019). Water network dynamics next to the oxygen-evolving complex of photosystem II. *Inorganics*, *7*(3), 39.

Renge, I., Van Grondelle, R., & Dekker, J. (2007). Pigment spectra and intermolecular interaction potentials in glasses and proteins. *Biophysical Journal*, *93*(7), 2491-2503.

Renger, G. (2004). Coupling of electron and proton transfer in oxidative water cleavage in photosynthesis. *Biochimica et Biophysica Acta (BBA) - Bioenergetics*, *1655*(0), 195-204.

Renger, G. (2011). Light induced oxidative water splitting in photosynthesis: energetics, kinetics and mechanism. *Journal of Photochemistry and Photobiology B: Biology*, *104*(1-2), 35-43.

Renger, G., Christen, G., Karge, M., Eckert, H.-J., & Irrgang, K.-D. (1998). Application of the Marcus theory for analysis of the temperature dependence of the reactions leading to photosynthetic water oxidation: results and implications°. *Journal of Biological Inorganic Chemistry*, *3*(4), 360-366.

Renger, G., & Hanssum, B. (1992). Studies on the reaction coordinates of the water oxidase in PS II membrane fragments from spinach. *FEBS letters*, *299*(1), 28-32.

Renger, G., & Hanssum, B. (2009). Oxygen detection in biological systems. *Photosynth Res*.

Renger, T., & Schlodder, E. (2008). The primary electron donor of photosystem II of the cyanobacterium Acaryochloris marina is a chlorophyll d and the water oxidation is driven by a chlorophyll a/chlorophyll d heterodimer. *The Journal of Physical Chemistry B*, *112*(25), 7351-7354.

Retegan, M., & Pantazis, D. A. (2016). Interaction of methanol with the oxygen-evolving complex: atomistic models, channel identification, species dependence, and mechanistic implications. *Chemical science*, *7*(10), 6463-6476.

Ringe, D., & Petsko, G. A. (2003). The `glass transition' in protein dynamics: what it is, why it occurs, and how to exploit it. *Biophysical Chemistry*, *105*(2-3), 667-680.

Rippka, R., Deruelles, J., Waterbury, J. B., Herdman, M., & Stanier, R. Y. (1979). Generic assignments, strain histories and properties of pure cultures of cyanobacteria. *Microbiology*, *111*(1), 1-61.

Ritchie, R. J. (2006). Consistent sets of spectrophotometric chlorophyll equations for acetone, methanol and ethanol solvents. *Photosynthesis research*, *89*(1), 27-41.

Rivalta, I., Amin, M., Luber, S., Vassiliev, S., Pokhrel, R., Umena, Y., Kawakami, K., Shen, J.-R., Kamiya, N., Bruce, D., Brudvig, G. W., Gunner, M. R., & Batista, V. S. (2011). Structural–functional role of chloride in Photosystem II. *Biochemistry*, *50*(29), 6312-6315.

Rutherford, A. W., Osyczka, A., & Rappaport, F. (2012). Back-reactions, short-circuits, leaks and other energy wasteful reactions in biological electron transfer: redox tuning to survive life in O2. *FEBS letters*, *586*(5), 603-616.

Saito, K., Rutherford, A. W., & Ishikita, H. (2015). Energetics of proton release on the first oxidation step in the water-oxidizing enzyme. *Nature communications*, *6*(1), 1-10.

Sakashita, N., Watanabe, H. C., Ikeda, T., Saito, K., & Ishikita, H. (2017). Origins of water molecules in the photosystem II crystal structure. *Biochemistry*, *56*(24), 3049-3057.

Schäfer, A. L. (2018). Activation energy of the oxygen evolving step in photosystem II investigated for various species by time resolved oxygen polarography. *Masterthesis*, *Freie Universität Berlin*.

Schiller, H., & Dau, H. (2000). Preparation protocols for high-activity photosystem II membrane particles of green algae and higher plants, pH dependence of oxygen evolution and comparison of the S_2-state multiline signal by X-band EPR spectroscopy. *Journal of Photochemistry and Photobiology B: Biology*, *55*(2-3), 138-144.

Schilstra, M. J., Rappaport, F., Nugent, J. H. A., Barnett, C. J., & Klug, D. R. (1998). Proton/hydrogen transfer affects the S-state-dependent microsecond phases of 680+ reduction during water splitting. *Biochemistry*, *37*(11), 3974-3981.

Schlodder, E., Brettel, K., & Witt, H. T. (1985). Relation between microsecond reduction kinetics of photooxidized chlorophyll aII (P-680) and photosynthetic water oxidation. *Biochimica et Biophysica Acta*, *808*, 123-131.

Schlodder, E., Çetin, M., & Lendzian, F. (2015). Temperature dependence of the oxidation kinetics of TyrZ and TyrD in oxygen-evolving photosystem II complexes throughout the range from 320 K to 5 K. *Biochimica et Biophysica Acta (BBA)-Bioenergetics*, *1847*(10), 1283-1296.

Schlodder, E., & Witt, H. T. (1999). Stoichiometry of proton release from the catalytic center in photosynthetic water oxidation. Reexamination by a glass electrode study at ph 5.5-7.2. *Journal of Biological Chemistry*, *274*(43), 30387-30392.

Schonbörn, M. (2017). Time-resolved step-scan FTIR spectroscopy on photosystem II. *Dissertation Freie Univ. Berlin,* https://refubium.fu-berlin.de/handle/fub188/1424.

Schraut, J., & Kaupp, M. (2014). On Ammonia Binding to the Oxygen-Evolving Complex of Photosystem II: A Quantum Chemical Study. *Chemistry-a European Journal*, *20*(24), 7300-7308.

Schuth, N., Liang, Z., Schonborn, M., Kussicke, A., Assunção, R., Zaharieva, I., Zilliges, Y., & Dau, H. (2017). Inhibitory and non-inhibitory NH_3 binding at the water-oxidizing manganese complex of photosystem II suggests possible sites and a rearrangement mode of substrate water molecules. *Biochemistry*, *56*(47), 6240-6256.

Schuth, N., Zaharieva, I., Chernev, P., Berggren, G., Anderlund, M., Styring, P., Dau, H., & Haumann, M. (2018). K_α Xray emission spectroscopy on the photosynthetic

oxygen-evolving complex supports manganese oxidation and water binding in the S_3 state. *Inorganic Chemistry*, *57*(16), 10424–10430.

Schuurmans, R., Matthijs, J., & Hellingwerf, K. (2017). Transition from exponential to linear photoautotrophic growth changes the physiology of Synechocystis sp. PCC 6803. *Photosynthesis research*, *132*(1), 69-82.

Serrano, B. (2018). The influence of water analogues on photosynthetic water oxidation investigated by time resolved experiments. *Bachelorthesis*, *Freie Universität Berlin*.

Service, R. J., Hillier, W., & Debus, R. J. (2010). Evidence from FTIR difference spectroscopy of an extensive network of hydrogen bonds near the oxygen-evolving Mn(4)Ca cluster of photosystem II involving D1-Glu65, D2-Glu312, and D1-Glu329. *Biochemistry*, *49*(31), 6655-6669.

Service, R. J., Hillier, W., & Debus, R. J. (2014). Network of Hydrogen Bonds near the Oxygen-Evolving Mn4CaO5 Cluster of Photosystem II Probed with FTIR Difference Spectroscopy. *Biochemistry*, *53*(6), 1001-1017.

Sevillano, E., Meuth, H., & Rehr, J. (1979). Extended x-ray absorption fine structure Debye-Waller factors. I. Monatomic crystals. *Physical Review B*, *20*(12), 4908.

Shevela, D., & Björn, L. O. (2017). Evolution of the Z-scheme of Photosynthesis: A Aerspective. *Photosynthesis research*, *133*(1), 5-15.

Shoji, M., Isobe, H., & Yamaguchi, K. (2015). QM/MM study of the S-2 to S-3 transition reaction in the oxygen-evolving complex of photosystem II. *Chemical Physics Letters*, *636*, 172-179.

Siddiqui, K. S., & Cavicchioli, R. (2006). Cold-adapted enzymes. *Annual Review of Biochemistry*, *75*, 403-433.

Siegbahn, P. E. (2009). Structures and energetics for O_2 formation in Photosystem II. *Acc. Chem. Res.*, *42*(12), 1871-1880.

Siegbahn, P. E. M. (2013). Water oxidation mechanism in photosystem II, including oxidations, proton release pathways, O—O bond formation and O_2 release. *Biochimica et Biophysica Acta (BBA) - Bioenergetics*, *1827*(8–9), 1003-1019.

Siegbahn, P. E. M. (2017). Nucleophilic water attack is not a possible mechanism for O-O bond formation in photosystem II. *Proceedings of the National Academy of Sciences of the United States of America*, *114*(19), 4966-4968.

Siegbahn, P. E. M. (2018). The S_2 to S_3 transition for water oxidation in PSII (photosystem II), revisited. *Physical Chemistry Chemical Physics*, *20*(35), 22926-22931.

Somero, G. N. (2004). Adaptation of enzymes to temperature: searching for basic "strategies". *Comparative Biochemistry and Physiology Part B: Biochemistry and Molecular Biology*, *139*(3), 321-333.

Sproviero, E. M., Gascon, J. A., McEvoy, J. P., Brudvig, G. W., & Batista, V. S. (2008). Quantum mechanics/molecular mechanics study of the catalytic cycle of water splitting in photosystem II. *J. Am. Chem. Soc.*, *130*(11), 3428-3442.

Strange, R. W., & Feiters, M. C. (2008). Biological X-ray absorption spectroscopy (BioXAS): a valuable tool for the study of trace elements in the life sciences. *Current opinion in structural biology*, *18*(5), 609-616.

Strickler, M. A., Hwang, H. J., Burnap, R. L., Yano, J., Walker, L. M., Service, R. J., Britt, R. D., Hillier, W., & Debus, R. J. (2008). Glutamate-354 of the CP43 polypeptide interacts with the oxygen-evolving Mn4Ca cluster of photosystem II: a preliminary characterization of the Glu354Gln mutant. *Philosophical Transactions of the Royal Society B-Biological Sciences*, *363*(1494), 1179-1187.

Strickler, M. A., Walker, L. M., Hillier, W., & Debus, R. J. (2005). Evidence from biosynthetically incorporated strontium and FTIR difference spectroscopy that the C-terminus of the D1 polypeptide of photosystem II does not ligate calcium. *Biochemistry*, *44*(24), 8571-8577.

Styring, S., & Rutherford, A. W. (1988). Deactivation Kinetics and Temperature-Dependence of the S-State Transitions in the Oxygen-Evolving System of Photosystem-Ii Measured by Electron-Paramagnetic-Res Spectroscopy. *Biochimica et Biophysica Acta*, *933*(2), 378-387.

Suga, M., Akita, F., Sugahara, M., Kubo, M., Nakajima, Y., Nakane, T., Yamashita, K., Umena, Y., Nakabayashi, M., Yamane, T., Nakano, T., Suzuki, M., Masuda, T., Inoue, S., Kimura, T., Nomura, T., Yonekura, S., Yu, L. J., Sakamoto, T., . . . Shen, J. R. (2017). Light-induced structural changes and the site of O=O bond formation in PSII caught by XFEL. *Nature*, *543*(7643), 131-135.

Suga, M., Akita, F., Yamashita, K., Nakajima, Y., Ueno, G., Li, H. J., Yamane, T., Hirata, K., Umena, Y., Yonekura, S., Yu, L. J., Murakami, H., Nomura, T., Kimura, T., Kubo, M., Baba, S., Kumasaka, T., Tono, K., Yabashi, M., . . . Shen, J. R. (2019). An oxyl/oxo mechanism for oxygen-oxygen coupling in PSII revealed by an x-ray free-electron laser. *Science*, *366*(6463), 334-+.

Tanaka-Kitatani, Y., Satoh, K., & Katoh, S. (1990). Interaction of benzoquinones with QA- and QB-in oxygen-evolving photosystem II particles from the thermophilic cyanobacterium Synechococcus elongatus. *Plant and cell physiology*, *31*(7), 1039-1047.

Tanaka, A., Fukushima, Y., & Kamiya, N. (2017). Two different structures of the oxygen-evolving complex in the same polypeptide frameworks of photosystem II. *Journal of the American Chemical Society*, *139*(5), 1718-1721.

Tang, X.-S., & Diner, B. A. (1994). Biochemical and Spectroscopic Characterization of a New Oxygen-Evolving Photosystem II Core Complex from the Cyanobacterium Synechocystis PCC 6803. *Biochemistry*, *33*, 4594-4603.

Tomo, T., Okubo, T., Akimoto, S., Yokono, M., Miyashita, H., Tsuchiya, T., Noguchi, T., & Mimuro, M. (2007). Identification of the special pair of photosystem II in a

chlorophyll d-dominated cyanobacterium. *Proceedings of the National Academy of Sciences*, *104*(17), 7283-7288.

Tournier, A. L., Xu, J., & Smith, J. C. (2003). Translational hydration water dynamics drives the protein glass transition. *Biophysical Journal*, *85*(3), 1871-1875.

Trampe, E., & Kühl, M. (2016). Chlorophyll f distribution and dynamics in cyanobacterial beachrock biofilms. *Journal of phycology*, *52*(6), 990-996.

Truhlar, D. G., Garrett, B. C., & Klippenstein, S. J. (1996). Current status of transition-state theory. *The Journal of physical chemistry*, *100*(31), 12771-12800.

Tsuno, M., Suzuki, H., Kondo, T., Mino, H., & Noguchi, T. (2011). Interaction and inhibitory effect of ammonium cation in the oxygen evolving center of photosystem II. *Biochemistry*, *50*(13), 2506-2514.

Umena, Y., Kawakami, K., Shen, J.-R., & Kamiya, N. (2011). Crystal structure of oxygen-evolving photosystem II at a resolution of 1.9 Å. *Nature*, *473*, 55-60.

van Gorkom, H. J., & Gast, P. (1996). Measurement of photosynthetic oxygen evolution. In *Biophysical techniques in photosynthesis* (pp. 391-405). Springer.

Vass, I., & Styring, S. (1991). pH-Dependent charge equilibria between tyrosine-D and the S states in photosystem II. Estimation of relative midpoint redox potentials. *Biochemistry*, *30*(3), 830-839.

Vassiliev, S., Zaraiskaya, T., & Bruce, D. (2012). Exploring the energetics of water permeation in photosystem II by multiple steered molecular dynamics simulations. *Biochimica Et Biophysica Acta-Bioenergetics*, *1817*(9), 1671-1678.

Vila, F. D., Rehr, J., Rossner, H., & Krappe, H. (2007). Theoretical x-ray absorption Debye-Waller factors. *Physical Review B*, *76*(1), 014301.

Vinyard, D. J., Askerka, M., Debus, R. J., Batista, V. S., & Brudvig, G. W. (2016). Ammonia binding in the second coordination sphere of the oxygen-evolving complex of photosystem II. *Biochemistry*, *55*(31), 4432-4436.

Vinyard, D. J., & Brudvig, G. W. (2017). Progress Toward a Molecular Mechanism of Water Oxidation in Photosystem II. *Annual Review of Physical Chemistry, Vol 68*, *68*, 101-116.

Vitkup, D., Ringe, D., Petsko, G. A., & Karplus, M. (2000). Solvent mobility and the protein'glass' transition. *Nature structural biology*, *7*(1), 34-38.

Vogt, L., Vinyard, D. J., Khan, S., & Brudvig, G. W. (2015). Oxygen-evolving complex of Photosystem II: an analysis of second-shell residues and hydrogen-bonding networks. *Current opinion in chemical biology*, *25*, 152-158.

Vos, M. H., van Gorkom, H. J., & Van Leeuwen, P. J. (1991). An electroluminescence study of stabilization reactions in the oxygen-evolving complex of photosystem II. *Biochimica et Biophysica Acta*, *1056*, 27-39.

Wang, J., Askerka, M., Brudvig, G. W., & Batista, V. S. (2017). Crystallographic Data Support the Carousel Mechanism of Water Supply to the Oxygen-Evolving Complex of Photosystem II. *ACS Energy Lett*, *2*(10), 2299-2306.

Wei, X., Su, X., Cao, P., Liu, X., Chang, W., Li, M., Zhang, X., & Liu, Z. (2016). Structure of spinach photosystem II–LHCII supercomplex at 3.2 Å resolution. *Nature*, *534*(7605), 69-74.

Wellburn, A. R. (1994). The spectral determination of chlorophylls a and b, as well as total carotenoids, using various solvents with spectrophotometers of different resolution. *Journal of plant physiology*, *144*(3), 307-313.

Wikstrom, M., Sharma, V., Kaila, V. R., Hosler, J. P., & Hummer, G. (2015). New perspectives on proton pumping in cellular respiration. *Chemical reviews*, *115*(5), 2196-2221.

Willert, C., Stasicki, B., Klinner, J., & Moessner, S. (2010). Pulsed operation of high-power light emitting diodes for imaging flow velocimetry. *Measurement Science and Technology*, *21*(7), 075402.

Wilson, S., Gustafson, G., Lincoln, D., Murari, K., & Johansen, C. (2015). Performance evaluation of an overdriven LED for high-speed schlieren imaging. *Journal of Visualization*, *18*(1), 35-45.

Xing, W., Yin, M., Lv, Q., Hu, Y., Liu, C., & Zhang, J. (2014). Oxygen solubility, diffusion coefficient, and solution viscosity. In *Rotating electrode methods and oxygen reduction electrocatalysts* (pp. 1-31). Elsevier.

Yamamoto, M., Nakamura, S., & Noguchi, T. (2020). Protonation structure of the photosynthetic water oxidizing complex in the S 0 state as revealed by normal mode analysis using quantum mechanics/molecular mechanics calculations. *Physical Chemistry Chemical Physics*, *22*(42), 24213-24225.

Yang, Q., Sang, P., & Liu, S.-Q. (2015). 155 The role of solvent mobility in protein dynamics. *Journal of Biomolecular Structure and Dynamics*, *33*(sup1), 100-101.

Yano, J., Kern, J., Pushkar, Y., Sauer, K., Glatzel, P., Bergmann, U., Messinger, J., Zouni, A., & Yachandra, V. K. (2008). High-resolution structure of the photosynthetic Mn4Ca catalyst from X-ray spectroscopy. *Philosophical Transactions of the Royal Society B: Biological Sciences*, *363*(1494), 1139-1147.

Yano, J., & Yachandra, V. (2014). Mn4Ca cluster in photosynthesis: where and how water is oxidized to dioxygen. *Chemical reviews*, *114*(8), 4175-4205.

Yano, J., & Yachandra, V. K. (2009). X-ray absorption spectroscopy. *Photosynthesis research*, *102*(2-3), 241-254.

Young, I. D., Ibrahim, M., Chatterjee, R., Gul, S., Fuller, F. D., Koroidov, S., Brewster, A. S., Tran, R., Alonso-Mori, R., Kroll, T., Michels-Clark, T., Laksmono, H., Sierra, R. G., Stan, C. A., Hussein, R., Zhang, M., Douthit, L., Kubin, M., de Lichtenberg, C., .

. . Yano, J. (2016). Structure of photosystem II and substrate binding at room temperature. *Nature*, *540*(7633), 453-457.

Yu, B. (2021). Kinetic of Electron Transfer in Manganese-Depleted Photosystem II. *Masterthesis*, *Freie Universität Berlin*.

Zaharieva, I., Chernev, P., Berggren, G., Anderlund, M., Styring, S., Dau, H., & Haumann, M. (2016). Room-temperature energy-sampling Kβ X-ray emission spectroscopy of the Mn_4Ca complex of photosynthesis reveals three Manganese-centered oxidation steps and suggests a coordination change prior to O_2 formation. *Biochemistry*, *55*(30), 4197-4211.

Zaharieva, I., & Dau, H. (2019). Energetics and Kinetics of S-State Transitions Monitored by Delayed Chlorophyll Fluorescence. *Frontiers in Plant Science*, *10*, ARTN 386.

Zaharieva, I., Dau, H., & Haumann, M. (2016). Sequential and coupled proton and electron transfer events in the S_2 -> S_3 transition of photosynthetic water oxidation revealed by time-resolved X-ray absorption spectroscopy. *Biochemistry*, *55*(50), 6996-7004.

Zaharieva, I., Grabolle, M., Chernev, P., & Dau, H. (2013). Water oxidation in photosystem II: Energetics and kinetics of intermediates formation in S_2->S_3 and S_3->S_0 transitions monitored by delayed chlorophyll fluorescence. In T. Kuang, C. Lu, & L. Zhang (Eds.), *Photosynthesis Research for Food, Fuel and Future* (pp. 234-238). Springer.

Zapata, M., Garrido, J. L., & Jeffrey, S. W. (2006). Chlorophyll c pigments: current status. In *Chlorophylls and bacteriochlorophylls* (pp. 39-53). Springer.

Zheng, Y., Xue, C., Chen, H., He, C., & Wang, Q. (2020). Low-temperature adaptation of the snow alga Chlamydomonas nivalis is associated with the photosynthetic system regulatory process. *Frontiers in Microbiology*, *11*, 1233.

Zouni, A., Witt, H. T., Kern, J., Fromme, P., Krauss, N., Saenger, W., & Orth, P. (2001). Crystal structure of photosystem II from *Synechococcus elongatus* at 3.8 Å resolution. *Nature*, *409*(6821), 739-743.

Appendix A – Buffer Compositions

A.1 Buffer composition for the preparation of BBY

Buffer A (pH 7.5)	
Sucrose	400 mM
HEPES	25 mM
EDTA	1 mM
NaCl	15 mM
$MgCl_2$	5 mM
$CaCl_2$	5 mM
BSA	2 g l^{-1}
Sodium Ascorbate	1 g l^{-1}

Note: For Buffer A the BASA and Sodium Ascorbate are added just before use.

Buffer B (pH 6.2)	
MES	25 mM
NaCl	150 mM
MgCl2	5 mM

Buffer C (pH 6.2)	
Betain	1 M
MES	25 mM
NaCl	15 mM
$MgCl_2$	10 mM
$CaCl_2$	5 mM

Note: Triton stock solution is made of 37.5 ml of Buffer C and 12.5 ml of Triton.

Buffer D (pH 6.2)

Betaine	1 M
MES	25 mM
NaCl	15 mM
$MgCl_2$	5 mM
$CaCl_2$	5 mM

A.2 Buffers for isolation of thylakoid membranes from *Synechocystis* sp. PCC 6803

Buffer TMB (pH 6.0)
(0.45 µm filtered)

MES	50 mM
Glycerol	10% (v/v)
Betaine	1.2 M
$MgCl_2$	5 mM
$CaCl_2$	5 mM

Buffer TMS (pH 6.0)
(0.45 µm filtered)

MES	50 mM
Glycerol	10% (v/v)
Betaine	1.2 M
$MgCl_2$	5 mM
$CaCl_2$	20 mM

A.3 Buffer composition for the O_2 activity measurement

Buffer O_2 (pH 6.2)	
Betaine	1 M
MES	25 mM
NaCl	15 mM
$CaCl_2$	5 mM

Note: The stock solutions of $K_3[Fe(CN)_6]$ in H_2O and 2,6-DCBQ in DMSO also used for the used O_2 activity measurement should both have a concentration of 50 mM.

A.4 O_2 polarography measurement Buffers

Used for the experiments described in Chapter 3

Buffer NC (pH 7.5)	
Betaine	1 M
MES	25 mM
MOPS	25 mM
HEPES	25 mM
$MgCl_2$	5 mM
$CaCl_2$	5 mM
NaCl	150 mM

Buffer NH (pH 7.5)

Betaine	1 M
MES	25 mM
MOPS	25 mM
HEPES	25 mM
$MgCl_2$	5 mM
$CaCl_2$	5 mM
NH_4Cl	150 mM

Used for the measurement of thylakoid membranes from cyanobacteria as described in Chapters 5-6.

Buffer D-NaCl (pH 6.2)

Betaine	1 M
MES	25 mM
NaCl	150 mM
$MgCl_2$	5 mM
$CaCl_2$	5 mM

Appendix B – Schematics

B.1 Schematics for the LED housing (Top part)

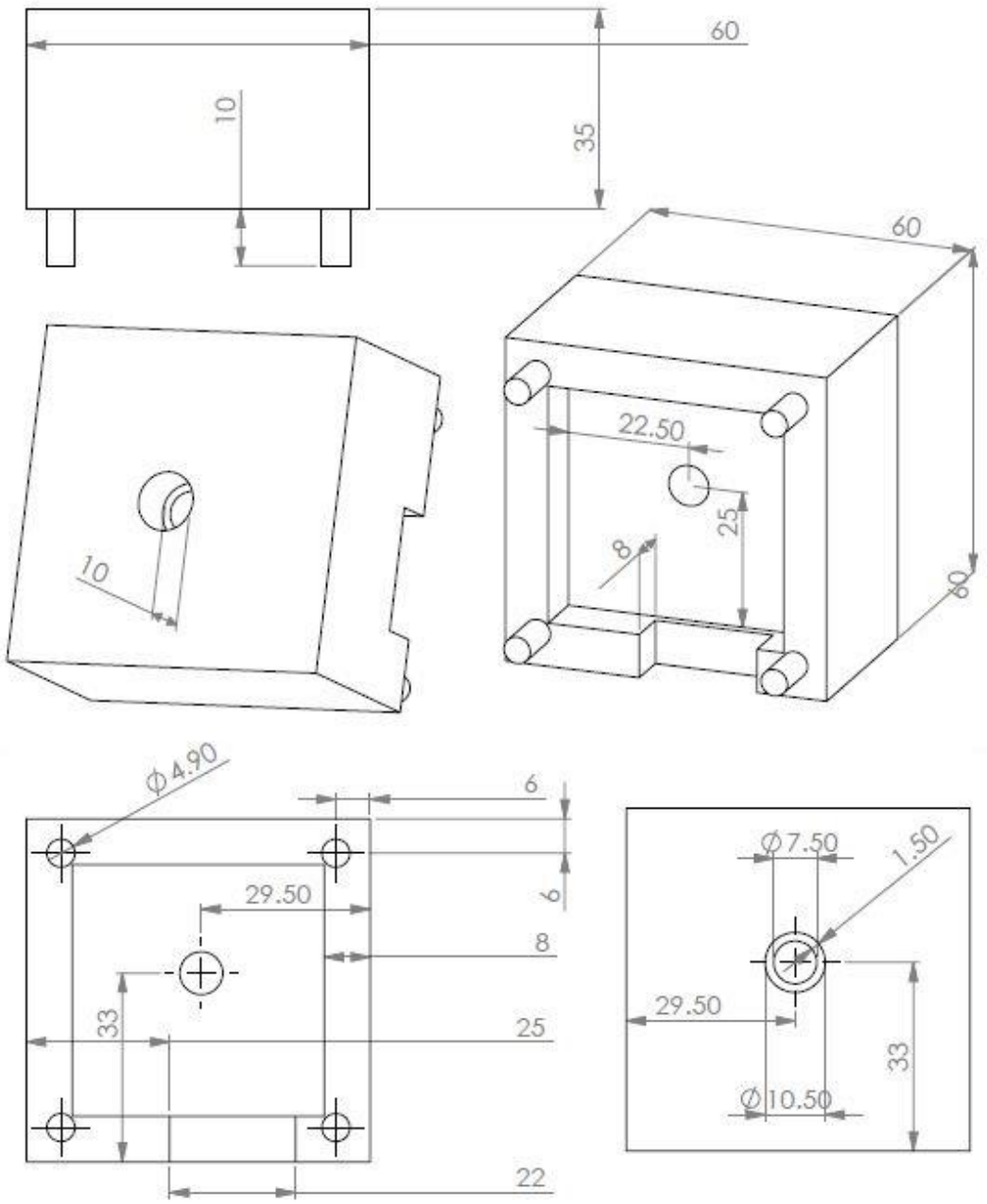

B.2 Schematics for the LED housing (Base)

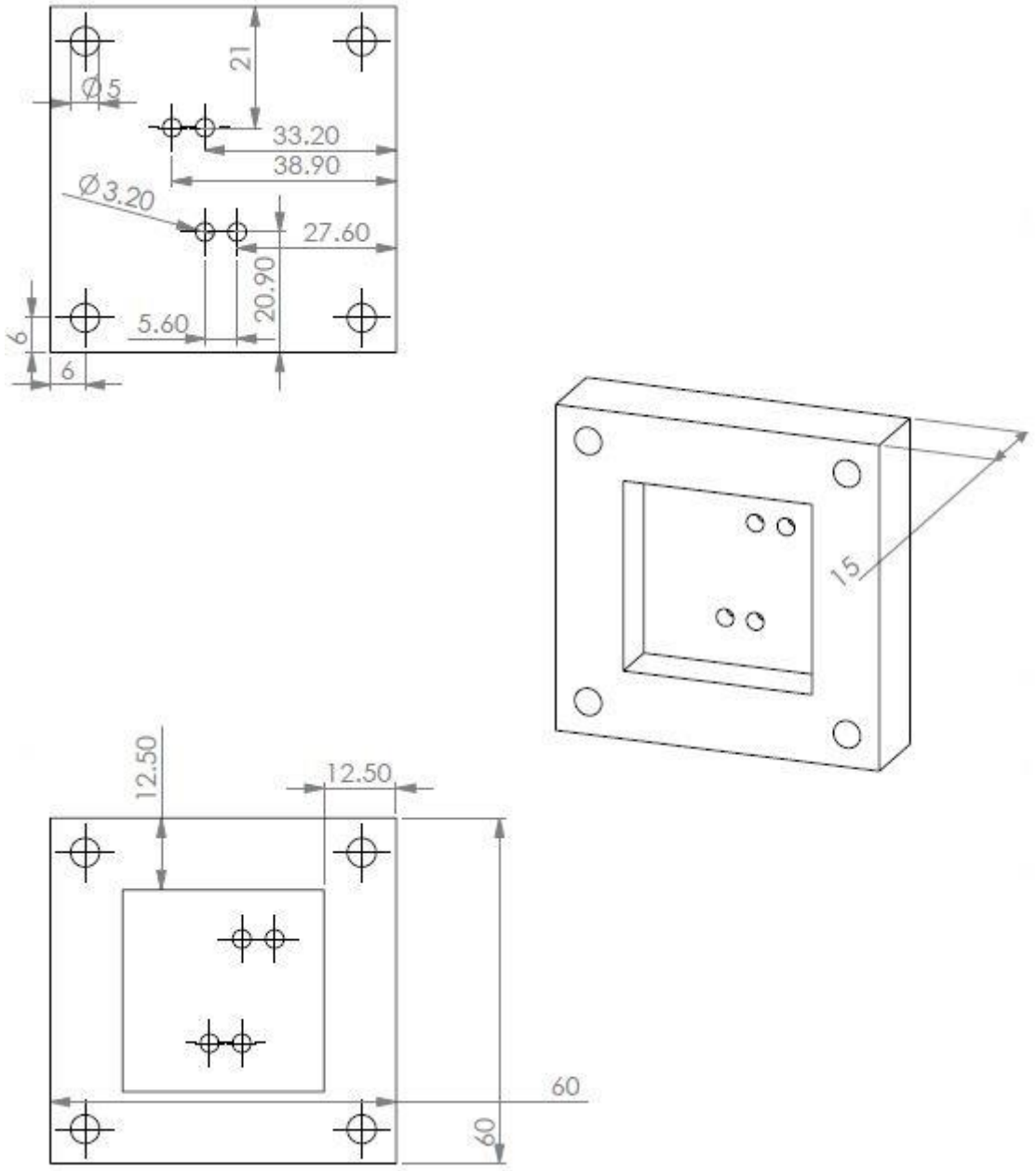

B.3 Schematics: Top body part of the polarography electrode

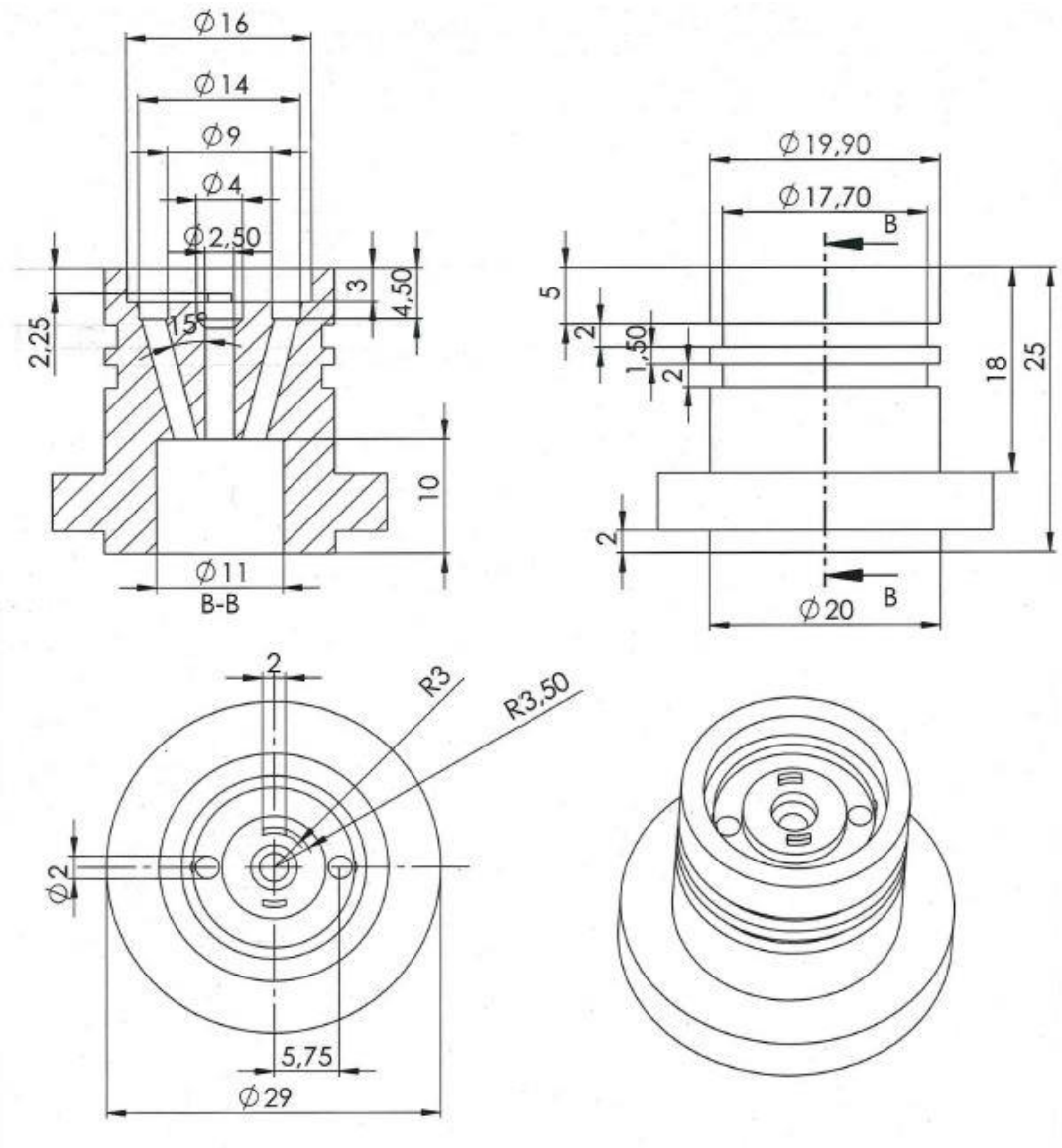

B.4 Schematics: Middle body part of the polarography electrode

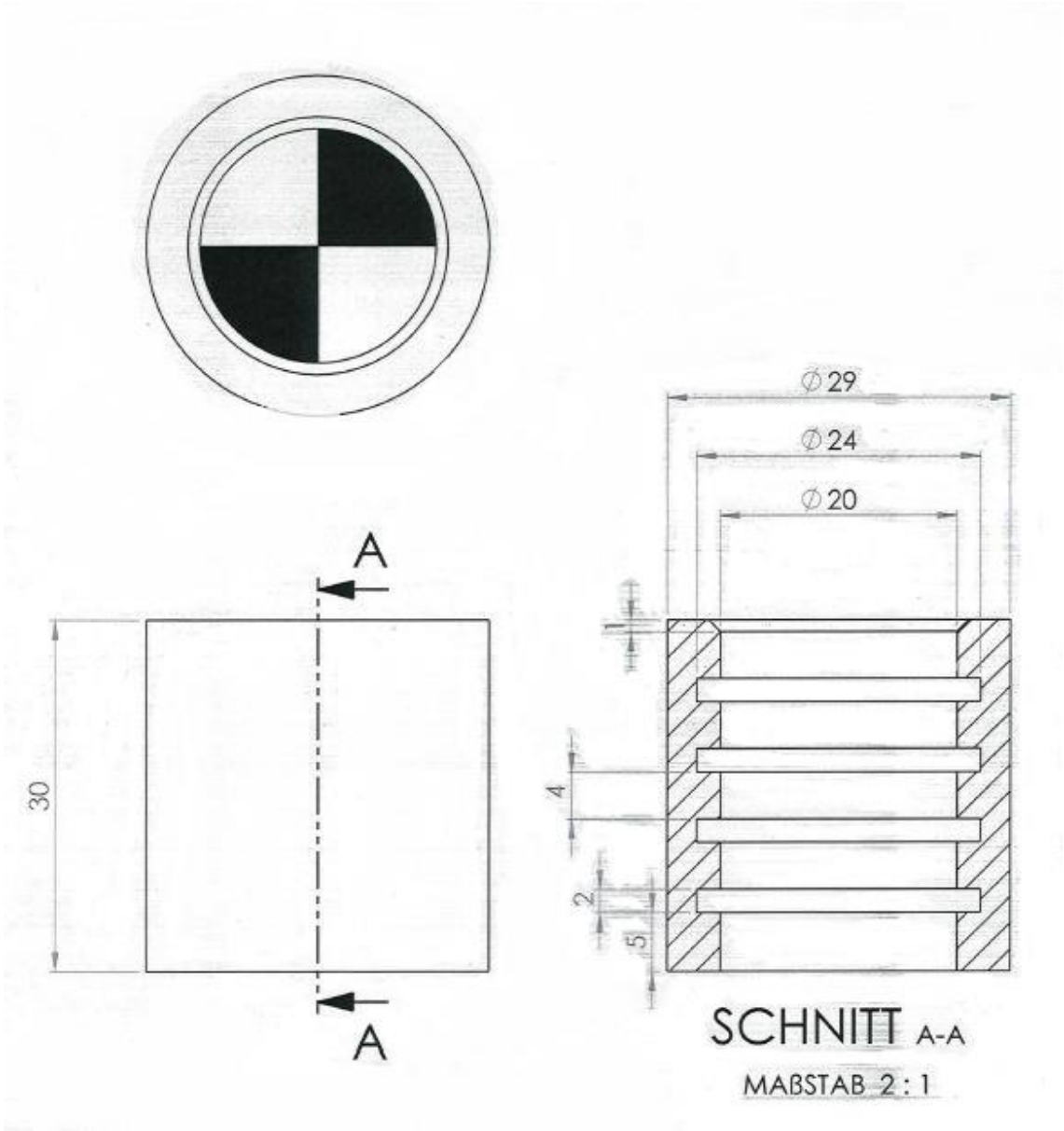

B.5 Schematics: Bottom body part of the polarography electrode

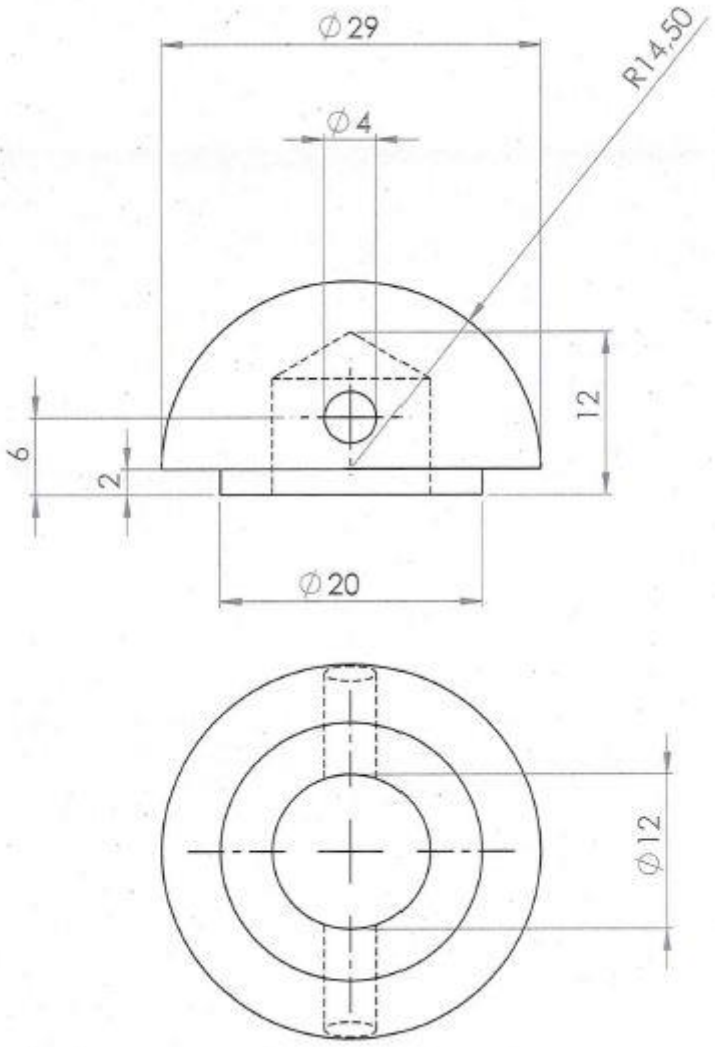

B.6 Schematics: Polarography electrode metal parts

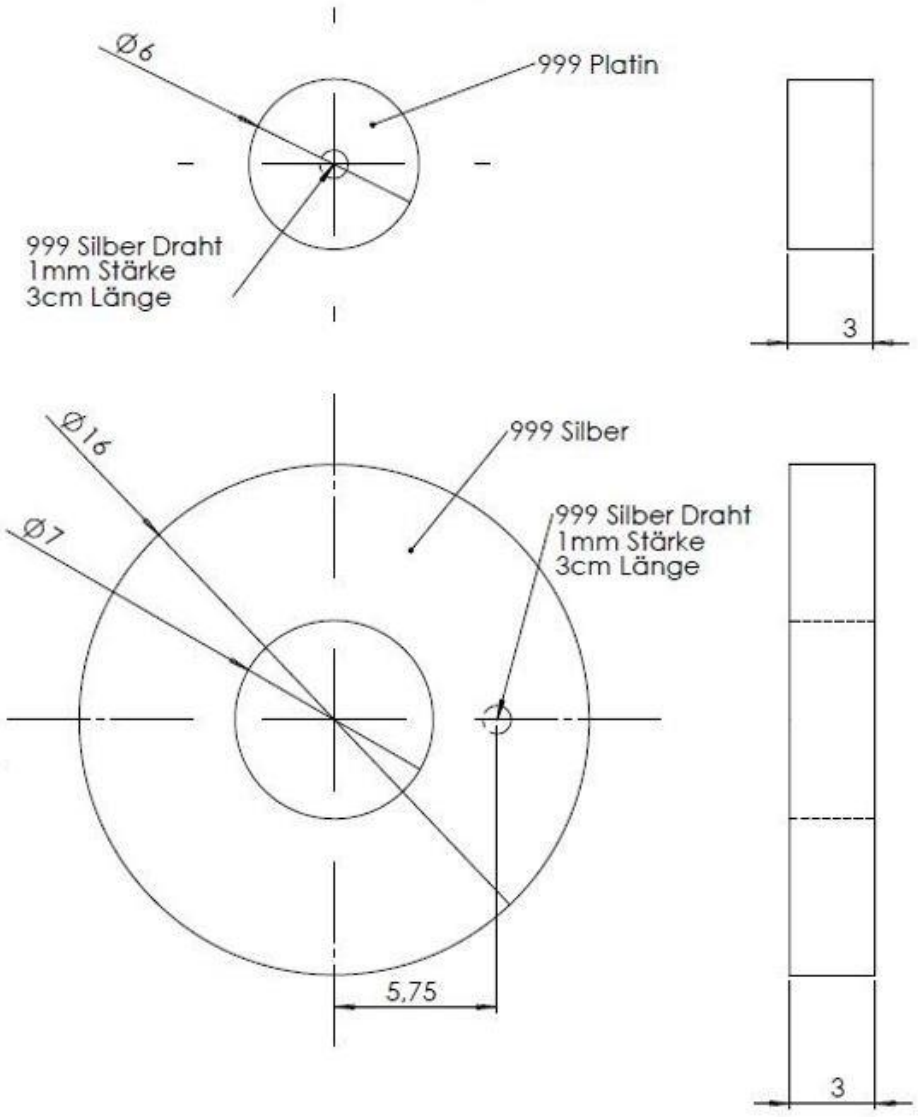

Appendix C – EXAFS simulation parameters

Table C.1 – EXAFS simulation parameters for each temperature point[a]

Temperature (K)		Mn-O	Mn-N/O	Mn-Mn	Mn-Mn/Ca	Mn-C/N/O	Mn-Mn/Ca	R_f (%)
20	**R**	1.829	2.015	2.734	3.222	2.986	3.763	7.5
	N	3.75*	2*	1.5*	1*	2*	0.5*	
	$2s^2$	8.01#	8.01#	3.64	11.12&	11.12&	11.12&	
36.5	**R**	1.835	2.003	2.727	3.224	3.042	3.765	11.8
	N	3.75*	2*	1.5*	1*	2*	0.5*	
	$2s^2$	1.047#	1.047#	4.8	14.73&	14.73&	14.73&	
55.8	**R**	1.831	2.006	2.731	3.262	2.997	3.747	9.6
	N	3.75*	2*	1.5*	1*	2*	0.5*	
	$2s^2$	8.66#	8.66#	3.34	11.66&	11.66&	11.66&	
76.3	**R**	1.83	2.015	2.74	3.244	2.993	3.761	8.5
	N	3.75*	2*	1.5*	1*	2*	0.5*	
	$2s^2$	8.14#	8.14#	3.66	11.68&	11.68&	11.68&	
95	**R**	1.83	2.001	2.732	3.252	2.964	3.769	9.1
	N	3.75*	2*	1.5*	1*	2*	0.5*	
	$2s^2$	9.15#	915#	3.41	10.48&	10.48&	10.48&	
116.7	**R**	1.829	1.992	2.732	3.288	3.039	3.721	12.5
	N	3.75*	2*	1.5*	1*	2*	0.5*	
	$2s^2$	8.58#	9.58#	3.18	10.51&	10.51&	10.51&	
137.1	**R**	1.83	2	2.736	3.204	2.92	3.743	11.7
	N	3.75*	2*	1.5*	1*	2*	0.5*	
	$2s^2$	10.36#	10.36#	2.59	13.70&	13.70&	13.70&	
156	**R**	1.83	2.002	2.73	3.288	2.998	3.735	14.7
	N	3.75*	2*	1.5*	1*	2*	0.5*	
	$2s^2$	8.19#	8.19#	4.07	11.91&	11.91&	11.91&	
175.5	**R**	1.83	2.004	2.742	3.26	2.979	3.77	9.1
	N	3.75*	2*	1.5*	1*	2*	0.5*	
	$2s^2$	7.73#	7.73#	2.9	10.51&	10.51&	10.51&	
196.7	**R**	1.829	1.974	2.742	3.297	3.008	3.702	8.7
	N	3.75*	2*	1.5*	1*	2*	0.5*	
	$2s^2$	9.19#	9.19#	2.88	9.96&	9.96&	9.96&	
215.5	**R**	1.831	1.995	2.741	3.272	2.973	3.761	10.4
	N	3.75*	2*	1.5*	1*	2*	0.5*	
	$2s^2$	9.17#	9.17#	3.3	11.51&	11.51&	11.51&	

236.9	**R**	1.827	1.983	2.746	3.265	3.032	3.717	14.4
	N	3.75*	2*	1.5*	1*	2*	0.5*	
	$2s^2$	9.86#	9.86#	5.9	10.33&	10.33&	10.33&	
255.7	**R**	1.831	2.015	2.739	3.262	2.966	3.785	8.8
	N	3.75*	2*	1.5*	1*	2*	0.5*	
	$2s^2$	10.37#	10.37#	5.23	13.31&	13.31&	13.31&	
276	**R**	1.829	2.002	2.733	3.217	2.914	3.783	10.6
	N	3.75*	2*	1.5*	1*	2*	0.5*	
	$2s^2$	12.79#	12.79#	7.85	15.42&	15.42&	15.42&	
292.7	**R**	1.834	2.015	2.736	3.292	2.984	3.751	12.6
	N	3.75*	2*	1.5*	1*	2*	0.5*	
	$2s^2$	13.04#	13.04#	8.98	18.16&	18.16&	18.16&	

[a]Fit results for the 15 Mn EXAFS spectrums of PSII in the S_1 state in the studied temperature range (20-295 K). N, coordination number per Mn; R, interatomic distance in Å; σ^2, Debye-Waller parameter in x10^3 $Å^2$; R_F, deviation in % between the fit curve and the Fourier-backtransformed k-space spectrum in a 1-3.5 Å reduced distance range. In the simulations, an amplitude reduction factor of S_0^2 = 0.75 and the following fit restraints were used: *, fixed N-values resembling the crystallographic metrics (Tanaka et al., 2017); #,&, coupled to yield equal values.

Appendix D – Comparison of O_2 polarography transients

D.1 *T.elongatus*, *M. laminosus* and *C. nivalis*

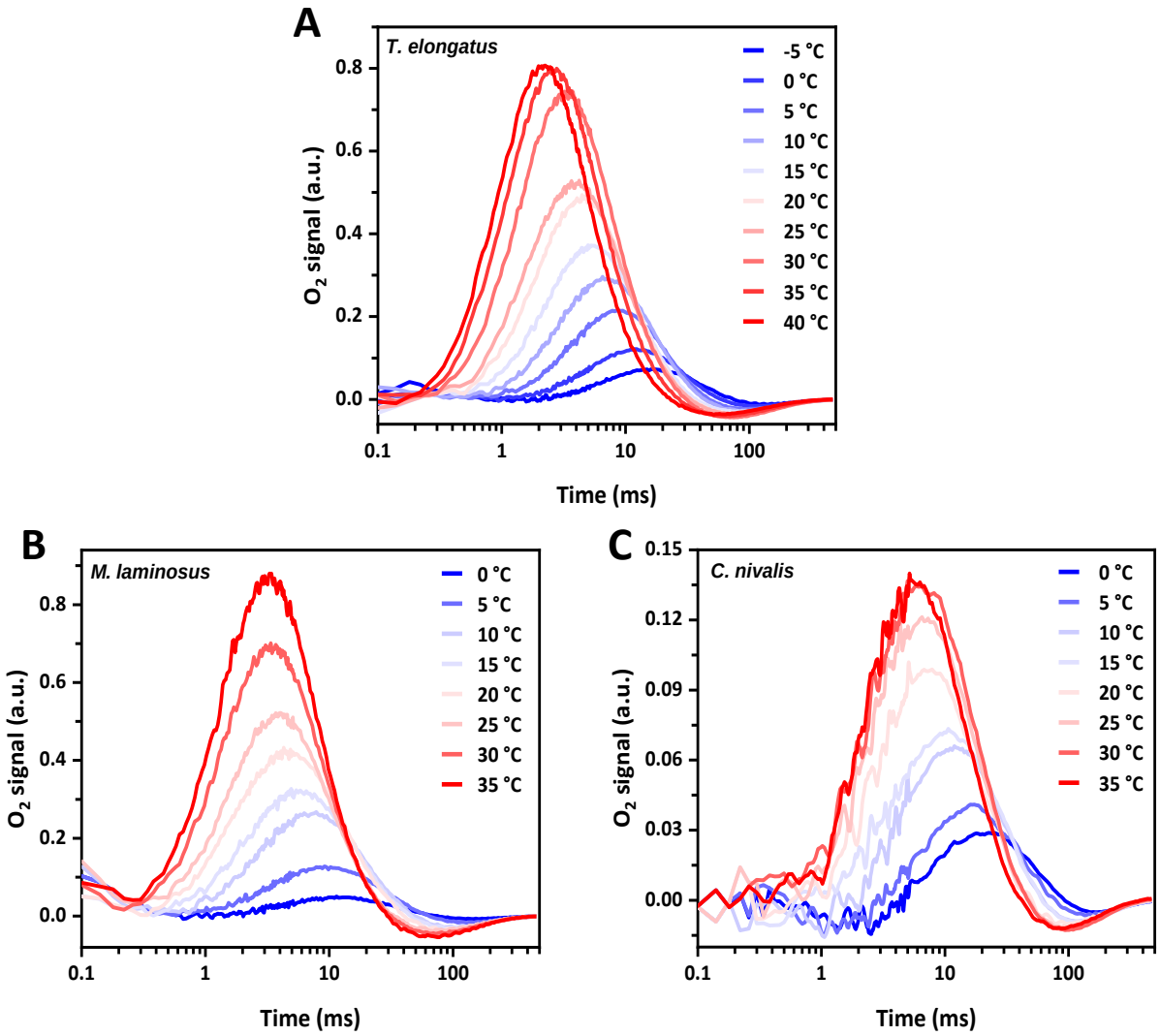

Figure D.1 – O_2-evolution transients obtained at various temperatures for thylakoid membranes from *T. elongatus (A)*, *M. laminosus* (C) and *C. nivalis (E)*. The temperature range was -5-40 °C for *T. elongatus* and 0-35°C for the other two. The measurements were performed using the red LED from time resolved O_2 polarography set-up. The kinetics are the average of 230 individual transients measured after each flash, summed up from three independent experiments on each condition.

D.2 *C. thermalis* WL vs. FRL

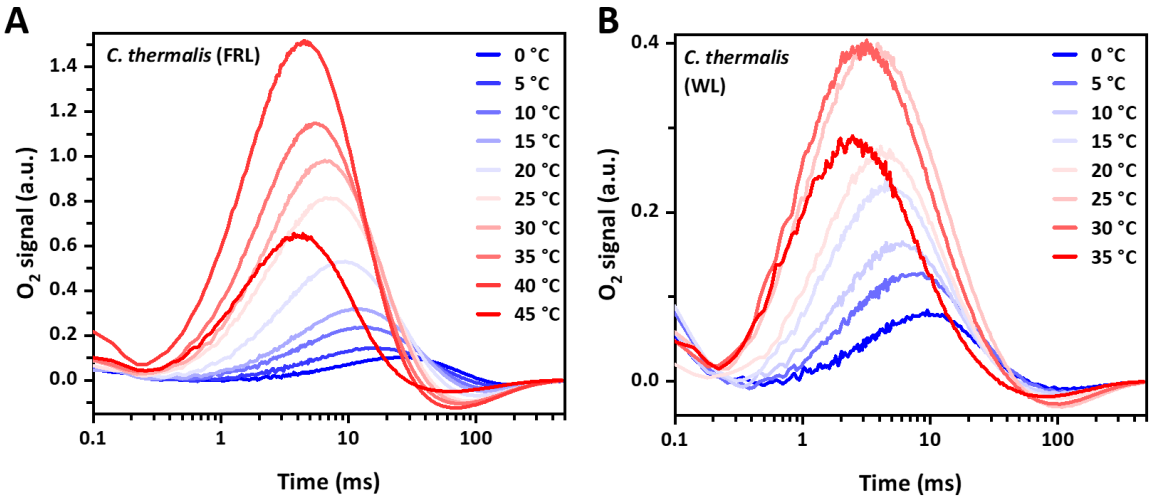

Figure D.2 – O_2-evolution transients obtained at various temperatures for thylakoid membranes from *C. thermalis* grown under FRL *(A*) and grown under WL (B). The temperature range was 0-45 °C for the FRL and 0-35°C for WL. The measurements were performed using the red LED from time resolved O_2 polarography set-up. The kinetics are the average of 230 individual transients measured after each flash, summed up from three independent experiments on each condition.

Appendix E – Fit parameters of the O_2 diffusion model

E.1 *Synechocystis* sp. PCC 6803 variants

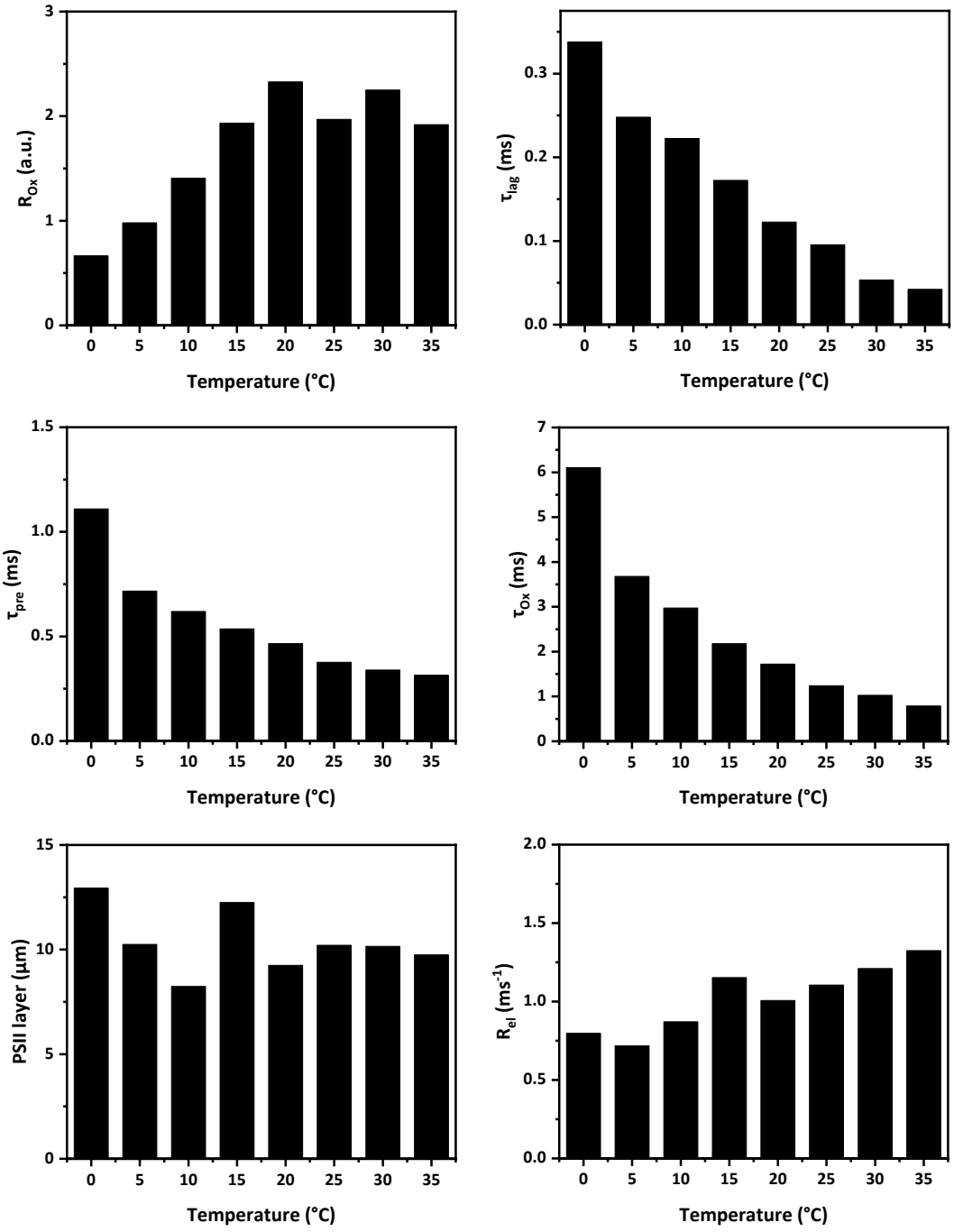

Figure E.1.1 – Fit parameters obtained employing the diffusion model (Dilbeck et al., 2012) for *Synechocystis* sp. PCC 6803 wilde type.

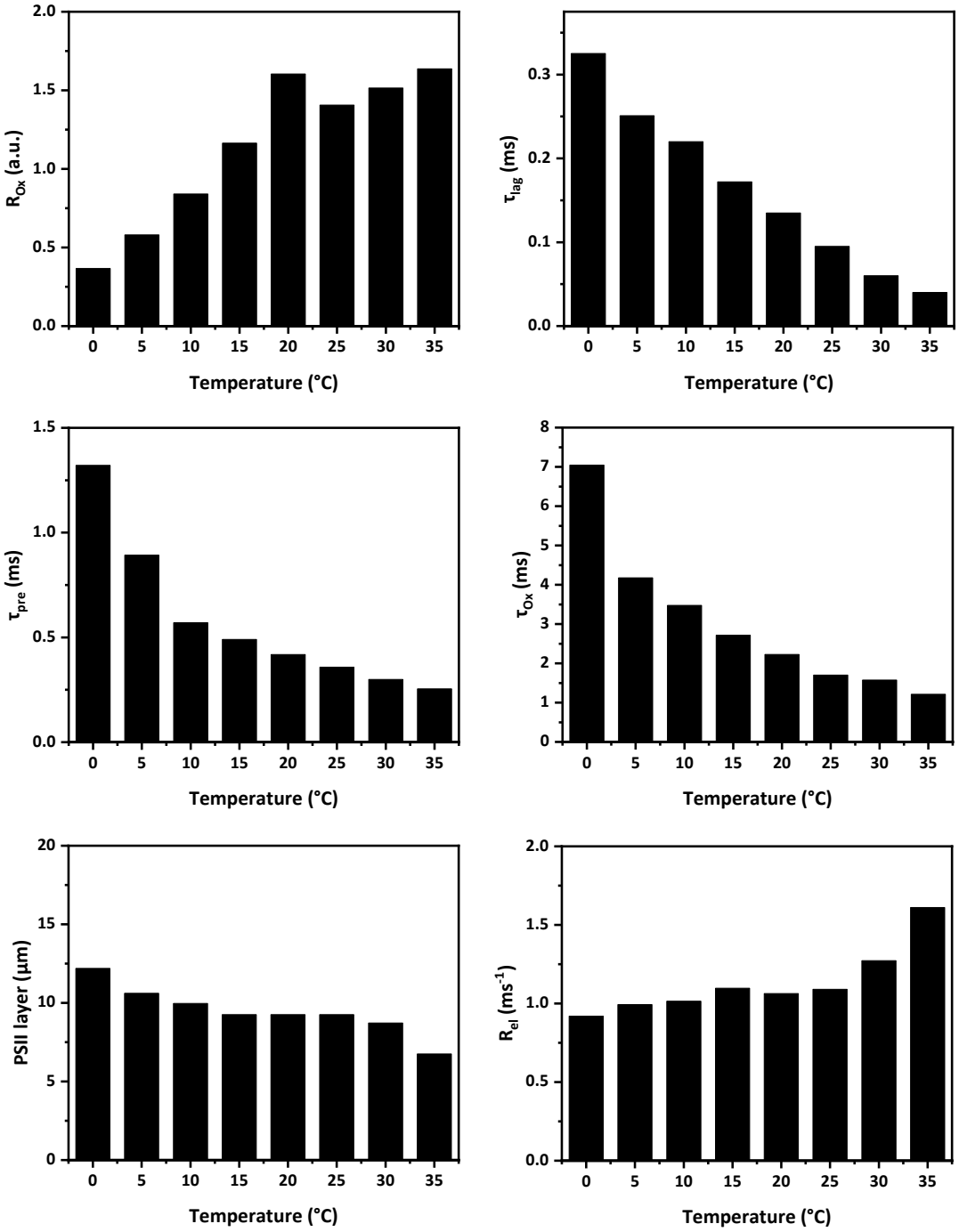

Figure E.1.2 – Fit parameters obtained employing the diffusion model (Dilbeck et al., 2012) for *Synechocystis* sp. PCC 6803 variant E312A.

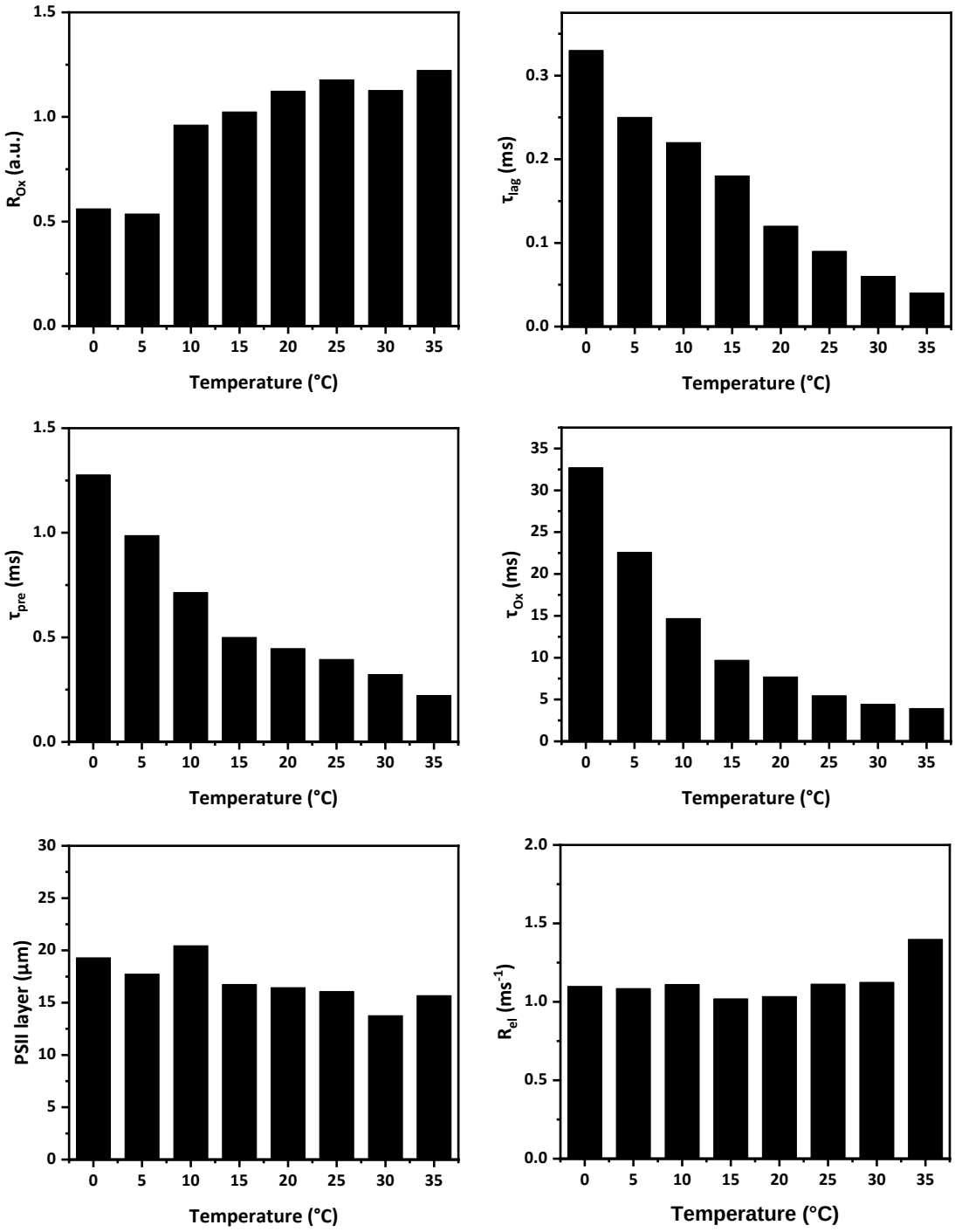

Figure E.1.3 – Fit parameters obtained employing the diffusion model (Dilbeck et al., 2012) for *Synechocystis* sp. PCC 6803 variant D61K.

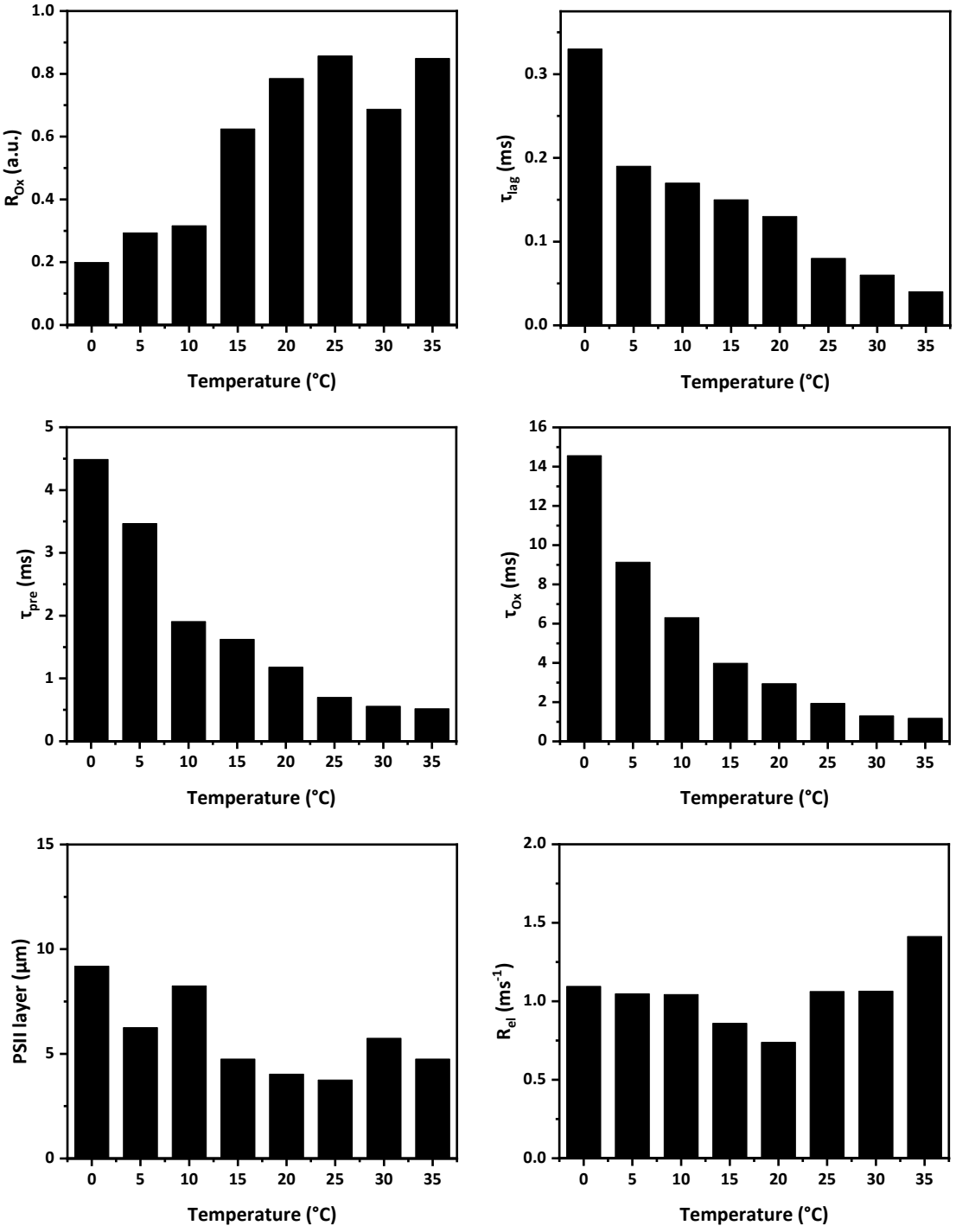

Figure E.1.4 – Fit parameters obtained employing the diffusion model (Dilbeck et al., 2012) for *Synechocystis* sp. PCC 6803 variant D59A.

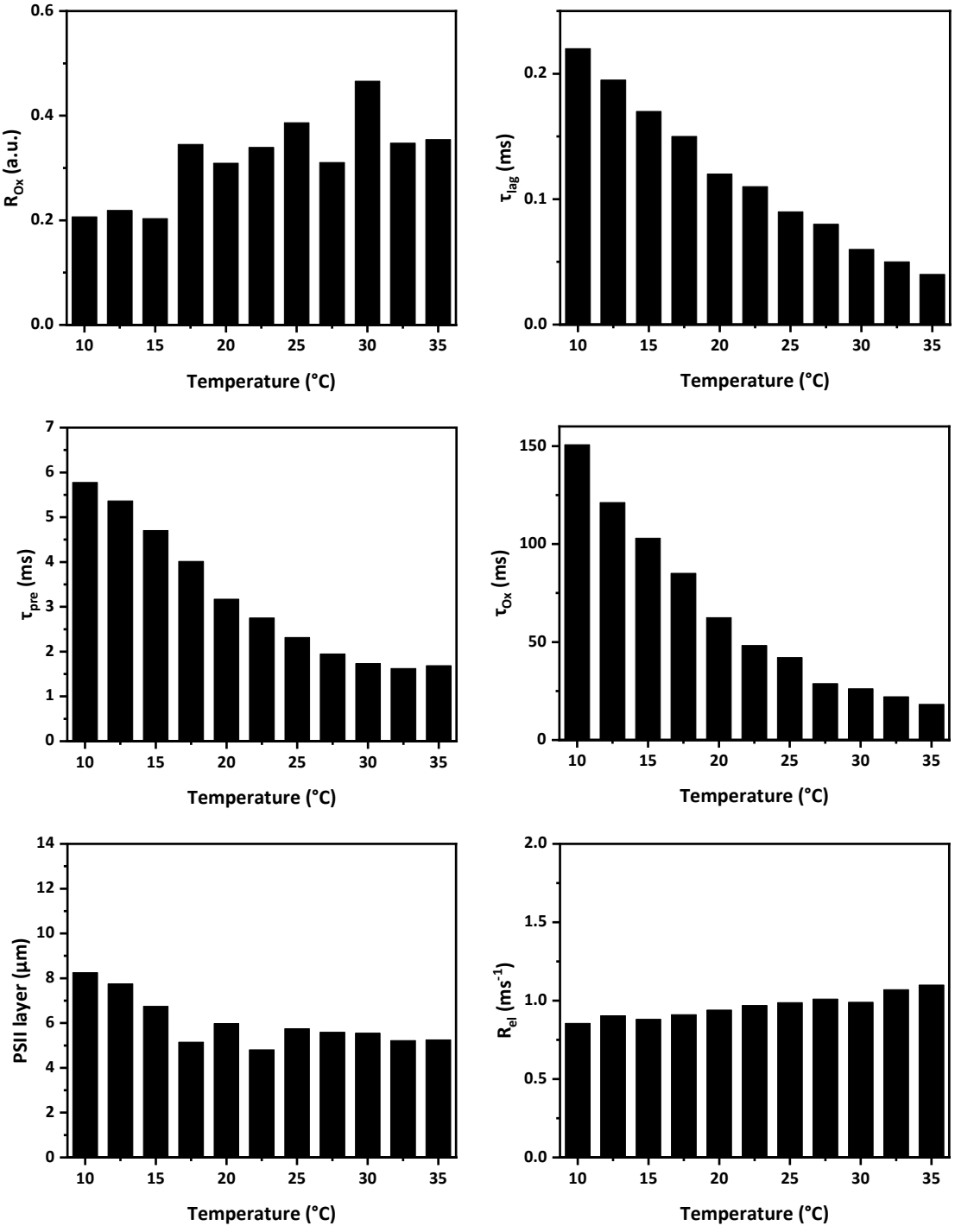

Figure E.1.5 – Fit parameters obtained employing the diffusion model (Dilbeck et al., 2012) for *Synechocystis* sp. PCC 6803 variant E65A.

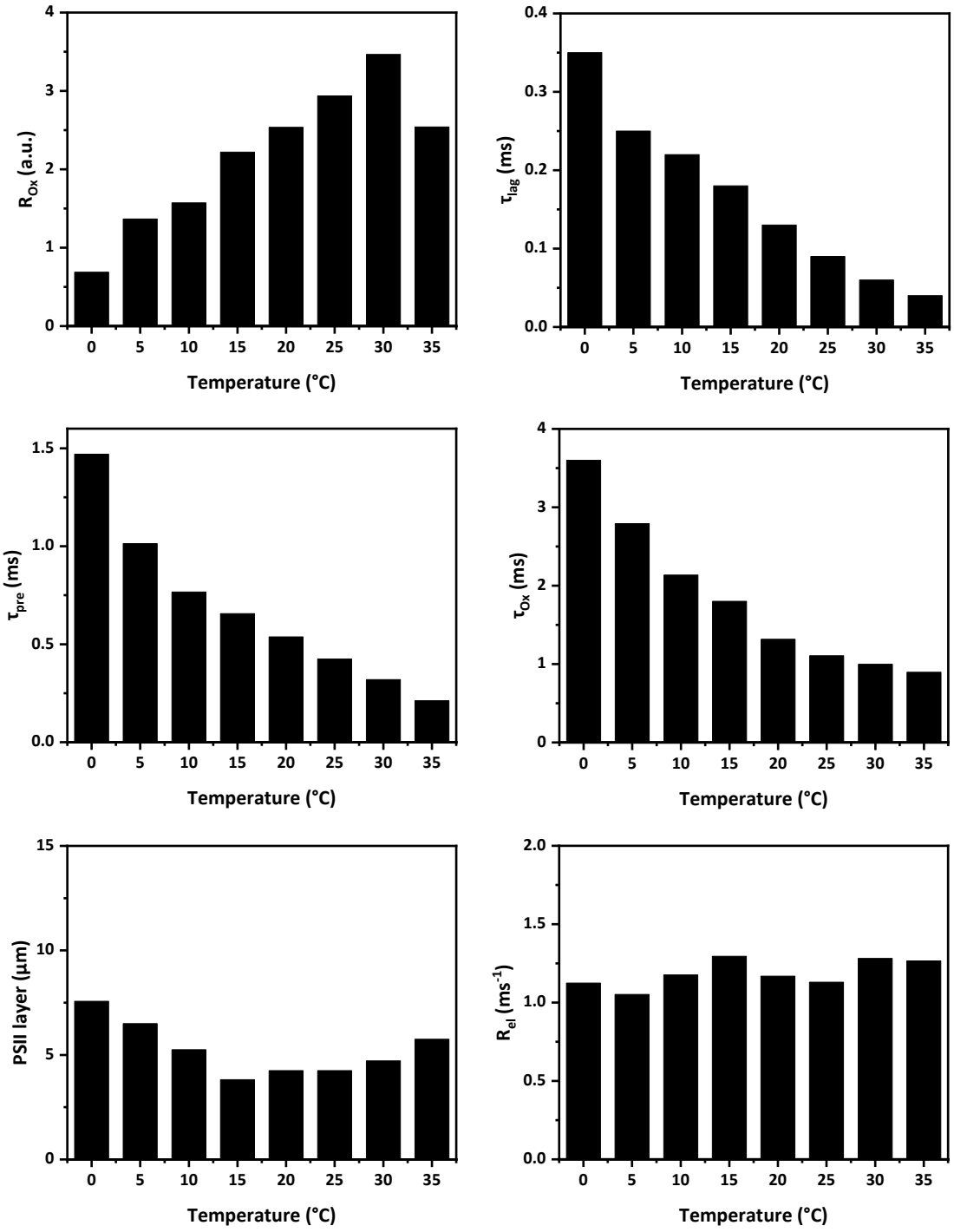

Figure E.1.6 – Fit parameters obtained employing the diffusion model (Dilbeck et al., 2012) for *Synechocystis* sp. PCC 6803 variant E329A.

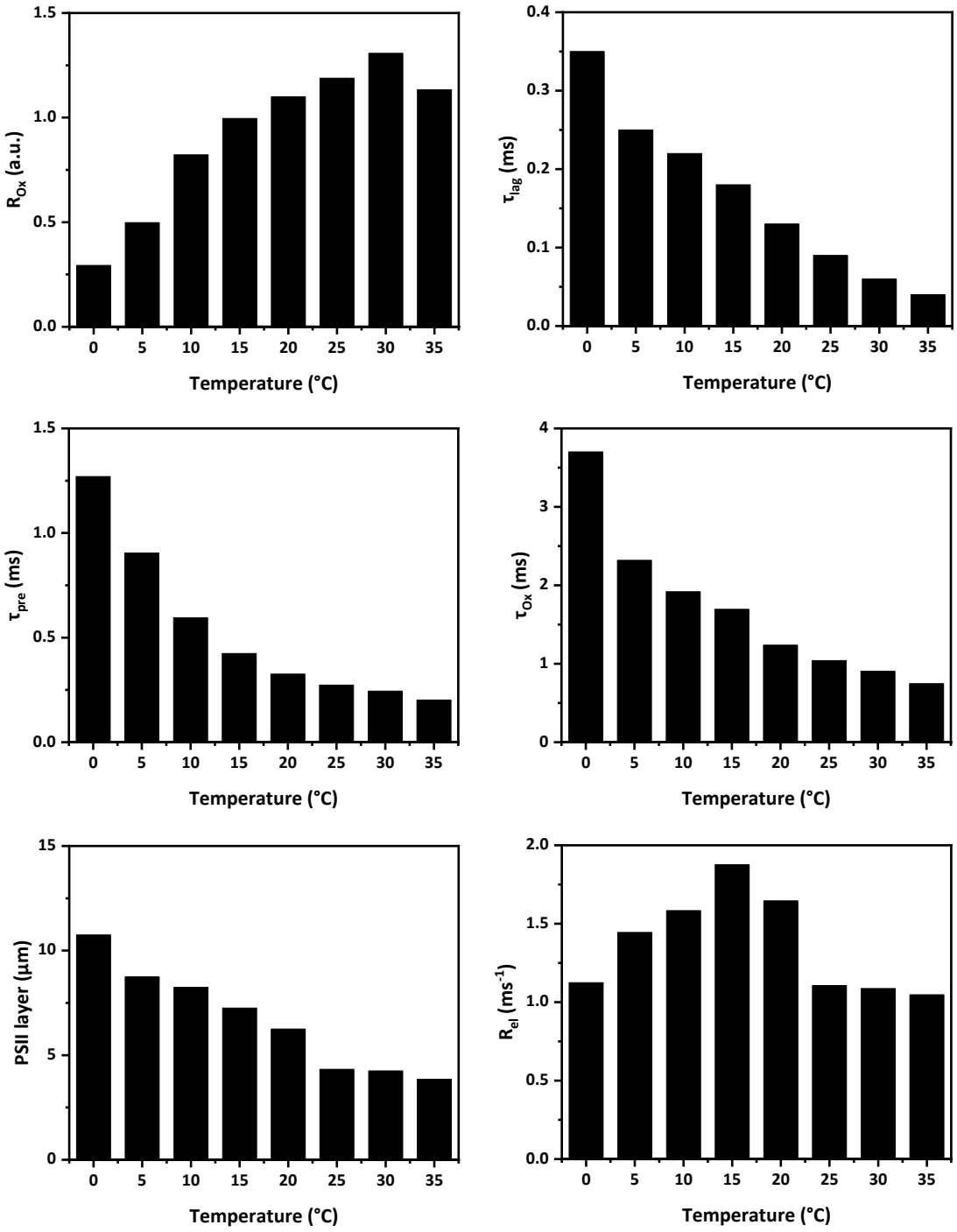

Figure E.1.7 – Fit parameters obtained employing the diffusion model (Dilbeck et al., 2012) for *Synechocystis* sp. PCC 6803 variant N298A.

E.2 *C. thermalis* WL and FRL

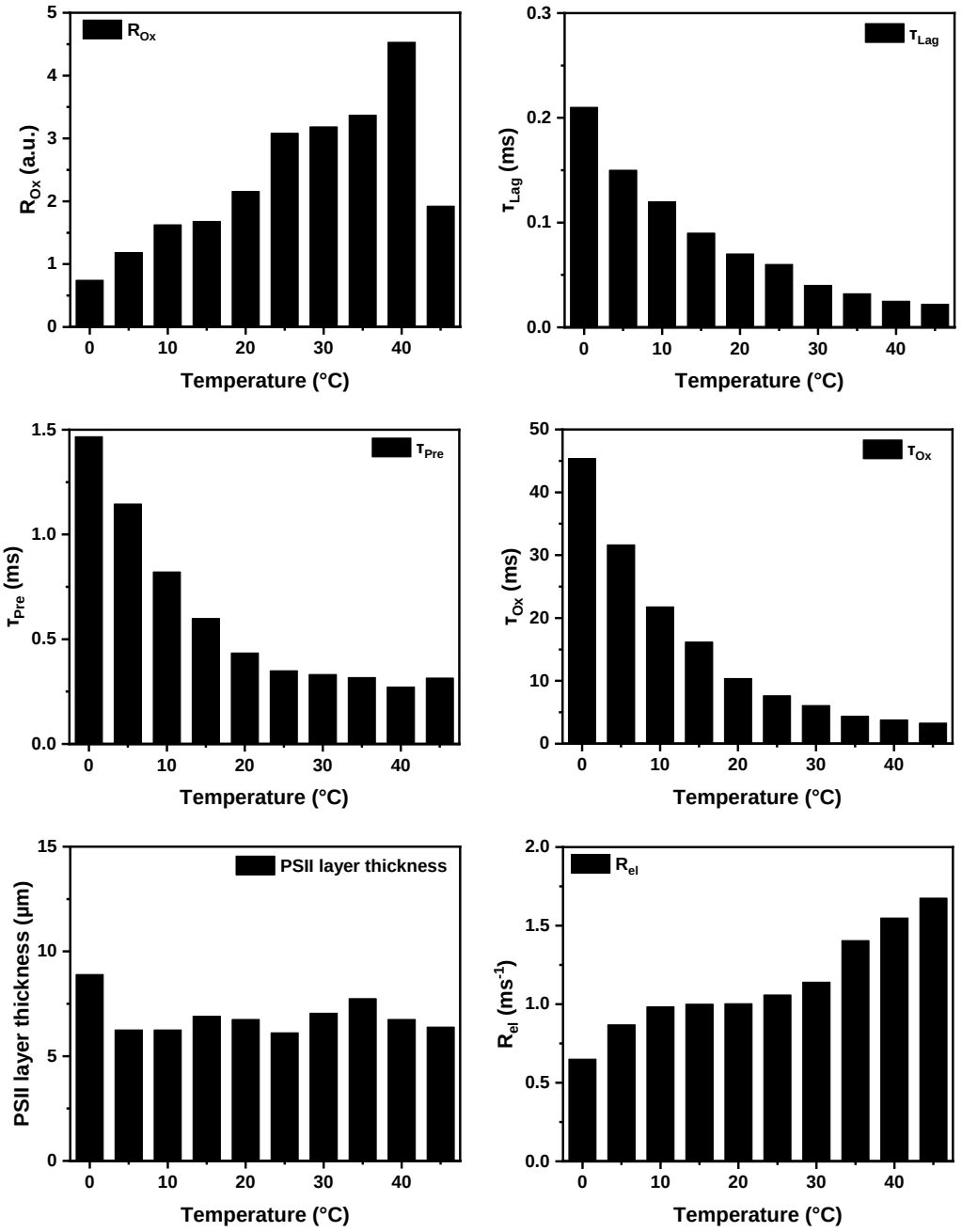

Figure E.2.1 – Fit parameters obtained from the simulations with the diffusion model (Dilbeck et al., 2012) for *C. thermalis* grown in FRL.

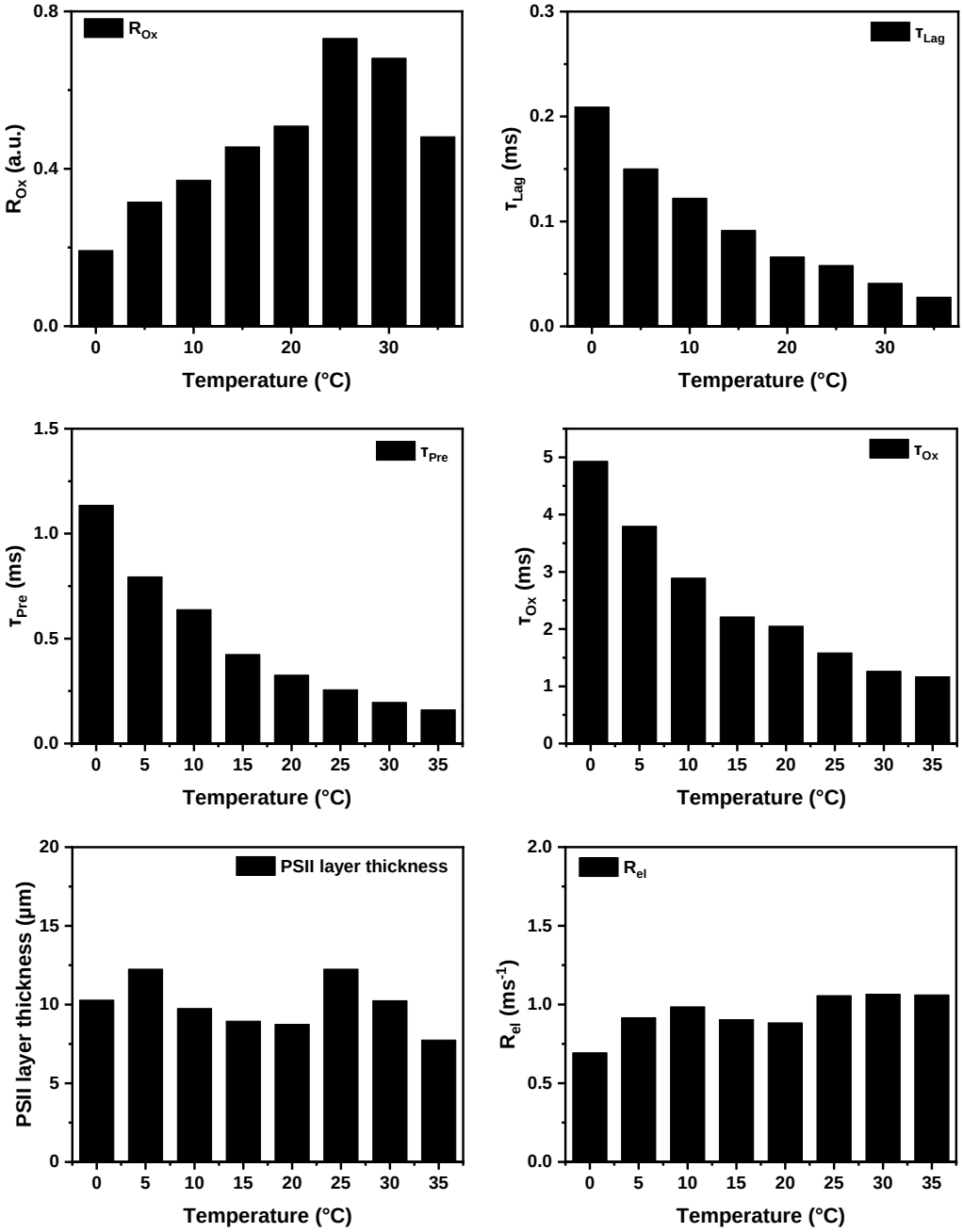

Figure E.2.2 – Fit parameters obtained from the simulations with the diffusion model (Dilbeck et al., 2012) for *C. thermalis* grown in WL.

E.3 *T.elongatus*, *M. laminosus* and *C. nivalis*

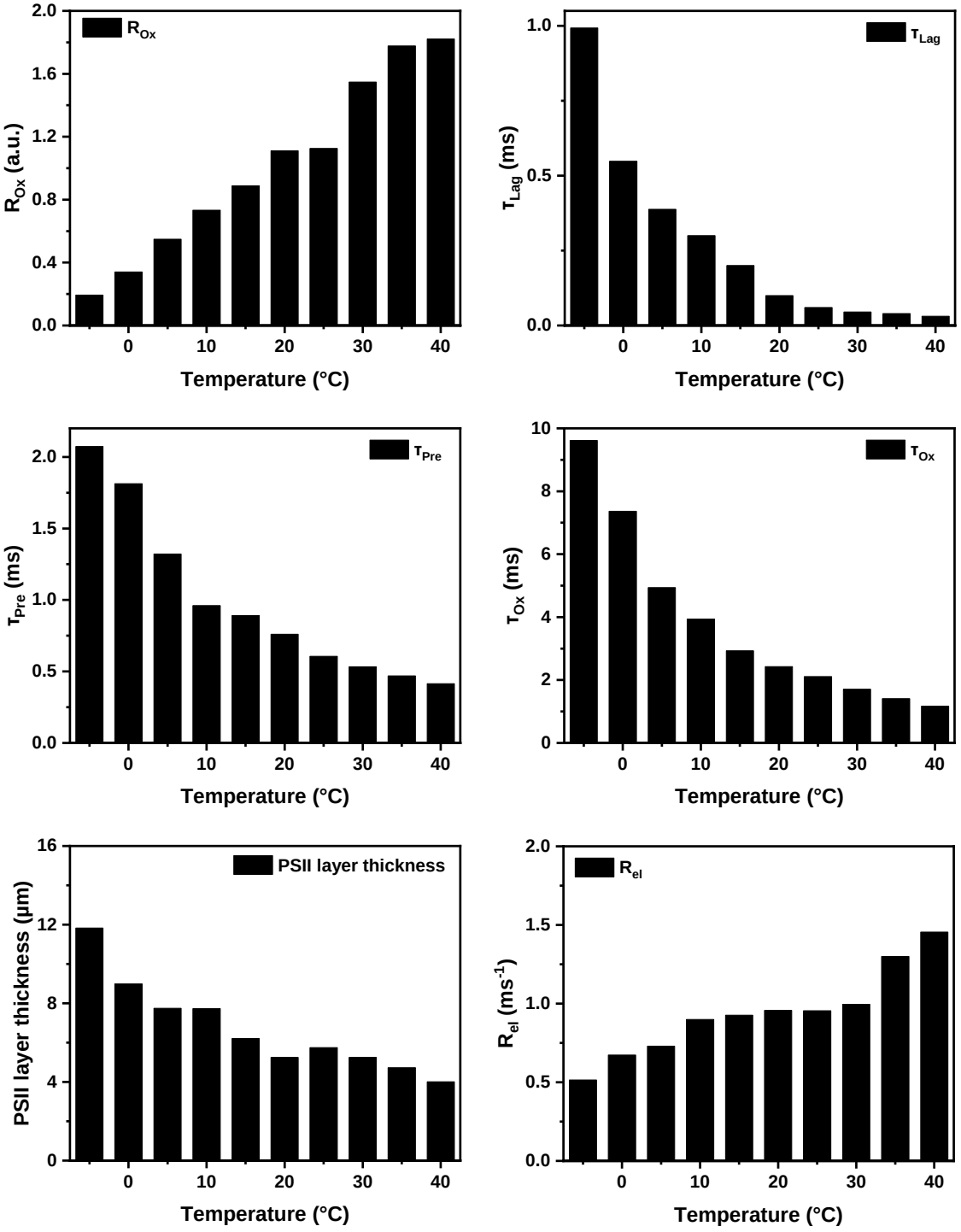

Figure E.3.1 – Fit parameters obtained from the simulations with the diffusion model (Dilbeck et al., 2012) for *T.elongatus*.

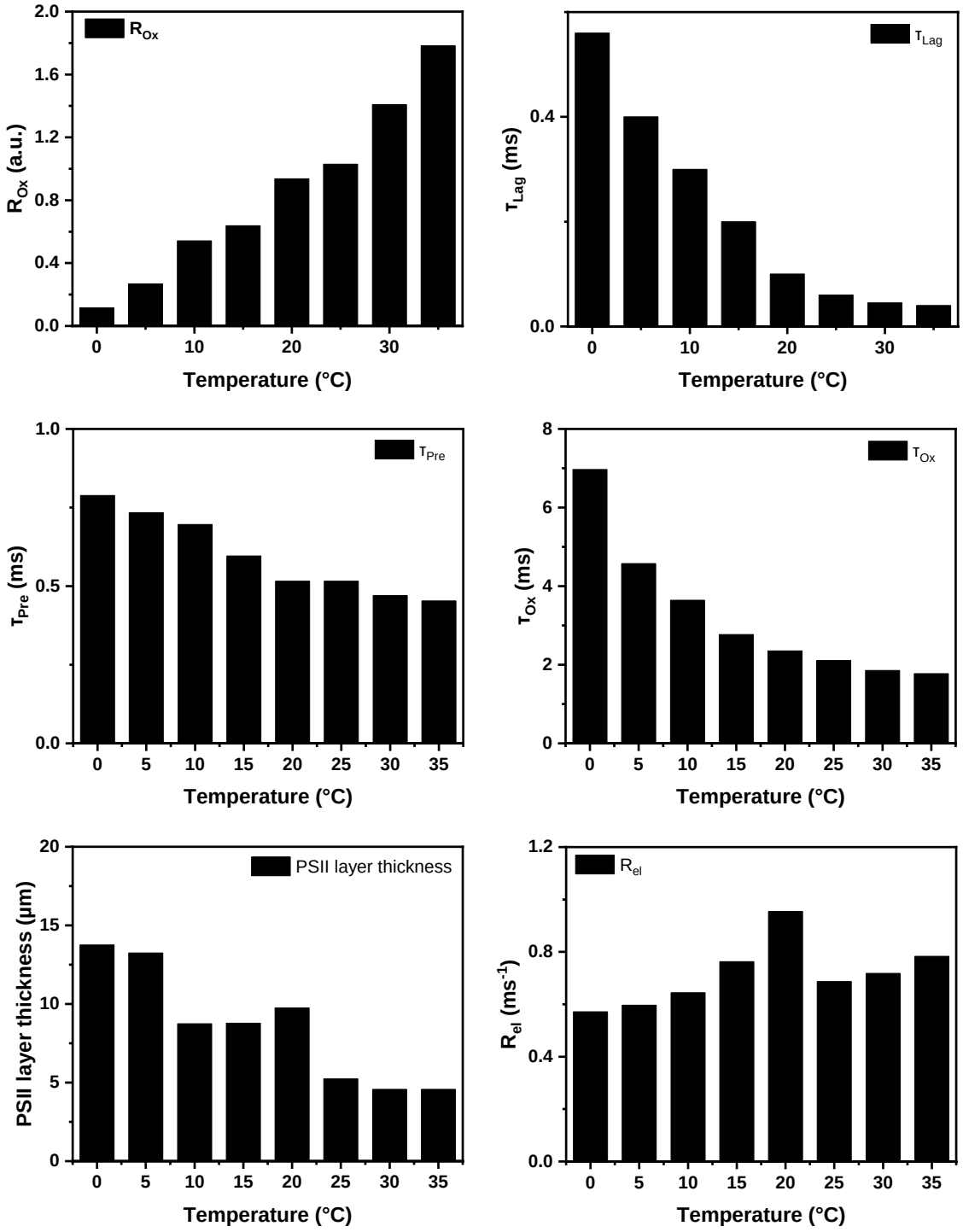

Figure E.3.2 – Fit parameters obtained from the simulations with the diffusion model (Dilbeck et al., 2012) for *M. laminosus*.

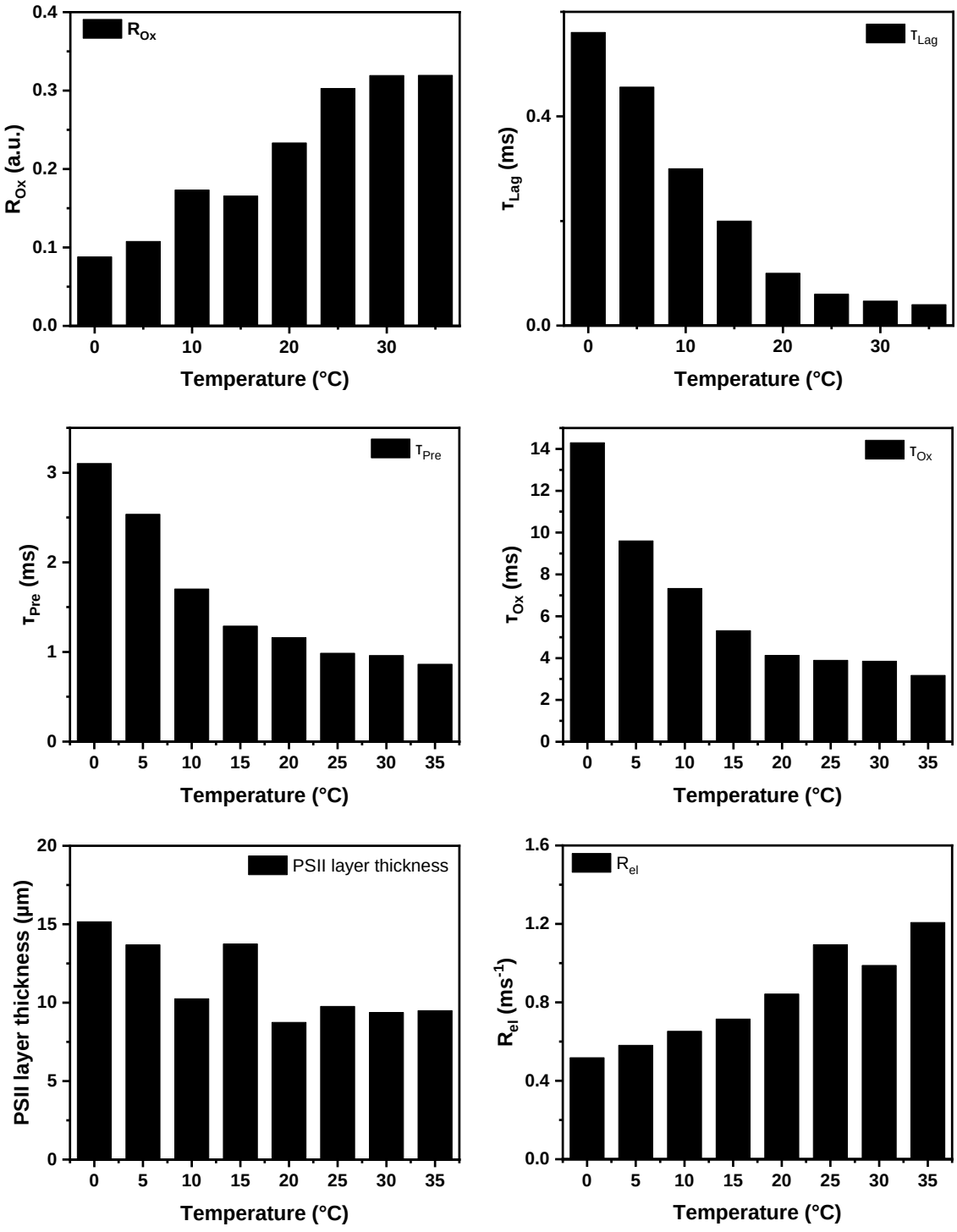

Figure E.3.3 – Fit parameters obtained from the simulations with the diffusion model (Dilbeck et al., 2012) for *C. nivalis*.

List of Publications

2023* **Glass-transition in structural dynamics at the water oxidizing complex of photosynthesis**

Ricardo Assunção, Nicolas Oliver, Dennis Nürnberg, Ivelina Zaharieva, Michael Haumann, Holger Dau

In preparation

2022* **Photosynthetic oxygen evolution by mastering the electron-proton bottleneck**

Paul Greife, Matthias Schönborn, Matteo Capone, **Ricardo Assunção**, Daniele Narzi, Leonardo Guidoni, Holger Dau

Nature, revised version in preparation

preprint available at Research Square: https://doi.org/10.21203/rs.3.rs-1210297/v1

2022 **Impact of energy limitations on function and resilience in long-wavelength Photosystem II**

Stefania Viola, William Roseby, Stefano Santabarbara, Dennis Nürnberg, **Ricardo Assunção**, Holger Dau, Julien Sellés, Alain Boussac, Andrea Fantuzzi, A William Rutherford

eLife, https://doi.org/10.7554/eLife.79890

2020 **Light-driven formation of manganese oxide by today's photosystem II supports evolutionarily ancient manganese-oxidizing photosynthesis**

Petko Chernev, Sophie Fischer, Jutta Hoffmann, Nicholas Oliver, **Ricardo Assunção**, Boram Yu, Robert L. Burnap, Ivelina Zaharieva, Dennis J. Nürnberg, Michael Haumann, Holger Dau

Nature communications, https://doi.org/10.1038/s41467-020-19852-0

* *Expected publishing year*

2019 **Ammonia as a substrate-water analogue in photosynthetic water oxidation: Influence on activation barrier of the O_2-formation step**

Ricardo Assunção, Ivelina Zaharieva, Holger Dau

Biochimica et Biophysica Acta (BBA)-Bioenergetics, https://doi.org/10.1016/j.bbabio.2019.04.005

2017 **Inhibitory and non-inhibitory NH_3 binding at the water-oxidizing manganese complex of photosystem II suggests possible sites and a rearrangement mode of substrate water molecules**

Nils Schuth, Zhiyong Liang, Matthias Schönborn, André Kussicke, **Ricardo Assunção**, Ivelina Zaharieva, Yvonne Zilliges, Holger Dau

Biochemistry, https://doi.org/10.1021/acs.biochem.7b00743

Selbständigkeitserklärung

Name: Assunção

Vorname: Ricardo

Ich erkläre gegenüber der Freien Universität Berlin, dass ich die vorliegende Dissertation selbstständig und ohne Benutzung anderer als der angegebenen Quellen und Hilfsmittel angefertigt habe. Die vorliegende Arbeit ist frei von Plagiaten. Alle Ausführungen, die wörtlich oder inhaltlich aus anderen Schriften entnommen sind, habe ich als solche kenntlich gemacht. Diese Dissertation wurde in gleicher oder ähnlicher Form noch in keinem früheren Promotionsverfahren eingereicht.

Mit einer Prüfung meiner Arbeit durch ein Plagiatsprüfungsprogramm erkläre ich mich einverstanden.

Datum: _____ Unterschrift: _____